CELLULAR AND MOLECULAR MECHANISMS OF EMPHYSEMA PATHOGENESIS

by

Jarrett Venezia

A dissertation submitted to Johns Hopkins University in conformity with the requirements for the degree of Doctor of Philosophy

Baltimore, Maryland

April 2023

Abstract

Emphysema is a progressive disease characterized by alveolar degradation, irreversible airway enlargement, and impaired gas exchange over time. We and others have theorized that innate immune cells, such as macrophages, become dysregulated in the emphysematous lung and ultimately cause long-term damage to tissue and airways. However, this claim is supported largely by circumstantial evidence, despite years of studying COPD pathogenesis in humans or mice. Herein, we applied several next-generation techniques for studying lung cell phenotypes and molecular mechanisms of disease pathogenesis in mice with elastase-induced emphysema. By the end of this Thesis, we suggest that severe damage post-elastase is likely orchestrated by a network of dysregulated immune cells; but CD63$^+$ alveolar macrophages, specifically, were identified as a candidate cell type with the functional capacity to damage lung tissue over time. Future consideration and characterization of CD63$^+$ alveolar macrophages may shed light on how dysregulated immune cells drive emphysema pathogenesis or the progression of related, degenerative diseases.

Primary Reader and Advisor: Alan Scott

Secondary Reader: Wayne Mitzner

Preface

The work presented in this dissertation is based on published and unpublished findings uncovered by James Limjunyawong and Matt Craig from the Mitzner and Scott labs, respectively, who refined our lab's experimental model for studying progressive lung damage and emphysema in mice (Craig et al., 2017; Limjunyawong et al., 2015). Highlighted in **Chapter 1**, Limjunyawong and Craig generated results that implicated lung macrophages as key innate cells that mediate emphysema-like changes in the lungs post-elastase. Molecularly, immune dysregulation was thought to be driven by three major cytokines – IL-33, IL-13, and IL-17A – each noted for enriched expression in the lung during early stages of experimental emphysema. The objective of my Thesis research was to validate and extend these findings, aiming to better understand the EIEE model and, by extension, human emphysema. We relied upon a diverse immunological toolkit for addressing concerns related to emphysema pathogenesis in mice, employing experimental designs that include use of genetic manipulation, *in vitro* cell activation, bulk and single-cell RNA sequencing, and metabolic reprograming.

Chapter 2 begins our investigation of cellular responses to IL-33, IL-13, and IL-17A by experimenting with alveolar macrophages and primary lung fibroblasts *in vitro.* Protein and RNA sequencing-based approaches were employed to support the idea that IL-33, IL-13, and IL-17A cooperatively activate lung fibroblasts, but not alveolar macrophages. The approach produced robust transcriptional readouts for characterizing novel inflammatory and wound healing phenotypes as well as providing evidence that lung fibroblasts likely play a key role in disease pathogenesis.

Chapter 3 outlines a series of findings ultimately supporting the longstanding hypothesis that progressive lung damage post-elastase is driven by innate immune mechanisms. To rigorously dissect immune pathways that drive emphysema *in vivo,* we challenged BALB/c *St2, Il13, Stat6, Il17a, Rag1, Rag2*γ_C global knockout animals with elastase doses standard to the BALB/cJ EIEE model. Some of these germline deletions prevented severe disease in mice post-elastase, but most single-gene knockouts that we studied yielded unremarkable outcomes in the EIEE model.

In **Chapter 4,** we present our interpretation of a single-cell RNA sequencing approach for uncovering novel, cellular and molecular mechanisms that drive disease progression in the EIEE model. Again focusing on lung macrophage biology, we go on to identify upregulated CD63 surface expression as a putative marker for studying an alveolar macrophage subpopulation that drives emphysema pathogenesis.

Finally, in **Chapter 5**, I will briefly discuss a series of attempts at modulating experimental emphysema severity by means of “macrophage reprogramming.” This therapeutic approach was promising in the context of modifying cell behavior within tumor microenvironments (DeNardo and Ruffell, 2019; Mantovani et al., 2022). We and others, for years, were eager to adapt these methods for modulating the severity of emphysema (Barnes and Stockle, 2005; Ogger and Byrne, 2021; Wang et al., 2020). Near the end of this chapter, I will outline the overall conclusions drawn from this body of work and detail my ideas for future directions.

Acknowledgments

Thank you for taking the time to read and assess this work, which, sentimentally, also represents years of intellectual growth and development. I had entered this program with limited skills and/or meaningful life experience but am now moderately employable and eager to contribute to the future of immunology research.

Our lab's collaborative effort began with my very first elastase time course in October 2018. Since then, I have been graciously guided by my mentors, Alan Scott and Wayne Mitzner. I am also thankful for the reliable effort and dedication from Jeffrey Loube, the lab's technician for most of my time as a PhD student. Jeff saw me fail countless times experimentally, but always remained optimistic and eager to troubleshoot or test a new theory. I was thrilled to see him move on to his own Ph.D. program during my 4th year.

A combination of generosity and mentorship had facilitated our lab's ability to conduct *in vitro* work for **Chapter 2.** Foremost, Yee Chan Li and Sam Collins graciously allowed me to work in their lab and exclusively shared their tissue culture hood with me for all experiments. Despite working in such a tight space, these individuals always welcomed me and were eager to lead me toward success. Yee and Sam both taught me fundamental techniques in immunology, including how to study, maintain, and conduct assays with macrophages in sterile culture.

For helping me expand on and support my work *in vitro*, I extend my eternal gratitude to Naina Gour and Stephane Lajoie. Similar to Yee and Sam, these individuals also took me under their wing, first teaching me how to isolate and maintain fibroblasts in culture. Later, they provided direct, hands-on support for implementing ELISA and flow cytometry into my workflow. **Without their selfless acts, I would have never generated the preliminary data for setting the foundation of my first author publication**. I am truly grateful that Naina and Stephane never cut corners with me. They spent a lot of time one-and-one with me and made sure I was comfortable with new techniques, start-to-finish, or prior to trying them on my own. Naina and Stephane did all of these favors for a **non**-member of their lab. Accordingly, all work herein is dedicated to Naina and Stephane. I am wholeheartedly grateful that you challenged me to think more intently about the preliminary data driving my work. Thank you for teaching me how to practice science with rigor and pride.

Indeed, I would have not met Yee, Sam, Naina, or Stephane if I were not part of the research umbrella of Alan Scott and Wayne Mitzner, whom I am proud to call my "co-mentors." It was a privilege to learn from two individuals with such unique perspectives and expertise. Wayne faithfully served as my lung function consult or expert in pulmonary physiology for this entire body of work, whereas Alan shaped my philosophy and understanding of immunology. Thank you for your guidance, and for introducing me to experts like Jay Bream, Nicola Heller, and Luigi Adamo, who all played an integral role in my success and development by serving on my Thesis Advisory Committee. Collectively, the five of you are among the most encouraging and genuine individuals I've met in my lifetime.

Personally, I want to extend my gratitude to Alan Scott for giving me so many RNA-sequencing projects during my Ph.D. (**Chapter 2** and **Chapter 4)**, despite my having limited knowledge on the topic when we started. By letting me take financial and experimental risk with my project, Dr. Scott broadened my perspective of biology and allowed me to walk away with a next-generation toolbox for conquering scientific questions throughout my career. An extended thank you also goes to Luigi Adamo, who played a critical role in shaping my single-cell analysis in **Chapter 4**. Thank you for finding the time to discuss sequencing and drink espresso with me.

Honorable mentions go out to James Limjunyawong and J. Matt Craig for driving the early stages of this project and helping secure the funding for this work. A special thank you also goes to Hurley Ryan for taking over for Jeff and helping conduct several experiments illustrated herein. I also appreciate the support received from core facilities across the Johns Hopkins Medical Institutes (JHMI), including those located in the department of Molecular Microbiology and Immunology (MMI) and School of Medicine. All my sequencing and analysis was made possible with help from the MMI Genomics Core and JHMI Transcriptomics facility. Hao Zhang from MMI Cell Sorting is an absolute pleasure to work with; and, one day, I hope to practice flow cytometry with as much skill and elegance as he does. On a related note, Ross Cytometry was also instrumental for helping me complete the final stages of my work. Finally, Research Animal Resources helped facilitate a large body of this work. There was a time when our lab was breeding mice extensively; and professionals at RAR like Dynishie "DJ" Johnson, Wayne Turnmire, and Dawn Hull were always in the vivarium working to keep my animals happy and healthy. You all taught me so much related to breeding, colony management, and ethics; and I would never have met my research needs without your help.

Table of Contents

List of Tables

List of Figures

Chapter 1. Introduction to Chronic Obstructive Pulmonary Disease and Elastase-Induced Experimental Emphysema.

The definition and public health impact of Chronic Obstructive Pulmonary Disease.

Chronic obstructive pulmonary disease (COPD), which includes bronchitis and emphysema, is a major threat to public health. According to the American Lung Association (2022), more than three million Americans live with emphysema; and symptom management is the only treatment available to patients. The burden of COPD extends internationally – not only is COPD the third leading cause of death worldwide, but also ~90% of fatalities occur in low-to-middle income countries (WHO, 2022).

While cigarette smoking has traditionally been considered the most frequent and important cause of COPD, recent work has underscored cigarette smoke-independent environmental, genetic, and immunological factors that are associated with the initiation and/or progression of this debilitating disease (Halpin et al., 2021; Yang et al., 2022). Non-tobacco-related environmental risk factors include exposure to household biomass smoke, outdoor air pollution, dust, and fumes, poorly controlled asthma, history of pulmonary tuberculosis, recurrent respiratory tract infections, low socioeconomic status, and aging, among others (Adeloye et al., 2022).

For years, our lab has focused on understanding the cellular and molecular mechanisms that control pathogenesis of emphysema, which is one of two major COPD subtypes. Emphysema has been defined previously by the National Institutes of Health as a lung disease characterized for progressive airspace enlargement resulting from abnormal degradation of alveolar walls (Snider et al., 1985). These structural changes have a major impact on lung function over time since alveoli are critical for gas exchange. Though descriptive, the historical definition of emphysema does not incorporate a role for the immune system and chronic inflammation as drivers of progressive changes in lung structure and function. Thus as immunologists, our motivation for studying emphysema is to understand the cellular and molecular events that contribute to alveolar destruction over time.

Experimental models for studying emphysema pathogenesis.

Experimentation with human samples is complicated by several limitations that affect our ability to study emphysema pathogenesis in affected individuals. As a result, results from human studies have been narrow in scope, often pointing to factors *associated* with emphysema progression, while indirectly speculating about cellular and molecular mechanisms that directly break down alveolar structures over time. Thus researchers have relied on diverse experimental models (Craig et al., 2017) that recapitulate "emphysematous" pathology in the mouse by challenging animals with cigarette smoke (CS) or porcine pancreatic elastase (PPE).

Historically, cigarette smoke has been relied upon for initiating emphysematous pathology in an experimental setting because this challenge is thought to mimic the response to CS in humans (Huber et al., 1981; Wright and Churg, 1990). We acknowledge that CS is a relevant and necessary model for making predictions about human disease. However, we avoid use of this model in our lab for logistical and biological reasons.

Foremost, there is an overwhelming cost and time-commitment to house and challenge mice with cigarette smoke for 6+ months. Even after daily, passive exposure to CS, mice only develop mild disease based on structural and functional readouts This model also ignores the fact that emphysema from CS is rarely guaranteed – in humans, only about 20% of heavy cigarette smokers go on to develop signs of progressive emphysema (Pauwels and Rabe, 2004). The lack of penetrance using the CS model was a concern because our lab is mostly interested in understanding the basis of ***progressive*** disease, as opposed to acute inflammatory events or ***initiation*** of disease in humans and mice. In other words, we aim to understand why lungs fail to heal post-challenge. Since a tremendous amount of effort is required just to initiate emphysematous changes in mice with CS, we explored comparable models that allow us to study disease progression.

The elastase or PPE model largely overcomes limitations pertaining to ***initiation***, like those discussed for CS model. Importantly, the PPE model requires just one, experimental challenge for establishing chronic lung disease in mice. By delivering the enzyme intratracheally, one can establish a robust inflammatory cascade in murine lungs by day 7, with signs of progressive emphysema as soon as day 21. Our lab recently established a standardized PPE model using male, BALB/cJ mice dosed at 3 units of elastase (Limjunyawong et al., 2015a). These parameters were optimized for establishing a state of chronic inflammation in murine lungs without killing the animal, as we have successfully studied males up to 96 days post-challenge. Despite one challenge, these mice experience progressive, structural and functional changes in their lungs over time. Chronic disease is thought to be largely immune-mediated, as other groups have suggested that only ~20% of lung damage results from the PPE itself (Lucey et al., 2002). This model provides a great opportunity to study progressive emphysema in mice, as we now have a tractable, long-term model for dissecting the cellular and molecular basis of emphysema and understanding what mechanisms, exactly, prevent elastase-challenged lungs from properly healing over time.

The JHU EIEE model.

Our lab was motivated to standardize the EIEE model because we wanted to address inconsistencies that make it difficult to integrate results from other groups, who often cherry-pick key parameters like strain, sex, dose, and time for supporting their readouts. In our 2015 adaptation of the model, we established the following guidelines for studying progressive emphysema in mice: challenge male, BALB/cJ animals <u>once</u> with 3U of PPE for studying the cellular and molecular basis of progressive disease at day 21. These stipulations allowed for reliable induction of progressive emphysema in BALB/cJ mice, while balancing the survivability necessary for long-term studies

For establishing this model, we simultaneously addressed issues related to sex, dose, and time by comparing the response to PPE in two common lab strains: C57Bl/6J and BALB/cJ. We noted that, while a single 3U dose of porcine pancreatic elastase (PPE) resulted in acute inflammation and mild emphysematous changes in B6 mice, experimental cohorts demonstrated variable disease penetrance with several animals failing to develop progressive emphysema. Some mice even showed signs of recovery when lung function was measured over time (note: a hallmark of <u>*progressive*</u> emphysema is its irreversibility). Penetrance did not improve when the dose was increased – though, the acute response to PPE challenge was presumably more vigorous, since many B6 animals died shortly after receiving doses greater than 3U PPE. In contrast, challenging male BALB/cJ mice with 3U PPE resulted in high penetrance and progressive disease without evidence of reversibility through 96 days post-challenge (Craig et al., 2017; Limjunyawong et al., 2015a). Thus it was concluded that BALB/cJ mice were superior to C57BL/6J mice for modeling chronic pathogenesis.

One of the major limitations of dosing standards defined by Limjunyawong et al. (2015) was the fact that studies were limited to male BALB/cJ animals. At least two reports have illustrated how sex differences affect experimental emphysema readouts (Aono et al., 2021; Niikura et al., 2015), and clinical findings also support the notion that females are more prone to severe disease (Aryal et al., 2013; Foreman et al., 2011). Considering these data, our lab prioritized studying emphysema in both sexes of BALB/c mice moving forward. At the start of my work with the EIEE model, I helped determined that challenging BALB/c females with 1.5U of PPE, as opposed to the 3U PPE, induced disease that was comparable to males as determined by lung function readouts (**Figure 1.1**). By Day 21, females challenged with 1.5U PPE experienced significant increases in total lung capacity (TLC) – a readout indictive of severe emphysema – but males were not responsive at this dose (**Figure 1.1A**). Males responded significantly to the standard 3U PPE, as expected, eliciting a functional readout similar to females instilled with 1.5U PPE. For appreciating the robust functional differences in females that received PPE, total lung capacity values can be transformed with a comparative method that calculates percent change from baseline (**Figure 1.1B**). By Day 21, males experienced an 18% increase in TLC with 1.5U PPE and a 61% increase at 3U. Females underwent a 74% and 105% change from baseline at 1.5U and 3U PPE, respectively. Moving forward, we continued using 3U PPE for males and began challenging females at 1.5U PPE for inducing EIEE.

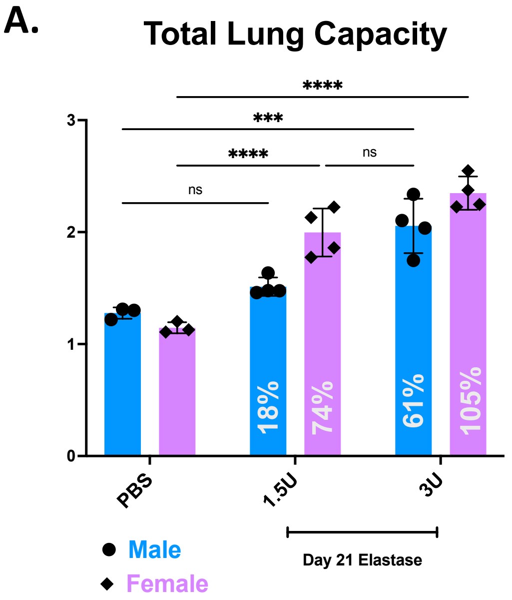

B. **Relative (%) change in Total Lung Capacity**

$$C = \frac{x_2 - x_1}{x_1}$$

C = relative change
x_1 = initial value
x_2 = final value

	1.5 U	3U
Male	18%	61%
Female	74%	105%

Figure 1.1 Absolute and relative total lung capacity dynamics that compare sex- and dose-dependent responses to elastase in the BALB/cJ EIEE model. (A) Male and female mice were compared (N=3 baseline, N=4 per elastase group). Total lung capacity was measured from total pressure volume curves as generated with a Flexivent (Scireq; Toronto, CA). Error bars represent standard deviation from the mean. Statistics were computed by two-way ANOVA with multiple comparisons (+ Tukey's post-hoc test). **** p<.0001; *** p=.0001; ns = not significant. Values for relative change (B) are illustrated within each bar, as this calculation is also illustrated in the figure. This experiment was not repeated explicitly; but the readout is supported by years of independent assays in which female and male BALB/cJh mice were challenged at 1.5U and 3U PPE, respectively, yielding comparable outcomes.

IL-33, IL-13, and IL-17A may activate lung immune cells and drive EIEE pathogenesis.

As part of their study, Limjunyawong and colleagues (2015) observed that cytokines IL-33, IL-13, and IL-17A was expressed prominently in the lung between Days 2-7 post-elastase. At the time, our data were supported by reports of IL-33-mediated immune activation in emphysematous lungs (John et al., 2016), as well as those describing elevated IL-33 in individuals with particularly severe COPD (Joo et al., 2021; Lee et al., 2019; Qiu et al., 2012; Singh, 2022). On the other hand, IL-13 was relatively underexplored for its role in emphysema pathology. Previously, IL-13 overexpression models had revealed that this cytokine may promote emphysematous changes in the lung (Balnis et al., 2020; Fulkerson et al., 2006; Zheng et al., 2000). Beyond this context, limited evidence was available at the time to accept or reject IL-13 as a driver of COPD (Doyle et al., 2019; Kang et al., 2012). Finally, significant experimental support existed for IL-17A as a driver of emphysema, including early reports of attenuation in cigarette smoke- or elastase-induced COPD models that compared responses of *Il17a*$^{-/-}$ or *Il17ra*$^{-/-}$ mice to wildtype (Chen et al., 2011; Kurimoto et al., 2013). However, as mentioned, cigarette-smoke models are relatively benign compared to the severe disease from PPE (Craig et al., 2017); and for these reports, each group studied <u>female</u> C57Bl/6 mice, exclusively. Thus, our group was eager to apply global knockout approaches to our BALB/c EIEE model and test emphysema phenotypes in both male and female animals.

Macrophage dysregulation is strongly associated with emphysema and severe disease outcomes in the lung.

For investigating EIEE pathogenesis and dysregulated wound healing pathways herein, we maintain experimental focus on dissecting the phenotypes of lung macrophages, specifically, which are perceived by our group and others to be major drivers of emphysematous pathology (Chen et al., 2011; Hautamaki et al., 1997; Hunninghake et al., 1981; O'Beirne et al., 2020; Shapiro, 1999; Shibata et al., 2018). Upon joining the lab in 2018, lung macrophages were being scrutinized with next-generation approaches (*I.e.,* bulk RNA-seq, single-cell RNA-seq, CHIP-seq, ATAC-seq) at an unprecedented rate (Dick et al., 2022; Gibbings et al., 2017; Lavin et al., 2014; Svedberg et al., 2019). We thus had plenty of resources to begin our investigation in the context of EIEE. However, at the time, several techniques we planned to use had not been extensively applied to COPD models until the end of our investigation (Hey et al., 2021; Li et al., 2021; Rao et al., 2020; Sauler et al., 2022). Thus for studying lung macrophage roles in emphysema, we considered reports from other disease models like pulmonary fibrosis and lung cancer, as these diseases also implicate macrophages as drivers of pathology (Adams et al., 2020; Mantovani et al., 2022; Misharin et al., 2017; Pittet et al., 2022).

Elastase-Induced Experimental Emphysema is a consequence of aberrant immune activity and improper wound healing.

The <u>*progressive*</u> nature of the disease observed in the EIEE model was consistent with the severe lung disease reported in humans that are exposed to environmental pathogens, toxins, or pollutants. In these contexts, the exposure itself is rarely perceived as being directly responsible for long-term or *progressive* damage to the lung. Chronic disease is thought to be orchestrated by lung cells that became dysregulated during recovery from the primary insult (Bhat et al., 2015; Martine et al., 2017; Wong and Perlman, 2022). In our emphysema model, the hypothesis is that a single dose of elastase initiates robust immune activity in the lungs, and a subset of innate cells that were activated for wound healing likely go on to directly cause progressive lung damage over time. Similarly, and if the experimental goal is fibrosis, a single bleomycin challenge can induce immune dysregulation and progressive disease outcomes in mice (Izbicki et al., 2002; Snider et al., 1978). Either way, readouts from common injury models such as EIEE or bleomycin-induced fibrosis have clearly supported the notion that chronic lung disease and dysregulated wound healing are strongly interrelated. From the perspective of an injury response in the lungs, fibrosis is well-characterized and thought to be a clear example of aberrant *tissue repair*, or pathways related to myofibroblast hypersecretion of extracellular matrix proteins (ECM) in the lung (III et al., 2018; Martine et al., 2017). In contrast, we theorize that EIEE pathogenesis is the consequence of dysregulated, immune-mediated *tissue remodeling* pathways that degrade alveolar ECM and subsequent reduction of the gas exchange surface over time. Molecularly, these responses are thought to be elicited largely by phagocytes through sustained, catabolic effector function (Craig et al., 2017; Hautamaki et al., 1997; Vannella and Wynn, 2017). Altogether, and upon the completion of James' work in 2015, we reshaped our philosophy prior to conducting experiments for this Thesis: in addition to serving as a tractable and versatile tool for studying 'emphysematous' pathology in mice, BALB/CJ EIEE was perceived to be the optimal model for studying aberrant tissue *remodeling*, mirroring how other groups rely on models like bleomycin-challenge to investigate dysregulated *repair* in fibrosis.

Chapter 2. Lung fibroblasts respond to IL-33, IL-13, and IL-17A by secreting factors that activate macrophages.

Overview

Mounting evidence suggests that macrophage-fibroblast communication is key to the understanding of disease processes. To gain insights into these relationships in the context of progressive lung damage, we measured changes in protein and RNA expression of pulmonary macrophages and fibroblasts upon exposure to IL-33, IL-13, and IL-17A, which are three cytokines often implicated in pathways driving chronic lung remodeling and severe disease like emphysema. Applying an *in vitro* culture system, bulk-RNA sequencing, and ELISA, it was determined that IL-33, IL-13, and IL-17A used alone or in combination activated mouse alveolar macrophages to a modest extent with IL-13 inducing the most vigorous response. While lung fibroblasts also responded modestly to single and paired treatments with IL-33, IL-13, and IL-17A, simultaneous exposure to all three cytokines induced significant activation that was characterized by expression of genes associated with immune cell trafficking and activation, tissue remodeling, and maintenance of the extracellular matrix. Factors secreted by triple-treated fibroblasts resulted in the activation of macrophages *in vitro*. These findings are the first to report cooperative interactions of IL-33, IL-13, and IL-17A and provide additional evidence that fibroblast-macrophage communication is a key component to repair and remodeling in the lung, as well as mechanisms that drive progression of emphysema.

Introduction

Chronic Lung Disease (CLD) is an umbrella term for disorders that are often the consequence of acute or repeat exposure to environmental agents such as pathogens, allergens, or toxins. Well-characterized examples of CLD include allergic asthma, chronic obstructive pulmonary disease (COPD), and idiopathic pulmonary fibrosis. COPD is the third leading cause of death worldwide (WHO, 2022); and COPD, as well as other CLDs, poses a significant threat to public health.

CLDs are characterized by their distinctive presentations, prognoses, and overall pathologies. This is true despite considerable overlap in terms of the cellular and molecular events thought to drive disease. For example, lung macrophages have been studied extensively over the years in the context of CLDs; and this cell type appears to contribute significantly to the development of both human and experimental animal models for asthma, COPD, and fibrosis (Bedoret et al., 2009; O'Beirne et al., 2020; Reyfman et al., 2018). Stromal cell dysregulation may also be partially responsible for the development of asthma (Ingram et al., 2011; Mostaço-Guidolin et al., 2019) and COPD (Hallgren et al., 2010; Togo et al., 2008), in addition to facilitating pathogenic fibrosis in the lung.

The cytokines IL-33, IL-13, and IL-17A have also been implicated in driving pathologies of CLD. All three cytokines have been studied extensively for their role in the development of human and experimental asthma (Aneas et al., 2021; Grunig et al., 1998; Lajoie et al., 2010; Wills-Karp et al., 1998). IL-33 and IL-17A signaling may contribute to the development of pulmonary fibrosis (Li et al., 2014; Mi et al., 2011; Zhang et al., 2019); but results from three clinical trials now suggest that *progression* of pulmonary fibrosis is IL-13-independent (Wijsenbeek et al., 2018). All three cytokines appear to contribute to COPD pathogenesis, as we and others previously demonstrated that increased IL-33, IL-13, and IL-17A expression was associated with severe pathology in emphysematous lungs (Limjunyawong et al., 2015a; Xia et al., 2015).

The goal of the work presented here was to explore the interaction of IL-33, IL-13, and IL-17A with the resident and recruited lung cells thought to contribute to pathogenesis of elastase-induced experimental emphysema (EIEE), introduced in **Chapter 1**. Employing transcriptional readouts and protein-based assays, it was determined that primary lung fibroblasts, and not alveolar macrophages, were the cells responsive to these cytokine treatments *in vitro* and that the most robust response occurred when the fibroblasts were treated with IL-33, IL-13, and IL-17A simultaneously. Transcriptional analysis of primary lung fibroblasts showed that triple-treated cells significantly upregulated molecules associated with inflammation and tissue-remodeling. These findings also suggested that IL-33, IL-13, and IL-17A induce stromal cells to secrete factors that modulate lung macrophages. Overall, these *in vitro* studies provide groundwork for further investigating IL-33, IL-13, and IL-17A dynamics and their impact on cellular responsiveness *in vivo*, specifically in the context of chronic lung disease.

Methods

Mice.

All experiments were conducted in accordance with the standards established by the United States Animal Welfare Acts, set forth in NIH guidelines and the Policy and Procedures Manual of the Johns Hopkins University Animal Care and Use Committee. Animals were maintained in filter-topped cages at approximately 72^{o}C, 50-60% humidity with 14:10 hour light/dark cycle and ad libitum access to food and water. Cells for *in vitro* studies were derived from male and female mice on the BALB/cJ background. Wildtype (WT) BALB/cJ were originally purchased from Jackson Laboratories (#00651). Mice were bred and housed in the Johns Hopkins School of Public Health animal facilities. Unless clearly stated otherwise in a figure legend, only offspring produced in-house were used for these studies. *St2* and *Stat6* knockout (KO) mice, both on a BALB/c background, were obtained from either lab or commercial sources (see **Table 2.1** below) and bred in-house. For the *in vitro* work described here, KO mice were maintained as homozygous breeding pairs.

Genotyping.

Tails snips were digested with Extract-N-Amp Tissue PCR Kit (Sigma, XNAT). Polymerase chain reaction was performed using made-to-order, genotype-specific oligonucleotides (IDT, Coralville IA); DNA sequences were amplified using Extract-N-Amp RedTaq (Sigma, R4775) using publicly available protocols, listed in **Table 2.1**:

Table 2.1: Knockout Mice used for *in vitro* Experiments

Genotype Protocol Availability	**Oligonucleotide Sequence (5′ to 3′)**
St2 $^{-/-}$ ('BALB/c') Andrew N.J. McKenzie, Ph.D. Cambridge, England Genotyping available upon request to ANJM.	• TTGGCTTCTTTTAATAGGCCC • CTATCAGGACATAGCGTTGGCTACC • TGTTGAAGCCAAGAGCTTACC
C;129S2-Stat6 $^{-/-}$ ('BALB/c') Strain #002828 – Jackson Labs Genotyping recommendations available online.	• AATCCATCTTGTTCAATGGCCGATC • ACTCCGGAAAGCCTCATCTT • AAGTGGGTCCCCTTCACTCT

Primary lung fibroblast cell cultures.

BALB/c mice (3-6 weeks old) were anesthetized by intraperitoneal (IP) injection with a mixture (1:1) of ketamine (100 mg/kg) and xylazine (10 mg/kg) in sterile water. Intact, non-perfused lungs were extracted and rinsed in cold Hanks Balanced Salt Solution (HBSS). Tissue digestion buffer (see **Table 2.2**, below) was added, and samples were homogenized by incubating for 25 minutes at 37^{o}C on a rotating platform set at 300 rpm. Post-digestion, homogenates were passed through a 40 µm cell strainer and rinsed with HBSS, centrifuged, and resuspended in culture media (**Table 2.2**). For the expansion and maintenance of primary lung fibroblasts, lung homogenates were directly plated in culture media. With time and at least 3 rounds of passage, lung-derived cells characteristic of myofibroblasts become the dominant population in culture (Edelman and Redente, 2018; Foster et al., 1990; Seluanov et al., 2010). Media was changed every other day, and cell passage was performed at 80% confluency. Only cells from passage 3-5 were used for experiments.

Table 2.2: Formulations for Media and Buffers

Tissue Digestion Buffer	Hank's Buffered Salt Solution (HBSS, Corning, 21-023-CV) Collagenase I 125U/mL (Sigma, C0130); Hyaluronidase I 60U/mL (Sigma, H3506); DNase I (Sigma, DN25)
Fluorescence Activated Cell Sorting (FACS) Buffer	Dulbecco's Phosphate Buffered Saline (dPBS, Corning 20-030-CV) 2mM EDTA (Corning, 46-034-CL); 2% heat-inactivated fetal bovine serum (HI-FBS, Corning, 35-010-CV)
Culture Medium	Dulbecco's Modified Eagle's Medium (DMEM, Corning, 10-017-CV) 1% Penicillin/Streptomycin (Gibco, 15140122); 10% HI-FBS
Bone Marrow Monocyte Differentiation Media	DMEM 1% Penicillin/Streptomycin; 10% HI-FBS, 20% L-Media
Bronchoalveolar Lavage (BAL) Buffer	dPBS 2mM EDTA; 1% HI-FBS

Primary alveolar macrophage cultures.

BALB/cJ mice (6-12 weeks old) were euthanized with an overdose of ketamine/xylazine and a tracheostomy was performed to insert an 18G canula. Bronchoalveolar lavage (BAL) was used to collect alveolar macrophages as previously described (Busch et al., 2019). BAL Buffer (**Table 2.2**), 900 µl pre-warmed to 37ºC, was introduced using a syringe via the canula and slowly drawn back from the lungs with a recovery of 500 to 800 µl. Cells were rinsed with cold BAL buffer and directly plated in culture media. After 20 minutes in standard culture conditions (37ºC, 5% CO_2), plates were rinsed with dPBS to remove nonadherent cells and replenished with fresh culture media. Alveolar macrophages were in culture for no longer than 24 hours. The purity and viability of alveolar macrophages were estimated by light microscopy and trypan blue staining.

Bone Marrow-Derived Macrophages (BMDM) cultures.

BALB/cJ mice (6-12 weeks old) were euthanized as outlined above, their tibias and femurs excised, washed with 70% ethanol, and rinsed in dPBS. Bone marrow was flushed with DMEM (**Table 2.2**) using a syringe fitted with a 28 G needle and passed through a 40 µm cell strainer. Cells were rinsed, centrifuged, and plated directly in bone marrow monocyte differentiation media (**Table 2.2**). Spent media was replaced every 3 days. BMDM were used after 7 days of culture in the differentiation media. Macrophages were harvested from culture by incubating in CellStripper (Corning) at 37ºC on a rotating platform at 150 rpm for 60 minutes.

Recombinant Cytokines.

Recombinant ('r') proteins were purchased from BioLegend. rIL-33 (580502), rIL-13 (575904), rIL-17A (576002), and rIL-4 (574302). The same concentrations were used for all experiments, regardless of cell type, unless clearly stated in the figure legend: 30 ng/mL (rIL-33), 20 ng/mL (rIL-13 or -4), 30 ng/mL (rIL-17A).

mRNA Preparation and cDNA synthesis.

Total RNA from fibroblasts or macrophages was prepared using commercially available RNeasy kits and protocols (Qiagen 74004 or 74104). For RT-PCR analysis, total RNA was reverse transcribed into cDNA with LunaScript RT Supermix (New England Biolabs, E3010) according to manufacturer's protocol. RNA was stored at –80ºC prior to use; and cDNA was stored at 4ºC.

Whole Transcriptome sequencing.

A total of 2.25 x 10^5 alveolar macrophages were seeded per well in 24-well plates (Corning 3524) and allowed to rest in fresh media for 3 hours. Macrophages were then stimulated with cytokines, and RNA lysates were collected 20 hours later (i.e. macrophages were outside of the mouse for less than 24 hours). For primary lung fibroblasts, 1.2 x 10^6 cells were seeded per well in 6-well plates (Corning 3516) and treated with cytokines for 20 hours. Total RNA was isolated for each cell type, as described above. RNA was sent directly to Novogene where QA/QC, library preparation, and sequencing with a NovaSeq 6000 (Illumina) were carried out. Computational and statistical analysis were performed in Partek Flow (St. Louis, MO) using .bam files that were previously aligned by NovoGene with the HISAT2 algorithm (Kim et al., 2019). A *Mus musculus* genome ('mm10' a.k.a. GRCm38) was referenced for alignment. Mapped reads were subjected to standard RNA-seq QA/QC to assess for nucleotide mismatches or library size differences between samples. Low quality reads were excluded from the dataset, and the remaining alignments were quantified with an Ensembl (release 102) annotation model (Zhao and Zhang, 2015). Count matrices were then processed in Partek Flow for data visualization and biological inference downstream. Principal component analysis, hierarchical clustering, and scatter plots were used for visualizing expression data. Differential gene expression (DGE) analysis was executed in Partek Flow with DESeq2 (Anders and Huber, 2010; Love et al., 2014) and results were visualized with volcano plots.

Enzyme-Linked Immunoassay (ELISA) for measuring secretion of murine GM-CSF.

Commercially available kits and manufacturer protocols from R&D Systems (mCsf2; DY416) were employed for ELISA. Unless clearly stated otherwise, 25,000 cells were seeded in 96-well assay plates for cytokine treatment. At the conclusion of each experiment, supernatants were collected and stored in low-binding 96-well plates (Greiner 655904) at –80ºC. Protein concentrations were measured from supernatants by ELISA and use of a fluorescent microplate reader, directly comparing the signal from each sample to that of a standard curve.

Generation of Fibroblast Conditioned Media.

Primary lung fibroblast cultures were treated with permutations of rIL-33/rIL-13/rIL-17A for generating fibroblast conditioned media (“FCM”). Fibroblast-only cultures were stimulated with cytokine combinations for 22 hours, rinsed vigorously three times with dPBS to remove residual recombinant cytokines, replenished with media, and incubated (37ºC, 5% CO_2) for an additional 20 hours as the source of FCM. Supernatants were collected from fibroblast-only cultures, sterilized with a 0.22 µm filter, and transferred to BMDM cultures (1 x 10^6 cells per well) at 20% v/v in DMEM (1% Penicillin/Streptomycin + 10% heat inactive-FBS). After 24 hours of exposure to FCM, total RNA was collected from BMDM, as described above.

Reverse Transcription – Quantitative Polymerase Chain Reaction (RT-qPCR).

Purified RNA was quantified using a Qubit 2.0 (Thermo Fisher, Q32886) and reverse transcribed, as described above. TaqMan-based qPCR was performed using EagleTaq Universal Master Mix (Roche, 7260288190), and data were acquired on a

StepOnePlus (Applied Biosystems, 4376600) with the following fluorescently-labeled probes: *Mmp12 (*Thermo Fisher*; Mm00500554_m1)*, *Arg1 (Mm00475988_m1), Rps14 (Mm00849906_g1), Ctsa (Mm00447197_m1), Retnla (Mm00445109_m1), Ym1 (Mm00657889_mH), Gapdh (Mm99999915_g1).* A commercial algorithm (RQ, Applied Biosystems) was used for determining expression values, or 'relative quantitation', of several genes. This computation is similar to the $2^{-\Delta\Delta Ct}$ method (Livak and Schmittgen, 2001). For calculating relative quantitation, expression of *Rps14, Ctsa* and *Gapdh* were acquired by qPCR in parallel as controls (i.e. 'housekeeping genes').

Flow Cytometry.

Cultured macrophages or fibroblasts were lifted non-enzymatically with CellStripper (Corning 25-056-Cl) for 60 minutes at room temperature and immediately processed for flow cytometry. In preparation for flow cytometry, macrophages or fibroblasts were suspended in PBS (for vitality dye only) or FACS Buffer (**Table 2.2**) and stained with combinations of the following: LIVE/DEAD Aqua (eBioscience), anti-mouse IL17ra-APC (clone 657643, R&D systems); anti-mouse T1/St2-FITC (clone DJ8, mdbioproducts), anti-mouse Csf2ra-Alexa 700 (clone 698423, R&D systems), or anti-mouse CD11b-BV785 (clone M1/70, BioLegend). Single-fluorophore controls were prepared using either cytometry beads (Becton Dickinson 552843) or cells isolated on the day of experimentation. Acquisition was performed on an LSR-II (Becton Dickinson, Franklin Lakes NJ). Samples were acquired using the BD FACSDiva software. Compensation was finalized in FlowJo (Becton Dickinson), and this software was also used for producing the illustrations supporting the analysis herein. For all cytometry experiments, unstained and fluorescence-minus-one control samples were prepared for facilitating analysis and for determining gates.

Statistical Analysis and Illustrations.

For ELISA and RT-q-PCR readouts, statistics were performed in GraphPad Prism (San Diego, CA), which was also employed for generating bar graphs. One- or Two-way ANOVA were the most utilized method per experiment; and further statistical details, such as multiple comparisons or post-hoc tests, are annotated in the specific figure legends. For RNAseq, all statistics and visualizations were generated with computational tasks in Partek Flow, including DGE analysis with DESeq2.

Results

in vitro stimulation of alveolar macrophages with cytokines associated with CLD.

The work outlined in this chapter extends published and unpublished findings of former members of the lab, J. Matt Craig and James Limjunyawong, who defined the molecular landscape of our elastase-induced experimental emphysema (EIEE) model in BALB/cJ mice (Craig et al., 2017; Limjunyawong et al., 2015a). They described a rapid increase in the levels of IL-33 in the lungs at 2-3 Days post-elastase challenge, followed by an increase in the levels of IL-13 and IL-17A by Day 7. These observations were significant because changes in IL-33/IL-13/IL-17A expression were highly correlated with the transition from acute stages of EIEE to the chronic, progressive form of lung destruction in this model. The potential importance of IL-33, IL-13 and IL-17A was underscored by reports that used animal models or human samples for implicating each cytokine in disease severity and/or progression of other CLD subtypes, like asthma or pulmonary fibrosis (Aneas et al., 2021; Grunig et al., 1998; Lajoie et al., 2010; Wills-Karp et al., 1998).

At the time, we and others were accumulating evidence that pointed to macrophages as candidate cells for eliciting a response to IL-33, IL-13, and IL-17A in the lungs (Barin et al., 2012; Chen et al., 2011; Ge et al., 2014; Kurowska-Stolarska et al., 2009). In consideration of the temporal dynamics of cytokine production and tissue damage in the EIEE model, we initially hypothesized that IL-33 served to prime lung macrophages, modulating their responsiveness for subsequent activation by IL-13 and IL-

17A. Together, all three cytokines were thought to generate a 'pathogenic' cellular phenotype capable of mediating prolonged destruction of alveolar tissue.

Experiments first were carried out using BAL-derived alveolar macrophages. These macrophages were stimulated as soon as possible after being extracted from the mouse, remaining in culture for less than 24 hours. Recombinant IL-33, IL-13, and IL-17A (rIL-33, rIL-13, and rIL-17A) were added to the cultures separately or in 2-way or 3-way combinations. These combinations are outlined in **Table 2.3,** employing the design illustrated in **Figure 2.1**.

Table 2.3: Treatment Groups for *in vitro* Assays

Groups	Recombinant (r) Cytokines		
Untreated	n/a - media only		
Single-	rIL-33	rIL-13	rIL-17A
Double-	rIL-33/rIL-13	rIL-33/IL-17A	rIL-13/rIL-17A
Triple-Treated	rIL-33/rIL-13/rIL-17A		

After a 20-hour incubation with the cytokines, total RNA from test and control alveolar macrophages was isolated and submitted for bulk transcriptome sequencing (RNA-seq). Principal component analysis (PCA) illustrated global, transcriptional differences among samples. The raw data (**Figure 2.2A**) were transformed using the Median Ratio method (MR; **Figure 2.2B**) and Transcripts per Million method (TPM; **Figure 2.2C**); but all illustrations yielded the same interpretation – by PCA, it was understood that alveolar macrophages are responsive, mainly, to combinations that include rIL-13 *in vitro*. Transcriptional readouts for the rIL-33-only, rIL-17A-only, and rIL-33/rIL-17A-treated cells overlapped significantly with that of untreated controls; but groups treated with rIL-13, rIL-13/rIL-17A, rIL-33/rIL-13, and rIL-33/rIL-13/rIL-17A all diverged from untreated alveolar macrophages by PCA, suggesting they were activated by cytokine treatment. These groups also overlapped with each other, though, indicating that cells receiving treatments with rIL-13 were transcriptionally similar.

To support observations from the PCA, Differential Gene Expression (DGE) analysis by DESeq2 was used to identify unique or overlaping aspects of gene expression between groups (**Figure 2.3**). Relative to untreated alveolar macrophages, no significant gene expression was noted in the following groups: rIL-33, rIL-17A, rIL-33/17A. In contrast, macrophages receiving rIL-13 or rIL-13/17A had relevant variation in 972 and 982 genes, respectively, compared to untreated controls. Similarly, 724 and 769 significant and differentially expressed genes were noted among macrophages stimulated with IL-33/13 or IL-33/13/17A. Significant transcriptional overlap was evident among all four groups, which received, at minimum, rIL-13; and each expressed genes otherwise expected for IL4rα-mediated signaling in macrophages like *Chil3 (Ym1), Cd36,* and *Ear2* (Das et al., 2018)*,* as well as genes involved in tissue remodelling in the lungs (*Mmp13, Mmp19*). Several genes known to be expressed by alveolar macrophages (Aegerter et al., 2022; Bain and MacDonald, 2022), such as *SiglecF* and *Spp1*, were downregulated as a consequence of stimulation.

To examine the influence of rIL-13 on related macrophage treatment groups in more depth, DGE analysis was applied directly to the following groups: rIL-13 only vs. rIL-33/13, -33/17A or -33/13/17A (**Figure 2.4A**). This approach revealed 72, 0, and 85 differentially expressed genes, respectively, per comparison. A direct comparison of rIL-33/13 vs. rIL-33/13/17a was also made (**Figure 2.4B**), noting 1 downregulated gene (a long non-coding RNA, *Gm20521*) when applying the same significance cutoffs used throughout.

Indeed, rIL-17A treatment had no demonstrable effect on alveolar macrophage transcription *in vitro*, despite detection and quantification of reads mapping to *Il17ra* and *Il17rc* by RNA-seq (**Figure 2.5A-B**). TPM-normalized *Il17ra* expression was noted at baseline and in all treatment groups, but this gene was likely downregulated by rIL-13-related stimulation of alveolar macrophages. *Il17rc* expression was detected, but levels were nominal compared to regulation of *Il17ra* at baseline. Additionally, under the conditions used in this study, rIL-33 may not affect alveolar macrophage polarization without rIL-13. This may be explained transcriptionally – very few reads aligning to *St2* were detected across groups, though this receptor may be positively regulated upon cytokine stimulation (**Figure 2.5C**).

As measured by this 20-hour *in vitro* treatment of alveolar macrophages, transcriptional analysis did not support our hypothesis that IL-33, IL-13 and IL-17A work together to activate lung macrophages for becoming pathogenic cells that mediate chronic lung destruction. PCA and DGE analysis indicated that only treatments with rIL-13 had activated alveolar macrophages *in vitro*. rIL-33 and rIL-17A, alone or in combination, had minimal or no effect on cell activation. We next explored the alternate hypothesis that IL-33, IL-13, and IL-17A work <u>*indirectly*</u> on alveolar macrophages through the activation of another cell – primary lung fibroblasts. This mechanism is supported by recent evidence suggesting that resident macrophage activation phenotypes are profoundly influenced by signals from tissue fibroblasts (Hou et al., 2019).

in vitro primary lung fibroblasts express receptors for cytokines associated with CLD.

To determine if fibroblasts had the capacity to respond to cytokine stimulation and contribute to macrophage activation, cells were isolated from whole lungs and primary lung fibroblasts were established in culture as outlined in the **Methods** and **Figure 2.6**. Flow cytometric analysis established that unstimulated primary lung fibroblasts had receptors for both IL-17A and IL-33 deployed on the surface (**Figure 2.7**). This analysis strongly suggested that primary lung fibroblasts at the 3rd passage *in vitro* had the means to respond to rIL-33 and/or rIL-17A treatment. Surface expression of IL4rα or IL13rα1 had already been reported on human (Doucet et al., 1998) and murine (Ingram et al., 2004) lung fibroblasts.

Lung fibroblasts were first incubated with rIL-33, rIL-13, and rIL-17A singly or in combinations, similar to what was outlined for alveolar macrophages in **Table 2.3**. Initially, ELISA was used to measure secretion of Csf2 (aka GM-CSF) by lung fibroblasts, since alveolar macrophages depend on this differentiation factor for proper development and maintenance *in vivo* (Gschwend et al., 2021; Guilliams et al., 2013). Single and double cytokine treatments resulted in nonsignificant increases over untreated control cultures, but substantial GM-CSF secretion was induced by the triple-treatment (**Figure 2.8A**). Notably, all groups receiving rIL-33 experienced a modest bump in GM-CSF secretion relative to treatment groups without rIL-33.

GM-CSF secretion was already known to be induced by IL-33 in several other cell types (Castro-Dopico et al., 2020; Eissmann et al., 2019; Montanari et al., 2016). Thus we aimed to study this mechanism briefly in lung fibroblasts. We isolated cells from the lungs of *St2*$^{-/-}$ mice, which cannot respond to IL-33, and stimulated them with the triple cytokine treatment. In two iterations that tested *St2*$^{-/-}$ fibroblasts, GM-CSF secretion did not exceed that of two unique controls (**Figure 2.8B, 2.8C**). In the first iteration of this assay, untreated *St2*$^{-/-}$ fibroblasts and those treated with rIL-33/rIL-13/rIL-17A produced nominal amounts of GM-CSF compared to WT fibroblasts stimulated under these conditions (**Figure 2.8B**). Upon repetition of this assay, lung fibroblasts were also isolated from *Stat6*$^{-/-}$ animals, which have functional *St2* but are unable to mediate IL-4/IL-13 signaling. Upon comparing *St2*$^{-/-}$ and *Stat6*$^{-/-}$ fibroblasts directly, no appreciable signal for GM-CSF was noted on behalf of untreated or triple-treated *St2*$^{-/-}$ fibroblasts (**Figure 2.8C**); however, *Stat6*$^{-/-}$ fibroblasts retained a diminished capacity to respond to triple-treatment, perceivably mediated by rIL-33/17a in the media, but not rIL-13. Taken together, these data demonstrated that primary lung fibroblasts can be stimulated *in vitro* with cytokines for eliciting IL-33/St2-associated GM-CSF secretion. Next, we aimed to expand on preliminary observations on the impact of rIL-33, rIL-13, and rIL-17A by interrogating the transcriptional response of lung fibroblasts with RNA-seq.

QA/QC of RNA-seq data and "first-pass" transcriptomic analysis of primary lung fibroblasts treated with combinations of rIL-33, IL-r13, and rIL-17A.

We sought to employ RNA-seq for a more detailed overview of fibroblast phenotypes generated by stimulation with cytokines *in vitro*. Preliminary findings suggested that while IL-33 was the dominant signal, concurrent exposure to rIL-13, rIL-33, and rIL-17A may synergistically regulate GM-CSF production in primary lung fibroblasts. For sequencing, we narrowed our investigation to just four combinations, maintaining emphasis on studying groups treated with, at minimum, rIL-33. A group of untreated fibroblasts were assayed as an additional control, as outlined in **Table 2.4**, below:

Table 2.4: Treatment Groups for Fibroblast RNA-seq

Groups	**Recombinant (r) Cytokines**	
Untreated	n/a - media only	
Single-treated	rIL-33	
Double-treated	rIL-33/rIL-13a	rIL-33/L-17a
Triple-treated	rIL-33/rIL-13a/rIL-17A	

After 20 hours of exposure to the cytokine combinations, the lung fibroblasts were harvested and processed for RNA-seq. We employed standard RNA-seq QA/QC metrics with mapped reads (.bam files), before and after quantification of the alignments (**Figure 2.9**). Prior to quantification, aligned reads were assessed for mismatches or 'base quality', as measured by Phred score (Ewing and Green, 1998; Ewing et al., 1998). Among the entire dataset, ≥75% or more reads scored 36 or higher by this metric (**Figure 2.9A**). This rank was above-average, and thus we chose to filter out aligned reads from the bulk dataset that scored less than 30. Next, we examined a 'coverage' report, which describes the depth of aligned reads on a per sample basis. After alignment and prior to quantification, most samples had read depths that were comparable. However, samples designated 'R6' and 'R14' may be technical outliers in the dataset. Before (**Figure 2.9B**) and after (**Figure 2.9C**) filtering, samples R6 and R14 consistently had the largest and smallest libaries or depth of aligned reads, respectively, when compared to others in the dataset. Library size differences were conserved after quantifying aligned reads with an Ensembl annotation model (**Figure 2.9D**). For this metric, features represent genes; and the number of transcripts per gene, or "counts", were illustrated across each sample.

Library size differences were anticipated and dealt with computationally, as needed, for downstream analysis. The two methods used throughout this workflow include Median Ratio normalization (**Figure 2.9E**), which is required for comparative analysis by DESeq2, and the transcripts per million method (**Figure 2.9F**), which is more appropriate for comparing absolute transcript abundances for select genes. By all indications, standard QA/QC metrics suggested that our experiment was a technical success. Anticipated differences in RNA libaries were easily identified; and their effects were relatively minor and computationally manageable as we proceeded with exploratory analysis.

We employed two approaches for visualizing global transcriptional differences between groups, as well as for elaborating on some of the inter- and intra-treatment variability noted earlier with QA/QC. In contrast to what was observed for alveolar macrophages (refer to **Figure 2.2**), and regardless of the normalization approach employed, all four treatment groups clearly diverged from the untreated fibroblast controls and were easily differentiated from one another by principal component analysis (PCA; **Figure 2.10**). Plots for raw counts, as well as those transformed with Median Ratio and Transcripts per Million, are illustrated. Variation within groups, at this stage of analysis, could be interpreted as biological, or simply the result of differences in library size between samples. The two outliers noted earlier, R6 and R14, were identified to be in the IL-33/17A and untreated fibroblast groups, respectively. Interestingly, both of these groups demonstrate considerable variability relative to the others illustrated by the raw PCA plot (**Figure 2.10A**). These trends reflect observations made at the level of read depth and feature distribution during QA/QC (refer to **Figure 2.9**).

Global transcriptional differences within and between groups were also computed in an unsupervised manner with hierarchical clustering (hclust), and the data were presented as a heatmap (**Figure 2.11**). This algorithm is particularly sensitive to batch effects, as large differences in library sizes of samples may skew results and overall interpration of the heatmap. Thus, hclust was performed on the normalized count matrix generated by DESeq2, which transforms data with the Median Ratio method. When applied to normalized data, this unsupervised algorithm grouped all samples within their expected treatment groups. Untreated and rIL-33-treated fibroblasts had similar global gene expression patterns by heatmap. The IL-33/13, IL-33/17A, and IL-33/13/17A groups were transcriptionally unique from baseline/rIL-33-treated cells but were not easily discriminated from each other by heatmap. Combinations of rIL-33, rIL-13, and rIL-17A may uniquely activate fibroblasts *in vitro,* but deeper analysis was required to highlight specific differences in double- and triple-treated groups.

Differential gene expression analysis of primary lung fibroblasts.

As with alveolar macrophages, we directly compared the transcriptional response of the lung fibroblast treatment groups using DESeq2. DGE analysis of rIL-33/rIL-13/rIL-17A-treated fibroblasts versus untreated control cells revealed 836 significantly upregulated and 806 significantly downregulated genes (1,642 genes total; **Figure 2.12A**). Genes differentially expressed include those encoding inflammatory and tissue-remodeling proteins like *Il33, Tslp, Cxcl2, Mmp10, Mcam, Acta2, Col4a2.* When compared to untreated cells, fibroblasts treated with rIL-33/rIL-13 or rIL-33/rIL-17A had significant differential expression in 1,536 and 1,228 genes, respectively (**Figure 2.12B-C**); while treatment with rIL-33 had induced differential expression in 473 genes total (**Figure 2.12D**).

Of the 1,642 statistically significant features (p<.0001) that were differentially expressed by triple-treated fibroblasts relative to untreated cells, only 268 genes remained significantly different when triple-treated fibroblasts were also compared to those stimulated with rIL-33/rIL-13, rIL-33/rIL-17A, or rIL-33 alone (features were eliminated if the comparison yielded a false discovery rate > .01; **Figure 2.13**). Gene ontology (GO) analysis (Ashburner et al., 2000) was performed on this gene set (**Figure 2.12E**), revealing significant fold enrichment for upregulated genes associated with cytokine activity (*Il1a, Il6, Tslp, Il33, Il1b, Il11*) and neutrophil trafficking (*Cxcl1, Cxcl2, Cxcl3, Cxcl5*), prostaglandin production (*Ptges, Ptgs2*), and enzymes that modify the composition of extracellular matrix (*Mmp10, Mmp13, Mmp12*). The GO analysis also identified that genes associated with the synthesis of extracellular matrix proteins (*Col6a3, Col11a1, Col4a5, Col15a1, Tgfb3, Lama2, Vcl*) and regulation of cell motility/adhesion (*Itga11, Itga5, Mcam, Pcdh19, Fbln5*) were downregulated. Differentially expressed genes from this list were grouped into functional categories to illustrate how triple-treatment impacted fibroblast activation when compared to cells stimulated with rIL-33, rIL-33/rIL-17A, or rIL-33/rIL-13 (**Figure 2.14**). Altogether, the triple-treated fibroblasts significantly upregulated genes for immune cell activation and tissue remodeling, but downregulated genes for extracellular matrix synthesis.

Functional Implications of lung fibroblast stimulation by IL-33, IL-13, and IL-17A.

The transcriptional data clearly indicated that fibroblasts stimulated with rIL-33/rIL-13/rIL-17A have a potential to produce multiple factors that target innate immune cells, including monocytes and macrophages. Although the evidence for the secretion of most of the factors was based on RNA expression patterns and thus indirect, the GM-CSF protein assays supported that at least one major gene product is transcribed and translated. Of note, GM-CSF expression trends first observed in fibroblasts at the protein level were recapitulated with RNA-seq (**Figure 2.15**; compare with **Figure 2.8**).

The experimental design used to test the potential for triple-treated lung fibroblasts to influence the phenotypes of macrophages is outlined in **Figure 2.16**. Cultures of $CD11b^+$ murine bone-marrow derived macrophages (BMDM) were established and confirmed to express at least one component of the heterodimeric receptor for GM-CSF (Csf2Rα) by flow cytometry (**Figure 2.17A**). For co-culture secretion assays, equal numbers of BMDM and fibroblasts were plated for stimulation with single, double, and triple cytokine treatments. The supernatants of lung fibroblast-BMDM co-cultures contained significantly lower levels of GM-CSF compared to lung fibroblast-only cultures carried out in parallel (**Figure 2.17B**). This consistent reduction in the levels of GM-CSF in the supernatant could be due to negative regulation or BMDM uptake of GM-CSF secreted by fibroblasts.

To investigate whether fibroblast-secreted factors could influence macrophage activation status *in vitro*, we treated BMDM with fibroblast-conditioned media (FCM), which was derived from independently cultured primary lung fibroblasts stimulated by various combinations of rIL-33, rIL-13, and rIL-17A. These fibroblasts were stimulated for 22 hours before being rinsed with PBS and replenished with culture medium to remove any recombinant cytokine that may be still active. FCM was added to BMDM cultures at 20% by volume of media per well and the BMDM were then incubated for 24 hours before harvesting total RNA for RT-qPCR analysis. The goal was to measure changes in the expression of genes encoding molecules associated with 'M2' or 'alternative' macrophage activation, which is often associated with repair or tissue-remodeling phenotypes (Ley, 2017; Mills et al., 2000), like those observed with fibroblasts transcriptionally with RNA-seq.

The FCM from double and triple-cytokine treated cells induced a robust increase in *Arg1* expression by qPCR (**Figure 2.18A**). A modest increase in *Mmp12* was observed among the triple-treated fibroblasts (**Figure 2.18B**). In most groups relative to baseline, however, nonsignificant changes in the expression of *Ym1* and *Retnla* were noted (**Figure 2.18C-D**). *Arg1* expression, especially *in vitro,* is associated with IL-4- and/or IL-13-mediated M2-macrophage phenotype (Gordon, 2003; Raes et al., 2005). Primary lung fibroblasts were not anticipated to produce these cytokines for activating macrophages in this manner, neither at baseline nor post-stimulation with cytokines. Indeed, no detectible reads aligned to *Il13* or *Il4* upon review of the raw count matrix for this experiment (**data not shown**). Media derived from stimulated fibroblasts were also assumed to be rIL-13-free because recombinant cytokines were thoroughly washed away 3x with PBS prior to allow activated fibroblasts to recondition the media. Therefore, expression of *Arg1* was likely induced in BMDM by other fibroblast-derived factors.

Mmp12 is not typically referred to as an ‘M2’ gene; however, this metalloprotease is induced by IL-4 and IL-13 in macrophages in a manner analogous to *Arg1* (**Figure 2.19**) and thus was included here. Although the result for *Mmp12* relies heavily on statistics, both the expression of *Arg1* and *Mmp12* are interesting in the context of negligible *Ym1* and *Retnla* expression*.*

These findings support the hypothesis that activating lung fibroblasts with rIL-33, rIL-13, and rIL-17A results in the production of factors that lead to the activation of macrophages with an expression profile that has elements of an “M2-like” phenotype. Additional experiments will be required for determining the specific factors produced by the treated fibroblasts that drive macrophage activation, as well as for improving the definition of this “M2-like” activation phenotype.

Discussion

In this study, we stimulated macrophages and fibroblasts *in vitro* with cytokine combinations that included recombinant IL-33, IL-13, and IL-17A. These cytokines are commonly associated with subtypes of chronic lung disease like COPD, asthma, and fibrosis. Contrary to our hypothesis derived from observations pertaining to lung macrophages in the EIEE model, airway or alveolar macrophages did not respond with transcriptional significance when directly treated with combinations of rIL-33 and/or rIL-17A. Only rIL-13, and in some scenarios, the addition of rIL-33, appeared to directly modulate macrophage activation to any major extent *in vitro.* Unique fibroblast phenotypes were noted, however, when these cytokines were delivered in four combinations that included, at minimum, rIL-33.

We contemplated re-assaying alveolar macrophages under different conditions, aiming to support our hypothesis for generating a 'pathogenic' cell type *in vitro* by means of rIL-33/13/17A stimulation. For instance, we now appreciate that alveolar macrophages can be maintained *ex vivo* long-term, simply by introducing microenvironmental signals into the media (Gorki et al., 2022; Luo et al., 2021; Subramanian et al., 2022). These studies were conducted because alveolar macrophage biology is environmentally-dictated and known to be strongly influenced by a variety of *in vivo* factors (Lavin et al., 2014; Svedberg et al., 2019). For recapitulating the emphysematous lung microenvironment, we had considered adding lung elastin peptides directly to the media in combination with rIL-33/13/17A. This microenvironmental signal is the product of

Mmp12-mediated degradation of native elastin in the alveolar space and, importantly, a known activator of monocytes and macrophages (Hunninghake et al., 1981; Sellami et al., 2016; Senior et al., 1980). Therefore, we hypothesize that, in combination with immune-relate cytokine signaling, many lung-derived factors also contribute to the development of 'pathogenic' alveolar macrophage phenotypes. However, rather than optimizing our assay by stimulating alveolar macrophages with additional signals *in vitro*, we decided to include a physical, microenvironmental and cellular counterpart – the primary lung fibroblast – as part of our work.

We first noted fibroblast activation by triple-treatment by measuring IL-33-mediated GM-CSF production with ELISA. As mentioned, GM-CSF has an obligatory role for alveolar macrophage development in the lung (Gschwend et al., 2021; Guilliams et al., 2013). Lack of *Csf2* expression results in immature alveolar macrophages with limited functional output, indirectly leading to a disorder called pulmonary alveolar proteinosis (Uchida et al., 2007). In our system, induced expression is perhaps an indicator of fibroblast-macrophage communication during an immune response. We supported this notion indirectly with our co-culture assays in which significantly less GM-CSF was noted in fibroblast-macrophage co-cultures when compared to fibroblast-only cultures. Indeed, two interpretations are possible, since the same number of cells were plated each time: either macrophages inhibit GM-CSF production or take up this protein when secreted by fibroblasts *in vitro.* A major limitation for supporting this communicative circuit, of course, includes lack of understanding whether these effects are similar *in vivo*. Notwithstanding, these *in vitro* observations may serve as a foundation for appreciating how this mesenchymal cell type communicates with macrophages in severe lung disease.

For gaining more insight into the fibroblast response to rIL-33 and, specifically, triple-treatment*,* we applied bulk RNA-sequencing. A potentially important finding from these studies is that combinations of rIL-33, rIL-13, and rIL-17A elicit a spectrum of pro-inflammatory, activation phenotypes in primary lung fibroblasts. These trends were complemented by downregulation in extracellular matrix repair genes that are normally robustly expressed by myofibroblasts (Tomasek et al., 2002). In addition to increased GM-CSF, several factors secreted by triple-treated fibroblasts were noted for their potential ability to activate macrophages.

As an entry-level approach for understanding if secreted factors can influence macrophage phenotypes, we treated bone marrow-derived macrophages with conditioned media from fibroblasts that were previously activated by combinations of these cytokines. Of the limited genes tested by qPCR (*Arg1, Mmp12, Ym1, Retnla)*, expression of *Arg1* was significantly increased in macrophages that received media conditioned by triple-treated fibroblasts. Changes in *Ym1* and *Retnla* expression were not observed by this method, so we began to appreciate that fibroblast conditioned media may at least partially stimulate macrophages toward an "M2-like" activation state. We did not investigate this mechanism to any major extent; however, the RNA-seq data of IL-33/IL-13/IL-17A activated fibroblasts *in vitro* may be useful for speculating which fibroblast-derived proteins elicit this "M2-like" phenotype. Of note, our conditioned media likely does <u>not</u> contain IL-13 nor IL-4, which are known inducers of 'M2' macrophage activation *in vitro* (Das et al., 2018; Gordon, 2003; Raes et al., 2005). We confirmed this indirectly, since aligned reads for *Il13* or *Il4* were not detected in the RNA-seq count matrix for triple-treated fibroblasts. Other activators were certainly noted, though. For example, *Saa3* has been associated with *Arg1* expression in macrophages and related cell types (Ather and Poynter, 2018). Evidence also suggests that GM-CSF, which was the sole gene product validated in our study at both RNA and protein levels, also modulates *Arg1* expression in responsive cell types (Su et al., 2021). To elaborate on this proposed "M2-like" phenotype, statistical observations were also made for *Mmp12*. Expression of this gene could be difficult to interpret, as treating macrophages with known activators of *Mmp12* only leads to about a 4-fold upregulation from baseline. In terms of the other genes tested by qPCR, and just as a technical note – I had confidence in our observation that *Ym1* and *Retnla* were not affected by FCM due to high C_T values and significant intra-group variability, which are both common qPCR readouts for genes with negligible expression.

At the very least, our work offers a major dataset to support future experiments with alveolar macrophages and primary lung fibroblasts. While additional studies are necessary for determining the nature and scope of lung fibroblast-induced macrophage activation *in vivo*, these *in vitro* observations provide a foundation for investigating how stromal cells communicate with macrophages during an injury response in the lungs.

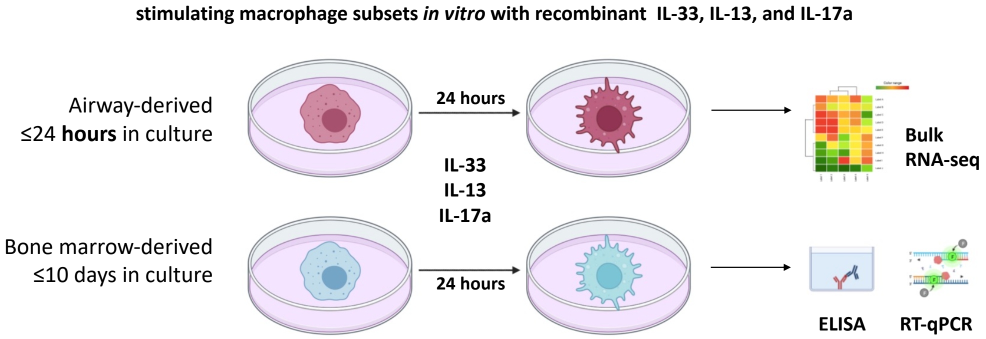

stimulating macrophage subsets *in vitro* with recombinant IL-33, IL-13, and IL-17a

Figure 2.1. Schematic for *in vitro* cytokine stimulation assays with airway- or bone marrow-derived macrophages.

Airway macrophages were obtained by bronchoalveolar lavage. Bone marrow-derived macrophages were differentiated *in vitro.* Both cell types were maintained under standard conditions for our lab (37 ºC, 5% CO_2, 10% serum). Macrophages were treated with cytokine combinations that include recombinant IL-33, IL-13, and IL-17A, as per **Table 2.3**. Readouts for measuring transcriptional regulation or protein secretion from cytokine stimulation included the following: bulk transcriptome sequencing for alveolar macrophages, as well as Enzyme-Linked Immunoassay and reverse-transcription quantitative polymerase chain reaction for analysis of bone marrow-derived macrophages.

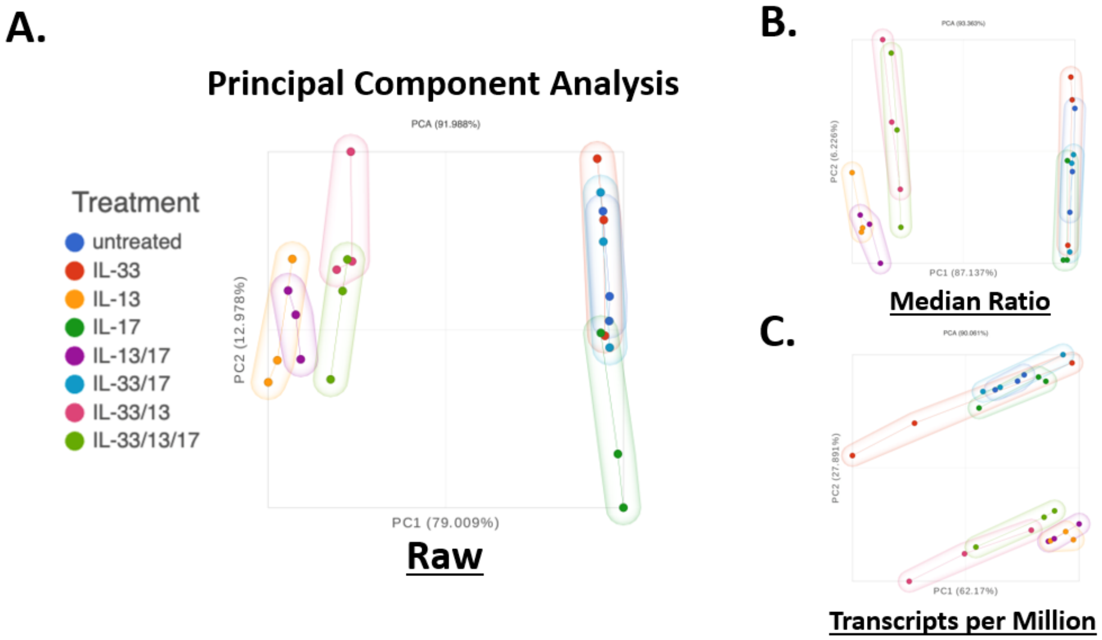

Figure 2.2. Principal Component Analysis of alveolar macrophages treated with combinations of recombinant IL-33, IL-13, and IL-17A.

Macrophages were extracted, plated, and stimulated in technical triplicate with combinations of recombinant cytokines, as described. Samples were submitted for RNA-seq, and reads were aligned to a *Mus musclus* reference genome. Alignments (.bam files) were uploaded to Partek Flow for analysis. Prior to exploratory analysis, QA/QC was performed on the raw, unfiltered RNA-seq data, followed by quantification of the aligned reads with an Ensembl annotation model (release 102). An alignment filter was applied for eliminating low quality reads or those with base mismatches. Among the twenty-four samples, aligned reads were quantified for determining expression levels for 17,017 genes, and the output was organized as a count matrix. Principal component analysis was computed with either raw (**A**) or normalized (**B,C**) count matrices, and the results were visualized with 3D scatter plots. Median ratio normalization was applied specifically because DESeq2, a comparative algorithm, was used for gene expression analysis downstream. Transcripts per million (TPM) normalization was applied for visualizing absolute transcript counts among samples.

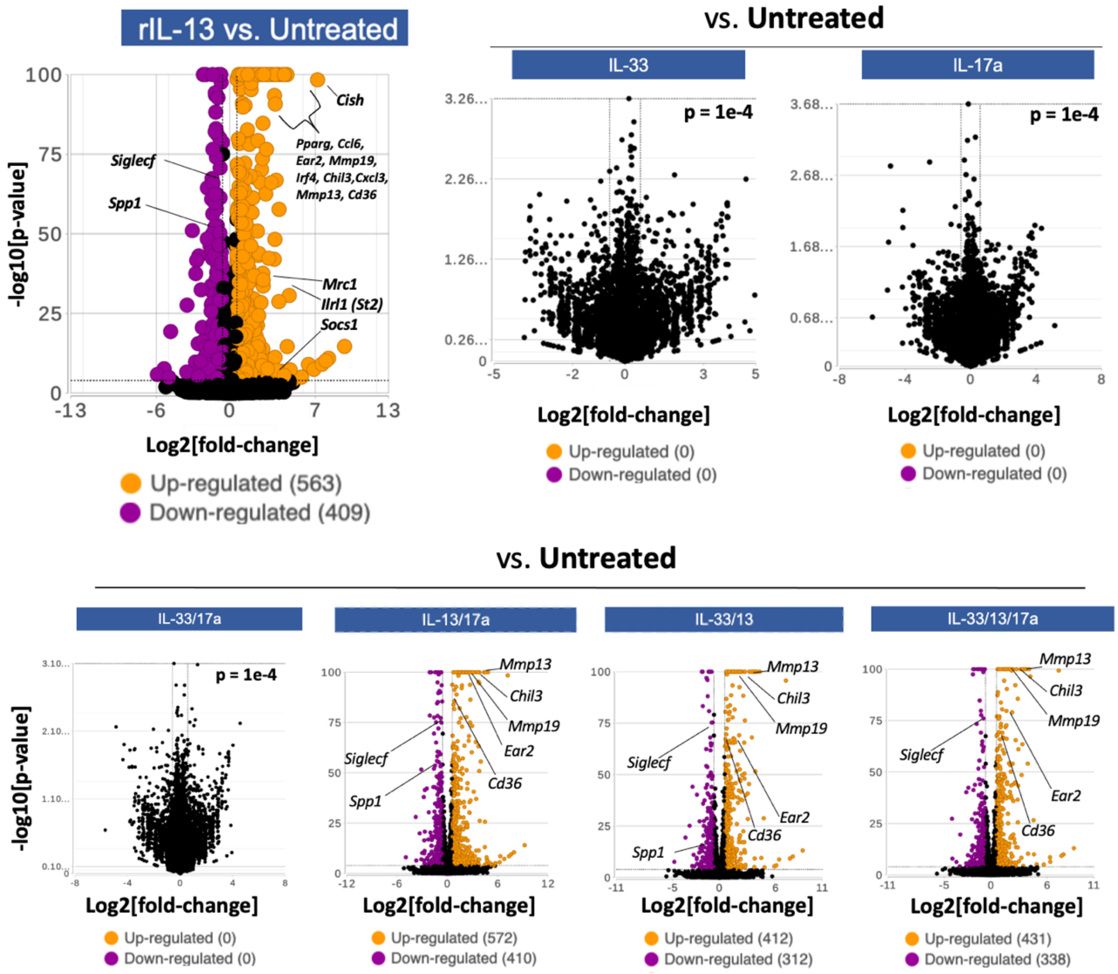

Figure 2.3. Transcriptional comparisons of alveolar macrophages treated with combinations of recombinant IL-33, IL-13, and IL-17A relative to baseline.

The algorithm DESeq2 was applied for identifying and ranking the significance of genes differentially expressed between macrophage treatment groups. DESeq2 computed an ANOVA table with the following statistical comparisons: p-value, fold-change, FDR step-up. Significantly up- or downregulated genes from the ANOVA table were illustrated by volcano plot, once transformed as function of -log10[p-value] (Y-axis) and log2[fold-change] (X-axis). Normalization of the data (median ratio) was also peformed with DESeq2 by default. (**ALL PANELS**) Seven unique alveolar macrophage treatment groups, having been stimulated with combinations of recombinant IL-33, IL-13, and/or IL-17A *in vitro*, were directly compared to the untreated control group. Significance cut-offs for this analysis was designated to be p-value <.0001, fold change = +/- 1.5. Gene identifiers in each visualization were manually annotated, and some lines are thus approximated due to size restraints of overlapping datapoints.

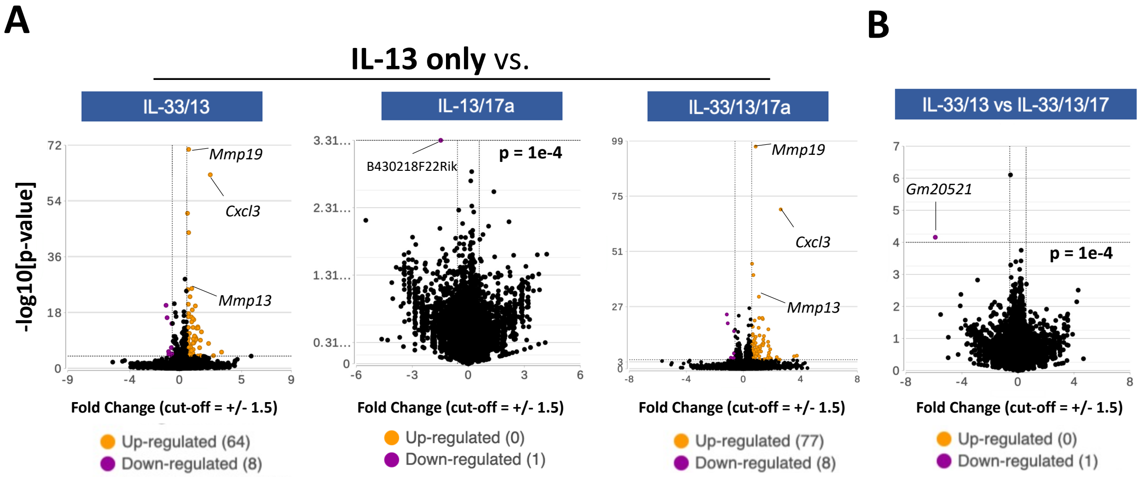

Figure 2.4. Differential Gene Expression analysis of alveolar macrophages treated with combinations that include, at least, recombinant IL-13.

The algorithm DESeq2 was used. Significantly up- or downregulated genes for each comparison are illusrated with volcano plots: -log10[p-value] (Y-axis) and log2[fold-change] (X-axis). Normalization (median ratio) and statistical comparisons (p-value, fold-change, FDR step-up) were also peformed in DESeq2 by default. (**A**) alveolar macrophage treatment groups that received, at mimimum, recombinant IL-13, were compared by volcano plot. (**B**) alveolar macrophages teated with recombinant IL-33/13/17a were also directly compared to those treated with IL-33/13 in duplicate. Significance cut-offs for this analysis was designated to be p-value <.0001, fold change = +/- 1.5.

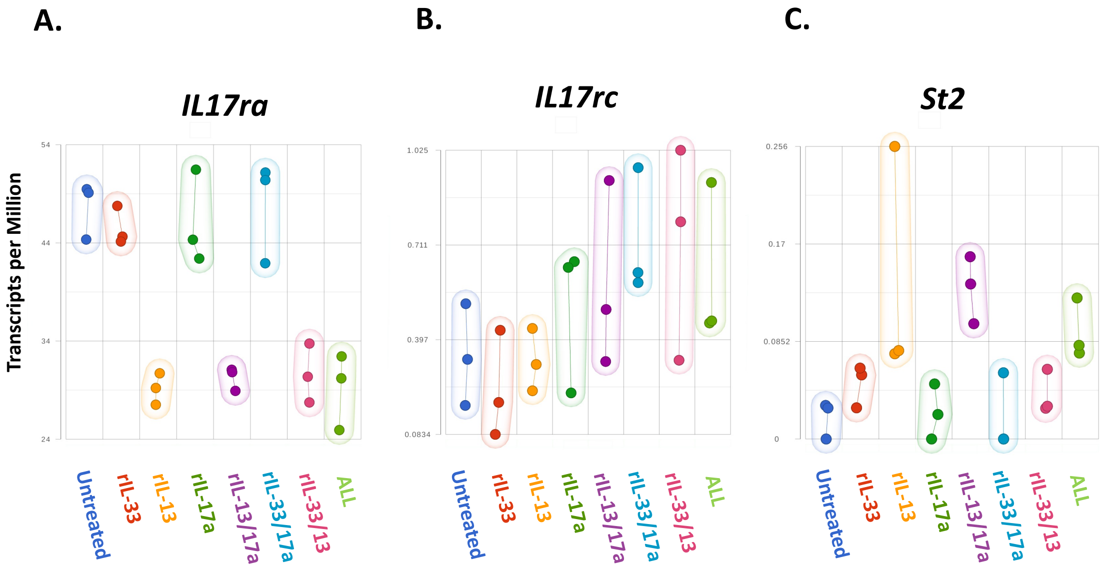

Figure 2.5. ***Il17ra, Il17rc,* and *St2* absolute transcript abundances in alveolar macrophages at baseline or post-cytokine stimulation.**

Illustrated by 2D scatter plot, each treatment group is portrayed on the X-axis; the Y axis represents transcript abundance (TPM-normalized) for following: (**A**) *Il17ra,* (**B**) *Il17rc,* (**C**) *St2*.

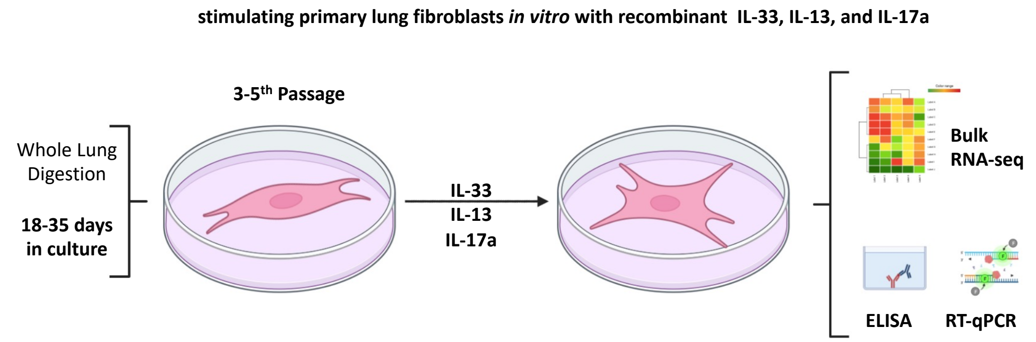

stimulating primary lung fibroblasts *in vitro* with recombinant IL-33, IL-13, and IL-17a

Figure 2.6. Schematic for *in vitro* cytokine stimulation assays with primary lung fibroblasts.

Whole lung tissue was extracted from wildtype (WT) Balb/c mice, digested, and single-cell suspensions were cultured under conditions standard for our lab (37 ºC, 5% $CO_{2,}$ 10% serum). For achieving purity and phenotypic homogeneity at baseline, fibroblasts were passaged 3 to 5 times prior to cytokine stimulation assays. We applied the same metrics as with alveolar macrophages for measuring changes in gene expression or protein secretion (RNA-seq, ELISA, RT-qPCR).

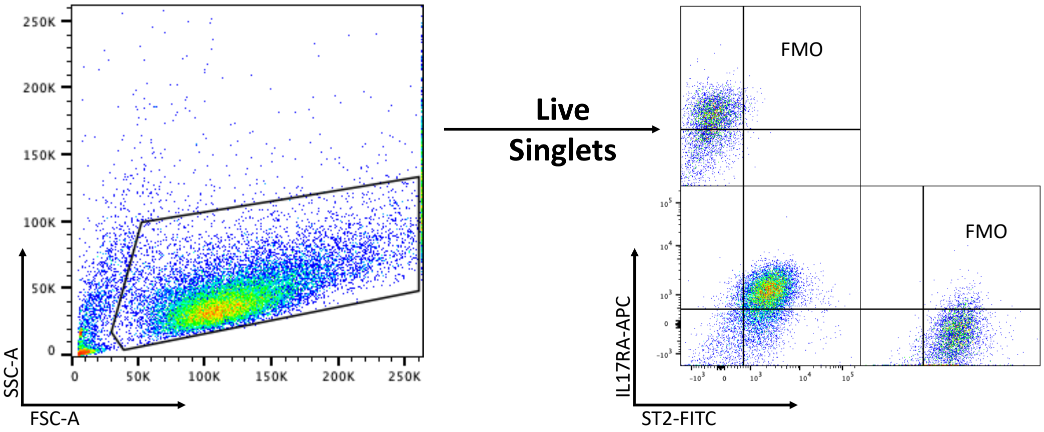

Figure 2.7. Primary lung fibroblasts express receptors for IL-17A and IL-33.

Lung-derived fibroblasts were placed in culture as outlined in the **Methods**. At passage three, the cells were harvested, immunostained with anti-IL17RA-APC and anti-ST2-FITC for flow cytometry. Acquisition was performed on an LSR-II (Becton Dickinson, Franklin Lakes NJ). Positive signal for each antibody was confirmed by comparing sample directly to a Fluorescence Minus One (FMO) control. Cytometry of WT lung fibroblasts was performed twice and in technical triplicate.

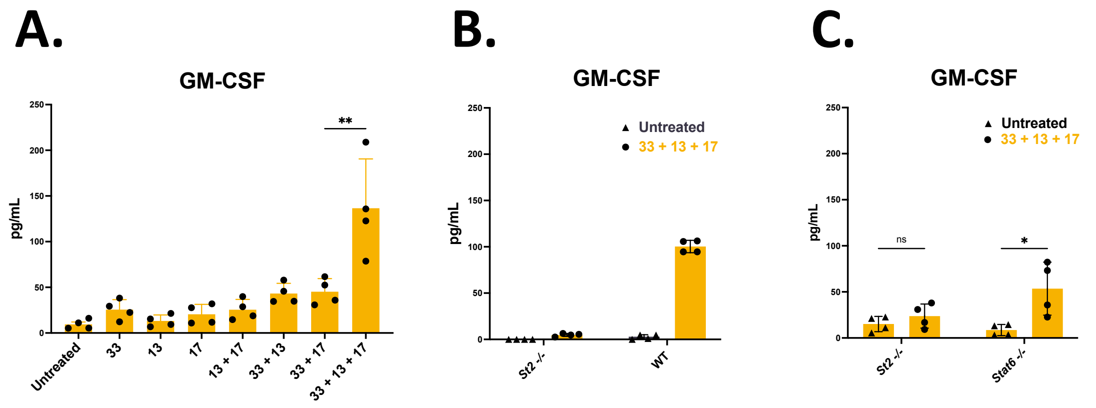

WT - all treatments **_St2_$^{-/-}$ vs. WT** **_St2_$^{-/-}$ vs. _Stat6_$^{-/-}$**

Figure 2.8. GM-CSF secretion in primary lung fibroblasts measured by ELISA.

Fibroblasts were plated and stimulated for each assay, as described, in technical quadruplicate. (**A**) Trends in GM-CSF secretion by primary lung fibroblasts treated with all permutations of recombinant IL-33, IL-13, and IL-17A *in vitro*. For initial work, only WT fibroblasts were studied. To support these findings mechanistically, *St2*$^{-/-}$ fibroblasts were compared to either WT (**B**) or *Stat6*$^{-/-}$ cells (**C**) upon triple-treatment *in vitro*. Error bars represent standard deviation of the mean. Significance was determined by ordinary, one- or two-way ANOVA with multiple comparisons (+ Tukey's post-hoc test). *<.05; **≤.005; ns = not significant.

A.

Average Base Quality ('Phred-33 score')

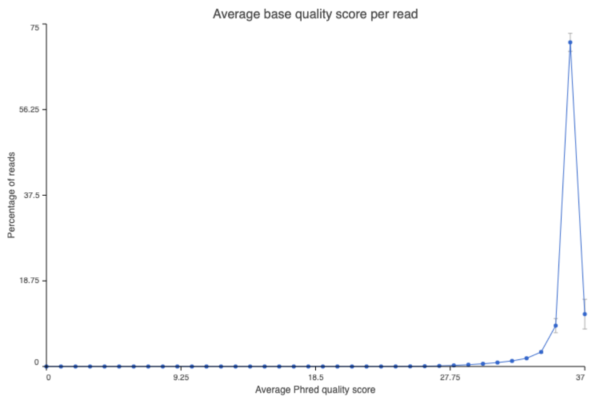

B. **Aligned Read Depth per Sample ('Coverage')**

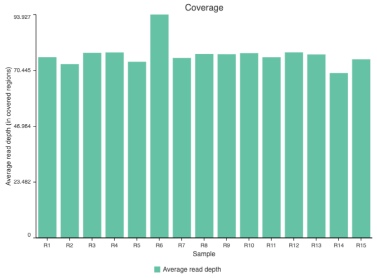

Unfiltered

C.

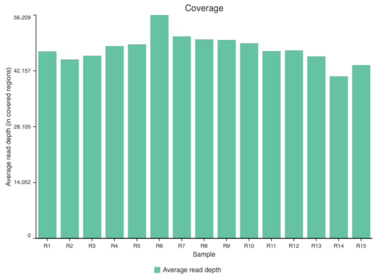

Filtered

D.

Feature Distribution ('RAW COUNTS')

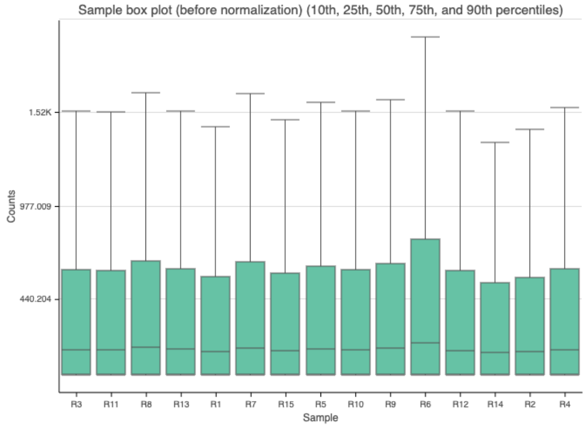

E.

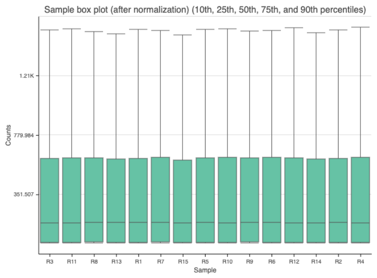

Median Ratio (DESeq2)

F.

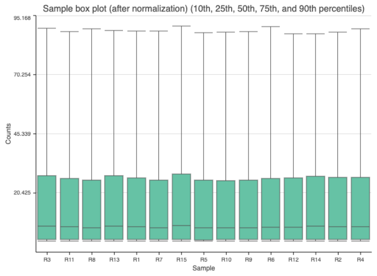

Transcripts per Million

Figure 2.9. Technical analysis of RNA-seq data with standard QA/QC metrics before and after quantification of aligned reads.

Fibroblasts were cultured and stimulated in technical triplicate with combinations of cytokines, as described. Samples were submitted for RNA-seq, and reads were aligned to a *Mus musclus* reference genome. Alignments (.bam files) were uploaded to Partek Flow for analysis, which included QA/QC of the sequenced dataset at various stages. (**A**) Prior to quantification, average base quality per sample was assessed by the Phred-33 index. Coverage reports describing the average depth of aligned reads per sample were also generated. Plots describing read depth per sample were illustrated for both unfiltered (**B**) or filtered (**C**) matrices. (**D**) Post-quantification, the distribution of features per sample, or 'raw counts', were visualized. Raw counts were normalized, as needed, with either the Median Ratio (**E**) or Transcripts per Million (**F**) methods. Bulk RNA-sequencing was performed just once in technical triplicate using primary lung fibroblasts stimulated *in vitro*.

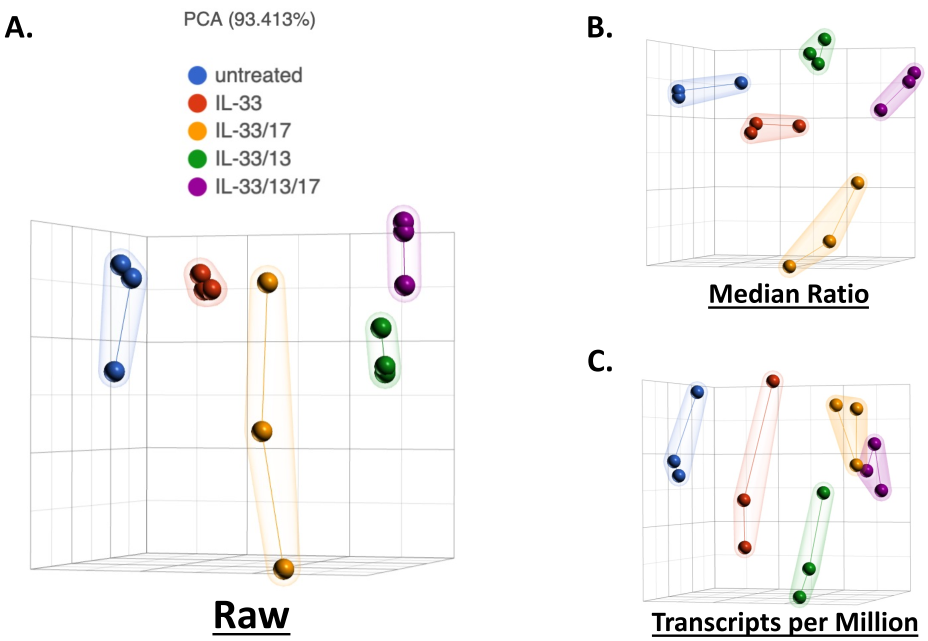

Figure 2.10. Principle component analysis of fibroblasts stimulated with combinations of rIL-33/13/17A.

Aligned reads from RNA-seq were quantified upstream by referencing a *Mus musculus* genome and transcriptome from the Ensembl annotation model (release 102). Among the fifteen samples, aligned reads were quantified for determining expression levels of 18,078 genes, and the output was organized as a count matrix. Principal component analysis was computed with either raw (**A**) or normalized (**B,C**) count matrices, and the results were illustrated with 3D scatter plots.

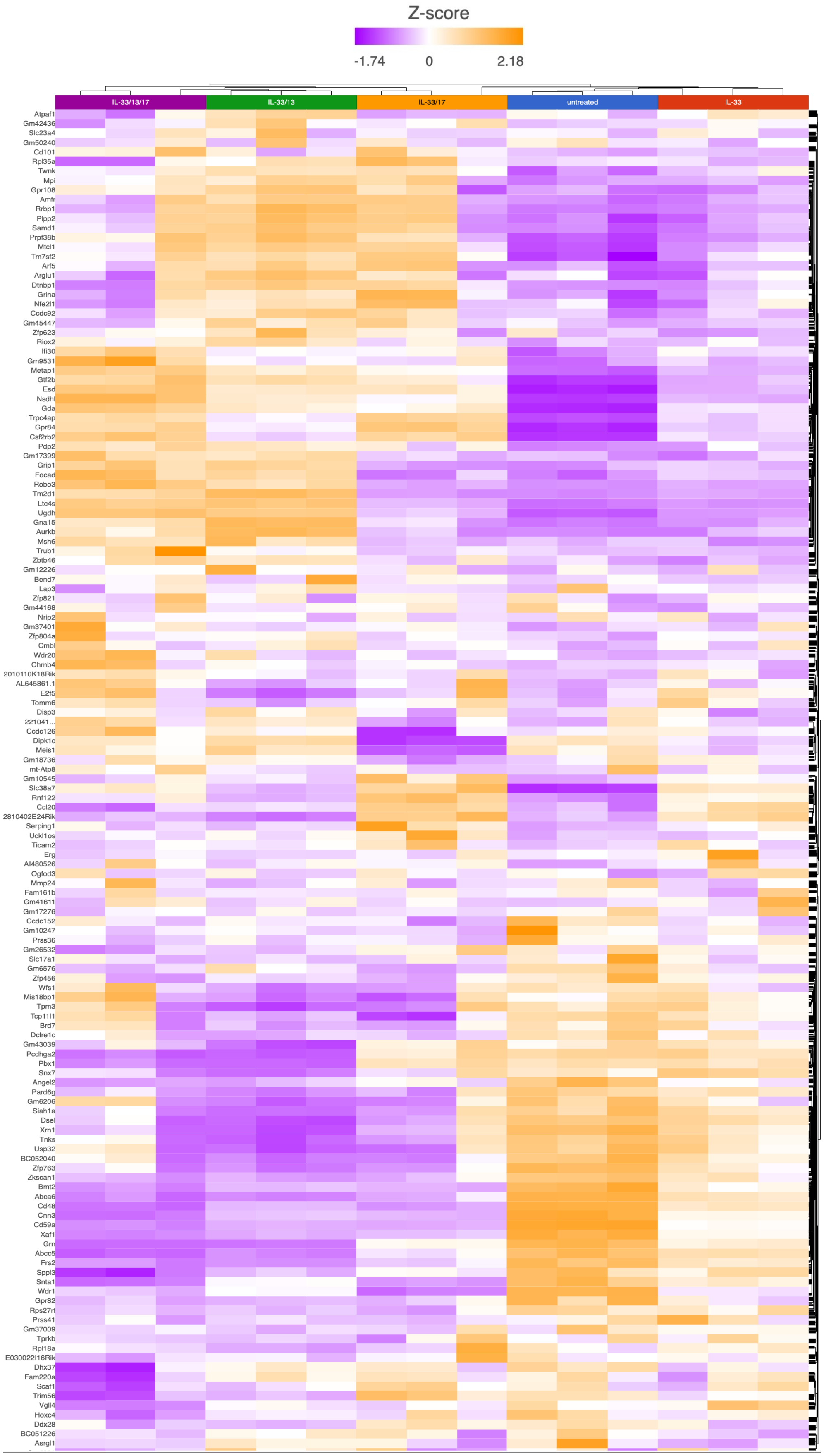
Z-score
-1.74
0
2.18
IL-33/13/17
IL-33/13
IL-33/17
untreated
IL-33
Atpaf1
Gm42436
Slc23a4
Gm50240
Cd101
Rpl35a
Twnk
Mpi
Gpr108
Amfr
Rrbp1
Plpp2
Samd1
Prpf38b
Mtcl1
Tm7sf2
Arf5
Arglu1
Dtnbp1
Grina
Nfe2l1
Ccdc92
Gm45447
Zfp623
Riox2
Ifi30
Gm9531
Metap1
Gtf2b
Esd
Nsdhl
Gda
Trpc4ap
Gpr84
Csf2rb2
Pdp2
Gm17399
Grip1
Focad
Robo3
Tm2d1
Ltc4s
Ugdh
Gna15
Aurkb
Msh6
Trub1
Zbtb46
Gm12226
Bend7
Lap3
Zfp821
Gm44168
Nrip2
Gm37401
Zfp804a
Cmbl
Wdr20
Chrnb4
2010110K18Rik
AL645861.1
E2f5
Tomm6
Disp3
221041...
Ccdc126
Dipk1c
Meis1
Gm18736
mt-Atp8
Gm10545
Slc38a7
Rnf122
Ccl20
2810402E24Rik
Serping1
Uckl1os
Ticam2
Erg
AI480526
Ogfod3
Mmp24
Fam161b
Gm41611
Gm17276
Ccdc152
Gm10247
Prss36
Gm26532
Slc17a1
Gm6576
Zfp456
Wfs1
Mis18bp1
Tpm3
Tcp11l1
Brd7
Dclre1c
Gm43039
Pcdhga2
Pbx1
Snx7
Angel2
Pard6g
Gm6206
Siah1a
Dsel
Xrn1
Tnks
Usp32
BC052040
Zfp763
Zkscan1
Bmt2
Abca6
Cd48
Cnn3
Cd59a
Xaf1
Grn
Abcc5
Frs2
Sppl3
Snta1
Wdr1
Gpr82
Rps27rt
Prss41
Gm37009
Tprkb
Rpl18a
E030022I16Rik
Dhx37
Fam220a
Scaf1
Trim56
Vgll4
Hoxc4
Ddx28
BC051226
Asrgl1

Figure 2.11. Applying hierarchical clustering for exploratory RNA-seq analysis of fibroblasts stimulated with rIL-33/13/17A.

The raw count matrix first was normalized in DESeq2, which applies the Median Ratio formula. Normalized counts were subjected to hierarchical clustering, and the data were illustrated as a heatmap. Columns are treatment groups and rows are genes. Each box is a representation of relative transcript abundance. Z-score is a scaling factor applied by the algorithm for making relative comparisons within rows (i.e. for determining whether a gene is **upregulated** or **downregulated** among samples in the dataset). Due to size restraints, not all genes can be shown; and each box in the heatmap actually represents a sum of genes for generating this global visualization (a method called 'binning'). Average linkage (cluster distance metric) and Pearson dissimilarity (point distance metric) were the statistical parameters applied for executing heirarchical clustering of this dataset.

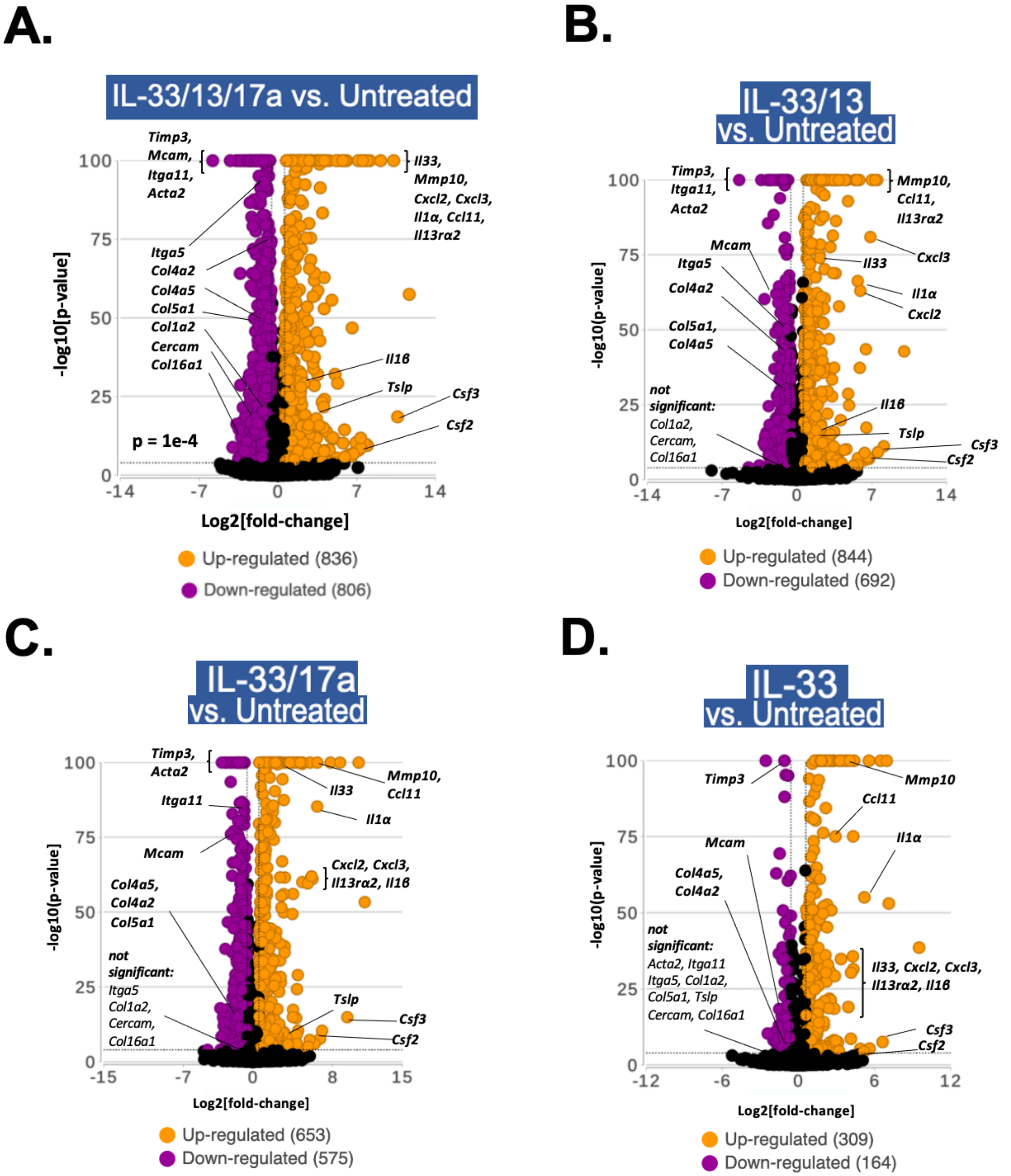

E.

Gene Set Enrichment

upregulated (137 genes)	enrichment score	P-value
cytokine activity	36.9	9x10^{-17}
chemotaxis	26.2	4.2x10^{-12}
neutrophil migration	16.5	7x10^{-8}
prostaglandin secretion	12.9	2.4x10^{-6}
extracellular matrix	9.7	6.2x10^{-5}
downregulated (131 genes)		
extracellular matrix	42.3	3.9x10^{-19}
regulation of cell motitilty	18.3	1.1x10^{-8}
cell adhesion	15.8	1.3x10^{-7}

Figure 2.12. Differential Gene Expression Analysis of fibroblast treatment groups.

The algorithm DESeq2 was applied for identifying and ranking the significance of genes differentially expressed between fibroblast treatment groups. DESeq2 computed an ANOVA table with the following statistical comparisons: p-value, fold-change, FDR step-up. Significantly up- or downregulated genes from the ANOVA table were illustrated by volcano plot, once transformed as function of -log10[p-value] (Y-axis) and log2[fold-change] (X-axis). Normalization of the data (median ratio) was also peformed with DESeq2 by default. (**A-D**) Each treatment group was independently compared to untreated control fibroblasts. Significance cut-offs for this analysis was designated to be p-value ≤.0001, fold change = +/- 1.5. Gene identifiers in each visualization were manually annotated, and some lines are thus approximated due to size restraints. (**E**) Gene Set enrichment of the top 238 genes differentially expressed by triple-treated fibroblasts when compared to all groups in the assay.

Significantly Increased Expression

			Fold change rIL-33/rIL13/rIL-17a vs			
RANK	GENE	ENSEMBL	untreated	r IL-33/rIL-13	rIL-33/rIL-17	r IL-33
1	Lcn2	ENSMUSG00000026822	3222.82	4.42	1.35	3.09
2	Csf3	ENSMUSG00000038067	1575.88	15.85	2.23	5.67
3	Nos2	ENSMUSG00000020826	1238.33	8.90	-1.26	14.25
4	Cxcl1	ENSMUSG00000029380	554.31	4.46	1.30	3.05
5	Cxcl5	ENSMUSG00000029371	284.20	3.18	1.29	2.22
6	Il13ra2	ENSMUSG00000031289	244.40	12.49	5.42	1.53
7	Cxcl3	ENSMUSG00000029379	209.24	10.42	3.33	1.79
8	Csf2	ENSMUSG00000018916	209.12	4.29	1.97	2.12
9	Cxcl2	ENSMUSG00000058427	184.80	10.38	3.15	3.04
10	Ccl11	ENSMUSG00000020676	168.09	22.26	10.42	1.21
11	Rassf10	ENSMUSG00000098132	162.33	26.76	3.12	2.02
12	Il1a	ENSMUSG00000027399	139.77	3.81	1.61	2.72
13	Upp1	ENSMUSG00000020407	95.82	13.74	5.89	1.64
14	Saa3	ENSMUSG00000040026	68.33	1.45	-1.28	1.60
15	Serpina3g	ENSMUSG00000041481	62.47	10.29	5.20	1.39
16	Trdc	ENSMUSG00000104876	54.69	8.11	2.59	3.01
17	Steap4	ENSMUSG00000012428	49.73	2.50	1.63	1.82
18	Lif	ENSMUSG00000034394	39.44	3.67	1.26	1.59
19	Penk	ENSMUSG00000045573	35.75	2.71	1.38	1.59
20	Mmp10	ENSMUSG00000047562	20.09	2.08	1.18	1.44
21	Il6	ENSMUSG00000025746	19.91	2.91	1.16	2.08
22	Slc7a2	ENSMUSG00000031596	17.57	5.22	2.78	1.45
23	Tslp	ENSMUSG00000024379	15.07	5.26	2.69	1.74
24	Pf4	ENSMUSG00000029373	13.52	3.39	2.02	1.40
25	Mmp13	ENSMUSG00000050578	13.46	2.84	2.22	1.27
26	Il33	ENSMUSG00000024810	13.15	5.08	2.15	2.99
27	Selp	ENSMUSG00000026580	11.61	2.60	1.77	1.62
28	Procr	ENSMUSG00000027611	11.59	4.02	1.92	1.78
29	Cp	ENSMUSG00000003617	10.98	2.36	1.46	1.67
30	Nfkbiz	ENSMUSG00000035356	9.75	2.78	-1.20	2.99
31	Aldh3a1	ENSMUSG00000019102	9.35	7.78	4.08	2.78
32	Il1b	ENSMUSG00000027398	8.96	1.53	-1.82	2.08
33	Crispld2	ENSMUSG00000031825	8.48	6.12	3.15	1.68
34	Cyp7b1	ENSMUSG00000039519	7.87	2.66	1.42	1.74
35	Il11	ENSMUSG00000004371	7.83	3.06	1.86	1.37
36	Mmp12	ENSMUSG00000049723	7.75	2.00	1.57	1.41
37	Ptges	ENSMUSG00000050737	7.56	2.28	1.31	1.36
38	Gm7993	ENSMUSG00000107092	7.48	3.66	1.80	1.71
39	Rgs16	ENSMUSG00000026475	7.27	2.53	1.33	1.13
40	Serpina3n	ENSMUSG00000021091	7.07	6.02	5.60	1.56
41	Ccl7	ENSMUSG00000035373	6.85	2.26	1.40	1.22
42	Gm2115	ENSMUSG00000097789	6.77	1.94	1.39	1.40
43	Ptgs2	ENSMUSG00000032487	6.01	2.44	1.26	1.84
44	Sod2	ENSMUSG00000006818	5.99	1.67	1.12	1.22
45	Dio2	ENSMUSG00000007682	5.95	3.44	1.87	1.80
46	Odc1	ENSMUSG00000011179	5.67	3.15	1.68	1.68
47	Abcb1a	ENSMUSG00000040584	5.64	2.87	1.75	1.50
48	Arg2	ENSMUSG00000021125	5.41	1.93	1.27	1.26
49	Ttc39c	ENSMUSG00000024424	5.39	2.34	1.79	1.32
50	Fam110c	ENSMUSG00000036136	4.90	2.10	1.25	1.44
51	Slc16a1	ENSMUSG00000032902	4.80	2.21	1.17	1.51
52	Clec4n	ENSMUSG00000023349	4.63	-1.42	-1.95	1.44
53	Rgs7bp	ENSMUSG00000021719	4.15	2.20	1.80	1.61
54	Gja1	ENSMUSG00000050953	4.14	2.44	1.81	1.33
55	Ccr1	ENSMUSG00000025804	4.02	1.36	1.21	1.19
56	Lrig1	ENSMUSG00000030029	3.86	1.79	-1.17	1.65
57	Pcolce2	ENSMUSG00000015354	3.85	3.82	3.87	-1.51
58	Phlda1	ENSMUSG00000020205	3.83	2.06	1.42	1.39
59	Gpm6b	ENSMUSG00000031342	3.71	1.80	1.52	1.20
60	Slco3a1	ENSMUSG00000025790	3.57	2.37	1.16	1.72
61	Rbp1	ENSMUSG00000046402	3.52	1.73	1.19	1.35
62	Pi15	ENSMUSG00000067780	3.47	1.58	-1.49	1.76
63	S1pr3	ENSMUSG00000067586	3.36	2.66	3.63	-1.28
64	Mt2	ENSMUSG00000031762	3.20	1.49	1.14	1.34
65	Crem	ENSMUSG00000063889	3.10	2.21	1.58	1.40
66	Srgn	ENSMUSG00000020077	3.01	2.11	1.91	1.31
67	Itgb3	ENSMUSG00000020689	2.98	2.36	1.53	1.26
68	Arrdc4	ENSMUSG00000042659	2.92	1.75	1.39	1.34
69	Pdpn	ENSMUSG00000028583	2.85	1.57	1.19	1.26
70	Acsl4	ENSMUSG00000031278	2.74	1.76	1.33	1.47
71	Cd38	ENSMUSG00000029084	2.68	1.59	1.46	1.31
72	Mpzl1	ENSMUSG00000026566	2.62	1.97	1.23	1.47
73	Trf	ENSMUSG00000032554	2.60	1.79	1.22	1.41
74	Plcb1	ENSMUSG00000051177	2.57	2.09	1.91	1.41
75	Igfbp5	ENSMUSG00000026185	2.55	1.55	-1.13	1.30
76	Slc39a14	ENSMUSG00000022094	2.51	1.40	1.12	1.12
77	Lrp8	ENSMUSG00000028613	2.49	1.73	1.43	1.27
78	Plau	ENSMUSG00000021822	2.48	1.62	1.28	1.21
79	Dcxr	ENSMUSG00000039450	2.42	1.77	1.46	1.28
80	Ptpn2	ENSMUSG00000024539	2.37	2.09	1.48	1.42
81	Gsto1	ENSMUSG00000025068	2.33	1.48	1.17	1.13
82	Pdia4	ENSMUSG00000025823	2.30	1.73	1.50	1.18
83	Sorcs1	ENSMUSG00000043531	2.28	1.74	1.55	1.24
84	Lmo4	ENSMUSG00000028266	2.26	1.81	1.60	1.29
85	Pla2g4a	ENSMUSG00000056220	2.25	1.55	1.12	1.26
86	Tnfrsf26	ENSMUSG00000045362	2.24	1.49	1.29	1.37
87	Nqo1	ENSMUSG00000003849	2.24	1.67	1.26	1.36
88	Fmnl2	ENSMUSG00000036053	2.24	1.64	1.36	1.23
89	Mllt11	ENSMUSG00000053192	2.23	1.67	1.36	1.65
90	Mt1	ENSMUSG00000031765	2.22	1.34	1.15	1.32
91	Vcam1	ENSMUSG00000027962	2.20	1.28	-1.11	1.43
92	Aif1l	ENSMUSG00000001864	2.18	4.30	5.66	-1.77
93	Ugt1a7c	ENSMUSG00000090124	2.14	1.78	1.36	1.28
94	Slc20a1	ENSMUSG00000027397	2.13	1.66	1.29	1.29
95	Cd47	ENSMUSG00000055447	2.12	1.63	1.42	1.34
96	Sema3a	ENSMUSG00000028883	2.12	1.94	2.34	1.25
97	Dusp6	ENSMUSG00000019960	2.11	1.54	1.29	1.18
98	Rdh10	ENSMUSG00000025921	2.10	1.87	1.31	1.39
99	Adamts9	ENSMUSG00000030022	2.07	1.45	1.24	1.25
100	Mmd	ENSMUSG00000003948	2.03	1.56	1.24	1.25
101	Rhbdf2	ENSMUSG00000020806	2.02	1.27	1.15	1.19
102	Fdps	ENSMUSG00000059743	2.01	1.45	1.20	1.16
103	Slc25a25	ENSMUSG00000026819	1.97	1.55	1.23	1.26
104	Pi4k2b	ENSMUSG00000029186	1.95	1.55	1.21	1.27
105	Vegfa	ENSMUSG00000023951	1.94	1.20	-1.13	1.28
106	St3gal1	ENSMUSG00000013846	1.90	1.70	1.37	1.16
107	Fchsd2	ENSMUSG00000030691	1.86	1.68	1.49	1.20
108	Kcne4	ENSMUSG00000047330	1.85	1.36	-1.28	1.30
109	Sema6d	ENSMUSG00000027200	1.85	1.77	1.65	1.36
110	Litaf	ENSMUSG00000022500	1.85	1.51	1.31	1.24
111	Idi1	ENSMUSG00000058258	1.84	1.37	1.29	1.35
112	Stambpl1	ENSMUSG00000024776	1.78	1.61	1.54	1.23
113	Ifngr2	ENSMUSG00000022965	1.77	1.48	1.31	1.15
114	Abcc1	ENSMUSG00000023088	1.73	1.39	1.19	1.32
115	Gstm1	ENSMUSG00000058135	1.72	1.51	1.45	1.31
116	Cdc20	ENSMUSG00000006398	1.72	1.33	1.31	-1.28
117	Grem1	ENSMUSG00000074934	1.71	1.34	1.11	1.23
118	Gpr39	ENSMUSG00000026343	1.70	1.28	1.32	-1.22
119	Rbpj	ENSMUSG00000039191	1.70	1.31	1.17	1.18
120	Hspa5	ENSMUSG00000026864	1.68	1.54	1.33	1.13
121	Xdh	ENSMUSG00000024066	1.66	1.79	1.91	-1.11
122	Epas1	ENSMUSG00000024140	1.66	1.65	1.41	1.35
123	Rnf149	ENSMUSG00000048234	1.66	1.25	-1.12	1.18
124	Car13	ENSMUSG00000027555	1.65	1.33	1.27	1.27
125	Tlr4	ENSMUSG00000039005	1.64	1.42	1.29	1.20
126	Pfn2	ENSMUSG00000027805	1.62	1.42	1.31	1.19
127	Pml	ENSMUSG00000036986	1.62	1.42	1.26	1.21
128	Serpinb1a	ENSMUSG00000044734	1.62	2.34	3.11	-1.25
129	Mapre2	ENSMUSG00000024277	1.62	1.37	1.14	1.26
130	Prickle1	ENSMUSG00000036158	1.60	1.59	1.29	1.27
131	Tmed5	ENSMUSG00000063406	1.58	1.45	1.28	1.32
132	Gnpnat1	ENSMUSG00000037722	1.57	1.42	1.36	1.24
133	Gng12	ENSMUSG00000036402	1.55	1.33	1.24	1.16
134	Tsc22d1	ENSMUSG00000022010	1.53	1.17	-1.22	1.43
135	Pafah2	ENSMUSG00000037366	1.51	1.39	1.22	1.23
136	Dock4	ENSMUSG00000035954	1.51	1.29	1.33	1.23
137	Scd1	ENSMUSG00000037071	1.51	1.35	1.19	1.24

Significantly Decreased Expression

			Fold change rIL-33/rIL13/rIL-17a vs			
RANK	GENE	ENSEMBL	untreated	r IL-33/rIL-13	rIL-33/rIL-17	r IL-33
1	Limch1	ENSMUSG00000037736	-18.86	-6.80	-2.71	-2.75
2	Angpt4	ENSMUSG00000027460	-11.61	-3.99	-2.70	-1.76
3	Timp3	ENSMUSG00000020044	-10.07	-4.70	-1.63	-1.82
4	Itga11	ENSMUSG00000032243	-10.06	-6.84	-4.00	-1.70
5	Mcam	ENSMUSG00000032135	-8.29	-3.90	-1.77	-2.14
6	Ccn5	ENSMUSG00000027656	-8.02	-4.91	-4.13	-1.55
7	Lmod1	ENSMUSG00000048096	-6.57	-4.11	-2.12	-2.82
8	Cav1	ENSMUSG00000007655	-6.22	-3.03	-1.46	-1.43
9	Col6a3	ENSMUSG00000048126	-5.71	-3.26	-2.06	-1.46
10	Lurap1l	ENSMUSG00000048706	-5.62	-3.82	-2.11	-1.78
11	Cnn1	ENSMUSG00000001349	-5.38	-3.52	-1.73	-1.96
12	Mrvi1	ENSMUSG00000005611	-5.08	-3.08	-1.70	-2.00
13	Myh11	ENSMUSG00000018830	-5.07	-3.03	-1.49	-1.66
14	Mylk	ENSMUSG00000022836	-5.03	-3.29	-1.72	-1.80
15	Hspb7	ENSMUSG00000006221	-4.85	-2.88	-1.59	-2.05
16	Lrrc15	ENSMUSG00000052316	-4.71	-3.30	-2.44	-1.39
17	Tgfb3	ENSMUSG00000021253	-4.65	-2.62	-1.24	-1.35
18	Nrep	ENSMUSG00000042834	-4.34	-3.62	-2.25	-1.48
19	Asb2	ENSMUSG00000021200	-4.23	-2.98	-1.84	-2.21
20	Acta2	ENSMUSG00000035783	-4.23	-3.04	-1.58	-1.80
21	Actg2	ENSMUSG00000059430	-4.07	-2.79	-1.44	-1.54
22	Cygb	ENSMUSG00000020810	-4.00	-2.87	-1.90	-1.66
23	Ccdc80	ENSMUSG00000022665	-3.97	-1.99	-1.28	-1.48
24	Lama2	ENSMUSG00000019899	-3.92	-2.57	-1.38	-1.43
25	Cd248	ENSMUSG00000056481	-3.85	-2.46	-1.37	-1.66
26	Aoc3	ENSMUSG00000019326	-3.84	-2.92	-1.94	-1.35
27	Cavin2	ENSMUSG00000045954	-3.83	-2.79	-1.33	-1.89
28	Fhl1	ENSMUSG00000023092	-3.67	-1.73	1.34	-1.42
29	Lims2	ENSMUSG00000024395	-3.64	-2.68	-1.39	-1.59
30	Lbh	ENSMUSG00000024063	-3.53	-2.47	-1.33	-1.79
31	Mycl	ENSMUSG00000028654	-3.52	-2.82	-2.13	-1.73
32	C1qtnf2	ENSMUSG00000046491	-3.50	-3.04	-2.12	-2.12
33	Mustn1	ENSMUSG00000042485	-3.44	-2.46	-1.77	-1.64
34	Myl9	ENSMUSG00000067818	-3.42	-2.57	-1.75	-1.97
35	Galnt17	ENSMUSG00000034040	-3.26	-1.96	-1.76	-1.42
36	Setbp1	ENSMUSG00000024548	-3.26	-2.16	-1.33	-1.34
37	Adgrd1	ENSMUSG00000044017	-3.23	-2.56	-1.26	-1.36
38	Cemip	ENSMUSG00000052353	-3.17	-2.08	-1.28	-1.14
39	Mn1	ENSMUSG00000070576	-3.12	-2.73	-1.85	-1.39
40	Col11a1	ENSMUSG00000027966	-2.95	-2.69	-1.79	-1.55
41	Tns1	ENSMUSG00000055322	-2.94	-2.03	-1.33	-1.35
42	Dmpk	ENSMUSG00000030409	-2.91	-2.09	-1.56	-1.33
43	Tinagl1	ENSMUSG00000028776	-2.85	-1.78	-1.24	-1.72
44	Cd72	ENSMUSG00000028459	-2.83	-1.31	-1.31	-1.25
45	Col4a5	ENSMUSG00000031274	-2.83	-1.69	-1.48	-1.34
46	Ttc28	ENSMUSG00000033209	-2.81	-2.10	-1.39	-1.41
47	Trnp1	ENSMUSG00000056596	-2.78	-2.47	-2.36	-1.74
48	Fbln5	ENSMUSG00000021186	-2.78	-1.67	-1.20	-1.25
49	Galnt18	ENSMUSG00000038296	-2.75	-2.32	-1.29	-1.50
50	Vcl	ENSMUSG00000021823	-2.75	-2.04	-1.19	-1.47
51	Col15a1	ENSMUSG00000028339	-2.70	-2.75	-2.26	-1.34
52	Tpm1	ENSMUSG00000032366	-2.69	-2.03	-1.35	-1.50
53	Ltbp1	ENSMUSG00000001870	-2.65	-2.09	-1.45	-1.27
54	Col5a1	ENSMUSG00000026837	-2.59	-2.00	-1.59	-1.27
55	Eno3	ENSMUSG00000060600	-2.58	-1.66	-1.34	-1.68
56	Cavin3	ENSMUSG00000037060	-2.53	-1.95	-1.29	-1.37
57	Fndc1	ENSMUSG00000071984	-2.50	-1.78	-1.39	-1.25
58	Ephb3	ENSMUSG00000005958	-2.45	-1.75	-1.51	-1.39
59	Csrp1	ENSMUSG00000026421	-2.44	-1.78	-1.26	-1.44
60	Fscn1	ENSMUSG00000029581	-2.44	-1.84	-1.23	-1.34
61	Vwa1	ENSMUSG00000042116	-2.42	-2.31	-1.59	-1.49
62	Tpm2	ENSMUSG00000028464	-2.42	-1.88	-1.45	-1.62
63	Zfp469	ENSMUSG00000043903	-2.38	-2.26	-2.04	-1.22
64	Bmper	ENSMUSG00000031963	-2.37	-1.81	-1.37	-1.24
65	Ccn2	ENSMUSG00000019997	-2.37	-2.16	-1.46	-1.57
66	P4ha3	ENSMUSG00000051048	-2.36	-2.07	-1.66	-1.28
67	Akap12	ENSMUSG00000038587	-2.32	-1.98	-1.49	-1.39
68	Jph2	ENSMUSG00000017817	-2.29	-1.80	-1.30	-1.59
69	Phldb2	ENSMUSG00000033149	-2.27	-1.87	-1.33	-1.36
70	Vgll3	ENSMUSG00000091243	-2.26	-1.90	-1.17	-1.35
71	Tagln	ENSMUSG00000032085	-2.17	-1.73	-1.30	-1.55
72	Htra1	ENSMUSG00000006205	-2.16	-1.48	-1.16	-1.17
73	Thbs2	ENSMUSG00000023885	-2.15	-2.24	-2.30	1.14
74	Dysf	ENSMUSG00000033788	-2.15	-1.57	-1.20	-1.18
75	Lsp1	ENSMUSG00000018819	-2.11	-1.68	-1.53	-1.23
76	Glis2	ENSMUSG00000014303	-2.10	-1.70	-1.24	-1.37
77	Amotl2	ENSMUSG00000032531	-2.09	-1.79	-1.31	-1.26
78	Olfml3	ENSMUSG00000027848	-2.09	-1.64	-1.61	-1.29
79	Nfix	ENSMUSG00000001911	-2.08	-1.66	-1.28	-1.27
80	Flot1	ENSMUSG00000059714	-2.07	-1.62	-1.21	-1.37
81	Tnk2	ENSMUSG00000022791	-2.07	-1.63	-1.31	-1.41
82	Mical1	ENSMUSG00000019823	-2.03	-1.69	-1.33	-1.25
83	Fbln2	ENSMUSG00000064080	-2.00	-1.63	-1.38	-1.24
84	Tnrc18	ENSMUSG00000039477	-1.99	-1.54	-1.31	-1.28
85	Ppp1r12b	ENSMUSG00000073557	-1.99	-1.47	-1.29	-1.25
86	Mical2	ENSMUSG00000038244	-1.98	-1.62	-1.40	-1.15
87	Cnn2	ENSMUSG00000004665	-1.97	-1.64	-1.31	-1.46
88	Tead3	ENSMUSG00000002249	-1.97	-1.61	-1.33	-1.43
89	Myh9	ENSMUSG00000022443	-1.96	-1.69	-1.47	-1.39
90	Cryab	ENSMUSG00000032060	-1.96	-1.29	1.23	-1.47
91	Cspg4	ENSMUSG00000032911	-1.95	-1.62	-1.31	-1.37
92	Hspa1b	ENSMUSG00000090877	-1.93	-1.48	-1.36	-1.25
93	Pck2	ENSMUSG00000040618	-1.91	-1.46	-1.41	-1.32
94	Itga5	ENSMUSG00000000555	-1.91	-1.91	-1.38	-1.22
95	Kank2	ENSMUSG00000032194	-1.90	-1.51	-1.15	-1.27
96	Msrb3	ENSMUSG00000051236	-1.89	-1.51	-1.18	-1.22
97	Ctxn1	ENSMUSG00000048644	-1.89	-1.89	-1.46	-1.30
98	Tspan18	ENSMUSG00000027217	-1.87	-1.86	-1.63	-1.20
99	Zfp651	ENSMUSG00000013419	-1.87	-1.48	-1.25	-1.25
100	Pdlim2	ENSMUSG00000022090	-1.86	-1.38	-1.47	-1.50
101	Ccn4	ENSMUSG00000005124	-1.85	-1.50	-1.69	1.57
102	Palld	ENSMUSG00000058056	-1.83	-1.59	-1.15	-1.14
103	Flnc	ENSMUSG00000068699	-1.82	-1.50	-1.17	-1.22
104	Stbd1	ENSMUSG00000047963	-1.81	-1.46	-1.24	-1.33
105	Wls	ENSMUSG00000028173	-1.81	-1.44	-1.22	-1.13
106	Pbxip1	ENSMUSG00000042613	-1.79	-1.49	-1.38	-1.17
107	Fzd2	ENSMUSG00000050288	-1.76	-1.56	-1.32	-1.25
108	Ddah2	ENSMUSG00000007039	-1.75	-1.53	-1.43	-1.33
109	Ahdc1	ENSMUSG00000037692	-1.74	-1.53	-1.44	-1.31
110	Hspg2	ENSMUSG00000028763	-1.73	-1.47	-1.24	-1.19
111	Col4a2	ENSMUSG00000031503	-1.72	-1.50	-1.42	-1.15
112	Arhgef25	ENSMUSG00000019467	-1.72	-1.44	-1.36	-1.28
113	Flna	ENSMUSG00000031328	-1.70	-1.48	-1.24	-1.26
114	Lhfp	ENSMUSG00000048332	-1.69	-1.40	-1.38	-1.19
115	Gsn	ENSMUSG00000026879	-1.66	-1.31	-1.24	-1.21
116	Kctd15	ENSMUSG00000030499	-1.66	-1.62	-1.55	-1.44
117	Actn1	ENSMUSG00000015143	-1.65	-1.40	-1.10	-1.16
118	Pcdh19	ENSMUSG00000051323	-1.65	-1.24	1.26	-1.23
119	Col1a2	ENSMUSG00000029661	-1.64	-1.43	-1.34	-1.25
120	Plekhg2	ENSMUSG00000037552	-1.64	-1.58	-1.27	-1.27
121	Myo1c	ENSMUSG00000017774	-1.63	-1.35	-1.11	-1.31
122	Snta1	ENSMUSG00000027488	-1.62	-1.45	-1.40	-1.42
123	Pea15a	ENSMUSG00000013698	-1.59	-1.27	-1.14	-1.12
124	Masp1	ENSMUSG00000022887	-1.58	1.46	1.78	-1.36
125	Actn4	ENSMUSG00000054808	-1.58	-1.38	-1.10	-1.19
126	Serpine1	ENSMUSG00000037411	-1.58	-1.60	-1.25	-1.19
127	Cercam	ENSMUSG00000039787	-1.57	-1.48	-1.29	-1.23
128	Galnt10	ENSMUSG00000020520	-1.57	-1.46	-1.25	-1.24
129	Lrrc32	ENSMUSG00000090958	-1.55	-1.39	-1.22	-1.14
130	Nbl1	ENSMUSG00000041120	-1.54	-1.46	-1.36	-1.32
131	Col16a1	ENSMUSG00000040690	-1.52	-1.49	-1.36	-1.35

Figure 2.13. List of 238 significantly up/downregulated genes expressed by lung fibroblasts after rIL-33/rIL-13/rIL-17A treatment.

Statistically significant (p<.0001), differential expression (fold change +/- 1.5) was noted initially for 1,642 genes when comparing rIL-33/13/17A-stimulated fibroblasts to untreated cells (refer to **Figure 2.12A**). We extended our comparative analysis by identifying statistically significant, differentially expressed genes in rIL-33/13/17A-stimulated fibroblasts relative to every group that received cytokine treatment during the assay (*i.e.,* vs. rIL-33/rIL-13, rIL-33/rIL-17A- and rIL-33-stimulated fibroblasts). From the original list of 1,642 genes (rIL-33/rIL-13/rIL-17A-stimulated fibroblasts vs. untreated), only 268 genes were statistically significant upon comparing rIL-33/rIL-13/rIL-17A cells to each remaining treatment group (false discovery rate <.01; 131 **downregulated** and 137 **upregulated**). Ultimately, we ranked gene expression in this filtered ANOVA table using the **fold-change value** derived from comparing rIL-33/rIL-13/rIL-17A-stimulated fibroblasts to untreated cells.

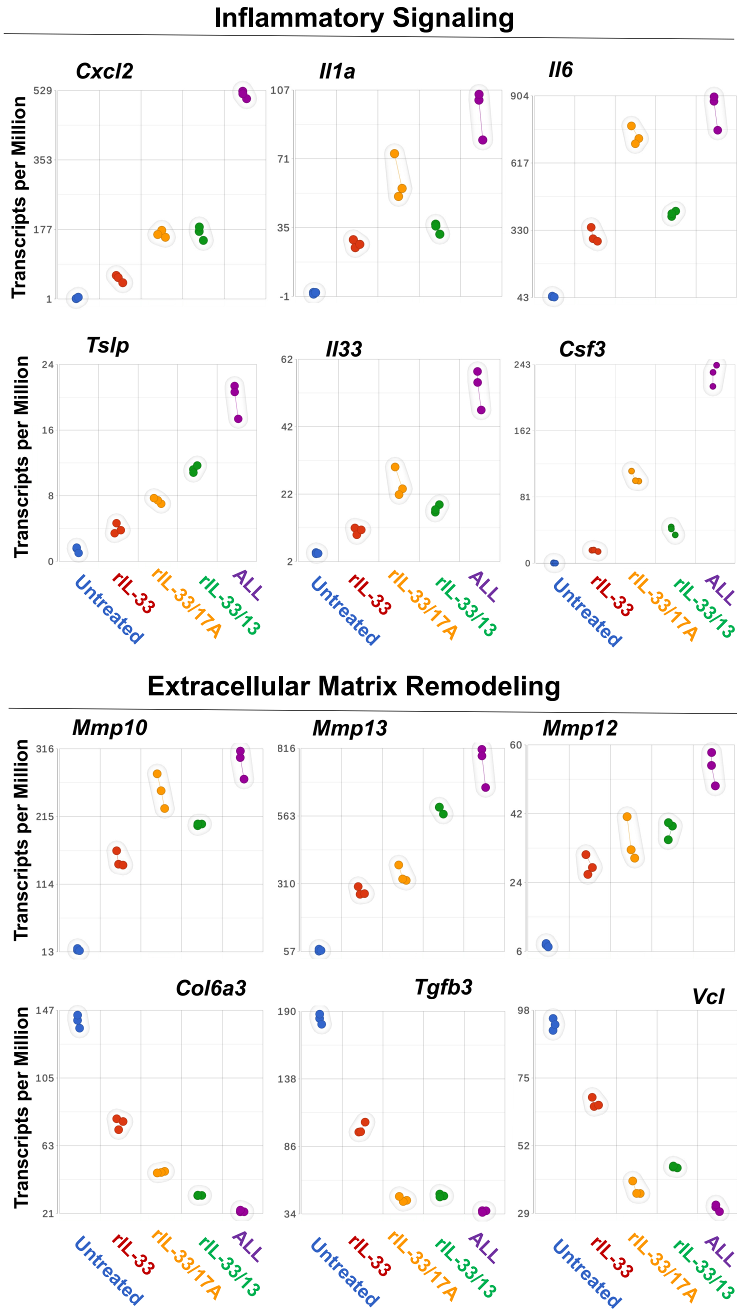

Figure 2.14. Direct comparison of primary lung fibroblasts at baseline or post-cytokine stimulation by absolute transcript abundance.

Genes among the top 238 (refer to **Figure 2.13**) were subsampled for visual representation of the dataset on a per-gene basis. Illustrated by 2D scatter plot, each treatment group is portrayed on the X-axis; the Y axis represents transcript abundance (TPM-normalized) for following: *Cxcl2, Il1a, Il6, Tslp, Il33, Csf3, Mmp10, Mmp13, Mmp12, Col6a3, Tgfb3, Vcl*. These genes are directly cited from **Figure 2.13**, which should be used as needed for referencing fold-change values for relevant comparisons.

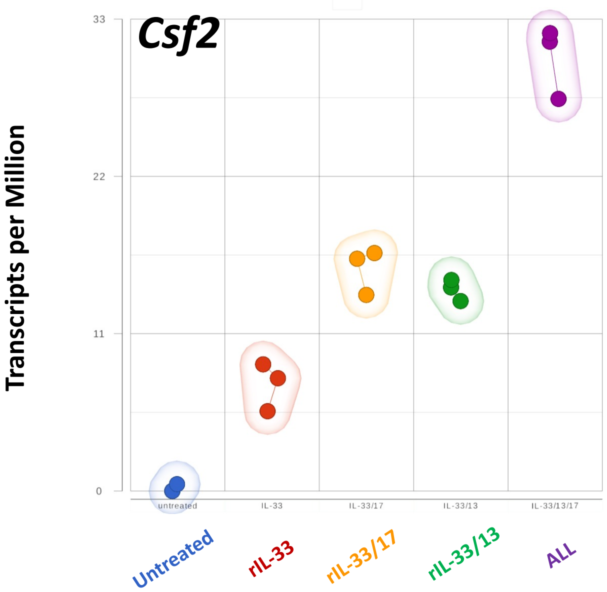

Figure 2.15. GM-CSF transcriptional regulation in primary lung fibroblasts determined by RNA-seq.

Illustrated by 2D scatter plot, each treatment group is portrayed on the X-axis; the Y axis represents transcript abundance (TPM-normalized).

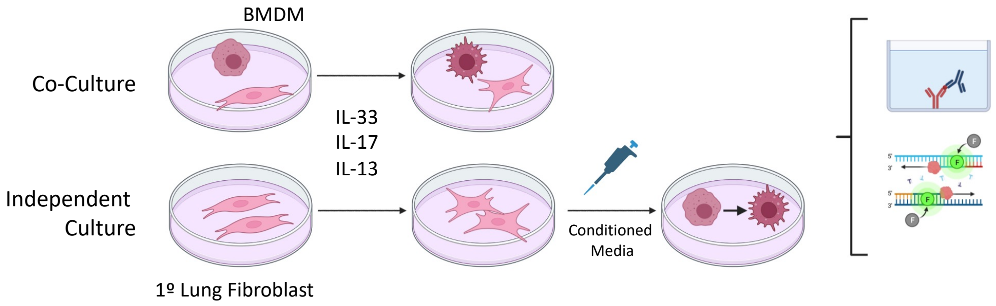

Figure 2.16. Schematic for *in vitro* cytokine stimulation assays that include both primary lung fibroblasts and macrophages.

Fibroblasts were isolated from digested whole lung, whereas macrophages (BMDM) were derived *in vitro* from monocytes in the bone marrow. For co-culture experiments, these two cell types were in direct contact and treated simultaneously with cytokines. Independent cultures of fibroblasts were also subjected to cytokine treatment, but for the purpose of harvesting fibroblast-conditioned media (FCM) that can be transferred to independent BMDM cultures. Activation phenotypes for BMDM were assessed mainly by ELISA and RT-qPCR.

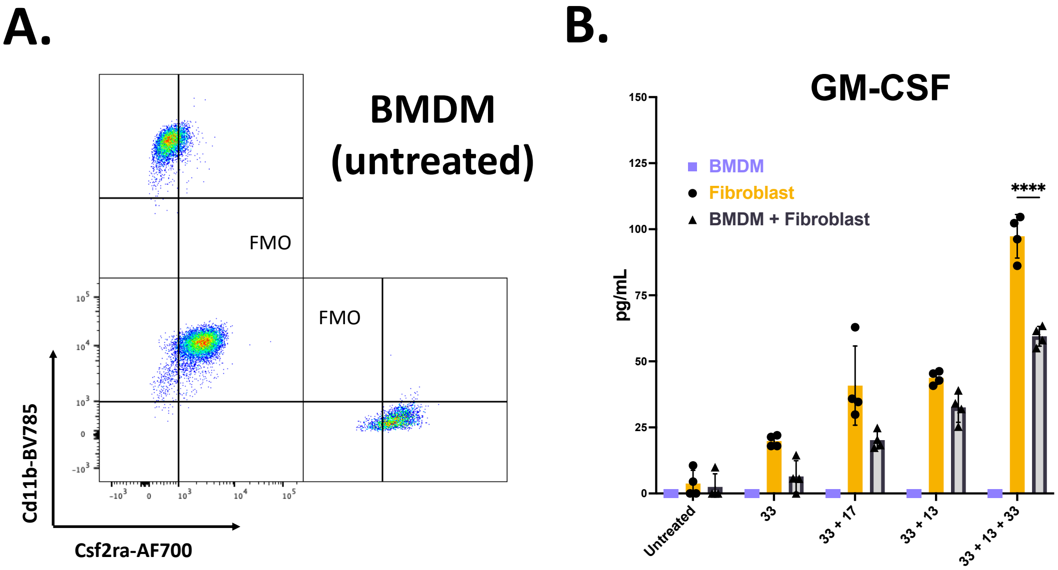

Figure 2.17. CD11b$^+$Csf2Rα^+ BMDM assayed in co-culture with primary lung fibroblasts.

For independent culture, macrophages were extracted and plated, as described, in technical triplicate. (**A**) Surface protein expression of CD11b and Csf2ra measured by flow cytometry. Positive signal for each protein was gated by comparing sample directly to a FMO control. Acquisition was performed on an LSR-II (Becton Dickinson, Franklin Lakes NJ). (**B**) For co-culture experiments, macrophages and fibroblasts were extracted and plated, as described, in technical quadruplicate. Total GM-CSF from fibroblast-macrophage co-culture assays was measured by ELISA and compared to independent cultures on the same plate. Representative image from an experiment repeated twice. Co- and independent cultures were always seeded with equal numbers of fibroblasts prior to conducting experiments. ****<.0001. Statistical testing performed with ordinary, two-way ANOVA with multiple comparisons (+ Tukey's post-hoc test).

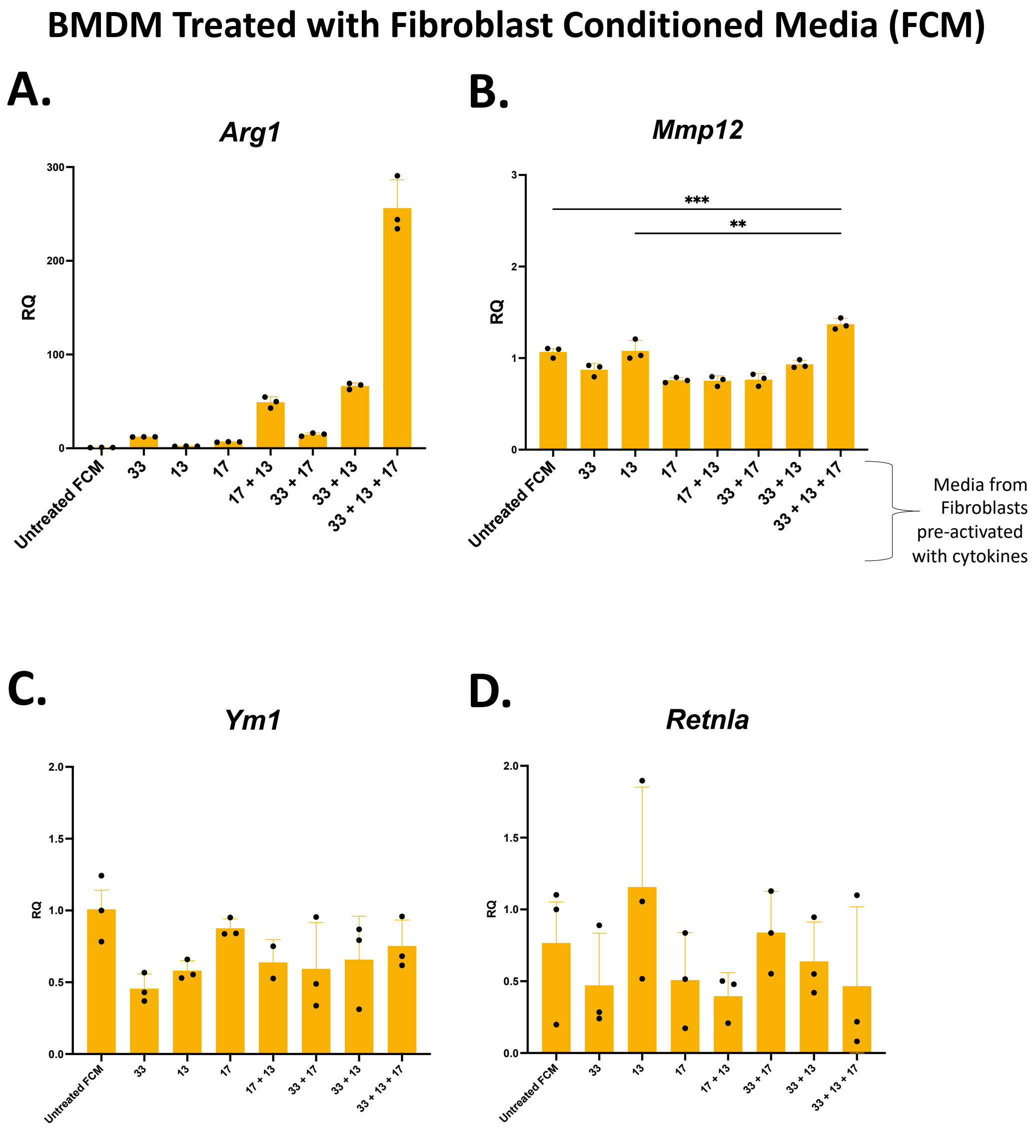

Figure 2.18. 'M2-like' BMDM activation with fibroblast-conditioned media.

FCM was harvested from fibroblast-only cultures that were pre-treated with cytokines. (**A-B**) Increased *Arg1* and statistically significant changes in *Mmp12* expression, specifically in BMDM activated with media conditioned by triple-treated fibroblasts. Data representative of results from an assay that was repeated in a modified, but comparable, manner. (**C, D**) *Ym1* and *Retnla* gene expression plots for the same cells from (**A, B**). There was no desire to replicate the assay for these two genes – minimal signal was detected upon initial readout by RT-qPCR, despite reasonable exponentiation of housekeeping genes assayed on the same PCR plate. Significance determined by ordinary, one- (D) or two-way (C) ANOVA with multiple comparisons (+ Tukey's post-hoc test). ***=.0008; **≤.005

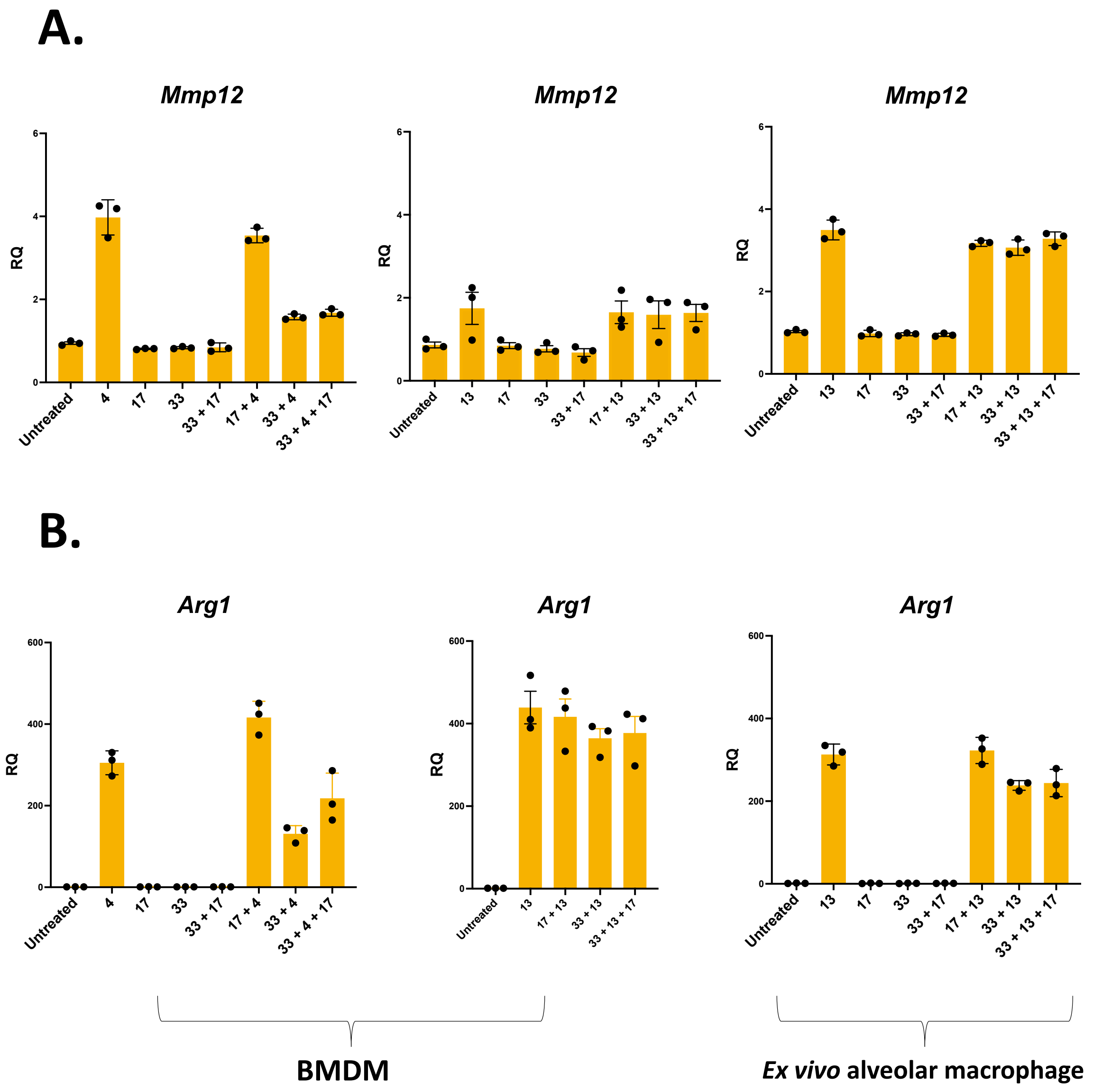

Figure 2.19. Anticipatory *in vitro* phenotypes define canonical and non-canonical 'M2' phenotypes across macrophage subtypes.

Canonical M2 activation is defined by macrophage polarization with rIL-4 *in vitro*, in contrast to non-canonical activation with rIL-13. (**A-B**) Plots comparing trends in *Mmp12* and *Arg1* expression in experimental iterations of canonical and non-canonical M2 activation of two, well-characterized macrophage subsets.

Chapter 3. EIEE pathogenesis in immunocompromised BALB/c mice.

Overview

IL-33, IL-13, and IL-17A have been implicated in the regulation of emphysema pathogenesis. In **Chapter 2**, we studied their combinatorial effects by stimulating primary lung fibroblasts and alveolar macrophages with each cytokine *in vitro*. To study these cytokines *in vivo* and in the context of EIEE, we elastase-challenged genetically manipulated animals that cannot respond to IL-33, IL-13, and/or IL-17A. Preliminary results indicated that BALB/c animals with germline deletions in *St2, Il13, Stat6,* or *Il17a* developed less severe emphysema post-elastase. Upon modifying the experimental design and including additional controls, however, gene deficient animals no longer showed measurable signs of disease attenuation. Additionally, *Rag1*$^{-/-}$ and *Rag2γ*$_{C}^{-/-}$ mice were challenged with elastase and assessed for disease attenuation elastase to study the contributions of the innate and adaptive immune responses in the EIEE model. *Rag1*$^{-/-}$ animals still demonstrated signs of progressive lung destruction post-elastase, while *Rag2γ*$_{C}^{-/-}$ males and females both had significantly attenuated responses to EIEE challenge. These results suggest that progressive disease in our model is independent of T cells and B cells and that common gamma chain family cytokines and/or innate immune mechanisms contribute significantly to disease development. Our results *in vivo* agree with the results in Chapter 2 that IL-33, IL-13, and IL-17A do not function independently for driving progressive lung destruction in EIEE.

Introduction

In this Chapter, the availability of genetically manipulated mice was exploited for addressing two outstanding questions pertaining to IL-33, IL-13, and IL-17A and their roles in the EIEE model. Previously, *in vitro* approaches (**Chapter 2**) determined that alveolar macrophages were responsive only to treatments containing recombinant IL-13. In contrast, lung fibroblasts were sensitive to recombinant IL-33, while also eliciting major inflammatory and tissue-remodeling responses upon triple-treatment with IL-33, IL-13, and IL-17A. These findings were intriguing but limited to an *in vitro* culture system. Ultimately, the possibility remained that IL-33, IL-13, and IL-17A behave differently in our model *in vivo*. Thus, in this work, we challenged global *St2, Il13, Stat6, and Il17a* knockout animals with elastase and assessed lung function over time. Ultimately, results from several littermate-controlled studies indicated that perturbation of genes related to IL-33, IL-13, and IL-17A signaling had limited effect on the progression of emphysema in BALB/c mice, and we began to question the utility of single-gene knockout models for studying inflammatory processes that drive EIEE.

The second important issue addressed here pertains to understanding the relative contributions of innate and adaptive mechanisms in the pathogenesis of COPD – perhaps, a controversial topic in the field. Some groups have posited that emphysematous pathology is orchestrated by adaptive immune cells, like CD4 and CD8 T cells (Meghraoui-Kheddar et al., 2017; Podolin et al., 2013; Tang et al., 2019). On the other hand, our group and others have reported that innate immune cells are the main drivers of elastase-induced damage and human emphysema (Chen et al., 2011; Doyle et al., 2019; Hautamaki et al., 1997; Limjunyawong et al., 2015a; Shibata et al., 2018). The literature is devoid of studies that address this issue by a global knockout approach; thus we challenged *Rag1*$^{-/-}$ and *Rag2*$^{-/-}$$\gamma_C^{-/-}$ mice and compared their response in the EIEE model. By the end, our findings support that innate immunity is sufficient to drive progressive lung damage and that γ_C signaling is likely necessary for cell-mediated damage in the EIEE model.

Methods

Mice.

All work was conducted in accordance with the standards established by the United States Animal Welfare Acts, set forth in NIH guidelines and the Policy and Procedures Manual of the Johns Hopkins University Animal Care and Use Committee. Animals were maintained in filter-topped cages at approximately 72°C, 50-60% humidity with 14:10-hour light/dark cycle and *ad libitum* access to food and water. Wild-type (WT) BALB/cJ were originally purchased from Jackson Laboratories (#000651). Knockout (KO) animals were derived from a variety of sources and were maintained and genotyped in-house (refer to **Table 3.1**, below**).** As noted, most experiments discussed herein were performed using littermate breeding of mice on the ‘BALB/c’ background. For this strategy, WT BALB/cJ mice were first bred with BALB/c KO ‘founder’ lines. Heterozygous offspring were then paired, producing littermates, which were genotyped and used directly for comparing KO to WT in the EIEE model. Other experiments applied conventional breeding standards, as noted, in which WT and KO BALB/c animals were not rederived, but maintained separately in homozygous breeding pairs.

Genotyping.

Tails snips were digested with Extract-N-Amp Tissue PCR Kit (Sigma, XNAT). Polymerase chain reaction was performed using made-to-order, genotype-specific oligonucleotides (IDT, Coralville IA); DNA sequences were amplified using Extract-N-Amp RedTaq (Sigma, R4775) using publicly available protocols, listed below in **Table 3.1**

Table 3.1: Knockout Mice for *in vivo* Experiments.

Genotype and Protocol Availability	Oligonucleotides (5’ to 3’)
C;129S4-Rag2$^{-/-}\gamma_c^{-/-}$ Strain #014593 (‘BALB/c’) Jackson Labs	*Rag2* • AGG TCC AAG CTG CTG CCA C • GTG TGG GAT ATA GCT GTT GG • GAG ATG TCC CTG AAC CCA GA • TTG AGT GAG GAT TGC ACT GG *Il2rg* • CCA GAG AAA GAA GAG CAA GCA • GAT CCA GAT TGC CAA GGT GA • AGC AGC AGT GAG GCA GAG A
C;129S7(B6)-Rag1$^{-/-}$ Strain #003145 (‘BALB/c’) ***B6.129S7-Rag1***$^{-/-}$ Strain #002216 (‘B6’) Jackson Labs	Applies to either: • TCT GGA CTT GCC TCC TCT GT • CAT TCC ATC GCA AGA CTC CT • TGG ATG TGG AAT GTG TGC GAG
C;129S2-Stat6$^{-/-}$ Strain #002828 (‘BALB/c’) Jackson Labs	• AATCCATCTTGTTCAATGGCCGATC • ACTCCGGAAAGCCTCATCTT • AAGTGGGTCCCCTTCACTCT
St2$^{-/-}$ (‘BALB/c’) Andrew N.J. Mckenzie, Ph.D. Cambridge, England	• TTGGCTTCTTTTAATAGGCCC • CTATCAGGACATAGCGTTGGCTACC • TGTTGAAGCCAAGAGCTTACC
Il13$^{-/-}$ ((‘BALB/c’) Andrew N.J. Mckenzie, Ph.D. Cambridge, England	• GTTGCTCAGCTCCTCAATAAGC • GGGTGACTGCAGTCCTGGCT • GGCGGATGAGCGGCATTTTCCGTG • GCCGAAAGGCGCGGTGCCGCGGC
Il17a$^{-/-}$ (‘BALB/c’) Nakae *et al. Immunity.* (2002) Genotyping protocol available in methods.	• ACTCTTCATCCACCTCACACGA • GCCATGATATA GACGTTGTGGC • CAGCATCAGAGACTAGAAGGGA

Elastase-Induced Experimental Emphysema (EIEE).

BALB/c mice (7-12 weeks old) were anesthetized by intraperitoneal (IP) injection with a mixture (1:1) of ketamine (100 mg/kg) and xylazine (10 mg/kg) in sterile water. Mice were then intubated with an 18G canula. EIEE was induced with one dose (50 µl) of 3U (male) or 1.5U (female) porcine pancreatic elastase suspended in PBS (PPE; Elastin Products Co., LE4205), instilled intratracheally (IT). Rarely, other doses were used, but noted in figure legends. Experimental endpoints were measured at Day 21 post-elastase, as mice were then sacrificed for pulmonary function testing and other readouts.

Pulmonary Function Testing.

Mice were anesthetized by IP injection with a mixture (1:1) of ketamine (100 mg/kg) and Xylazine (10 mg/kg) in sterile water and then a tracheostomy was performed with an 18G canula. The Diffusion Capacity for carbon monoxide was measured first by inflating the lungs with tracer amounts of CO and Neon, holding volume for 9 sec, and then measuring the gas concentrations on a gas chromatograph (Fallica et al., 2011). Animals were then directly connected to a FlexiVent (Scireq; Toronto, CA) for measuring dynamic respiratory mechanics as well as quasistatic total pressure volume curves, which was used to quantify total lung capacity or compliance (Limjunyawong et al., 2015b). Mice were paralyzed with succinyl choline (200 mg/mL), administered by intramuscular injection (50 ul) prior to data acquisition.

Statistical Analysis and Illustrations.

GraphPad Prism 9.4.1 (San Diego, CA) was used for statistical testing with multiple comparisons as well as for the generation of figures. When possible, the same statistical test and hyperparameters were applied for supporting comparisons between assays. Figure legends include specific details, but ordinary two-way ANOVA with Tukey’s post-hoc test was applied most often for making statistical comparisons.

Results

Preliminary lung function analysis comparing *St2$^{-/-}$*, *Stat6$^{-/-}$*, and *Il17a$^{-/-}$* 'BALB/c' mice to WT BALB/cJ in the standard EIEE time course.

First, we conducted preliminary EIEE studies by comparing male KO BALB/c strains to WT BALB/cJ mice from Jackson Labs. BALB/c KOs were obtained from outside sources, maintained in-house, and bred as homozygous pairs (refer to **Methods**). Adhering to the model's default time course, 3U was delivered intratracheally and mice were assessed for disease progression at Day 21. Statistically, we observed a notable difference in total lung capacity (TLC) when comparing elastase-treated *St2*$^{-/-}$ mice to WT animals challenged with the same dose. Total lung capacity, which is a measure of lung volume and maximum inflation, is known to significantly increase in mice with emphysema. Attenuation was suggested by this assay because no significant difference was observed when comparing elastase-treated *St2*$^{-/-}$ animals to PBS control mice by day 21 (**Figure 3.1A).** Readouts for the diffusion factor of carbon monoxide (DFCO) were less confirmatory, though, and statistically meaningful changes were not observed by this metric post-elastase (**Figure 3.1B**). When comparing *Stat6*$^{-/-}$ mice to WT, we again noted statistical and quantitative differences in TLC (**Figure 3.1C)**; while changes in DFCO were, again, difficult to interpret (**Figure 3.1D**). However, *Il17a*$^{-/-}$ mice experienced convincing statistical and quantitative changes in lung function after three independent trials measuring TLC (**Figure 3.1E)** and DFCO (**Figure 3.1F**) when compared to WT BALB/cJ. Altogether, these data were mechanistically enticing, and implied that IL-33, IL-13, and/or IL-17A could have independent control over severe disease phenotypes post-elastase.

Cautious of misinterpretation, however, we contemplated other factors that could be affecting our results in KO mice post-elastase. Multiple reports now detail instances where global knockout studies are misinterpreted due to unexpected differences in background genetics between knockouts and their wild-type comparators (FitzPatrick et al., 2020; Holmdahl and Malissen, 2012). As mentioned, Limjunyawong and colleagues (2015) defined our EIEE model at 3U PPE with male, BALB/cJ mice bred in-house at Hopkins, but first purchased from **J**ackson Laboratories. In parallel to our KO studies, we challenged the BALB/cJ 'equivalent' from Taconic Laboratories (BALB/cTac) and compared their response to BALB/cJ at standard PPE doses. As expected, WT BALB/cJ mice experienced appreciable changes in TLC and a decline in DFCO at 3U PPE (**Figure 3.2A-B**); but WT BALB/cTac were nonresponsive at this dose, showing no signs of disease progression at day 21. In at least one iteration of this work, we directly compared BALB/cJ purchased from Jackson to those bred for several weeks in the Hopkins vivarium (BALB/cJh), which were assumed to be identical beyond relatively minor changes in microbiota. Negligible variation in TLC and DFCO was observed between these two 'strains' at day 21. Overall, discrepancies in the response of BALB/cJ vs. BALB/cTac post-elastase were striking, as we began to question our preliminary interpretation of 'BALB/c' KOs responses to elastase: was attenuated emphysema in KO animals a reflection of cytokine biology, or merely the consequence of fundamental genetic differences that exist among ‘BALB/c’ from different vendors? Clearly, a modified global approach was necessary for determining the roles of IL-33/IL-13/IL-17A signaling pathways in EIEE.

Lung function analysis comparing *St2*$^{-/-}$, *Stat6*$^{-/-}$, and *Il13*$^{-/-}$ ‘BALB/c’ mice to WT littermates in the standard EIEE time course.

Several ‘BALB/c’ KOs studied preliminarily had not been derived using Jackson WT animals, which was concerning in the context of readouts that compared BALB/cJ to BALB/cTac at 3U PPE. The stark difference in the response of BALB/cJ versus BALB/cTac could be the result of subtle background variation (SNPs, indels, etc.) among related ‘BALB/c’ strains. In this context, we posited that ‘BALB/c’ KO experiments were prone to misinterpretation if not properly controlled.

To modify our approach, littermate breeding was considered (FitzPatrick et al., 2020; Holmdahl and Malissen, 2012). For our purposes, littermate or ‘het x het’ breeding describes a strategy for crossing KO ‘BALB/c’ founder lines from various sources with a BALB/c**J** WT mouse. WT or KO littermate offspring are then re-derived by paring heterozygous ‘F1’ offspring from the initial cross. These animals were genotyped before and after experimentation. This method is well-established as a means for controlling for differences in microbiota among related strains (Robertson et al., 2019); but we also perceived littermate breeding as a method for controlling for differences in background genetics between seemingly related, ‘BALB/c’ strains.

We applied littermate breeding for retesting *St2*$^{-/-}$ and *Stat6*$^{-/-}$ attenuation phenotypes observed in the EIEE model with our previous approach. We were also gifted *Il13*$^{-/-}$ mice for this approach (Stephane Lajoie/Andrew N.J. McKenzie), which were tested in the EIEE model to supplement our interpretation of *Stat6*$^{-/-}$ readouts. For each assay, TLC, primarily, was measured as a readout for severe disease in either sex.

In contrast to our preliminary work, WT and *St2*$^{-/-}$ littermate males had experienced significant increases in TLC by day 21 of the EIEE model (**Figure 3.3A**). Female *St2*$^{-/-}$ littermates may experience some degree of attenuation (**Figure 3.3B**). Similar results were achieved by day 21 upon challenging WT and *Il13*$^{-/-}$ male an female littermates in the EIEE model (**Figure 3.4**). Even though disease burden appeared to be quite severe in *Il13*$^{-/-}$ animals, we proceeded with follow-up experiments that assessed emphysema development in *Stat6*$^{-/-}$ 'BALB/c' littermates. Unexpectedly, and for reasons to be discussed later, a higher dose of PPE was required to induce disease in these littermates. Comparisons were relatively straightforward to interpret for males, as WT and *Stat6*$^{-/-}$ littermates, as each experienced quantitative and statistically significant changes in TLC post-elastase (**Figure 3.5**). An attenuation phenotype may be apparent when comparing WT and *Stat6*$^{-/-}$ elastase-treated males directly to their respective baseline controls (**Figure 3.5A**). However, statistically significant differences in TLC were not computed when comparing male WT and *Stat6*$^{-/-}$ elastase-treated animals directly. Based on TLC, *Stat6*$^{-/-}$ elastase-treated females experienced significant disease burden by day 21 in the EIEE model (**Figure 3.5B**).

Altogether, littermate studies now suggest that mice with germline deletions in *St2* and *Stat6* develop severe emphysema post-elastase. *Il13*$^{-/-}$ mice, which were not previously tested, also developed significant disease that was comparable to WT littermates. Taken together, IL-33 may not independently control severe disease outcomes in the drastic manner implied by our preliminary efforts (refer back to **Figure 3.1**); and IL-4rα-mediated signaling also does not appear to dictate severe disease phenotypes by day 21, either.

Lung function analysis comparing *Il17a*$^{-/-}$ 'BALB/c' mice to WT littermates.

Intriguing observations were made when comparing *Il17a*$^{-/-}$ male and female 'BALB/c' mice to WT littermates, some worthy of extended analysis. Upon intratracheal delivery of the standard elastase dosage for BALB/cJ males (3U PPE), WT littermates no longer developed severe disease, limiting our ability to compare to *Il17a*$^{-/-}$ mice for interpreting an attenuation phenotype (**Figure 3.6A**). As a reminder, we experienced this issue previously when testing *Stat6*$^{-/-}$ animals at doses standard for the EIEE model. On the other hand, female *Il17a*$^{-/-}$ mice demonstrated well-validated, quantitative, and statistically significant attenuation in response to the standard challenge for BALB/cJ EIEE (1.5U PPE). Attenuation was noted first by TLC readouts, which suggested absence of severe disease in *Il17a*$^{-/-}$ females (**Figure 3.6B**). These observations held up when other pulmonary function metrics were assessed, including compliance (**Figure 3.6C**) and diffusion capacity of carbon monoxide (**Figure 3.6D**). By all measures, female WT littermates challenged with had developed significant disease relative to their baseline comparators, whereas *Il17a*$^{-/-}$ female mice showed signs of attenuation. Not only do these readouts for female mice support experimental findings in the literature and observations in the clinic (Aryal et al., 2013; Chen et al., 2011; Foreman et al., 2011;

Kurimoto et al., 2013), but we posit their differences are quantitatively and statistically more convincing than other results reported herein.

Innate immune mechanisms in progressive lung disease.

Experiments were also performed at the global knockout level for determining the relative contributions of innate and adaptive mechanisms in the progressive pathology observed in the EIEE model. Upon intratracheal delivery of the standard elastase dosage for BALB/cJ males or females (3U or 1.5U PPE), T cell- and B cell-deficient *Rag1*$^{-/-}$ males showed signs of disease at Day 21 by TLC readouts (**Figure 3.7A**). Across two experiments, *Rag1*$^{-/-}$ males experienced a 45% change in TLC from baseline. These differences in *Rag1*$^{-/-}$ males were less severe compared the response to 3U PPE in WT mice, which experienced a 74% change from baseline overall. Functional changes in both strains were quantitatively and statistically significant, suggesting that 3U PPE induced severe disease in males independent of a functional, adaptive immune response. *Rag1*$^{-/-}$ females demonstrated modest attenuation with standard EIEE challenge compared to WT animals from the same assay (**Figure 3.7B**). For enhancing our interpretation of data reflected on the 'BALB/c' background, we assayed C57Bl/6J *Rag1*$^{-/-}$ animals at standard doses, and both sexes developed pathology that was quantitatively and statistically comparable to their WT counterparts (**Figure 3.7C –** male**; Figure 3.7D –** female). As noted in work done by Limjunyawong and colleagues (2015), mice on this background require a boost in elastase dose (6 units) for initiating disease and are best utilized for studying the acute damage responses in the lung. Notwithstanding, based on a preponderance of the evidence collected across sex and strain, we concluded that adaptive immune cells are not major drivers of emphysema pathogenesis in our model.

To validate and extend findings in *Rag1*$^{-/-}$ animals, we elastase-challenged *Rag2*$^{-/-}$$\gamma_C^{-/-}$ mice, which are deficient in T cells, B cell, NK cells, and the ability to respond to several cytokines (IL-2, IL-4, IL-7, IL-9, IL-15, IL-21). *Rag2*$^{-/-}$$\gamma_C^{-/-}$ males experienced a modest, nonsignificant 14% change from baseline TLC post-elastase across three independent experiments (**Figure 3.8A**). This was nominal compared to the 60% change, on average, experienced by WT BALB/cJ counterparts. Attenuation was also appreciable in females (**Figure 3.8B**). Littermates again were not used for testing immunosuppressed mice, considering the logistical complexity and laborious nature of crossing double knockout animals in this manner. Taken together, we deemed results from *Rag1*$^{-/-}$ and *Rag2*$^{-/-}$$\gamma_C^{-/-}$ experiments as reasonable evidence to suggest that EIEE has an appreciable immune basis for pathogenesis. Indeed, extensive lung damage observed in this model is not simply the result of PPE degrading elastin directly; and despite the limitations of these KO experiments, the data still supports the idea that EIEE is orchestrated by cells of the *innate* immune system.

Discussion

In this work, we revisited our preliminary interpretation for global knockout phenotypes observed in 'BALB/c' *St2*$^{-/-}$, *Stat6*$^{-/-}$, and *Il17a*$^{-/-}$ mice challenged with elastase. We applied a modestly logistical technique that controls for background genetics and other confounds with littermate breeding. This work also allowed us to test females in our model, which was not done previously by our group. Upon confirmation of an attenuated response to elastase, our terminal goal for this work was to develop a strategy for targeting each signaling pathway therapeutically in EIEE, as proposed in the context of emphysema and related lung diseases (Barnes, 2018; Ogger and Byrne, 2021).

A utility for littermate breeding has been suggested by reports in the literature (FitzPatrick et al., 2020; Holmdahl and Malissen, 2012; Robertson et al., 2019); but it is not clear whether these publications have served as any major impetus for rethinking the way KO mice are tested in certain disease models. Our main concern for rethinking global KO experiments was to develop a method for controlling variation among seemingly related 'BALB/c' strains, which may begin to explain the striking 'attenuation' phenotype observed for BALB/cTac relative to BALB/cJ at 3U PPE. In an extension of the project, we performed whole genome sequencing of WT BALB/c from Charles River, Harlan and Taconic Laboratories, as well as the BALB/cByJ or BALB/cJ from Jackson. Previously, we had generated evidence that excludes a role for the microbiome in the development of severe disease post-elastase (James Limjunyawong & J. Matt Craig – **data not shown)**. Though outside the scope of this thesis, we posit these independent experiments and sequencing data will provide insight into the germline differences that may account for notable resistance to 3U of elastase in BALB/cTac relative to BALB/cJ in the EIEE model.

By the end of our littermate studies, we concluded that IL-33 and IL-13 do not independently control over severe disease outcomes in the lungs of mice post-elastase. For studying these cytokines *in vivo*, we used *St2*$^{-/-}$ and *Il13*$^{-/-}$ animals. These mice were donated from another lab in-house (Stephane Lajoie) with the permission of Andrew N.J. McKenzie (Cambridge, U.K.), who is one of the most generous and reputable pioneers in mucosal immunology and mouse genetics. The number of McKenzie-derivative or backcrossed strains worldwide is unknown, but lines other than *St2*$^{-/-}$ or *Il13*$^{-/-}$ exist. It is appreciated that *St2*$^{-/-}$ was developed first with C57Bl/6 mice and blastocysts (vendor not reported), which were ultimately crossed with a 129S mouse (Townsend et al., 2000). The same is true for early reports of *Il13*$^{-/-}$ mice (McKenzie et al., 1998a; McKenzie et al., 1998b). Since then, multiple groups have backcrossed *St2*$^{-/-}$ to BALB/c, including the wild-type from Charles River (Wieland et al., 2009) and, perhaps, Jackson Labs (Mangan et al., 2007), though methods from these early reports are not always clear. In several publications, *Il13*$^{-/-}$ mice were backcrossed to 'BALB/c' (Hofmann et al., 2014; Matthews et al., 2000), though similar flaws are noted in the reporting of each wild-type vendor or source. Nobody appears to be at-fault for these cryptic explanations of materials & methods, as underreporting was clearly an unperceived consequence of publication standards at the time. Nonetheless, I opine that these early reports are examples of how laboratories, including ours, has for years taken for granted the reproducibility of genetic background, and what it means to be 'BALB/c.'

Two strains for our study, *Stat6*$^{-/-}$ and *Il17a*$^{-/-}$, also came from reputable sources, but have not been employed for research use as often as *St2*$^{-/-}$ or *Il13*$^{-/-}$ mice. *Stat6*$^{-/-}$ mice were purchased directly from Jackson Labs, and the original line was derived using BALB/c blastocysts (Kaplan et al., 1996). Regardless, Jackson nomenclature (i.e., 'C.129S2', see **Methods**) suggests this strain has mixed origins. This strain is now cryopreserved but can still be purchased from Jackson; and, as per the website, the BALB/cJ is the 'approximate' comparator recommended by the manufacturer. However, I posit this advice from Jackson is not definitive, and rederiving strains in-house should still be considered. Recent work supports a role for IL-4 in the C57Bl/6 elastase model (Shibata et al., 2018). However, our *Stat6*$^{-/-}$ data do not strongly implicate IL-4 or IL-13 as master regulators of chronic-progressive disease in the BALB/cJ model of severe emphysema.

Upon littermate breeding of the *Il17a* KO strain, we no longer observed an attenuation effect at the standard 3U PPE dose in males. Though, a very robust attenuation phenotype was observed using our default 1.5U PPE in female *Il17a*$^{-/-}$ mice when compared to WT littermates. We were unsurprised that 1.5 PPE elicited an appreciable and interpretable readout for comparing WT and *Il17a*$^{-/-}$ female littermates, despite lack of response in male counterparts at 3U PPE – females are inherently more sensitive to elastase challenge, as we have demonstrated throughout (Aryal et al., 2013; Foreman et al., 2011). Plus, phenotypes observed for *Il17a*$^{-/-}$ BALB/c female littermates were consistent with readouts previously reported by other groups. For instance, attenuated disease was noted in *Il17ra*$^{-/-}$ B6 females exposed to cigarette-smoke (Chen et al., 2011), and B6 *Il17a*$^{-/-}$ females challenged with elastase also develop less severe emphysema (Kurimoto et al., 2013). Since males did not respond to their standard 3U dose, our interpretation may benefit from retesting this sex at a higher dose. Currently, we do not consider *Il17a* expression to be an independent factor in the development of severe emphysema in males.

The greatest limitation of this work, perhaps, is a direct consequence of what this strategy aims to balance, biologically and logistically. Some littermate assays, for example, contained few biological replicates. Such was a direct consequence of Mendelian genetics and the overall difficulty of obtaining large numbers of WT and KO offspring when using heterozygous breeding strategies, especially with multiple lines at once. Further, we only rederive, or backcross, each KO with a BALB/cJ mouse once, generating "F1" heterozygous offspring, which were used downstream for breeding littermate offspring. Obviously, rederiving mice in this way does not hold the experimental power of backcrossing each KO line 5+ times with BALB/cJ animals; but logistical barriers strongly discouraged us from applying this methodology. Plus, weighing the risk vs. reward for this project became increasingly difficult, since most assays did not result in attenuated emphysema.

Lastly, for the *Stat6* strain, we again noted that WT littermates no longer responded to the standard 3U PPE (**data not shown**). To overcome any 'inherited resistance' to standard PPE challenge, we adjusted the dose to 4U and 2U for challenging males and female littermates, respectively. Similar approaches were taken by Limjunyawong and colleagues (2015) upon realizing that C57Bl/6J mice required significantly more PPE for eliciting severe lung damage (6U) relative to BALB/cJ mice (3U).

Clearly, issues related to dose and strain were not definitively resolved by our approach, but we deem that progress was made through littermate breeding. As implied by **Chapter 2**, stimulation with all three cytokines (IL-33, IL-13, and IL-17A) was necessary for robust activation of primary lung fibroblasts and driving expression of inflammatory genes *in vitro*. Indirectly, our work *in vivo* is consistent with such a readout – IL-33, IL-13, and IL-17A do not have ***independent*** control over severe emphysema phenotypes post-elastase.

In the same light, we hypothesize that this whole global knockout strategy should be reapproached by crossing multiple knockout strains for studying effects of IL-33, IL-13, or IL-17A simultaneously *in vivo*. This task is laborious and logistically challenging, but assaying double and/or triple knockout mice in our model may be more insightful for understanding how IL-33, IL-13, or IL-17A regulate inflammatory processes in EIEE.

Afterword

In the next chapter, we apply single-cell RNA-sequencing for analyzing thousands of immune cells in the lung at different stages of EIEE. We and others posit that EIEE is the consequence of immune cell dysregulation post-challenge, which we supported by challenging $Rag1^{-/-}$ and $Rag2^{-/-}\gamma_C^{-/-}$ animals with elastase. True for both sexes, BALB/c $Rag2^{-/-}\gamma_C^{-/-}$ mice do not develop progressive emphysema post-elastase. BALB/c $Rag1^{-/-}$ females also showed signs of attenuation, but males still appeared to develop severe disease. Regretfully, $Rag1^{-/-}$ and $Rag2^{-/-}\gamma_C^{-/-}$ mice were never tested under littermate-controlled settings. We did not rederive $Rag1^{-/-}$ animals because disease burden was clearly evident in both BALB/c and B6 males treated with standard elastase doses. The $Rag2^{-/-}\gamma_C^{-/-}$ experiments were not littermate-controlled because of the significant logistical obstacle of rederiving a double-knockout strain. Regardless, this attenuation phenotype held significant weight for several reasons. First, in this mouse, two major genes are perturbed. The *Rag2* deletion directly renders B and T cells nonfunctional; and the γ_c deletion bears major implications at the level of innate immunity. Natural killer cells do not mature, and several other myeloid or innate populations are dysfunctional due to inability to respond to IL-2, -4, -7, -9, -15, and -21. In other words, the effects of these deletions go well-beyond the quantity of genes perturbed. We argue that $Rag2^{-/-}\gamma_C^{-/-}$ attenuation phenotypes relative to $Rag1^{-/-}$ and WT readouts were a strong indicator that the innate immune system, collectively, may drive chronic disease phenotypes in the BALB/c EIEE model.

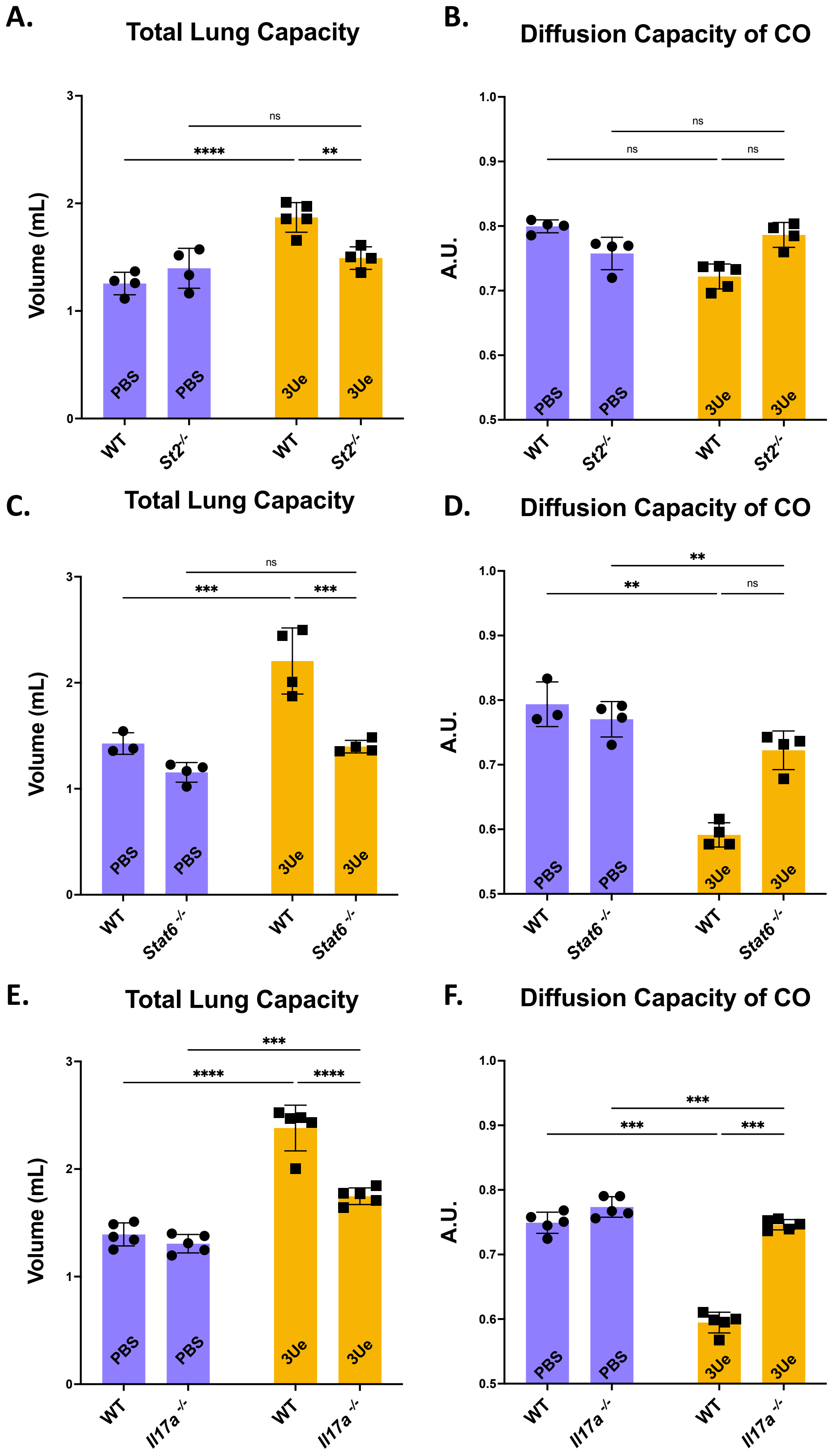
A.
Total Lung Capacity
Volume (mL)
0
1
2
3
ns
****
**
PBS
PBS
3Ue
3Ue
WT
St2-/-
WT
St2-/-
B.
Diffusion Capacity of CO
A.U.
0.5
0.6
0.7
0.8
0.9
1.0
ns
ns
ns
PBS
PBS
3Ue
3Ue
WT
St2-/-
WT
St2-/-
C.
Total Lung Capacity
Volume (mL)
0
1
2
3
ns
***
***
PBS
PBS
3Ue
3Ue
WT
Stat6 -/-
WT
Stat6 -/-
D.
Diffusion Capacity of CO
A.U.
0.5
0.6
0.7
0.8
0.9
1.0
**
**
ns
PBS
PBS
3Ue
3Ue
WT
Stat6 -/-
WT
Stat6 -/-
E.
Total Lung Capacity
Volume (mL)
0
1
2
3
***
****
****
PBS
PBS
3Ue
3Ue
WT
Il17a -/-
WT
Il17a -/-
F.
Diffusion Capacity of CO
A.U.
0.5
0.6
0.7
0.8
0.9
1.0
***
***
***
PBS
PBS
3Ue
3Ue
WT
Il17a -/-
WT
Il17a -/-

Figure 3.1. Preliminary lung function analysis of *St2*$^{-/-}$, *Stat6*$^{-/-}$, and *Il17a*$^{-/-}$ animals twenty-one days post-elastase relative to BALB/cJ animals and PBS controls.

Male WT or knockout (KO) BALB/c mice (N≥3 baseline, N≥4 per experimental group) were challenged with 3U PPE for lung function analysis at Day 21. (**A, C, D**) Animals were directly connected to a FlexiVent for assessing total lung capacity. (**B, D, E**) Diffusion capacity of carbon monoxide (CO) was collected prior to FlexiVent analysis using a gas chromatograph. A.U. = Arbitrary Units. Error bars represent standard deviation from the mean. Statistics were computed by two-way ANOVA with multiple comparisons (+ Tukey's post-hoc test).**** p<0001; ns = not significant; (**A**) **p=.0054; (**C**) ***p≤.006; (**D**) ** p<.005; (**E ,F**) ***p<.005. (**A, B**) represent mice from the same experiment, which was never repeated. Prior to this trial, comparable observations were made when WT and *St2*$^{-/-}$ mice were challenged with 3U PPE by intranasal aspiration and tested for changes in lung function twenty-one or forty-two days later. (**C, D**) represent the same experiment, which was repeated. (**E, F**) illustrate data from the same experiment, performed at least three times. (**A, B**) were designed and carried out by James Limjunyawong and J. Matt Craig in 2013. (**C, D**) was performed by Jeffrey Loube and me in 2021; though, the original experiment was designed and carried out by James in 2014. (**E, F**) represent one of two trials performed by James between 2013 and 2014.

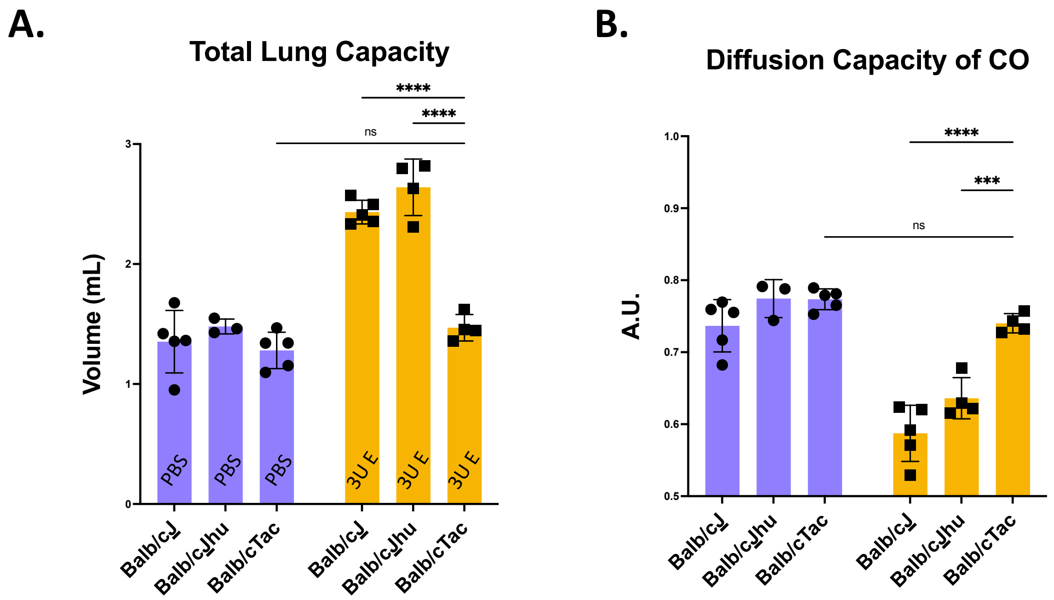

Figure 3.2. Pulmonary function tests comparing disease severity post-elastase in BALB/cJ (Jackson Labs) vs. BALB/cTac (Taconic Labs).

Male ‘BALB/c’ mice (N≥3 baseline, N≥4 per experimental group) were challenged with 3U PPE for lung function analysis at Day 21. (**A**) Animals were directly connected to a FlexiVent for assessing total lung capacity. (**B**) Diffusion capacity of carbon monoxide (CO) was measured prior to FlexiVent ventilation using a 9-second breath-hold of sample gas with analysis on a gas chromatograph. A.U. = Arbitrary Units. Error bars represent standard deviation from the mean. Statistics were computed by two-way ANOVA with multiple comparisons (+ Tukey’s post-hoc test). **** p<0001; *** p=.007; ns = not significant. This specific assay was not repeated. Rather, BALB/cJ were compared directly to BALB/cTac in a modified repetition of this challenge (N=6 per elastase group), producing similar outcomes. Both iterations of this work were designed by James Limjunyawong and J. Matt Craig, and experiments were conducted by Jeffrey Loube and me.

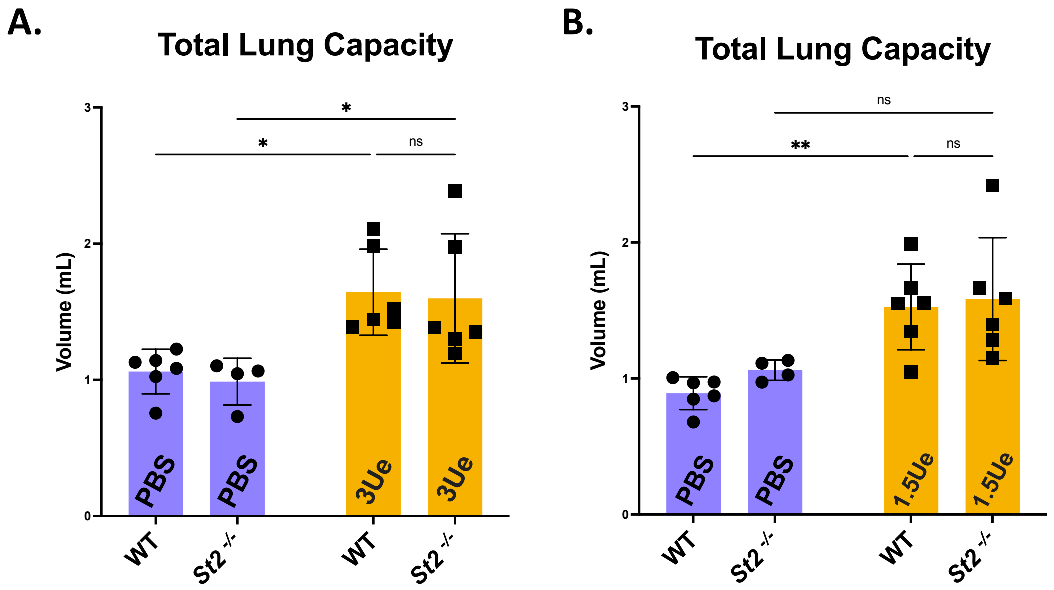

Figure 3.3. Total lung capacity analysis comparing male and female *St2$^{-/-}$* mice to WT littermates twenty-one days post-elastase.

WT or *St2$^{-/-}$* BALB/c littermates were challenged with sex-specific PPE doses for lung function analysis at Day 21. (**A**) Male animals were directly connected to a FlexiVent for assessing total lung capacity. (**B**) Females were also assayed independently and measured by this readout. Error bars represent standard deviation from the mean. Statistics were computed by two-way ANOVA with multiple comparisons (+ Tukey's post-hoc test). ** p=.0084; * p<.05; n.s. = not significant. Both plots are representative of pooled data from N=2 independent assays. (**A**) At least N=3 males per strain were challenged with elastase and assayed for each repetition. (**B**) The first experiment assayed N=4 females per group; additional mice were assayed later and pooled with the first dataset.

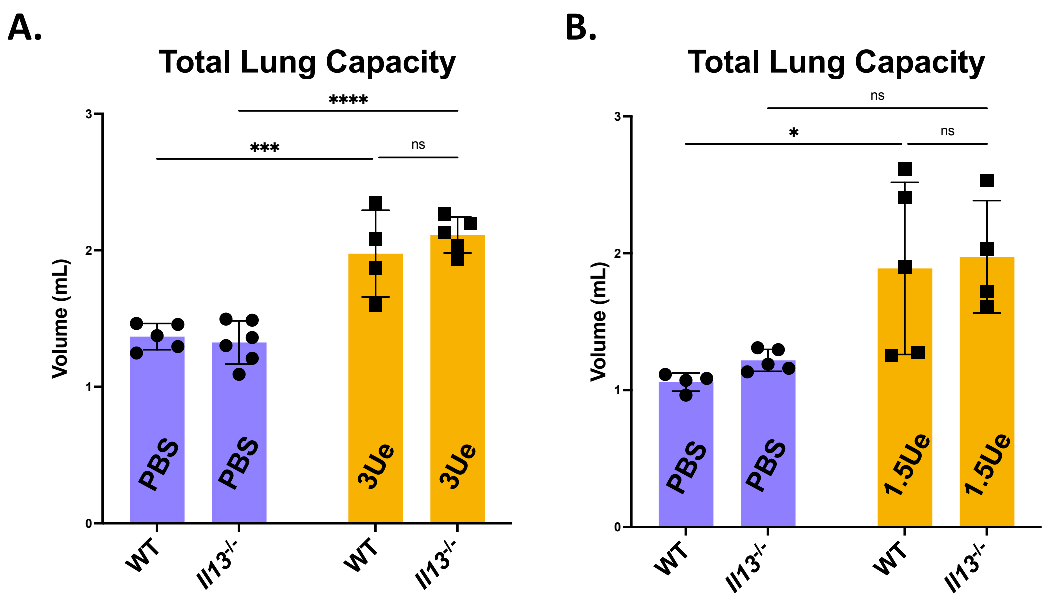

Figure 3.4. Total lung capacity analysis comparing male and female *Il13*$^{-/-}$ mice to WT littermates twenty-one days post-elastase.

WT or *Il13*$^{-/-}$ BALB/c littermates were challenged with sex-specific PPE doses for lung function analysis at Day 21. (**A**) Male animals were directly connected to a FlexiVent for assessing total lung capacity. (**B**) Females were also assayed independently and measured by this readout. Error bars represent standard deviation from the mean. Statistics were computed by two-way ANOVA with multiple comparisons (+ Tukey's post-hoc test). **** p<.0001; *** p=.0007; * p=.0304; n.s. = not significant. Both plots are representative of pooled data from N=2 independent assays. Initial experiments for each sex assayed at least N=3 animals per group. Lung function testing was performed on additional mice (at least N=2 animals per experimental group) at a later time, and results were pooled with the initial readouts.

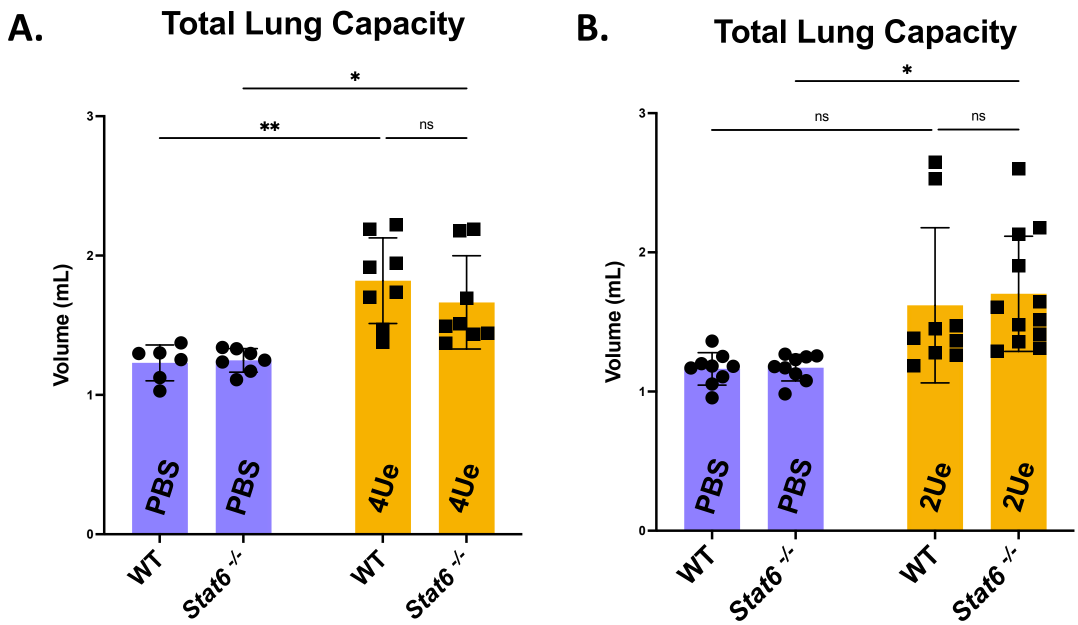

Figure 3.5. Total lung capacity analysis comparing male and female *Stat6$^{-/-}$* mice to WT littermates twenty-one days after receiving 4U and 2U elastase, respectively.

WT or *Stat6$^{-/-}$* BALB/c littermates were challenged with sex-specific PPE doses for lung function analysis at Day 21. (**A**) Male animals were directly connected to a FlexiVent for assessing total lung capacity. (**B**) Females were also assayed independently and measured by this readout. Error bars represent standard deviation from the mean. Statistics were computed by two-way ANOVA with multiple comparisons (+ Tukey's post-hoc test).** p=.0011; * p<.05; n.s. = not significant. Both plots are representative of pooled data from N=2 independent assays. (**A**) At least N=3 males per strain were challenged with elastase and assayed with each repetition. (**B**) The first repetition assayed N≥3 females per group; upon repeat, and data were pooled with results from an experiment that tested N≥4 females per group.

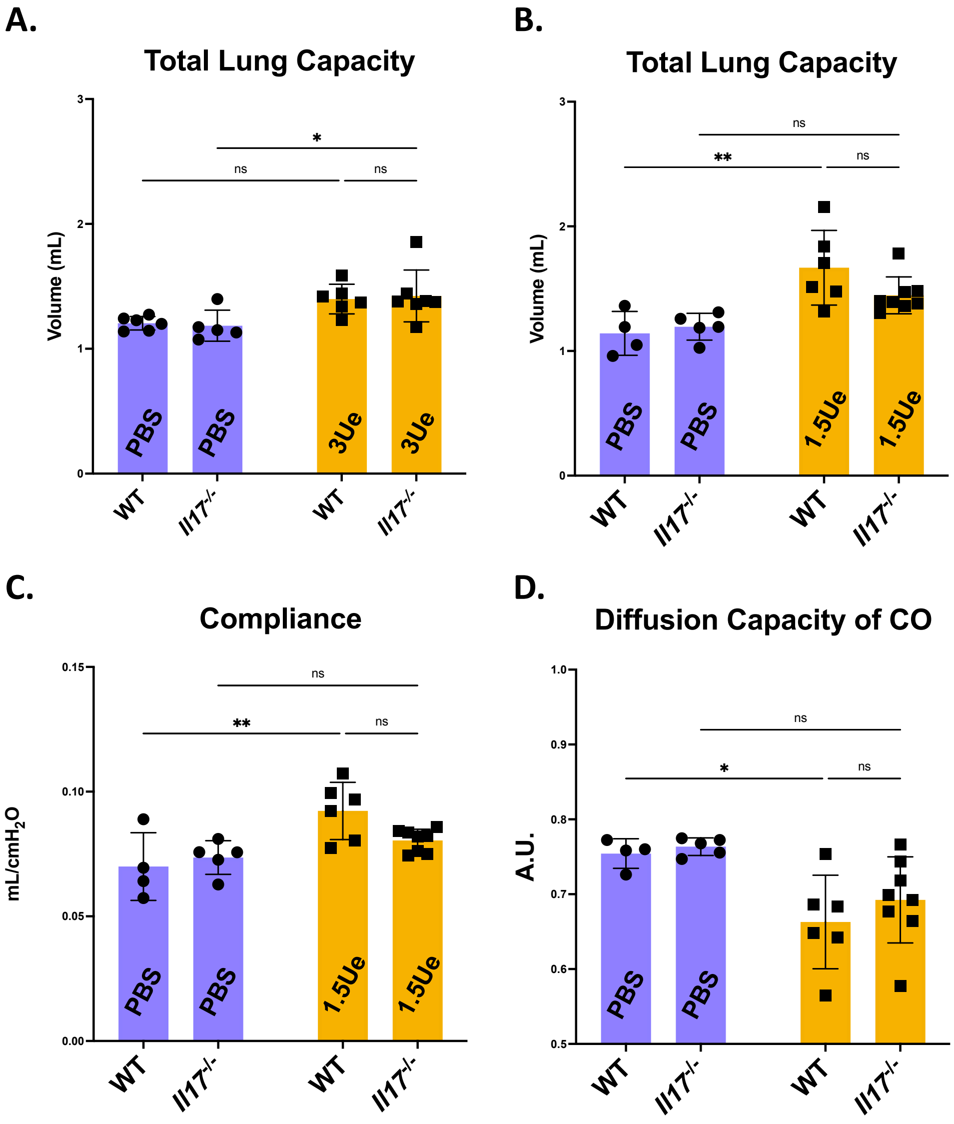

Figure 3.6. Pulmonary function test readouts comparing *Il17a*$^{-/-}$ male (A) and females (B-D) to WT littermates twenty-one days post-elastase.

WT or *Il17a*$^{-/-}$ BALB/c littermates were challenged with sex-specific PPE doses for lung function analysis at Day 21. (**A**) Male animals were directly connected to a FlexiVent for assessing changes in total lung capacity, among other function readouts. (**B**) Females were also assayed independently and analyzed by these methods. Measurements for airway compliance (**C**) and diffusion capacity of CO (**D**) were also reported herein, specifically, for assessing functional changes in female *Il17a*$^{-/-}$ mice. Error bars represent standard deviation from the mean. Statistics were computed by two-way ANOVA with multiple comparisons (+ Tukey's post-hoc test). **p=.0029; *p<.05; n.s. = not significant. Both plots are representative of pooled data from N=2 independent assays (**A**) At least N=3 males per strain were challenged with elastase and assayed with each repetition. (**B, C, D**) The first repetition assayed N=3 females per elastase group; upon repeat, N≥3 females per elastase group were tested and the data were pooled.

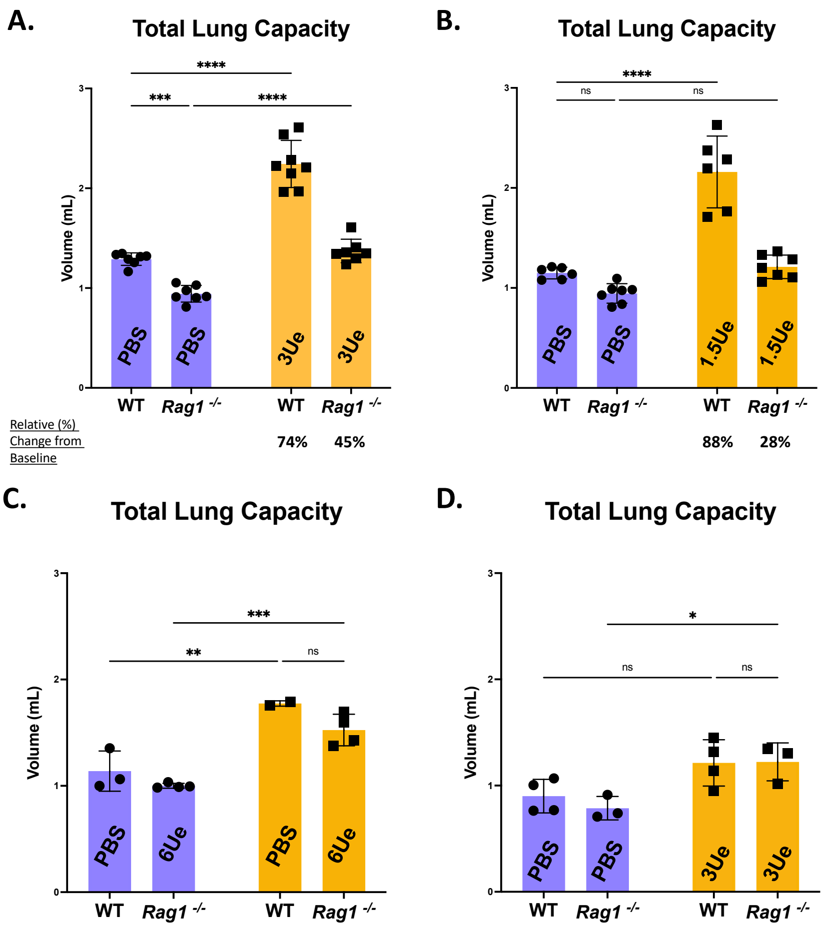

Figure 3.7. Total lung capacity analysis comparing male and female *Rag1*$^{-/-}$ strains to WT controls twenty-one days after challenge with variable doses of elastase.

WT or *Rag1*$^{-/-}$ animals were challenged with sex- and strain-specific PPE doses for lung function analysis at Day 21. (**A**) Male BALB/c WT or KO animals were directly connected to a FlexiVent for assessing changes in total lung capacity, among other function readouts, twenty-one days after receiving 3U PPE intratracheally. (**B**) Female BALB/c WT or KO animals challenged with 1.5U PPE were assayed independently for changes in total lung capacity. Relative change was calculated as described previously **(Chapter 1**), and values are illustrated as part of plots (**A**) and (**B**). Male (**C**) and female (**D**) C57Bl/6 mice were also challenged at their standard 6U or 3U PPE dose, respectively, and total lung capacity was measured for comparing readouts with those from the BALB/c model. Error bars represent standard deviation from the mean. Statistics were computed by two-way ANOVA with multiple comparisons (+ Tukey's post-hoc test). **** p<.0001; ***p=.0009; n.s. = not significant. (**A, B**) are representative of pooled data from N=2 independent assays. For males, the initial experiment tested N=4 animals per group. Upon repeat, N≥3 mice were used per group, yielding similar outcomes. For females, both iterations had uneven group sizes, but N≥3 animals per group were tested in reproducible, independent assays. (**C, D**) Experiments were performed only once per sex (N≥3 per elastase group). Of note, James Limjunyawong independently performed his own iteration of this work 2013, yielding comparable results in both the C57Bl/6J and BALB/cJ *Rag1*$^{-/-}$ EIEE model.

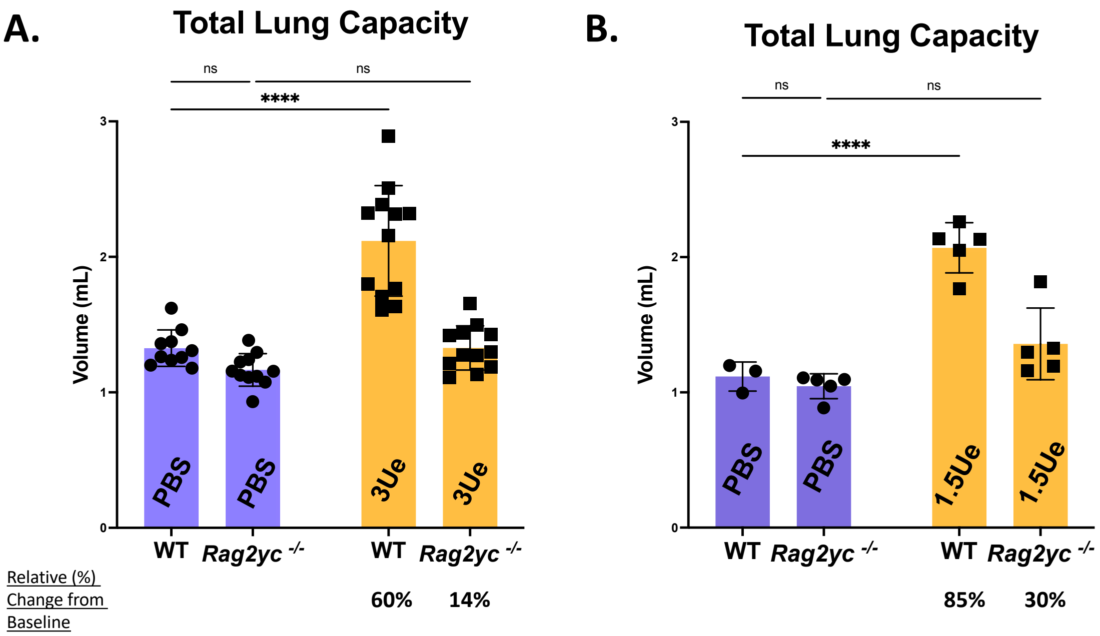

Figure 3.8. Total lung capacity analysis comparing male and female *Rag2γc*$^{-/-}$ mice to WT controls twenty-one days post-elastase.

WT or *Rag2γc*$^{-/-}$ BALB/c animals were challenged with sex-specific PPE doses for lung function analysis at Day 21. (**A**) Male animals were directly connected to a FlexiVent for assessing total lung capacity. (**B**) Females were also assayed independently and measured by this readout. Error bars represent standard deviation from the mean. Relative change was calculated as described previously (**Chapter 1**). Statistics were computed by two-way ANOVA with multiple comparisons (+ Tukey's post-hoc test). ****p<.0001; n.s. = not significant. (**A**) represents data from three iterations of the same experiment. For each repetition, N≥3 males were tested per group. (**B**) illustrates data from one experiment (N≥3 females per group) that was not repeated in its native form. Downstream efforts with *Rag2γc*$^{-/-}$ females in related assays has supported that, on average, these mice experience ~30% in TLC post-elastase.

Chapter 4. Characterizing myeloid subsets that drive EIEE at single-cell resolution.

Overview

Two macrophage subsets reside in unique pulmonary niches at homeostasis: alveolar macrophages that are found in the alveolar spaces and interstitial macrophages that occupy the lung parenchyma. Our appreciation for the roles that macrophages play in the pathogenesis of chronic inflammatory disease in the lungs is inadequately understood. Therefore, we applied a single-cell RNA sequencing approach to examine transcriptional dynamics of myeloid cells from BALB/cJ lungs in the elastase-induced experimental emphysema (EIEE) model of progressive lung destruction. We hypothesized that chronic damage is driven by a 'pathogenic' macrophage subset that maintains residency in the diseased lung post-elastase. The goal was to define the dynamics of macrophage phenotypes transcriptionally at 7 and 21 days post-elastase challenge and validate the translation of key gene products with protein-based assays. Employing scRNAseq we annotated macrophage, monocyte, neutrophil and dendritic cell subsets at single-cell resolution. Upon comparing cellular subsets from diseased lungs to those at baseline, we focused in on a population of post-elastase alveolar macrophages defined by their sustained transcription and translation of *Cd63* and *Cd9*. Expression of secreted factors like *Mmp12* and *Ctsk* may begin to explain, functionally, how this subset of alveolar macrophages drives chronic lung destruction in emphysema.

Introduction

Key technical advances have facilitated the study of cellular dynamics in complex, biological systems. In the last decade alone, multiple groups have used advanced fate-mapping and parabiotic strategies that reshaped our interpretation of the basis of macrophage subsets that occupy organs (Hashimoto et al., 2013; Yona et al., 2013). Reports highlighting macrophage development in the heart, brain, skin, and lungs (Epelman et al., 2014; Furth and Cohn, 1968; Ginhoux et al., 2010; Hoeffel et al., 2012; Tan and Krasnow, 2016) indicate that self-renewing tissue-resident macrophages have embryonic origins and are derived from the yolk sac or fetal liver. Post-birth, many tissues depend on systematic replacement of resident macrophages over time with monocyte-derived cells derived from the bone marrow (Li et al., 2022; Misharin et al., 2017). Having reshaped our understanding of macrophage ontogeny, the focus has shifted toward examining macrophage behavior, or effector function, at baseline and under inflammatory conditions.

Single-cell RNA sequencing (scRNAseq) has facilitated efforts to characterize macrophage phenotypes across diverse organs. Immunologists are now able to make sophisticated predictions related to cellular dynamics within a system by analyzing transcriptomes at the single cell resolution (Jaitin et al., 2014; Tang et al., 2009; Zheng et al., 2017). The human lung has been characterized by scRNAseq (Travaglini et al., 2020); and ‘pathogenic’ macrophages have been identified transcriptionally and validated functionally from humans with idiopathic pulmonary fibrosis (Adams et al., 2020;

Reyfman et al., 2018). The murine lung transcriptome has also been studied extensively using scRNAseq, and novel macrophage subsets with intriguing transcriptional signatures have been highlighted at baseline or at different stages of an inflammatory response (Aran et al., 2019; Dick et al., 2022; Evren et al., 2021; Li et al., 2022; Mould et al., 2019; Pisu et al., 2021; Ural et al., 2020; Xu-Vanpala et al., 2020). Only recently has scRNAseq been applied to the study of lungs affected by COPD (Li et al., 2021; Liegeois et al., 2022; Rao et al., 2020; Sauler et al., 2022). Therefore, we aimed to apply this method for investigating macrophage and other cell dynamics in our BALB/cJ EIEE model.

We analyzed $CD45^{+}CD64^{+}$ cells from lungs of naïve and diseased mice at two timepoints post-elastase challenge: day 7 and day 21. We purified these cells first by FACS, anticipating that our broad gating strategy would capture the three, mononuclear phagocyte populations in healthy or diseased mice: alveolar macrophages, interstitial macrophages, and monocytes. We hypothesized that progressive damage from elastase was driven by an aberrant, or dysregulated, cellular subset belonging to one or more of these populations in the lung. We anticipated that scRNAseq would provide the appropriate resolution to identify putative ’pathogenic’ cell subsets by their transcriptional signature. Based on several reports (Adams et al., 2020; Aran et al., 2019; Xie et al., 2018), it was predicted that this putative subset would be evident primarily in diseased, but not healthy lungs. We first created an atlas to annotate the $CD45^{+}CD64^{+}$ landscape at steady-state, which served as our guide and transcriptional comparator for analyzing diseased lungs at single-cell resolution. We then highlighted macrophage populations that may contribute to emphysema pathogenesis, validating our findings at the protein level with flow cytometry. Ultimately, we narrowed our study to investigate $CD9^+CD63^+$ alveolar macrophages in EIEE. These cells express genes for catabolic enzymes like *Mmp12* and *Ctsk* and may be candidates for the proposed subset of ‘pathogenic’ macrophage capable of mediating long-term, progressive damage to the lung. These findings provide the bases for studies to extend molecular, cellular and functional studies for understanding the role of macrophages in the pathogenesis of chronic-progressive diseases like emphysema.

Methods

Mice.

Wild-type (WT) BALB/cJ animals for these studies were originally purchased from Jackson Laboratories (#000651). All animal work was conducted in accordance with the standards established by the United States Animal Welfare Acts, set forth in NIH guidelines and the Policy and Procedures Manual of the Johns Hopkins University (JHU) Animal Care and Use Committee. Animals were maintained in filter-topped cages at approximately 72°C, 50-60% humidity with 14:10 hour light/dark cycle and *ad libitum* access to food and water.

Elastase-Induced Experimental Emphysema (EIEE).

Male BALB/cJ mice (7-10 weeks old) were anesthetized by intraperitoneal injection with a mixture (1:1) of ketamine (100 mg/kg) and xylazine (10 mg/kg) in sterile water. Mice were then intubated with an 18G canula, and EIEE was induced with a single dose of 3U porcine pancreatic elastase (PPE, suspended in 50 µl of PBS; Elastin Products Co., LE4205), instilled intratracheally (IT).

Whole Lung Digestion and Tissue Preparation.

After administering an overdose ketamine/xylazine, intact whole lungs were perfused with cold Hanks Balanced Salt Solution (HBSS) and removed from the mouse. Lungs were finely minced with a razor blade and placed on ice in HBSS. Tissue digestion buffer (refer to **Chapter 2, Table 2.2**) was added and the lung tissue was homogenized by incubating for 25 minutes at 37^{o}C on a rotating platform set at 300 rpm. Post-digestion, homogenates were passed through a 40 µm cell strainer and rinsed with HBSS. Red blood cells were eliminated by treating each sample with 5 mL of ammonium chloride-potassium lysis buffer for 2 minutes. Lysis was 'quenched' by adding 15 mL HBSS, and samples were centrifuged, and resuspended in FACS buffer (refer to **Chapter 2, Table 2.2**) for staining.

Single-cell RNA Sequencing of CD45^{+}CD64^{+} cells.

Animals in the experimental cohorts received 3U porcine pancreatic elastase (PPE, Elastin Products Company, Owensville, MO) IT either 7 or 21 days prior to isolating lungs for single-cell sequencing. Lungs from age-matched naïve animals served as controls. Elastase challenges were staggered, so that all animals (N=2 per group) could be sacrificed and the lungs processed on the same day. Single-cells in FACS buffer were stained with anti-mouse CD45-APC-Cy7 (Clone 30-F11, BioLegend), anti-mouse CD64-PE (X54-5/7.1, BioLegend) and propidium iodide (Invitrogen, P1304MP). The CD45^{+}CD64^{+} cell population was sort-purified in the MMI BD Immunology and Flow Cytometry Core Facility using a MoFlo XDP (Beckman Coulter). Approximately 100,000 cells were sort-purified per experimental and control lung sample. The sort-purified CD45^{+}CD64^{+} lung cells were then immediately subsampled (approximately 10,000 cells per replicate) for library preparation and single-cell sequencing using the 10x Genomics 3' Reagent Kit (v3 Chemistry) and Chromium Controller (Zheng et al., 2017). These steps were carried out by the Johns Hopkins Medical Institute Transcriptomics Core Facility. Raw sequencing files were uploaded to Partek Flow (St. Louis, Missouri) for deconvolution and analysis. Barcodes and unique molecular identifiers (Islam et al., 2014) were demultiplexed with 10x Cell Ranger 6.0.0, which also mapped high-quality reads to the Genome Reference Consortium Mouse Build 38 (GRCm38) genome and to the mm10-2020-A reference transcriptome. The number of cells captured by 10x ranged from 4,160 to 7,949 per sample (sum = 35,912 cells across six libraries). Per sample, single-cells were represented by total reads in the range of 401,959,301 to 452,130,213. Median counts and number of genes expressed per cell were scrutinized for assessing the overall quality of each library. Extended QA/QC, normalization, and visual analysis were performed with algorithms in Partek Flow. Single-cells bearing low gene detection as well as cells that had a high percentage of mitochondrial-to-cytoplasmic transcripts were eliminated from each library as dead or 'apoptotic' cells. Remaining datapoints were then normalized by one of two methods depending on the immediate goal for analysis downstream: for visualizing subsets and gene expression patterns at single-cell resolution or creating scatter plots, we applied the recent version of the Seurat-based algorithm, scTransform (Hafemeister and Satija, 2019). For directly comparing gene expression between clusters and conducting statistical analysis, data were transformed as counts per million (CPM) with the formula: $Log_2[CPM+1]$. Dimensionality reduction of the dataset was accomplished first with principal component analysis, and data were visualized with the Uniform Manifold Approximation and Projection algorithm – UMAP (Becht et al., 2018). Unsupervised, graph-based clustering was the primary method for identifying putative cell populations in our dataset (Waltman and Van Eck, 2013). In our final representation of the dataset, we used Harmony (Korsunsky et al., 2019) for reducing batch effects and integrated all six libraries (31,730 single-cells with count values normalized for 11,680 features in total) for identifying cell types that were conserved across timepoints in EIEE Although not formally discussed herein, we performed a separate, merged analysis with the Seurat3 Integration algorithm (Butler et al., 2018; Stuart et al., 2019), yielding clustering and annotation outputs similar to results achieved with Harmony.

Flow Cytometry.

Animals in the experimental cohorts received 3U PPE IT and control animals received PBS IT either 4, 7, 14, or 21 days prior to flow cytometry (variable N per experiment – noted in figure legends). Elastase challenges were staggered, so that all animals could be sacrificed for data acquisition on the same day. Acquisition was performed on either an LSR-II (Becton Dickinson, Franklin Lakes NJ) or an Aurora 4L: 16V-14B-10YG-8R (Cytek Biosciences, Fremont CA), as noted in the figure legends. In preparation for flow cytometry, cell homogenates were suspended in FACS Buffer and stained with the following: Zombie Near-IR (BioLegend; Aurora only) or LIVE/DEAD Aqua (eBioscience; LSR-II only), anti-mouse CD45 (30-F11, eBioscience; Alexa 532 or BV711), anti-mouse CD64 (X54-5/7.1, BioLegend; BV421 or Alexa 647), anti-mouse SiglecF (clone, eBioscience; PerCP-Cy5.5., PE-Cy7, or SB600), anti-mouse CD9 (clone, BioLegend; FITC or BV605), anti-mouse CD63 (AA4.1, BioLegend; PE-Cy7 or Alexa 647), anti-mouse MerTK (DS55MER, eBioscience; APC or PE), anti-mouse CD11b (M1/70, eBioscience; Alexa 700 or FITC). Single-fluorophore controls were prepared using either cytometry beads

(Invitrogen, 01-3333-41) or lung cells isolated on the day of experimentation. For compensation-based cytometry, samples were acquired using the BD FACSDiva software; for spectral cytometry, acquisition and live unmixing were executed in Cytek's SpectroFlo software. Compensation or spectral unmixing were both finalized in FlowJo (Becton Dickinson). For all cytometry experiments, unstained and fluorescence-minus-one control samples were prepared for facilitating analysis and for determining gates.

Statistics and Illustrations.

For scRNAseq, all stats and visualizations were generated using computational algorithms in Partek Flow. As noted in-text, Student's t-test and the Hurdle model (Finak et al., 2015) were applied for determining statistical significance of differential gene expression comparisons made between clusters at single-cell resolution. For flow cytometry, illustrations were generated as part of FlowJo analysis. Statistical comparisons (Mann-Whitney U-test, significance defined as $p < .05$) were performed in GraphPad Prism 9 (San Diego, California).

Results

Preliminary flow cytometry defining myeloid cell dynamics in EIEE.

Macrophages are indispensable for pulmonary defense through their capacity to survey airways and regulate innate and adaptive immunity. There is a large body of evidence implicating alveolar macrophages (AM) and interstitial macrophages (IM) in the pathogenesis of COPD (Hautamaki et al., 1997; Shapiro, 1999; Shibata et al., 2018). In preliminary studies we employed flow cytometry to identify an IM population that was reported to cause significant damage post-elastase (Shibata et al., 2018). We aimed not only to corroborate this IM observation in the EIEE model, but also examine other phagocyte populations that exist in the lung, such as alveolar macrophages (AM). We isolated cells from lungs of mice at 4, 7, 14, and 21 days post-elastase and compared dynamics to cells from time-matched PBS-instilled controls by flow cytometry. The gating strategy for identifying AM and IM is outlined in **Figure 4.1**. IM were designated as $CD45^{+}CD11b^{+}CD11c^{-}SiglecF^{-}CD64^{+}MerTK^{+}$ (**Figures 4.1 and 4.2**) whereas AM were identified as $CD45^{+}CD11b^{-}CD11c^{+}SiglecF^{+}CD64^{+}$ (**Figures 4.1 and 4.3**). As described by Shibata *et al.* (2018), we observed a drastic increase in IM numbers post-elastase, particularly at days 4 and 7, relative to PBS-treated mice (**Figure 4.2**). By days 14 and 21, the population leveled off, approaching baseline values.

Quantification and interpretation of AM dynamics in EIEE was difficult to achieve by this approach, largely due to technical limitations that included significant autofluorescence emanating from this sentinel lung cell population (Edelson et al., 1985;

Misharin et al., 2013; Tighe et al., 2019). Thus, when defining AM with surface markers like SiglecF and CD11c, it appeared that our results aligned with findings by Shibata *et al.* (2018), who reported that AM population dynamics were relatively stable over time after elastase challenge (**Figure 4.3**). We concluded that, for quantifying broad cell populations in the post-elastase lung, flow cytometry was indeed useful, but resolution was limited by a major technical bias – this technique requires use of *known* surface markers for immunophenotyping macrophage subsets – most of which were developed to identify macrophages at steady state. Our current strategy did not allow for exploration of novel surface molecules that could be used to characterize 'pathogenic' macrophage subsets in EIEE. Thus, we made the decision to employ single-cell RNA sequencing (scRNAseq) as an unbiased, multidimensional approach for identifying macrophage subsets in EIEE. We hypothesized that one or more 'pathogenic' mononuclear phagocyte sub-population(s) arises post-elastase challenge and persists in the lungs at day 21. Ultimately, our goal was to identify candidate subsets by scRNAseq and FACS-purify these cells to conduct functional assays for testing their ability to damage lung tissue.

Single-cell RNA-sequencing QA/QC.

On the day of processing for scRNAseq, lungs from six mice (N=2 animals per timepoint, including naïve controls) were harvested after receiving 3U PPE either 7 or 21 days earlier. The choices of days 7 and 21 were based on our extensive experience in the EIEE model: day 7 represents the time point where progressive disease is first discernable by lung function tests and histology, and day 21 represents a time point in the EIEE model where progressive disease is fully established based on the same readouts (Craig et al., 2017; Limjunyawong et al., 2015).

Single cell suspensions were generated, and the $CD45^+CD64^+$ cells were sort-purified and sequenced with the 10x Genomics Chromium platform. It was decided to cast a wide net and sort cells using $CD45^+CD64^+$ surface protein expression (**Figure 4.4**), as opposed to enriching for macrophages with widely used markers like CD11b, CD11c, SiglecF or MerTK (Chakarov et al., 2019; Schyns et al., 2019; Ural et al., 2020; Yao et al., 2020), which we knew from experience did not capture the diversity of activated macrophages and monocytes in the lungs. We hypothesized that a broader gating strategy would be a more informative for using scRNAseq to identify activation states of lung mononuclear phagocyte populations, like alveolar macrophages, interstitial macrophages, and monocytes.

To process the single-cell sequencing data, raw data (.fastq) were uploaded to Partek Flow. High-quality barcodes and unique molecular identifiers (UMIs) were extracted with Cell Ranger 6.0.0, a program written by 10x Genomics. This program was useful for demultiplexing raw sequencing data and aligning reads to the GRCm38 build reference genome and the mm10-2020-A reference transcriptome. Standard QA/QC calculations with Cell Ranger supported the assertion that all six transcriptional libraries were acquired successfully by the 10x Chromium Controller. For example, the lung homogenized and sequenced from baseline control 1 (**B1**) yielded 5,197 cells, which were represented transcriptionally by 431,597,465 reads. Both values were technically feasible, based on the experimental design for our 10x pipeline (refer to **Methods**). For

B1, total reads mapped to 19,721 murine genes – a value deemed biologically acceptable. Baseline Control 2 (**B2**) had comparable values for each metric, respectively: 4,160 cells were captured, and 452,130,213 reads were sequenced, mapping to 19,489 genes. The median number of genes expressed and median UMI counts per cell were also calculated with Cell Ranger and reported in **Table 4.1**, below, which portrays summary QA/QC statistics for all experimental timepoints from this study:

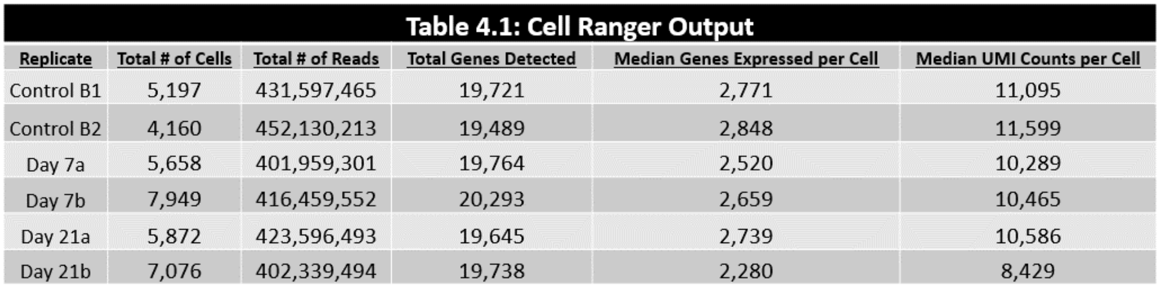

Table 4.1: Cell Ranger Output

Replicate	Total # of Cells	Total # of Reads	Total Genes Detected	Median Genes Expressed per Cell	Median UMI Counts per Cell
Control B1	5,197	431,597,465	19,721	2,771	11,095
Control B2	4,160	452,130,213	19,489	2,848	11,599
Day 7a	5,658	401,959,301	19,764	2,520	10,289
Day 7b	7,949	416,459,552	20,293	2,659	10,465
Day 21a	5,872	423,596,493	19,645	2,739	10,586
Day 21b	7,076	402,339,494	19,738	2,280	8,429

Importantly, values for all six experimental samples were comparable, and the experiment was deemed to be a technical success at this stage.

QA/QC was finalized in Partek Flow. First, we roughly visualized each baseline control replicate at single-cell resolution using the Uniform Manifold Approximation and Projection (UMAP) algorithm and applied graph-based clustering (GBC; **Figure 4.5A**). The goal of single-cell QA/QC at this step of analysis was to remove dead or apoptotic cells from the dataset (Ilicic et al., 2016). Clusters designated to be low-quality or from dead cells within each control had lower transcript counts (**Figure 4.5B**) and fewer genes detected (**Figure 4.5C**) when compared to others in the dataset. In baseline control B1, such cells existed in Clusters 5 and 6. In control B2, Clusters 6 and 7 appeared to contain low-quality data by these metrics. Cell populations with high percentage of mitochondrial counts (%mito) were also removed as a component of single-cell QA/QC. This QA/QC metric directly compares abundance of mitochondrial-based RNA to cytoplasmic transcripts detected per cell. At single-cell resolution, dead or apoptotic cell libraries tend to be overrepresented by mitochondrial-based transcripts. Biologically, this phenomenon is thought to occur when cytoplasmic RNA is expelled from porous, apoptotic cells at a rate faster than mitochondrial-derived transcripts (Galluzzi et al., 2012; Ilicic et al., 2016). Importantly, Clusters 5/6 (B1) and Clusters 6/7 (B2), which had low counts and detected genes overall, also had high %mito values relative to neighboring clusters (**Figure 4.5D**). Clusters 5/6 (**B1**) and Clusters 6/7 (**B2**) had therefore failed single-cell QA/QC and were excluded from downstream analysis. This process was repeated for remaining samples in this study, and results were listed in **Table 4.2**, below:

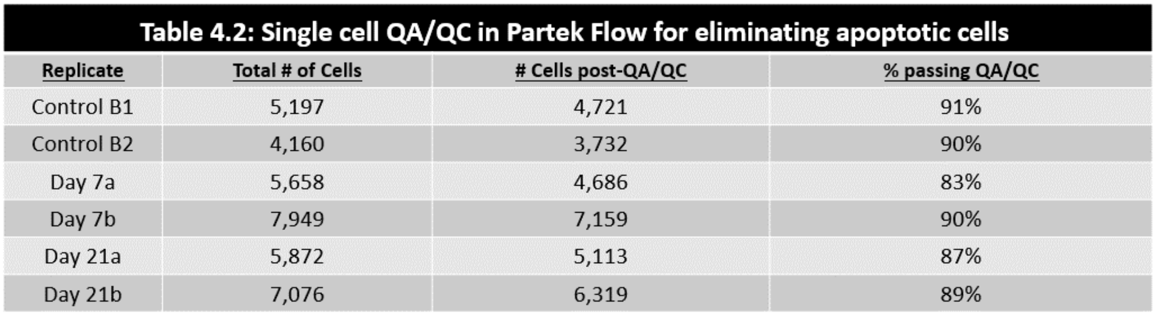

Table 4.2: Single cell QA/QC in Partek Flow for eliminating apoptotic cells

Replicate	Total # of Cells	# Cells post-QA/QC	% passing QA/QC
Control B1	5,197	4,721	91%
Control B2	4,160	3,732	90%
Day 7a	5,658	4,686	83%
Day 7b	7,949	7,159	90%
Day 21a	5,872	5,113	87%
Day 21b	7,076	6,319	89%

This analysis indicated that the sequencing was a technical success and worthy of extended computational analysis and biological interpretation. Prior to comparing transcriptional dynamics over time in our progressive disease model, we set out to comprehensively outline the CD45$^+$CD64$^+$ landscape in BALB/c lungs at steady-state. Single-cell RNA libraries derived from naïve animals (i.e., **B1** and **B2**) were our primary comparators for this time course and cell clusters had to be annotated first to appreciate transcriptional variation over time or to identify populations unique to diseased lungs at day 7 or day 21 post-elastase.

Exploratory transcriptomics and statistical methods for annotating CD45$^+$CD64$^+$ lung cells at steady-state.

Raw counts from single-cells that had passed QA/QC were normalized (refer to **Methods** for transformation details), organized by UMAP, and GBC was carried out. Sample **B1** was now represented by nine clusters (**Figure 4.6A**), and sample **B2** had eight clusters (**Figure 4.6B**). For understanding this difference among biological replicates, we compared the transcription profile of one cluster at a time vs. all others using a differential gene expression algorithm and Student's t-test. For each cluster, the Top 20 most differentially expressed features (sorted by P-value) were listed in **Tables 4.3 and 4.4, below:**

Table 4.3: Sample B1 Top Features (P-value; determined by Student’s t-test)

RANK	1	2	3	4	5	6	7	8	9
1	*Plet1*	*Fn1*	***Cd300e***	***H2-Aa***	*F7*	***C1qa***	*Ifit2*	***Nusap1***	***S100a9***
2	*Kcnn3*	*Hp*	*Eno3*	***H2-Ab1***	*Cd2*	***C1qb***	*Rsad2*	*Rrm2*	***Retnlg***
3	*Slc7a2*	***S100a4***	*Slc12a2*	***H2-DMb1***	*Dmxl2*	***C1qc***	*Ifit3*	*Pclaf*	*Stfa2l1*
4	*Lpin1*	***F13a1***	*Ace*	***H2-Eb1***	*Ear1*	*Pf4*	*Oasl2*	*Birc5*	*Cstdc4*
5	*Atp6v0d2*	***S100a6***	*Pglyrp1*	***Cd74***	*Dapk1*	*Fxyd2*	*Usp18*	***Mki67***	*Dhrs9*
6	*Krt19*	***Ly6c1***	***Cd300ld***	***Tmem176b***	*Acaa1b*	*Igfbp4*	*Phf11b*	***Ccna2***	*Acod1*
7	*Mgll*	***Ly6c2***	*Adgre4*	***H2-DMb2***	*Cidec*	*Gas6*	*Ifit1*	*Top2a*	*Il1f9*
8	*Fpr1*	*Ifitm6*	*Fabp4*	***Tmem176a***	*Fabp1*	*Sdc4*	*Isg15*	*Cenpf*	*Mmp9*
9	*Lrp12*	*Ms4a4c*	*Treml4*	***Cd209a***	*Kcnip4*	*Pmepa1*	*Trim30d*	*Ube2c*	*Lcn2*
10	***Lpl***	***Ccr2***	*Pou2f2*	*Plbd1*	*Ralgds*	*Blnk*	*Slfn1*	*Prc1*	*Cxcr2*
11	*Flvcr2*	*Thbs1*	*Hes1*	*Aif1*	*Cyb561a3*	*Pmp22*	*Phf11d*	*Hmmr*	*Hdc*
12	***Spp1***	*Plac8*	*Stap1*	*Ciita*	*Card11*	*Mgl2*	*Oas3*	*Kif11*	***S100a8***
13	*Slc6a4*	*Ifitm3*	*Apoc2*	*Ccr2*	*Tns1*	*Stab1*	*Ifi44*	*Cdca3*	*Csf1*
14	*B3gnt7*	*Ms4a6c*	*Ceacam1*	*S100a6*	*Pros1*	*C3ar1*	*Ifit3b*	*Knl1*	*Lrg1*
15	*C530008M17Rik*	*Plbd1*	*S1pr5*	*Rps29*	*Trerf1*	*Fcrls*	*Ifi47*	*Aspm*	*Rdh12*
16	*Vstm2a*	*Lyz2*	*Cyfip2*	*Ms4a4c*	*Adarb1*	***Folr2***	*Ifi44l*	*Cenpe*	*Il1r2*
17	*Ly75*	*Cd52*	*Tmem26*	*S100a4*	*Nav2*	***Cd72***	*Ifi209*	*Iqgap3*	*Ankrd33b*
18	*Plekhg1*	*Cd177*	*Fyb*	*Cd52*	*Mertk*	*Ms4a7*	*Zbp1*	*Esco2*	*G0s2*
19	***Car4***	*Ifi27l2a*	*Slc11a1*	*Tpt1*	*F11r*	*Pla2g2d*	*Trim30c*	*Kif15*	*Klra17*
20	*Adarb1*	*H3f3a*	*Cd244a*	*Ifitm3*	*Flt1*	*Ctla2b*	*Rtp4*	*Ncapg*	*Gm16556*
	TRAM	**Mono**	***Cd300* Cells**	**MHC-II^{Hi} Mono/DC**	**AM-like**	**IM**	**“*Ifi-*” Cells**	**Pro-cells**	**Neutrophil**

NOTE: Bolded ***Features*** were described in-text for provisionally **annotating** each graph-based cluster

Table 4.4: Sample B2 Top Features

RANK	1	2	3	4	5	6	7	8
1	*Plet1*	***Ly6c2***	*Ablim1*	***Cd300e***	***H2-Eb1***	***C1qa***	***S1009***	***Nusap1***
2	*Lpin1*	***Ly6c1***	*Ccr7*	*Ace*	***H2-Aa***	*Pf4*	***Retnlg***	*Birc5*
3	*Slc6a4*	*Thbs1*	*Gimap1*	*Adgre4*	***H2-Ab1***	***C1qc***	***S100a8***	*Rrm2*
4	*Slc7a2*	*Fn1*	*Gimap4*	*Slc12a2*	***H2-DMb1***	***C1qb***	*Cstdc4*	*Top2a*
5	*Atp6v0d2*	*Ms4a4c*	*Gimap6*	*Pglyrp1*	***Cd74***	*Fxyd2*	*Stfa2l1*	*Pclaf*
6	***Lpl***	*Hp*	*P2ry10*	*Eno3*	***Cd209a***	***Folr2***	*Acod1*	***Ccna2***
7	*Fpr1*	***S100a4***	*Trbc2*	***Cd300ld***	***Tmem176b***	*Fcrls*	*Lrg1*	*Ube2c*
8	***Siglecf***	***S100a6***	*Gimap3*	*Stap1*	***Tmem176a***	*Gas6*	*Il1f9*	*Kif11*
9	*Krt19*	***F13a1***	*4930523C07Rik*	*Treml4*	***H2-DMb2***	*Stab1*	*Cxcr2*	*Cenpf*
10	***Ear1***	*Plac8*	*Ptprcap*	*Pou2f2*	*Ciita*	*Pmp22*	*Hdc*	*Knl1*
11	*Bhlhe41*	*Ifitm6*	*Sept1*	*Fabp4*	*Aif1*	*Mgl2*	*Dhrs9*	*Prc1*
12	*Fabp1*	***Ccr2***	*Cd3e*	*Ceacam1*	*Plbd1*	*C3ar1*	*Mmp9*	*Hmmr*
13	*F7*	*Ifitm3*	*Ppp1r16b*	*Apoc2*	*Ms4a4c*	*Sdc4*	*Ankrd33b*	*Iqgap3*
14	*Kcnn3*	*Ms4a6c*	*Ebf1*	*Hes1*	*Cd52*	*Igfbp4*	*Il1r2*	*Esco2*
15	*Hvcn1*	*Ifi27l2a*	*S1pr1*	*S1pr5*	*Tpt1*	*Pmepa1*	*Slc2a3*	*Aspm*
16	*Ttyh2*	*Ly6e*	*Arap2*	*Cyfip2*	*Ifitm3*	*Ms4a7*	*Steap4*	*Pbk*
17	*Ly75*	*Plbd1*	*Nedd4*	*Tmem26*	*S100a4*	*Cp*	*AW011738*	*Kif15*
18	*Flvcr2*	*Cd52*	*Il7r*	*Cd244a*	*S100a6*	*Blnk*	*G0s2*	*Cdk1*
19	*Mgll*	*Adgre5*	*Mast4*	*Fyb*	*Ms4a6c*	***Lyve1***	*Lcn2*	*Cenpe*
20	*Perp*	*Ms4a6b*	*Satb1*	*Clec4a1*	*Ifi27l2a*	*Cacna1a*	*Csf1*	*Nuf2*
	TRAM	**Mono**	**T-cell**	***Cd300* Cells**	**MHC-II^{Hi} Mono/DC**	**IM**	**Neutrophil**	**Pro-cells**

Cluster 1 from samples B1 and B2 had differential expression of genes encoding arginine and serotonin transporters (*Slc7a2* and *Sla6a4*, respectively), keratin 19 (*Krt19*), vacuolar ATPase (*Atp6vod2*), the C-type lectin DC205 (*Ly75*), osteopontin (*Spp1),* carbonic anhydrase IV *(Ca4/Car4),* lipoprotein lipase *(Lpl),* sialic acid binding Ig-like lectin f (*Siglecf),* and the transcription factor *Ear1* – all of which have been identified as transcriptional markers for classifying "TRAM," or tissue-resident alveolar macrophages in mice (Bain and MacDonald, 2022; Cohen et al., 2018; Gibbings et al., 2017; Yla-Herttuala et al., 1991; Yu et al., 2017). In replicates B1 and B2, Cluster 2 was transcriptionally consistent with monocytes ("Mono"; *Ly6c, F13a1, S100a4, S100a6, Ccr2),* which have been previously annotated at single-cell resolution (Cohen et al., 2018; Evren et al., 2021). Cluster 3 in B1, which corresponded to Cluster 4 in B2, had a perplexing transcriptional signature. We were unable to classify these populations in a manner that was biologically informative, though expression of *Cd300*-related genes was noted for being unique to these clusters. At this exploratory level, we were also unable to classify Clusters 5 and 8 (B1) or Clusters 3 and 8 (B2) with much confidence. Cluster 8 in B1 and B2 was clearly defined by expression of cell-cycle genes like *Nusap1, mki67, Ccna2, etc*. and likely a subset of myeloid cells undergoing cell division (Buettner et al., 2015). Also difficult to interpret, Cluster 5 from sample B1 appeared to be alveolar macrophage-like, as expression of the genes encoding for *Ear1* and the receptor tyrosine kinase *Mertk* were noted among top ranked features. Cluster 3 in replicate B2 produced transcripts related to T-cell biology (*Trbc2, Cd3e*). Of the remaining populations, Cluster 4 in replicate B1 likely represented a population of dendritic cells (DC) based on the prominence of *H2-DMb1/2, H2-*

Aa/Ab1/Eb1, Cd74 (MHC-II invariant chain)*, Cd209a* (DC-SIGN), *Tmem176a/b* (negative regulator of DC differentiation) transcription (Evren et al., 2021; Lancien et al., 2021). Cluster 4 localized tightly with monocyte Cluster 2 in UMAP space, so this population could also be an MHC-II^{Hi} monocyte subset at baseline. For replicate B2, this MHC-II^{Hi} population corresponded to Cluster 5. Cluster 6 in B1 and B2 was transcriptionally consistent with interstitial macrophages ("IM"; folate receptor beta*, Folr2,* complement genes *C1qa/b/c*, and lymphatic vessel endothelial hyaluronan receptor, *Lyve1*), which sparsely occupy the lung at baseline (Chakarov et al., 2019; Dick et al., 2022; Gibbings et al., 2017; Schyns et al., 2019). Cluster 7's signature was unique to replicate B1, and this cell grouping too was not formally identified; though, this population clearly expressed interferon-inducible genes (*Ifi2, Ifi3, Ifi47*, etc.) and thus was provisionally labelled *"Ifi-"* cells. Finally, in replicate B1, the transcriptional signature of Cluster 9 (resistin-like gamma, *Retnlg,* calprotectin, *S100a8/9*) implied that neutrophils represented a minor portion of the dataset (0.64%). This population corresponded to Cluster 7 in replicate B2 (2.17%). Neutrophils were unanticipated and may reflect a small population of cells that express CD64, and their signature does not appear to be artifact (Cohen et al., 2018; Jaitin et al., 2019).

Overall, seven clusters in biological replicate B2 were represented among the nine in B1. Both replicate libraries contain transcriptionally-defined populations of cells that include monocytes, macrophages, neutrophils, and an unnamed cell type defined by *Cd300* expression. Annotations from this first-pass, composite view of CD45^{+}CD64^{+} lung cells (**Tables 4.3** and **4.4**) were informative, but several clusters lacked firm characterization. Therefore, we needed to extend our analysis of baseline replicates B1 and B2 by implementing more in-depth approaches and batch correction for improving single-cell readouts. Batch correction was necessary because the steady-state libraries B1 and B2 had slightly different transcriptional outputs by GBC and UMAP, despite their known status as biological replicates. Two populations, *"Ifi-"* cells and AM-like, were recognized by GBC only in sample B1; and replicate B2 may uniquely contain a cluster of T cells. Batch effects could be related to library size differences between replicates (*i.e.,* total number of cells or number of reads); or they may simply be a consequence of the algorithmic hyperparameters used for clustering.

Employing the integration algorithm Harmony (Korsunsky et al., 2019), we pooled biological replicates for improving the annotations for CD45^{+}CD64^{+} lung cells at baseline. Harmony identifies populations that are conserved in two or more, related single-cell libraries. If a population is not shared amongst libraries, this subset should stand out visually and statistically by UMAP and GBC. This transformation resulted in the identification of ten CD45^{+}CD64^{+} populations at steady-state, illustrated by UMAP (**Figure 4.7A**). The algorithm aligned common cell types, and no single cluster appeared to be unique to replicate B1 or B2 post-integration **(Figure 4.7B)**. Transcriptional signatures for each cluster, again, were determined with differential gene expression algorithms supported by Student's t-test (**Figure 4.7C**); and the output largely reflected observations made during independent analysis of replicates B1 and B2 (refer to **Tables 4.3 and 4.4**).

Having recalculated GBC and UMAP using 8,453 pooled steady-state cells, we identified the following populations in the merged baseline ($^{\mathbf{b}}$) dataset: TRAM (Cluster 1$^{\mathbf{b}}$, *Lpl, Car4, Spp1, Ear1, Siglecf*), *Cd14*$^{+}$ Mono (Cluster 2$^{\mathbf{b}}$, *S100a4, F13a1, S100a6, Ly6c, Ccr2, Cd14*), *Cd300* cells (Cluster 3$^{\mathbf{b}}$, *Cd300e, Cd300ld)*, MHC-II^{Hi} Mono/DC (Cluster 4$^{\mathbf{b}}$, *H2-DMb1/2, H2-Aa/Ab1/Eb1, Cd74, Cd209a*, *Tmem176a/b)*, IM (Cluster 6$^{\mathbf{b}}$, *C1qa/b/c, Folr2, Lyve1, Cd163*), plasmacytoid DC (Cluster 7$^{\mathbf{b}}$, *Ifit1/2/3, ifi44/44l/47/209/214)*, Pro-AM (Cluster 8$^{\mathbf{b}}$, *Nusap1, mki67, Ccna2, etc.*), and neutrophils (Cluster 9$^{\mathbf{b}}$, *S100a8/9, Retnlg*). Additionally, a very minor population defined by a clear lymphocyte signature (Cluster 10$^{\mathbf{b}}$, *Cd79a, Trbc2, Cd3d/e, Igkc*) was noted, suggesting that B and T cells were captured in our FACS-enriched cells. Cluster 5$^{\mathbf{b}}$ had a transcriptional readout too perplexing for identification with t-tests alone; thus we employed the Hurdle model (Finak et al., 2015) for generating more sophisticated, statistical comparisons between clusters at baseline.

Fine-tuning CD45^{+}CD64^{+} annotations at baseline by employing the Hurdle model.

Initial analysis used Student's t-tests for comparing gene expression between clusters (**Table 4.3 and 4.4**) because this method was efficient for generating 'first-pass' annotations of CD45^{+}CD64^{+} clusters, which were expected to have gene expression patterns representative of macrophages and monocytes. However, this computation makes several assumptions; and key changes in gene expression may be overlooked, affecting our ability to annotate each cluster with precision. For instance, scRNAseq count matrices contain several zero values, as it is not uncommon for one or more genes to be highly specific for one cluster and not expressed in others. These conditions are suboptimal for t-tests, which expect the comparison to yield values that follow a normal distribution. Thus Finak *et al.* (2015) introduced a Hurdle model-based approach for optimizing statistical analyses of non-normal scRNAseq data, as this two-part computation can assess significant differences in gene expression between clusters regardless of the distribution of zero or non-zero values in a dataset.

The Hurdle model analysis was particularly useful for expanding on the transcriptional phenotypes of TRAM at baseline, and we updated our annotations for integrated Clusters $8^{\mathbf{b}}$ and $5^{\mathbf{b}}$ in the process. Upon visualizing expression of quintessential, alveolar macrophage ‘markers’ like *Chil3*, *SiglecF*, *Cd11c* (Aegerter et al., 2022), in addition to those already mentioned, we noted that Clusters $5^{\mathbf{b}}$ and $8^{\mathbf{b}}$ had transcriptional characteristics that overlapped with TRAM Cluster 1 (**Figure 4.8A**) and were therefore designated alveolar macrophage subsets. In consideration of Cluster $8^{\mathbf{b}}$’s propensity to express cell-cycle genes (*Nusap1, mki67, Ccna2*; noted earlier in **Figure 4.7C**), this population was now designated to be a subset of proliferative alveolar macrophages (“pro-AM”). Cluster $5^{\mathbf{b}}$ localized in between TRAM and monocytic subsets by UMAP and expressed alveolar macrophage genes (*Chil3, SiglecF, Cd11c*), but also transcribed monocyte-associated genes like *Cd11b*, *Ccr2, F13a1,* and *Cd14* (**Figures 4.8A-B**). Thus, we posited that Cluster $5^{\mathbf{b}}$ was a population of monocyte-derived alveolar macrophages (“MoAM”); though only recently have significant differences between TRAM and MoAM been appreciated by conventional, protein-based methods (Li et al., 2022; Misharin et al., 2017). Functionally, all three of the presumed alveolar macrophage clusters demonstrated expression patterns reflective of baseline roles for fatty acid catabolism, which included expression of the adiponectin receptor 2, lipase A, and lipoprotein lipase (*Adipor2, Lipa, and Lpl,* respectively*;* **Figure 4.8C**). Additional genes that were expressed prominently in these clusters included enzymes associated with tissue remodeling, such as cathepsins, metalloproteases and protease inhibitors (*Ctsd, Mmp19, Slpi).* Indeed, nearly all genes visualized were expressed most prominently by TRAM Cluster $1^{\mathbf{b}}$, but also noted in Cluster 8^{b} (pro-AM) and Cluster 5^{b} (MoAM).

One surface-associated marker, *Cd9*, was appreciated for having relatively specific expression among all three putative alveolar macrophage clusters (**Figure 4.8A**). This surface tetraspanin was noted because it may serve as a technically feasible and abundant protein marker for studying this cell type with protein-based approaches downstream.

The Hurdle model statistics were also used to extend our analysis of IM at baseline, which was the preliminary classification for Cluster $6^{\mathbf{b}}$ in the merged baseline dataset (**Figure 4.9**). Currently, the consensus is that three IM subpopulations occupy the lung parenchyma at baseline at levels of about one-tenth or less the numbers of AM (Chakarov et al., 2019; Dick et al., 2022; Gibbings et al., 2017; Schyns et al., 2019). Because of the inherently low numbers of IM at baseline, we did not capture enough IMs to resolve three unique subsets among $CD45^{+}CD64^{+}$ cells at baseline with graph-based clustering. Based on these reports, however, we identified IMs in our dataset for expression of *C1qa,* MHC-II-related genes (i.e., *Cd74*), *Folr*2, and *Lyve1* (**Figure 4.9A**)*.* An additional gene encoding a lysosomal-associated tetraspanin, *Cd63,* was noted among top ranked features because expression of this gene appeared to be relatively specific to IM at baseline (**Figure 4.8B**). Some transcriptional overlap may exist for *Cd63* in terms of IM and TRAM; but TRAM are also enriched for expression of the tetraspanin *Cd9*, whereas IM are not (refer to **Figure 4.8A**). Thus we speculated that *Cd63* could serve as another surface marker for interrogating IM and AM subtypes downstream with protein-based approaches. Interestingly, both CD63 and CD9 are associated with extracellular vesicle production (Termini and Gillette, 2017) – a function that may be relevant to understanding macrophage immunology post-elastase. Based on relative population size, localization in UMAP space, and differential gene expression readouts, it was concluded that, at baseline, Cluster $6^{\mathbf{b}}$ represented IM.

Lastly, once applied to comparisons within our Harmonized dataset, the Hurdle model aided in re-classifying the cell population noted initially for interferon-inducible transcription (*"ifi-"* cells). Cluster $7^{\mathbf{b}}$ was now thought to represent plasmacytoid dendritic cells ("pDC"; **Figure 4.10**). This decision was made by comparing Cluster $7^{\mathbf{b}}$ to others in the dataset directly, specifically TRAM and *Cd14*$^{+}$ Mono, which revealed enriched transcription of hallmark pDC genes *Bst2*/*Cd317* and *Irf7* (Ning et al., 2011; Reizis, 2019).

In summary, the multistep annotation process of the baseline samples provided a detailed cluster map of the CD45^{+}CD64^{+} cell populations. As anticipated, **t**issue **r**esident **a**lveolar **m**acrophages (**TRAM**) were readily identifiable; and two minor subsets of **a**lveolar **m**acrophages were also noted - one subset with markers for **pro**liferation (**pro-AM**), and another that may be derived from bone marrow **mo**nocytes (**MoAM**). We also identified a large **mono**cytic cluster (***Cd14***$^{+}$ **Mono),** as well as **I**nterstitial **M**acrophages (**IM**), which are thought to be monocyte-derived. An **MHC-II**$^{\mathbf{Hi}}$ **mono**cyte cluster may exist as well, or this population may represent dendritic cells (**DC**), considering a heterogenous transcriptional profile consistent with both cell types. We also identified **neutrophils**, as well as a relatively minor population of myeloid cells that remained unclassified, but uniquely expressed genes like ***Cd300e*** or ***Cd300ld*** at baseline. Finally, **P**lasmacytoid

dendritic **c**ells (**pDC**, initially *"ifi-"* cells) were identified with canonical genes *Bst2*/*Cd317* and *Irf7,* and a mixed population of lymphocytes (**B/T cells**) was also recognized. Upon establishing the composition of the CD45$^+$CD64$^+$ cells at baseline, the next step was to carry out a similar analysis pipeline for the transcriptional profiles of CD45$^+$CD64$^+$ cells isolated on days 7 and 21 to determine if novel subsets of myeloid cells emerge in the lung post-elastase.

Transcriptomic analysis of CD45$^+$CD64$^+$ lung cells at day 7 in EIEE.

Single-cell libraries from diseased mice were independently filtered and normalized. Analysis of steady-state lungs had set the expectation that TRAM, IM, monocyte, neutrophil, lymphocyte, and dendritic cell subsets comprised the CD45$^+$CD64$^+$ myeloid compartment of the lung. We anticipated that several clusters noted at baseline would undergo transcriptional inflammation-induced changes over time that reflected their biological response to elastase challenge. If true for our model, new cell subsets should be recognizable initially at day 7 and persist through day 21.

As outlined for the control baseline samples, the transcriptional data from day 7 were first assessed independently and then replicates (single-cell libraries **7a** and **7b**) were integrated with Harmony. Annotation of the cells from the challenged lungs was UMAP-guided and supported statistically with graph-based clustering and differential gene expression analysis. For this timepoint, 11,845 pooled cells that had passed single-cell QA/QC were represented by 11 graph-based clusters (**Figure 4.11A**). Differential gene expression analysis was carried out for determining how these eleven graph-based clusters at day 7 post-elastase compared to the ten myeloid populations annotated at baseline. The following cell types were re-identified: **TRAM, *Cd14*$^{+}$ Mono, MHC-II$^{\mathbf{Hi}}$ Mo/DC, pDC, IM, *Cd300* cells, neutrophil, pro-AM, T/B cells**. Two clusters were 'novel' at day 7 ($^{\mathbf{d7}}$) compared to baseline. First, graph-based clustering resolved a small dendritic cell-like population (Cluster 10$^{\mathbf{d7}}$) near the conserved MHC-II^{HI} monocyte/DC population, or Cluster 3$^{\mathbf{d7}}$. Cluster 10$^{\mathbf{d7}}$ (denoted **'*Slamf7*$^{+}$ DCs'**; **Figure 4.11B**). was characterized for expression of genes encoding the immune signaling molecule *Slamf7,* DC-SIGN (*Cd209a*), the DC-specific transmembrane protein *Dcstamp*, and the receptor for IL-33 (*St2*). This phenotype was intriguing and, based on recent reports, is associated with pro-inflammatory events in the lung (Simmons et al., 2022; Wu et al., 2023).

The additional population noted at day 7, Cluster 4$^{\mathbf{d7}}$, was arguably more relevant to our outstanding hypothesis because this **"Trans-AM"** population shared features with alveolar macrophages while clustering independently from the conserved TRAM/Cluster 1$^{\mathbf{d7}}$ and pro-AM/Cluster 8$^{\mathbf{d7}}$ cells by UMAP (**Figure 4.11A**). The Trans-AM/Cluster 4$^{\mathbf{d7}}$ did not strongly resemble MoAM/Cluster 5^{b}, which was the third AM-like cluster identified previously at baseline, but not identifiable at day 7. While Trans-AM had modest expression levels of *Chil3*, *Cd9,* and *Cd63* (**Figure 4.11C**), differential expression analysis suggested that Trans-AM were relatively enriched for expression of genes associated with cellular catabolism and tissue-remodeling, such as *Ecm1* (extracellular matrix protein 1)*, Ctsl* (cathepsin L)*, Pdpn* (podoplanin)*,* and *Trem2* (triggering receptor expressed on myeloid cells 2; associated with chronic inflammation – **Figure 4.11D**). *Mmp12,* which is a well-known lung macrophage-derived remodeling protease associated with chronic lung damage (Chen et al., 2011; Hautamaki et al., 1997; Shibata et al., 2018) was enriched in Trans-AM cells and others at day 7 (Clusters 1^{d7}, 5^{d7}, 10^{d7}; **Figure 4.11E**). In search of a novel surface marker for flow cytometry-based validation and possible sort-enrichment of Cluster 4^{d7}, expression of *Cd93* (encoding the complement C1q receptor) was noted (**Figure 4.11F**). Though not a macrophage marker *per se*, *Cd93* was found to be expressed by a putative AM cluster in a recent report (Yu et al., 2017). Also noted at this time point, *Cd63* expression was now highly prevalent in Cluster 4^{d7} and Cluster 1^{d7} at levels comparable to that of IM (**Figure 4.11C**), which was not previously observed at baseline.

Overall, Cluster 4^{d7} might be a novel, *transitional* cell population (hence **Trans-AM**) which may explain an expression profile that overlapped with various myeloid subsets post-elastase. Alternatively, Trans-AM could be a newly recruited cell population or a reprogrammed subset of MoAM responding to tissue damage and poised for tissue-remodeling. Having identified a cluster with a transcriptional potential to drive aberrant wound healing in the post-elastase lung, the goal was to assess whether this phenotype was preserved in lungs collected at day 21 in EIEE.

Transcriptomic analysis of $CD45^+CD64^+$ lung cells at day 21 in EIEE.

Adhering to our computational strategy, we scrutinized the day 21 samples independently and then integrated the replicates for improving resolution at this timepoint. For day 21 post-elastase, 11,432 pooled cells that had passed single-cell QA/QC were represented by 11 graph-based clusters (**Figure 4.12A**). The following cell types at day 21 (^{d21}) were re-identified: **TRAM, *Cd14*$^+$ Mono, MHC-II^{Hi} Mo/DC, *Slamf*$^+$ DC, pDC, IM, *Cd300* cells, neutrophil, pro-AM, T/B cells**. An alveolar macrophage-like population was observed (Cluster 5$^{\mathbf{d21}}$), and this population localized directly adjacent to the TRAM/Cluster 1^{d21} in UMAP space. The expression profile of Cluster 5$^{\mathbf{d21}}$ strongly resembled that of baseline MoAM/Cluster 5$^{\mathbf{b}}$ (refer to **Figure 4.8A-B**) more than what we observed for Trans-AM/Cluster 4$^{\mathbf{d7}}$ during acute stage of EIEE (refer to **Figure 4.11C-F**). In fact, the gene markers used for defining Trans-AM/Cluster 4$^{\mathbf{d7}}$ at day 7 (*Ecm1, Pdpn, Cd93*) were now enriched within TRAM/Cluster 1$^{\mathbf{d21}}$ by UMAP (**Figure 4.12B**). It is possible that, from day 7 to day 21, Trans-AM (Cluster 4$^{\mathbf{d7}}$) experienced additional transcriptional changes, adopting a TRAM-like phenotype over time. Or, if Trans-AM exist at day 21, samples collected for our study may lack sufficient cells for independent clustering in our analysis.

Integrated single-cell atlas illustrating the CD45$^+$CD64$^+$ lung myeloid compartment across timepoints in EIEE.

In a final attempt to identify 'novel' cell populations that arise in the post-elastase lung, an alternate strategy was employed by combining **all six** libraries with Harmony (31,730 cells total) and recomputing UMAP and GBC (**Figure 4.13A-B**). We still anticipated that Trans-AM (Cluster 4$^{\mathbf{d7}}$) could be re-identified post-integration, and that this presumably tissue-destructive population would persist in the lungs by 21 days post-elastase. First, **TRAM, *Cd14*$^+$ Mono, *Cd300* cells, IM, pDC, neutrophil, pro-AM, and B/T cells** were each reidentified in the Harmonized dataset (**Figure 4.13C**). Upon merging every timepoint from our study ($^{\mathbf{ALL}}$), Cluster 5$^{\mathbf{ALL}}$ had hallmarks of both Trans-AM/ Cluster 4$^{\mathbf{d7}}$ and MoAM/Cluster 5^{b} (**Figure 4.13D**). This style of analysis also resulted in a **Mixed DC** cluster, which included both *Cd209a*$^+$*Slamf7*$^+$ and *Cd209a*$^+$*Slamf7*$^-$ DCs (**Figure 4.13E**).

With dendritic cells now clustering independently in the dataset, the **MHC-II^{Hi}** myeloid population observed several times during this analysis was thought to be comprised only of monocytes. The twelfth harmonized cluster was difficult to annotate, requiring several differential gene comparisons for identifying genes that were uniquely expressed. This population was transcriptionally consistent with *Cd300* cells but had significantly more expression of MHC-II-related genes (**data not shown**). A gene encoding the long non-coding RNA termed ***Gm26917*** was used to identify this population from others in the dataset (**Figure 4.13F**). The significance of this extremely minor cell population generated by harmonizing the dataset is unknown.

Unsatisfied with our annotation of Cluster 5^{ALL} (Mo-/Trans-AM), we filtered the harmonized dataset once more for the purpose of improving resolution of several populations. We retained the following cell types for conducting differential comparisons of clusters illustrated in UMAP space: **TRAM, *Cd14*$^{+}$ Mono, pro-AM, and Cluster 5^{ALL}** (**Figure 4.14A**). By this approach, Cluster 5^{ALL} was, again, nominally split between two potentially related AM-like clusters: *Cd93*$^{+}$ Trans-AM and MoAM (**Figure 4.14B**). *Cd93*$^{+}$ Trans-AM appear to be most prominent at day 7 in EIEE.

For the remainder of our analysis, we were interested in conducting in-depth analysis of *Cd93*$^{+}$ Trans-AM/Cluster 4^{d7}, validating their existence by flow cytometry. However, despite multiple attempts to optimize the reactions, we did not reproducibly identify CD45^{+}CD64^{+}CD93^{+} cells at day 7. Given our lack of ability to validate the presence of *Cd93*$^{+}$ Trans-AM/Cluster 4^{d7} cells, we focused on two clusters from the harmonized dataset – tissue resident alveolar macrophages (TRAM) and interstitial macrophages (IM)

– to address the following, modified hypothesis: *cells within the TRAM and IM clusters undergo modest but significant transcriptional changes to become pathogenic cells that mediate progressive lung damage*. We updated our hypothesis because, clearly, CD45$^+$CD64$^+$ cells are largely conserved over time post-elastase. Rather than searching for 'novel' cell types, the goal now was to assess intra-cluster transcriptional changes in EIEE. Sustained, transcriptional perturbations in conserved cell types could be a signature of dysregulation in the post-elastase lung. Akin to the potentially tissue-destructive phenotypes observed for fibroblasts in **Chapter 1**, we expect that several genes affected over time in conserved cell types will relate to processes of tissue repair or remodeling in the lung.

First, we validated an IM phenotype recently reported by Shibata and colleagues (2018). Early in our study, we recapitulated this group's quantitative observations of IM dynamics in the post-elastase lung (refer to **Figure 4.2**). Further, Shibata *et al.* identified a putative *Mmp12*$^+$ 'pathogenic' IM subset, which was also identifiable in our Harmonized single-cell dataset (**Figure 4.15A**). Because of the technical limitations of our single-cell approach, it was difficult to state whether these *Mmp12*$^+$ IM*s* persist in relevant quantities over time, limiting our ability to speculate how they might contribute to disease progression. Though, *Mmp12*$^+$ IM may be enriched for MHC-II-related expression (i.e., *Cd74*$^{\mathrm{HI}}$) and negative for *Folr2* expression – genes previously mentioned for characterizing IMs at baseline (refer to **Figure 4.9A**). We also noted two transcriptional trends highly relevant for IM function in lungs after elastase challenge. First, we noted that *Cd74*$^{\mathrm{LO\text{-}MID}}$*Folr2*$^+$ IMs are major expressors of *Timp2*, the protein largely responsible for inhibiting degradative metalloproteases like *Mmp12* in the lung (**Figure 4.15B**). Next, we noted that the same *Cd74*$^{\text{LO-MID}}$*Folr2* portion of the IM cluster was highly enriched for *Ccl2* (**Figure 4.15C**), which is a chemoattractant for recruiting monocytes at the site of injury. TRAM, shown in each panel for comparison, do not express relevant levels of *Timp2* or *Ccl2*. These dynamics were intriguing, especially if validation shows that they are specific for *Cd74*$^{\text{LO-MID}}$*Folr2*$^{+}$ IMs as opposed to *Cd74*$^{\text{HI}}$*Mmp12*$^{+}$ IMs.

CD9^{+}CD63^{+} TRAM Dynamics in EIEE.

TRAM was the largest cluster at baseline and was conserved over time in the EIEE model. As before, we used differential gene expression analysis for identifying networks relevant to changes in TRAM biology in the lung post-elastase. There is substantial evidence in the literature that AMs produce *Mmp12* in COPD lungs (Chen et al., 2011; Hautamaki et al., 1997). Expression of *Mmp12* was noted in AMs at baseline and may increase over time in the EIEE model, based on the Harmonized UMAP (**Figure 4.16A**). More intriguing were the dynamics of transcripts encoding cathepsin K (*Ctsk*) and the lysosomal membrane-associated tetraspanin CD63 (*Cd63*). Expression of *Ctsk* drastically increased post-elastase and was sustained by day 21 (**Figure 4.16B**). Though initially considered to be a marker for IM at baseline (refer to **Figure 4.9B**), *Cd63* upregulation in TRAM was previously observed at day 7 in EIEE (refer to **Figure 4.11C**). Importantly, high expression levels were sustained by TRAM at day 21 (**Figure 4.16C**).

CD63 has perceived functional significance, especially in the context of CD9, which TRAM also express (refer to **Figure 4.11C**). CD9 and CD63 are tetraspanins and among the most abundant proteins found on the surface of extracellular vesicles, which faciltate cell-cell communication and delivery of secreted factors (Termini and Gillette, 2017). We validated expression for CD9 and CD63 by alveolar macrophages at the protein level, first by applying a ‘conventional’ gating strategy formalized by Svedberg *et al.* (2019) and identifying total CD45$^+$CD64$^+$MerTK$^+$ macrophages in the lung. Surface expression of CD63 and CD9 on SiglecF$^+$CD11b$^-$ alveolar macrophages at day 21 in EIEE is summarized in **Figure 4.17** (gating strategy) and **Figure 4.18A-B** (results from N=2 independent experiments). At baseline, alevolar macrophages may express some degree of CD63 protein on their surface; however, these cells clearly upregulate expression of this tetraspanin by day 21 in EIEE, determined qualitiatively by flow cytometry and quantitatively by calculating the median fluorescence intensity (MFI) of alveolar macrophages stained with anti-CD63 antibody. Altogether, expression of both CD9 and CD63 by alveolar macrophages was validated at the protein level, which may begin to explain a role for TRAM in the post-elastase lung.

Discussion

The goal of this study was to identify myeloid subsets that drive the progressive lung destruction observed in the EIEE model. The analysis of the scRNAseq data derived from $CD45^+CD64^+$ cells isolated from the lungs at days 0, 7, and 21 lead to the following conclusions:

- At baseline, the $CD45^+CD64^+$ cells from the lungs of BALB/cJ mice could be resolved into 10 clusters with ~42% identified as tissue resident alveolar macrophages (TRAM/Cluster 1^b), ~4% identified as interstitial macrophages (IM/Cluster 6^b), and ~36% identified as monocytes or monocyte-derived subsets (Clusters 2^b, 3^b, 4^b, among others).
- Independent analysis of single-cell libraries representing mice with EIEE revealed 'novel' clusters post-challenge at day 7 (Cluster $4^{\mathbf{d7}}$/Trans-AM & Cluster $10^{\mathbf{d7}}$/*Slamf7*$^+$ DCs) and at day 21 (Cluster $7^{\mathbf{d21}}$/*Slamf7*$^+$ DCs), meaning these populations were not identifiable during independent analysis of baseline replicates. These findings supported the hypothesis that new, potentially pathogenic subsets of myeloid cells occupy lungs undergoing progressive emphysematous changes. Despite these findings, the expression profiles of the cells that comprised these novel subsets did not provide sufficient information to designate one subset as transcriptionally 'pathogenic.'

- Integration of all six libraries (baseline, day 7, and day 21 replicates) implied that several clusters in UMAP space were conserved over time in the EIEE model. We noted significant expression trends within the TRAM and the IM clusters that could be indicative of a cell type with 'pathogenic' potential in the emphysematous lung.
- While the scRNAseq approach holds promise as a strategy for identifying subsets of cells that mediate progressive lung damage, we must revise the experimental design to allow for more replicates, cells, and time points to gain a higher resolution mapping of cell dynamics and fate during EIEE pathogenesis.

The advent of scRNAseq has facilitated discovery of novel macrophage phenotypes at baseline and in diverse model systems employed for studying inflammation (Aran et al., 2019; Dick et al., 2022; Evren et al., 2021; Li et al., 2022; Mould et al., 2019; Pisu et al., 2021; Ural et al., 2020; Xu-Vanpala et al., 2020). At the same time of our study, this approach was being used to study lungs of mice and humans affected by COPD (Li et al., 2021; Liegeois et al., 2022; Rao et al., 2020; Sauler et al., 2022). Previous reports have used CD45$^+$ alone for enrichment of lung immune cells prior to scRNAseq (Cohen et al., 2018; Sauler et al., 2022; Xu-Vanpala et al., 2020), which certainly resulted in reasonable detection of lung macrophages within single-cell landscapes; but these datasets were also dominated by lymphocytes which resulted in a sub-optimal sampling of the macrophage/monocyte compartment. We chose to cast a moderately wide net prior to sequencing by FACS-enriching cells for CD45$^+$CD64$^+$ surface protein expression, which largely eliminated lymphocytes while avoiding biases that come from sorting with macrophage-specific markers (*i.e.,* CD11b SiglecF, CD11c, MerTK). Others have used macrophage-specific gating as an effective means for studying these cell types at baseline (Chakarov et al., 2019; Schyns et al., 2019; Ural et al., 2020; Yao et al., 2020); but since we were interested in comparing dynamics in healthy and diseased mice, it was unknown whether steady-state markers would be useful for analyzing macrophages post-elastase. Ultimately, our gating strategy captured enough cells and reads for interpreting macrophage biology at single-cell resolution while leaving room for discovery of novel, phagocytic populations.

Perhaps no standardized, single-cell RNA sequencing workflow exists, but most pipelines begin with QA/QC of raw data (Andrews et al., 2021; Stegle et al., 2015). We too initiated analysis in this manner and were pleased with the outcome, as we deemed scRNAseq to be a technical success. During single-cell QA/QC, we likely could have excluded proliferating cells from the dataset to improve clustering, similar to how we eliminated cells perceived to be dead or undergoing apoptosis. At single-cell resolution, proliferating cells are sometimes classified as an additional source of noise, or unwanted variation within a dataset (Buettner et al., 2015). Proliferating cells can be removed by enriching for cell-cycle genes, similar to how we identified and filtered out dead cells based on high %mito, among other metrics (Ilicic et al., 2016). We opted to keep dividing cells in our dataset, leading to the identification of **Pro**liferating **A**lveolar **M**acrophages (**Pro-AM**) as the only cluster with enrichment of cell cycle genes in each library. A presumed subset of **T**issue **R**esident **A**lveolar **M**acrophages (**TRAM**) in our dataset, the existence of Pro-AM in all six libraries makes biological sense, as alveolar macrophages have been previously shown to self-renew at baseline and after lung injury (Hashimoto et al., 2013; Yona et al., 2013). Quantitatively, Pro-AM were minor relative to TRAM, which was the largest cluster in our dataset.

Monocyte-derived **A**lveolar **M**acrophages (**MoAM**) were identified as another subset of TRAM at several stages of this analysis, consistent with new reports that point to alveolar macrophage differentiation from bone-marrow monocytes as an additional mechanism for regeneration post-injury (Li et al., 2022; Misharin et al., 2017). In the libraries which they were present, MoAM were similar to TRAM but may retain expression of several monocyte-related genes (*i.e., Ccr2 and Cd14)*. Beyond phenotypes expected for alveolar macrophages (*i.e.*, expression of *Cd11c, Siglecf, Chil3/Ym1),* lipid catabolism genes were also expressed by TRAM, Pro-AM, and MoAM at baseline. By day 7 in EIEE, a transcriptional subset of alveolar macrophage that was poised for tissue-remodelling may exist in the lung (denoted "Trans-AM" throughout). Upon integration of all six libraries, however, graph-based clustering had grouped MoAM and Trans-AM into one, alveolar macrophage-like population (Cluster $5^{\mathbf{ALL}}$). Ultimately, we were unsuccessful at validating the existence of $CD93^+$ Trans-AM with flow cytometry for several reasons. These validation experiments were carried out on cells isolated at day 21 based on a preconception that *Cd93*$^+$ macrophages would persist through later timepoints in EIEE. Given what we know now about the dynamics of the $CD45^+CD64^+$ cells, I should have looked earlier at day 7 when this cell type is apparently more abundant, according to our scRNAseq results.

We eventually focused on validating translation of *Cd63* and *Cd9 by* alveolar macrophages. We confirmed that CD63 and CD9 were co-expressed on the surface of alveolar macrophages at day 21 in EIEE using flow cytometry. We posit that if CD9$^+$ alveolar macrophages are upregulating CD63 post-elastase, this dual expression may have functional implications regarding extracellular vesicle (EV) production in diseased lungs. The biology of EVs is an emerging topic in chronic disease immunology, as extracellular vesicles are thought to be vehicles for molecules like cytokines, chemokines, proteases, miRNA, and growth factors (Termini and Gillette, 2017). The surface of EVs are covered in tetraspanins CD9 and CD63, alluding to a potential mechanism for the CD9$^+$CD63$^+$ subset of alveolar macrophages. Significant, dual expression of these tetraspanins has been confirmed on lipid-associated macrophages that contribute to remodeling of adipose tissue (Hill et al., 2018; Jaitin et al., 2019). From our own analysis, we posit that expression of enzymes like *Mmp12* and *Ctsk* may be part of the cargo of extracellular vesicles produced by CD9$^+$CD63$^+$ alveolar macrophages in EIEE pathogenesis. Each were differentially expressed over time in EIEE, though this result was more visually apparent for *Ctsk*. Cathepsins, in general, are known for breaking down celluar or tissue-derived macromolecules, and *Ctsk* specifically has recently been scrutinized for its degradative potential in the lung (Fabrik et al., 2022). As mentioned, *Mmp12* has a perceived, historical signficance and association with driving emphysema (Chen et al., 2011; Hautamaki et al., 1997; Spix et al., 2022).

Even with expression of these degradative enzymes, I do not propose that CD9$^+$CD63$^+$ alveolar macrophages are solely responsible for driving emphysema. In light of several, cellular and molecular phenotypes discussed herein, EIEE pathogenesis may be explained by a network of dysregulation – one driven, possibly, by several cell types like those identified in our atlas. In addition to alveolar macrophages, we scrutinized intersitial macrophages during our analysis. In general, the study of IM biology in the lung and other organs had exploded since Shibata and colleagues (2018) first presented evidence implicating *Mmp12*$^{+}$ IMs as mediators of lung destruction in experimental emphysema. Beyond this description, this IM phenotype lacked depth. Only one group at the time (Gibbings et al., 2017) had applied next-generation approaches for studying lung IM biology. Using CD11b, CD11c, and MHC-II to sort-purify three lung IM populations, this group applied whole transcriptome sequencing for gaining functional insight about each subset at baseline. The IM transcriptional profiles published by Gibbings and colleagues (2017) were largely validated with single-cell landscapes generated by independent groups (Chakarov et al., 2019; Dick et al., 2022; Schyns et al., 2019; Ural et al., 2020). Collectively, these scRNAseq experiments suggested that markers like *Folr2, Lyve1, MHC-II* and/or *Ccr2*, when used together, are optimal for studying three IM subsets that occupy unique microenvironmental niches in murine lungs. Functionally, IM subsets were speculated to be immunomodulatory, or regulatory cell types. MHC-II$^{\text{MID-HI}}$ IMs are thought to have superior anti-inflammatory potential due to interactions with regulatory T cells, but MHC-II$^{\text{LO}}$Folr2$^{\text{HI}}$ IMs produce more IL-10 overall and may help reduce severity of bleomycin-induced lung fibrosis (Chakarov et al., 2019). This novel interpretation of IM biology was contrary to the *Mmp12*$^{+}$ ‘pathogenic’ IM readout proposed by Shibata *et al.* (2018). However, we provide transcriptional evidence supporting this group's efforts, as we identified an *Mmp12*$^{+}$ IM subset that localized tightly with the MHC-II$^{\mathrm{HI}}$, Folr2$^{\mathrm{LO}}$ portion of the IM cluster from our finalized UMAP. On the other hand, the MHC-II$^{\mathrm{LO}}$, Folr2$^{\mathrm{HI}}$ IM cluster may be potent expressors of *Timp2,* a metalloprotease inhibitor, and *Ccl2,* a macrophage chemoattractant. This could be relevant for interpreting EIEE pathogenesis. Now armed with transcriptional and protein-based evidence (Shibata et al., 2018) suggesting that MHC-II$^{\mathrm{Hi}}$*Mmp12*$^{+}$ IMs occupy the post-elastase lung, we devised a theory that this 'pathogenic' subset plays a competing role with MHC-II$^{\mathrm{LO}}$*Folr2*$^{\mathrm{HI}}$*Timp2*$^{+}$ IMs in the lung, as emphysema for years has been understood to be a consequence of protease:anti-protease imbalance in the lung. Dominant *Ccl2* expression by the MHC-II$^{\mathrm{LO}}$*Folr2*$^{\mathrm{HI}}$*Timp2*$^{+}$ IM subset may also represent a biological need for recruiting additional IMs from the bone marrow post-elastase; perhaps, this pattern could reflect an example of dysregulation in our model. In either case, IM biology needs to be investigated further, as we support observations made by Shibata and colleagues (2018) and offer more perspective for how these cells behave post-elastase.

For this entry-level study, the decision was made to manually annotate cell clusters from each single-cell library, though we had considered using an unsupervised or referenced-based approach. Machine-learning algorithms like SingleR have been used to perform unbiased cell recognition and identification of macrophage subtypes in single-cell libraries (Adams et al., 2020; Aran et al., 2019). We still deem that relying on an informed bias from the literature and annotations from modern single-cell reports was appropriate for defining the clusters in the EIEE model. In addition to macrophages, we identified several monocytic clusters. The largest were ***Cd14***$^{+}$ monocytes, though **MHC-II**$^{\mathbf{HI}}$ monocyte numbers also were substantial across timepoints in EIEE. We then identified ***Cd300***$^{+}$ monocytes within our dataset, which is similar to the signature of monocyte subsets identified previously at single-cell resolution (Villani et al., 2017; Zilionis et al., 2019), thus confirming their association with *Cd14*$^{+}$ and MHC-II^{Hi} monocytes cluster. *CD300* encodes a surface-associated protein found on monocytes and lymphocytes that plays roles in regulating innate immune signaling molecules have been discussed for their immunoregulatory potential (Borrego, 2013). There are no known reports that define the functional role for *Cd300*-expressing monocytes in healthy or diseased lungs. Given that we observed abundant *Cd300* monocytes in all six replicates, this cell type is probably relevant and should be investigated further, starting with basic validation to support that its transcriptome is reflected at the protein level.

From a cell discovery standpoint, perhaps we were rewarded using our broader gating strategy, as we captured an intriguing population denoted ***Slamf7***$^{+}$ dendritic cells (DC). This unique subset was resolved during independent analysis of day 7 and day 21 libraries but was not apparent at baseline. In the final representation of the Harmonized dataset, they fell into the “Mixed DC” cluster. The *Slamf7*$^{+}$ subset expressed DC gene sets that included *Cd209a* (DC-SIGN), *Dcstamp*, and *Tmem176a/b.* In the merged representation, we also noted that *Slamf7*$^{+}$ DCs were an enriched source of *Mmp12* in the dataset, which was unexpected; and this subset may be the only cell type among CD45^{+}CD64^{+} cells to express relevant *St2* levels in EIEE. We chose *Slamf7* as the identifier for this population, but we are not entirely sure how this relates to any potential function in EIEE. *Slamf7* has emerged recently in the literature for its expression by macrophages and cancer cells and for involvement in pathways that include phagocytosis, regulation of interferon genes, and immune cell activation (He et al., 2019; O'Connell et al., 2019; Simmons et al., 2022).

Additionally, we found **p**lasmacytoid **d**endritic **c**ells (**pDC**) in our dataset, though we did not explore their biology in detail. **Neutrophils** were identified for expression of *Csf3r, S100a8/9, Retnlg,* and *Mmp9.* Their presence was entirely unexpected, as we had excluded conventional Ly6g$^+$CD64$^-$ neutrophils by FACS. However, several groups have pointed out similar transcriptional signatures for neutrophils at single-cell resolution in the lung and other organs (Cohen et al., 2018; Jaitin et al., 2019). Lastly, and since they were so minor in our dataset, we were comfortable annotating **T/B cells** based on common knowledge of their expression of genes like *Trbc2* (t cell receptor beta) and *Igkc* (kappa light chain). Evidently, none of our resources could solve the mystery of Cluster 12$^{\mathbf{ALL}}$ in the final representation of the data, which was enriched for a long noncoding RNA *Gm26917.* Unfortunately – and true for several interpretations at this molecular and cellular resolution – ***Gm26917* cells** could be real or just artifact, as non-coding transcripts have also been associated with noise in single-cell datasets (Ilicic et al., 2016).

An obvious gap in this study is that we were unable to validate the functional significance of CD9$^+$CD63$^+$ alveolar macrophages in driving pathology of EIEE. We merely proved evidence for the existance of this cell type in the post-elastase lung. Our studies fell short at the protein level when charaterizing other cell types, too, such as the intriguing expression profiles noted for IMs in our study. Ultimately, we will prioritize adoptive transfer models as the method for exploring a caustive role for any cell type perceived to be 'pathogenic' in EIEE. The goal is to transfer the candidate tissue-destrutive cells into *Rag2*$^{-/-}$*γc*$^{-/-}$ mice that are resistant to progressive disease in in the EIEE model (refer to **Chapter 3**). To supplement this *in vivo* approach, we also devised a strategy for plating extracellular matrix proteins in tissue-culture dishes for testing the degradative abilities of 'pathogenic' cell types like CD9^{+}CD63^{+} alveolar macrophages. In theory, this technique may reveal quantitative differences in the ability of CD9^{+}CD63^{+} alveolar macrophage to degrade extracellular matrix proteins relative to CD9^{+} alveolar macrophages in the same assay, which are found primarily in naïve BALB/cJ lungs and not diseased mice. Finally, we also plan to re-characterize the 'pathogenic' signature of CD9^{+}CD63^{+} alveolar macrophages at the transcriptional level with bulk RNAseq studies. Despite being the largest cluster in our single-cell dataset, enrichment of CD9^{+}CD63^{+} alveolar macrophages by FACS, followed by bulk RNA-seq, could reveal novel expression patterns that were overlooked during our analysis. Further, enrichment studies will help corroborate the significance of transcriptional readouts that are difficult to measure at the protein level, such as changes in *Ctsk* and *Mmp12* over time in CD9^{+}CD63^{+} alveolar macrophages.

Ultimately, the future of scRNAseq will depend heavily on robust functional validation of transcriptional phenotypes. Several groups have already extensively scrutinized and validated interstitial macrophage biology at baseline with next-generation approaches. Now, the same must be done for studying alveolar macrophages, and both cell types need to be dissected at high molecular resolution in diverse, inflammatory contexts. Certainly, the in-house approach that our lab designed for studying EIEE with scRNAseq and flow cytometry can be applied to several other models for the discovery of novel or, evidently, conserved cell types that contribute to chronic-progressive diseases like emphysema.

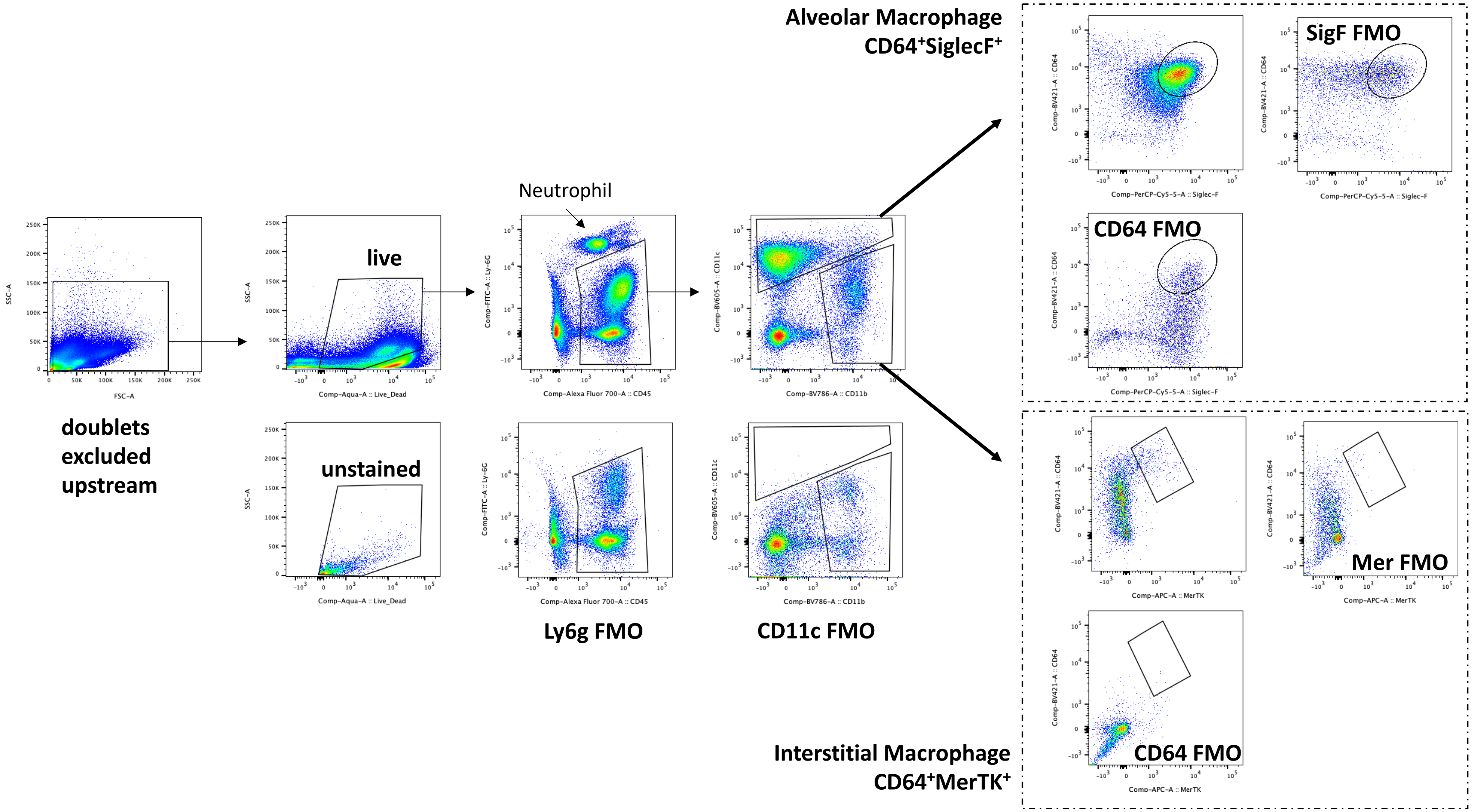
doublets excluded upstream
live
unstained
Neutrophil
Ly6g FMO
CD11c FMO
Alveolar Macrophage
CD64⁺SiglecF⁺
SigF FMO
CD64 FMO
Interstitial Macrophage
CD64⁺MerTK⁺
Mer FMO
CD64 FMO
SSC-A
FSC-A
Comp-Aqua-A :: Live_Dead
Comp-FITC-A :: Ly-6G
Comp-Alexa Fluor 700-A :: CD45
Comp-BV605-A :: CD11c
Comp-BV786-A :: CD11b
Comp-BV421-A :: CD64
Comp-PerCP-Cy5-5-A :: Siglec-F
Comp-APC-A :: MerTK

Figure 4.1. Gating strategy used for identifying alveolar and interstitial macrophagesin EIEE.

Cells from one, naïve murine lung are illustrated here for demonstrating gating of, specifically, alveolar and interstitial macrophages, by flow cytometry. Live (Aqua^{-}), CD45^{+}Ly6g^{-} myeloid cells were discriminated based on relatively dichotomous expression of CD11c and CD11b. Mature CD11c^{+} alveolar macrophages are known to express CD64 and SiglecF. CD11b^{+} interstitial macrophages, which do not express SiglecF or nearly as much CD11c as their alveolar counterparts, can be identified with CD64 and MerTK. This illustration was generated from a larger experiment, repeated twice, in which cellular dynamics were compared across timepoints in EIEE (day 4, 7, 14, and 21), in biological triplicate and relative to PBS controls. Samples were acquired on a LSR-II (Becton Dickinson). For gating, samples were compared directly to fluorescent minus one (FMO) controls.

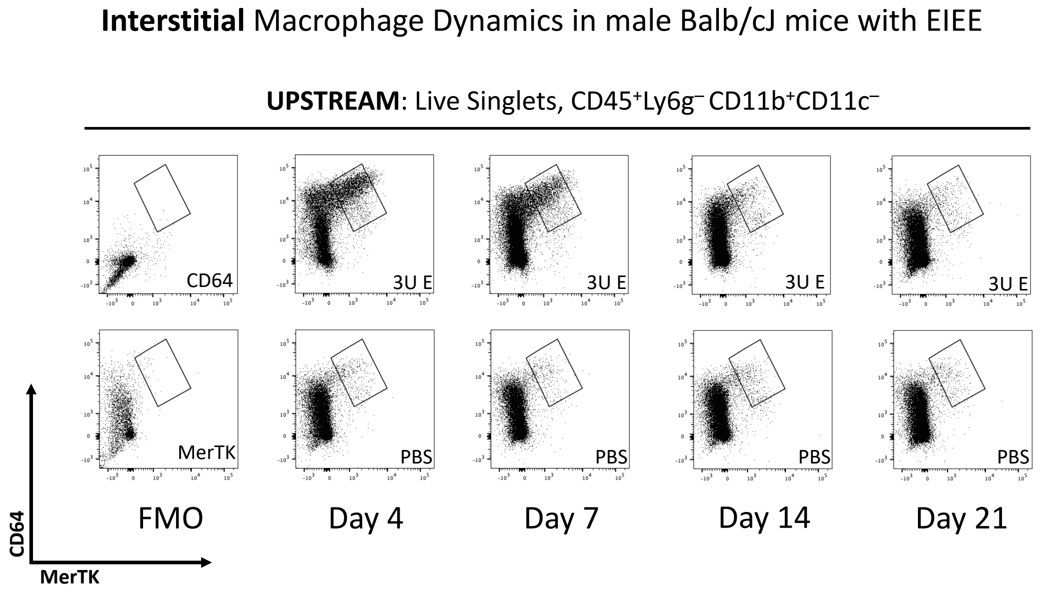

Figure 4.2. Basic flow cytometric analysis of interstitial macrophage dynamics in EIEE.

Interstitial macrophages are $CD45^{+}Ly6g^{-}$ $Cd11b^{+}$ $CD11c^{-}CD64^{+}$ and $MertK^{+}$. Dynamics were assessed across four timepoints in EIEE relative to PBS controls. Cytometry plots were concatenated, representing N=3 replicates per timepoint. For gating, samples were compared directly to fluorescent minus one (FMO) controls. This experiment was repeated twice, yielding similar patterns.

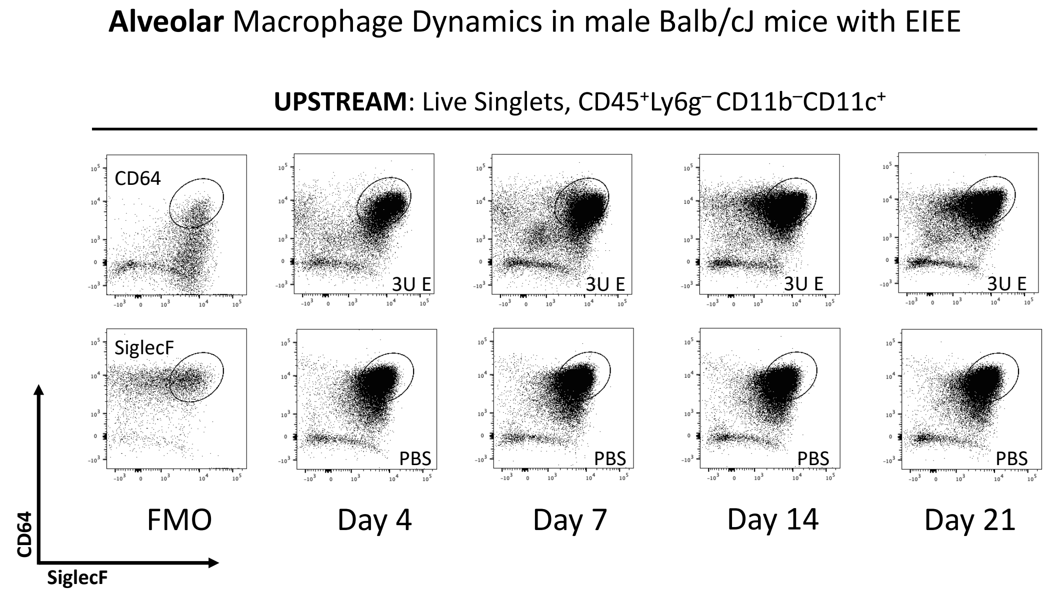

Figure 4.3. Basic flow cytometric analysis of alveolar macrophage dynamics in EIEE.

Alveolar macrophages are CD45$^+$Ly6g$^-$ Cd11b$^-$ CD11c$^+$CD64$^+$ and SiglecF$^+$. Dynamics were assessed across four timepoints in EIEE relative to PBS controls. Cytometry plots were concatenated, representing N=3 replicates per timepoint. For gating, samples were compared directly to fluorescent minus one (FMO) controls. This experiment was repeated twice, yielding similar patterns.

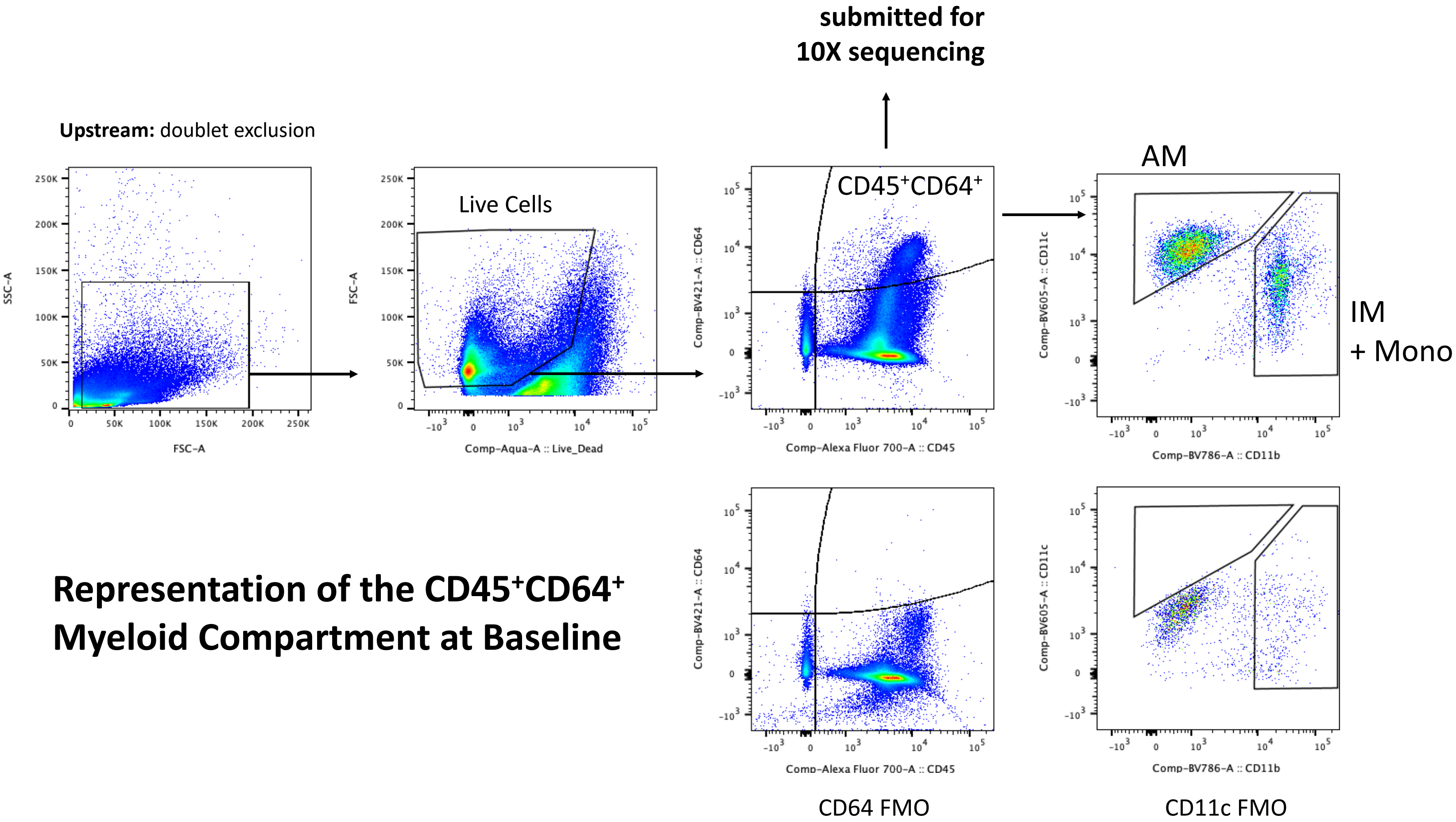

Representation of the CD45$^+$CD64$^+$ Myeloid Compartment at Baseline

Figure 4.4. Enrichment of $CD45^+CD64^+$ lung cells by FACS prior to assessing cellular dynamics with scRNAseq.

Images representative of one, naïve mouse lung. Samples for this illustration were acquired by our lab on an LSR-II (Becton Dickinson); but FACS was ultimately performed by Hao Zhang, M.D. with a MoFlo XDP (Beckman Coulter). For scRNAseq, cells from duplicate animals at three timepoints (naive vs. days 7/21 post-elastase) were sort-purified and analyzed at single cell resolution. scRNAseq of timepoints in EIEE was performed only once.

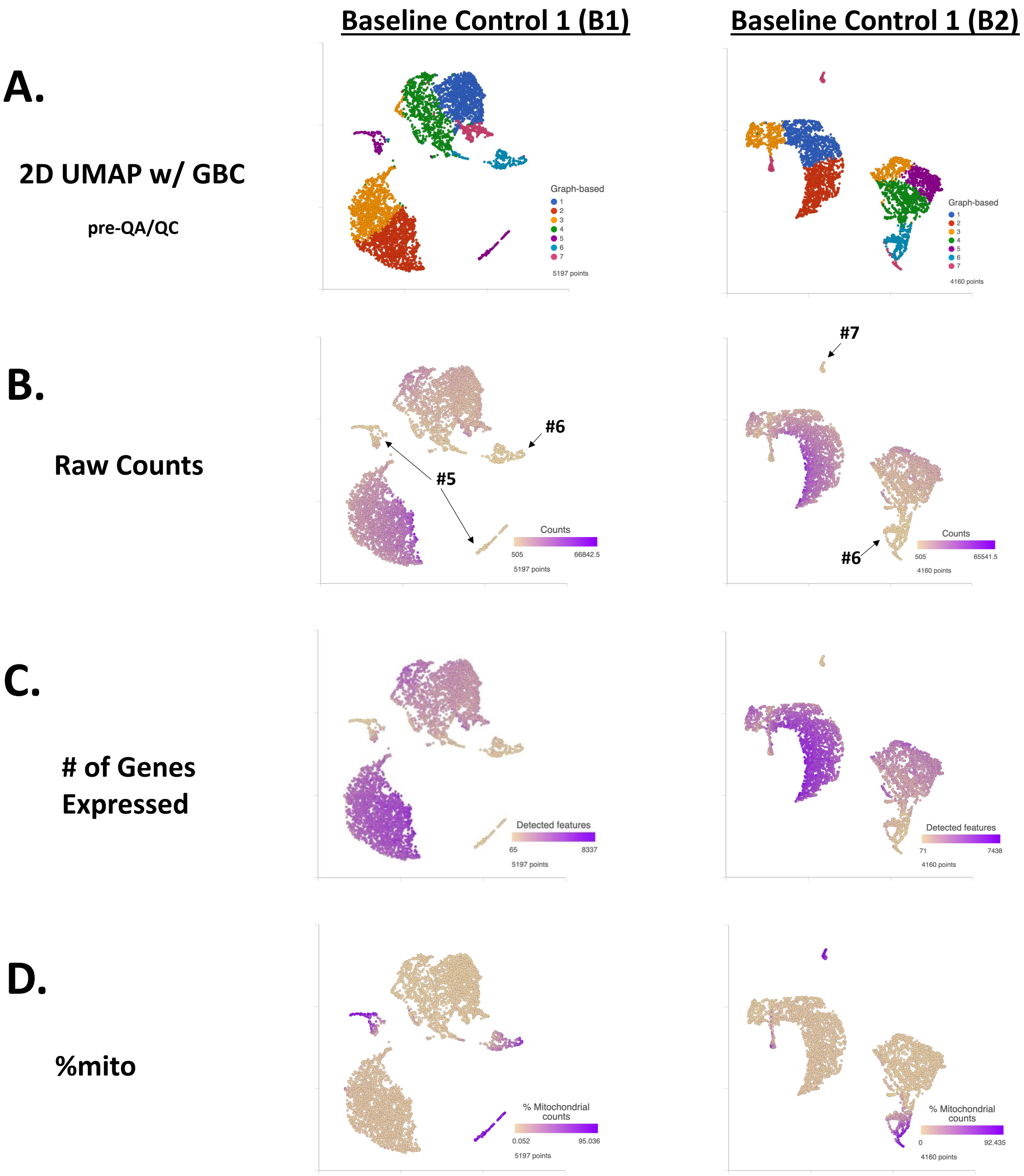Baseline Control 1 (B1)
Baseline Control 1 (B2)
A.
2D UMAP w/ GBC
pre-QA/QC
Graph-based
1
2
3
4
5
6
7
5197 points
4160 points
B.
Raw Counts
#5
#6
#7
Counts
505
66842.5
65541.5
C.
# of Genes Expressed
Detected features
65
8337
71
7438
D.
%mito
% Mitochondrial counts
0.052
95.036
0
92.435

Figure 4.5. Visually guided single-cell QA/QC of CD45$^+$CD64$^+$ lung cells at baseline.

Raw scRNAseq libraries acquired from mouse lungs at steady state (B1 and B2) were transformed upstream of UMAP and graph-based clustering using principal component analysis. All programs were executed as computational tasks in Partek Flow. (**A**) Samples B1 and B2 were visualized with UMAP, and graph-based clustering was used to calculate transcriptionally unique cell populations in each library. Low-quality cells were then removed for containing low abundance of features (**B**) and counts (**C**) relative to other populations in the dataset, as well as for containing a higher percentage of mitochondrial counts (**D**; %mito).

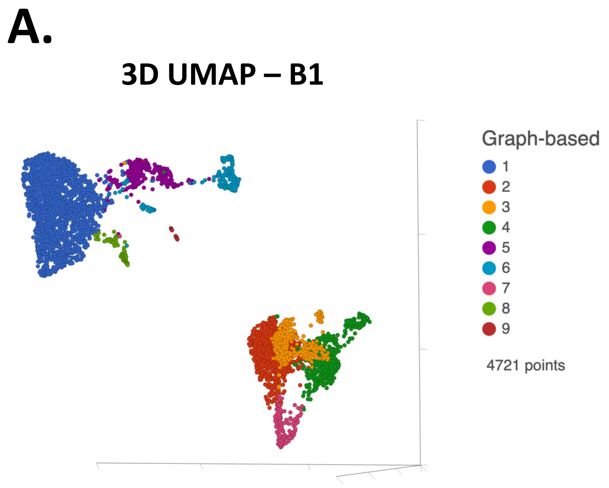

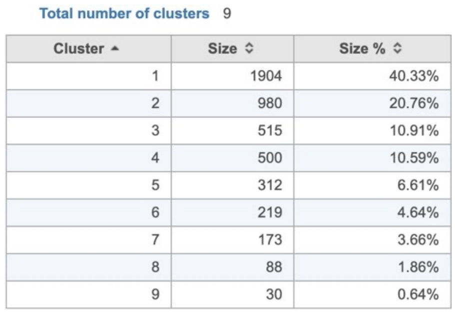

Total number of clusters 9

Cluster ▲	Size ⇕	Size % ⇕
1	1904	40.33%
2	980	20.76%
3	515	10.91%
4	500	10.59%
5	312	6.61%
6	219	4.64%
7	173	3.66%
8	88	1.86%
9	30	0.64%

post-QA/QC
counts normalized with scTransform

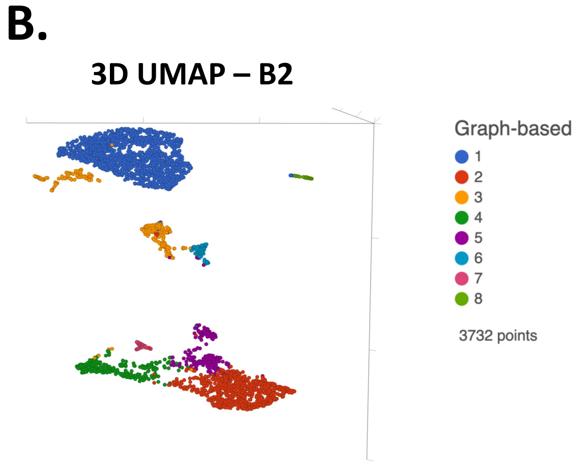

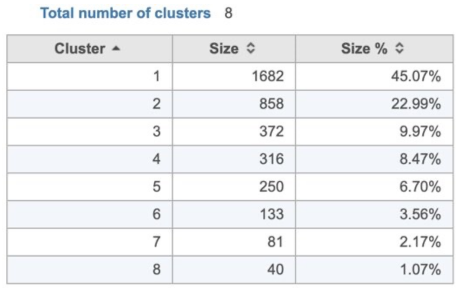

Total number of clusters 8

Cluster ▲	Size ⇕	Size % ⇕
1	1682	45.07%
2	858	22.99%
3	372	9.97%
4	316	8.47%
5	250	6.70%
6	133	3.56%
7	81	2.17%
8	40	1.07%

post-QA/QC
counts normalized with scTransform

Figure 4.6. Preliminary UMAP and graph-based clustering of steady-state replicates post-QA/QC.

Raw counts from each scRNAseq were normalized using the program scTransform. Data were then dimensionally reduced with principal component analysis, prior to visualizing results with UMAP and graph-based clustering. (**A**-**B**) UMAP visualizations, graph-based clustering, and summary statistics for broadly characterizing steady-state replicates B1 or B2 at single-cell resolution.

A.

3D UMAP – CD45$^+$CD64$^+$ cells at Steady-State

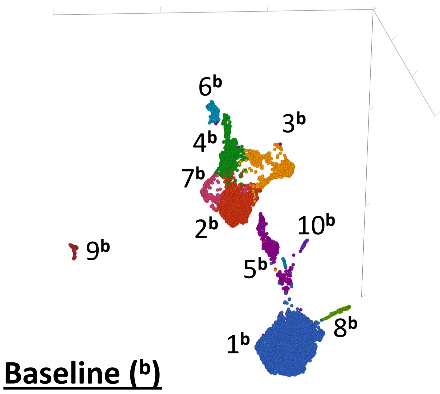

Samples B1+B2 Merged (Harmony)

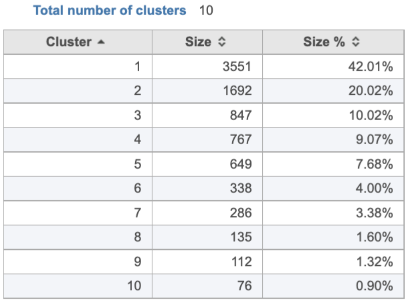

Total number of clusters 10

Cluster ▲	Size ⇕	Size % ⇕
1	3551	42.01%
2	1692	20.02%
3	847	10.02%
4	767	9.07%
5	649	7.68%
6	338	4.00%
7	286	3.38%
8	135	1.60%
9	112	1.32%
10	76	0.90%

TRAM ● 1
Cd14$^+$ Mono ● 2
Cd300 ● 3
MHC-II^{Hi} Mono or DC ● 4
MoAM ● 5
IM ● 6
pDC ● 7
Pro-AM ● 8
Neutrophil ● 9
T/B Cell ● 10

B.

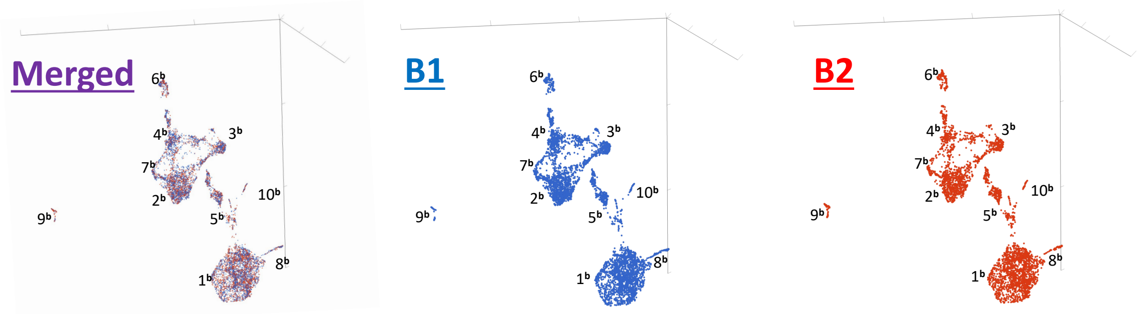

C.

Rank	1	2	3	4	5	6	7	8	9	10
1	*Plet1*	*Cd177*	***Cd300e***	***H2-Aa***	*Kcnip4*	***C1qa***	***Ifit2***	***Nusap1***	***S100a9***	***Cd79a***
2	*Slc7a2*	*Fn1*	*Eno3*	***H2-Ab1***	*Nav2*	***C1qb***	*Rsad2*	*Birc5*	***S100a8***	***Trbc2***
3	*Lpin1*	*Hp*	*Ace*	***H2-DMb1***	*Gm42418*	***C1qc***	***Ifit3***	*Rrm2*	***Retnlg***	*Ebf1*
4	*Atp6v0d2*	***S100a4***	*Slc12a2*	***H2-Eb1***	*Flt3*	*Pf4*	***Ifit1***	*Pclaf*	*Cstdc4*	*Gimap3*
5	*Kcnn3*	*Thbs1*	*S1pr5*	***Cd74***	*Clmn*	***Folr2***	*Usp18*	***Mki67***	*Stfa2l1*	*Gimap6*
6	*Fpr1*	***F13a1***	*Tmem26*	***Tmem176b***	*Cd209a*	*Ccl7*	*Oasl2*	*Top2a*	*Acod1*	***Cd3d***
7	***Lpl***	***S100a6***	*Fabp4*	***Tmem176a***	*Gm26917*	*Ccl12*	*Phf11d*	***Ccna2***	*Lcn2*	*Gimap4*
8	*Slc6a4*	*AI839979*	*Pglyrp1*	***Cd209a***	*P2ry10*	***Lyve1***	*Isg15*	*Ube2c*	*Cxcr2*	***Cd3e***
9	***Car4***	***Ly6c1***	***Cd300ld***	***H2-DMb2***	*Fam189a2*	*Fxyd2*	*Phf11b*	*Cenpf*	*Il1f9*	*Gimap1*
10	*Flvcr2*	***Ly6c2***	*Adgre4*	*Plbd1*	*Vdr*	*Gas6*	***Ifi44***	*Prc1*	*Dhrs9*	*Ptprcap*
11	*Lrp12*	*Ifitm6*	*Treml4*	*Ciita*	*Kmo*	*Fcrls*	*Oas3*	*Kif11*	*Lrg1*	*Ccr7*
12	*Mgll*	***Ccr2***	*Cyfip2*	*Aif1*	*Galnt6*	*Ccl8*	***Ifi209***	*Hmmr*	*Hdc*	*Ablim1*
13	*Krt19*	***Cd14***	*Ceacam1*	*Ms4a4c*	*Gabbr1*	*Pmp22*	*Trim30d*	*Knl1*	*Steap4*	***Igkc***
14	*Plekhg1*	*Gm50022*	*Stap1*	*S100a6*	*Smyd5*	*Stab1*	***Ifi44l***	*Aspm*	*Mmp9*	*P2ry10*
15	***Spp1***	*Wfdc17*	*Pou2f2*	*Ccr2*	*Btla*	*Pla2g2d*	***Ifi47***	*Cdca3*	*Il1r2*	*Satb1*
16	*Gpnmb*	*Emb*	*Apoc2*	*Cd52*	*Hip1r*	***Cd163***	***Ifi214***	*Iqgap3*	*Slc2a3*	*Ets1*
17	*Fabp1*	*Ifi27l2a*	*Hes1*	*S100a4*	*Mettl1*	*Col14a1*	*Slfn1*	*Esco2*	*Ankrd33b*	*4930523C07Rik*
18	***Ear1***	*Ifitm3*	*Fyb*	*Tpt1*	*Ablim1*	*Vcam1*	*Rtp4*	*Cenpe*	*Csf1*	*S1pr1*
19	*Aldoc*	*Cd52*	*Cd244a*	*Ifitm3*	*Nop2*	*Pmepa1*	*Zbp1*	*Kif15*	*G0s2*	*Cd55*
20	***Siglecf***	*Ms4a6c*	*Slc11a1*	*Ms4a6c*	*Slc27a1*	*Cbr2*	*Trim30c*	*Pbk*	*AW011738*	*Txk*
	TRAM	Mono	*Cd300* Cells	MHC-II^{Hi} Mono/DC	?	IM	pDC	Pro-AM	Neutrophil	T-cell

NOTE: Bolded ***Features*** were described in-text for provisionally annotating each graph-based cluster

Figure 4.7. Removing batch effects and integrating biological replicates at steady-state with Harmony.

All computational tasks were performed in Partek Flow. Baseline libraries B1 and B2 were acquired in paralell by the 10x platform and normalized data (scTransform) were computationally integrated with Harmony for generating this completed illustration. (**A-B**) UMAP visualizations and graph-based clustering of B1 and B2, having been computationally integrated. (**C**) Basic differential gene expression analysis supported by Student's t-test for identifying top upregulated features (sorted by P-value) within clusters upon comparison to others in the harmonized single-cell library. For conducting differential analysis, count values were transformed as counts per million (CPM) with the formula: $\mathrm{Log}_2[\mathrm{CPM}+1]$

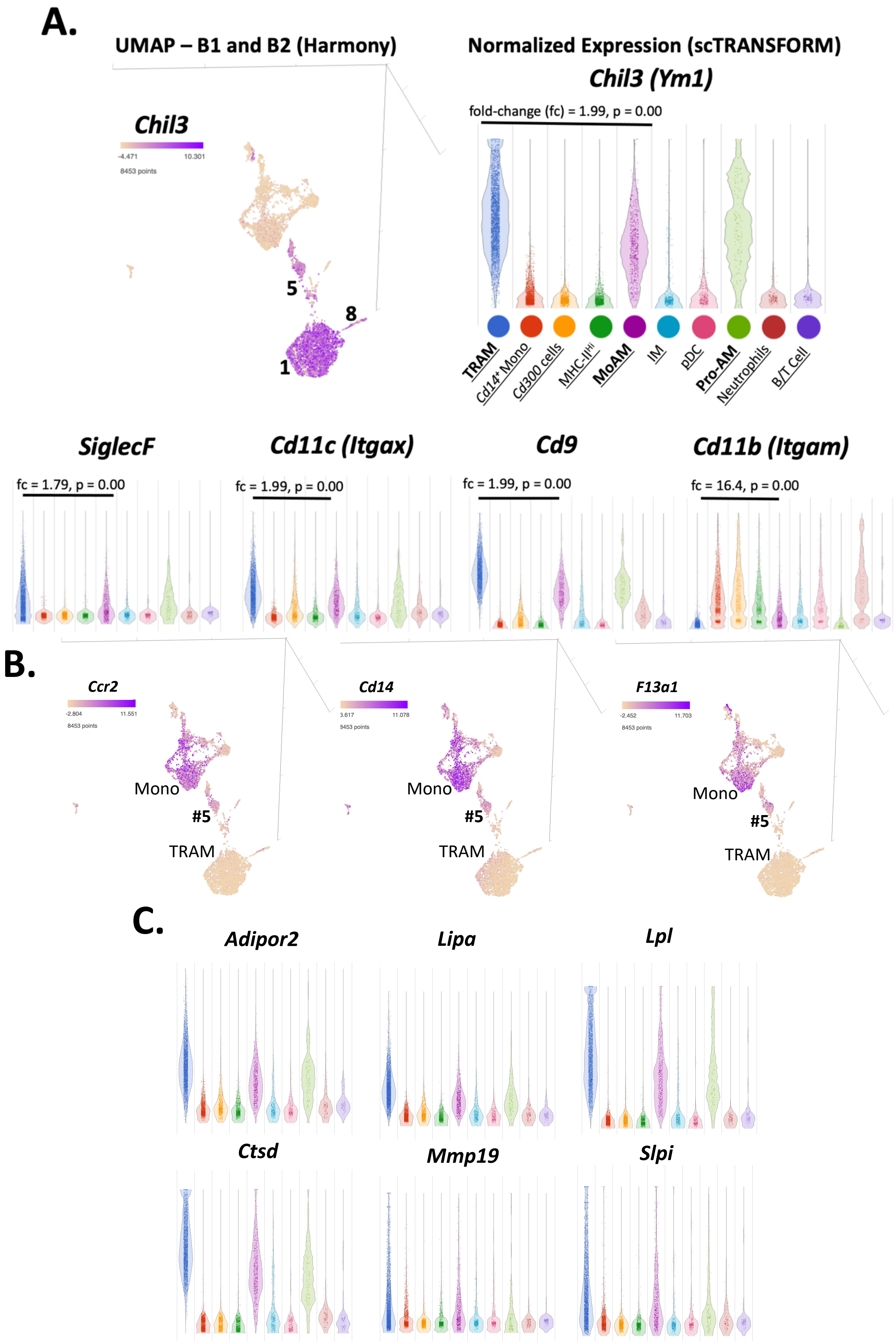
A.
UMAP – B1 and B2 (Harmony)
Chil3
-4.471
10.301
8453 points
5
8
1
Normalized Expression (scTRANSFORM)
Chil3 (Ym1)
fold-change (fc) = 1.99, p = 0.00
TRAM
Cd14+ Mono
Cd300 cells
MHC-II^Hi
MoAM
IM
pDC
Pro-AM
Neutrophils
B/T Cell
SiglecF
fc = 1.79, p = 0.00
Cd11c (Itgax)
fc = 1.99, p = 0.00
Cd9
fc = 1.99, p = 0.00
Cd11b (Itgam)
fc = 16.4, p = 0.00
B.
Ccr2
-2.804
11.551
8453 points
Mono
#5
TRAM
Cd14
3.617
11.078
8453 points
Mono
#5
TRAM
F13a1
-2.452
11.703
8453 points
Mono
#5
TRAM
C.
Adipor2
Lipa
Lpl
Ctsd
Mmp19
Slpi

Figure 4.8. Detailed transcriptional signatures representing three putative 'alveolar macrophage' populations from BALB/cJ lungs at baseline.

All computational tasks were performed in Partek Flow. (**A**) UMAP and gene expression plots at single cell resolution, highlighting *Chil3*, *Itgax/CD11c*, *SiglecF* and *Cd9* as genes that define alveolar macrophages in our dataset. For conducting differential analysis, count values were transformed as counts per million (CPM) with the formula: Log_2[CPM+1]. fc = fold change. Statistically significant comparisons (Hurdle model) for TRAM vs. MoAM are shown. (**B**) UMAP representations of clusters enriched for monocyte genes *Ccr2, Cd14,* and *F13a1.* (**C**) Normalized expression plots (*Adipor2, Lipa, Lpl, Ctsd, Mmp19, Slpi)* for characterizing functional roles for alveolar macrophages in our dataset.

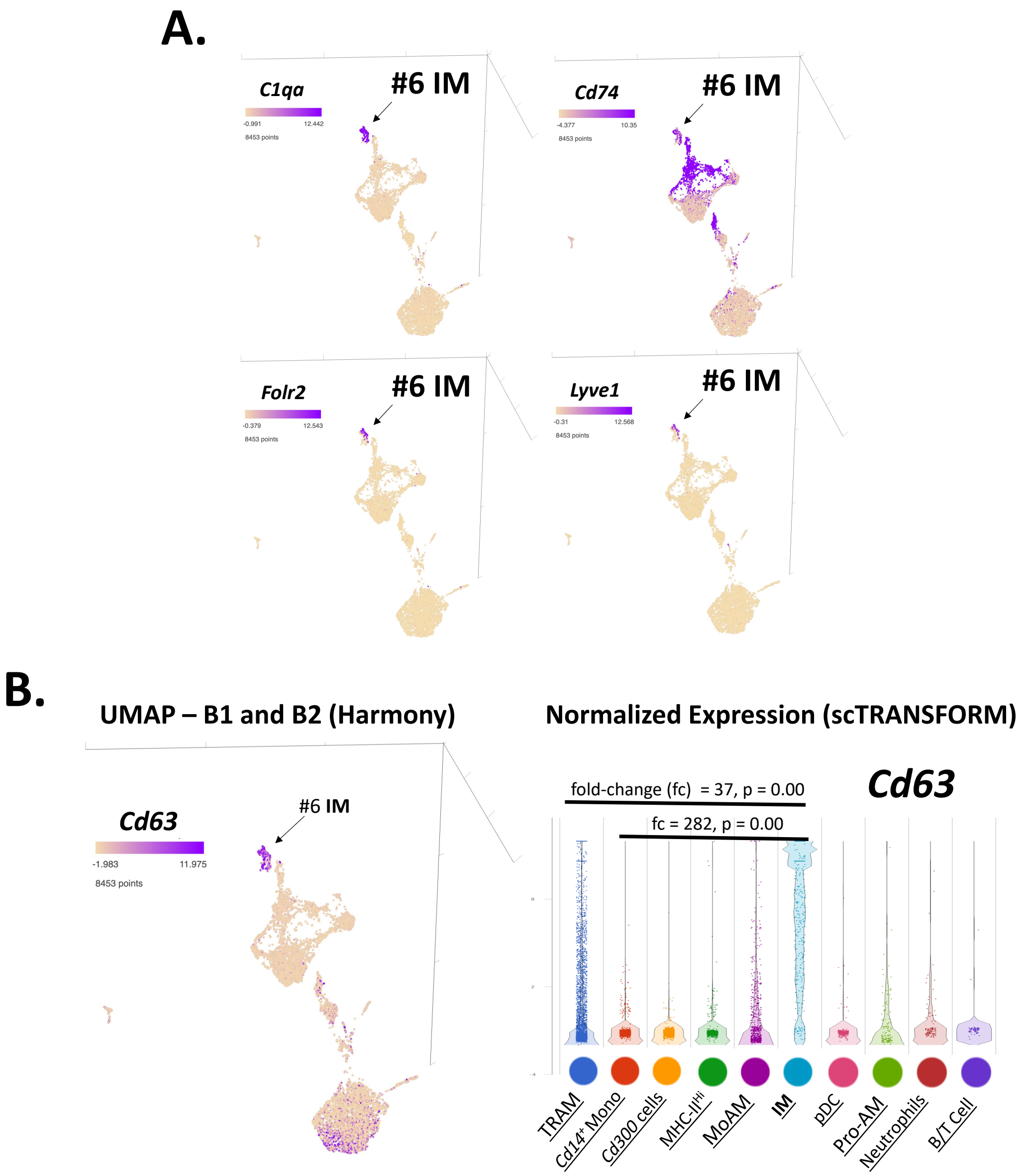

Figure 4.9. Detailed transcriptional visualizations and statistics for defining interstitial macrophages at baseline.

All computational tasks were performed in Partek Flow. (**A**) UMAP highlighting expression of *C1qa, Cd74*, *Folr2*, *Lyve1, Ccl2,* and *Timp2* in IM (**B**) Scatter plot illustrating statistical significance ($p < .05$, determined by Hurdle Model) of *Cd63* expression by IM at steady-state. For conducting differential analysis, count values were transformed as counts per million (CPM) with the formula: $\text{Log}_2[\text{CPM}+1]$. fc = fold change.

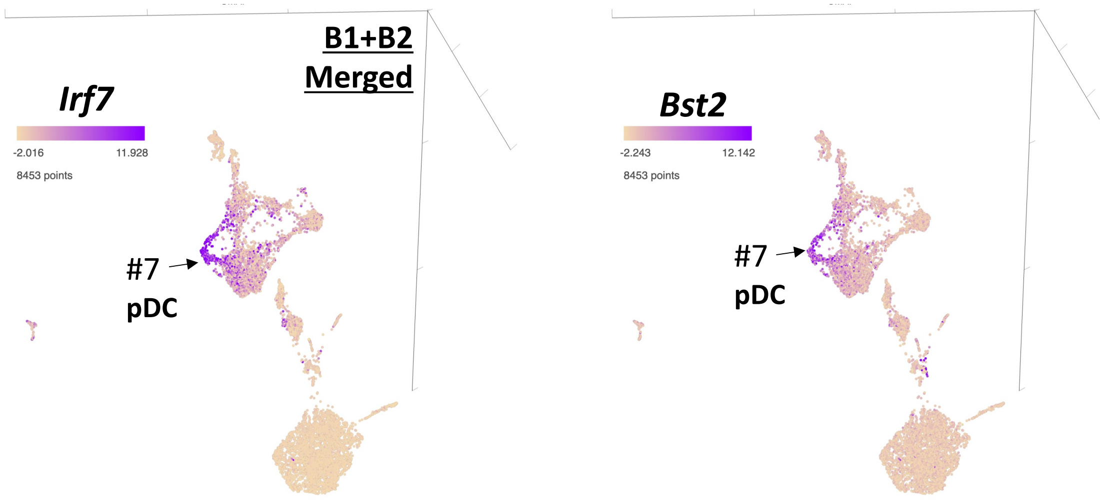

Figure 4.10. Characterizing plasmacytoid dendritic cells at baseline using the Hurdle model.

All computational tasks were performed in Partek Flow. Clusters in the merged dataset were directly compared, transcriptionally, for improving our annotation of $CD45^+CD64^+$ myeloid cells at steady-state. Cluster 7 was identified as a minor population of plasmacytoid dendritic cells (pDC) by directly comparing their transcriptional output to other clusters at baseline by aid of the Hurdle model. For conducting differential analysis, count values were transformed as counts per million (CPM) with the formula: $Log_2[CPM+1]$.

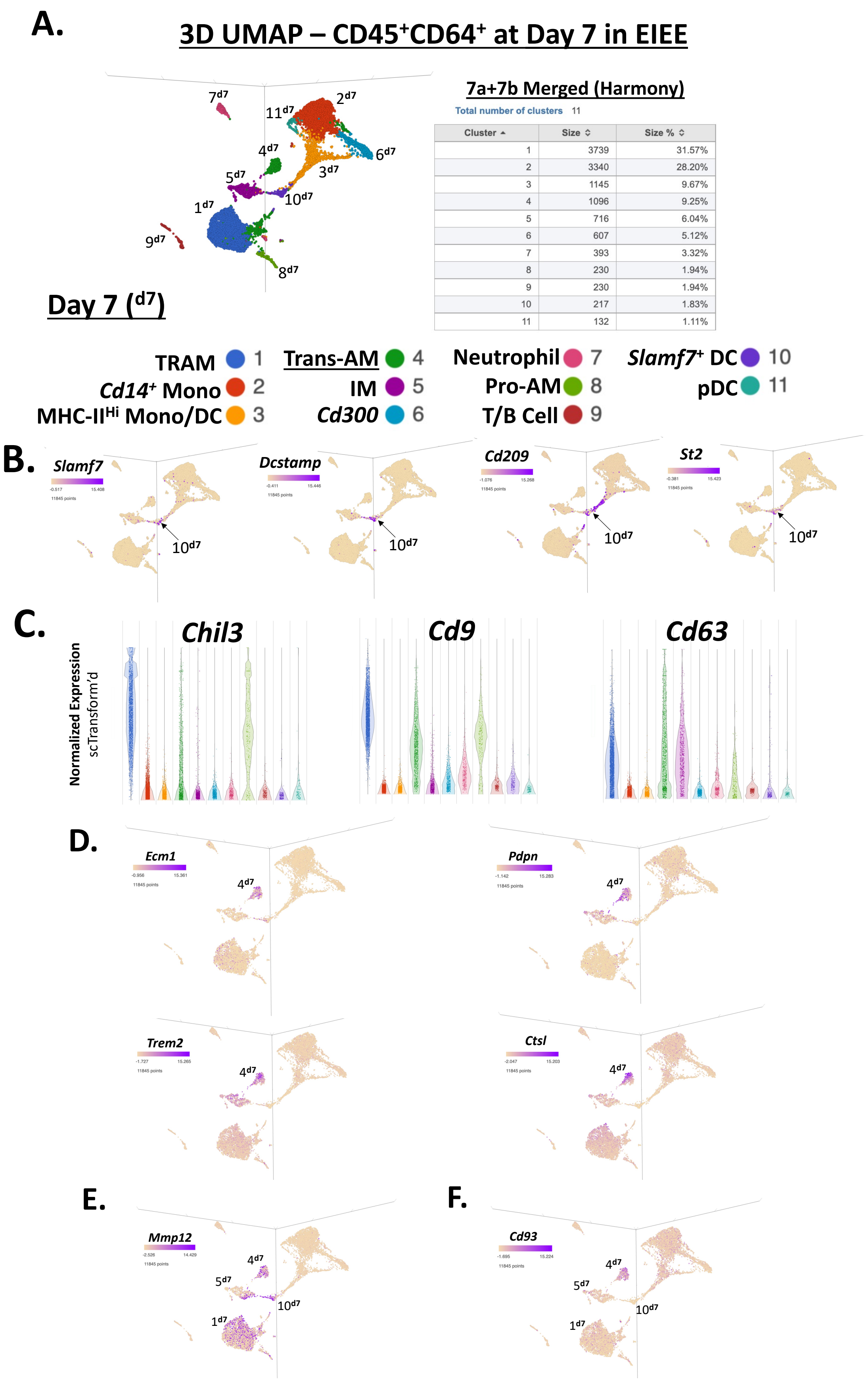

7a+7b Merged (Harmony)

Total number of clusters 11

Cluster ▲	Size ⇕	Size % ⇕
1	3739	31.57%
2	3340	28.20%
3	1145	9.67%
4	1096	9.25%
5	716	6.04%
6	607	5.12%
7	393	3.32%
8	230	1.94%
9	230	1.94%
10	217	1.83%
11	132	1.11%

Figure 4.11. Analysis of of harmonized scRNAseq libraries aquired from mouse lungs at day 7 post-elastase challenge.

All computational tasks were performed in Partek Flow. (**A**) Day 7 libraries (7a and 7b) were acquired in paralell by the 10x platform and computationally integrated with Harmony for generating this completed UMAP with graph-based clustering. (**B**) Cluster 10 at day 7 in EIEE was identified as a population of dendritic cells that express *Slamf7, Dcstamp, Cd209a (DC-SIGN), Il1rl1 (St2).* (**C**-**F**) For annotating Trans-AM (Cluster 4^{d7}) post-elastase, UMAP illustrations were enriched for *Ecm1, Pdpn, Trem2, Ctsl, Mmp12,* and *Cd93.*

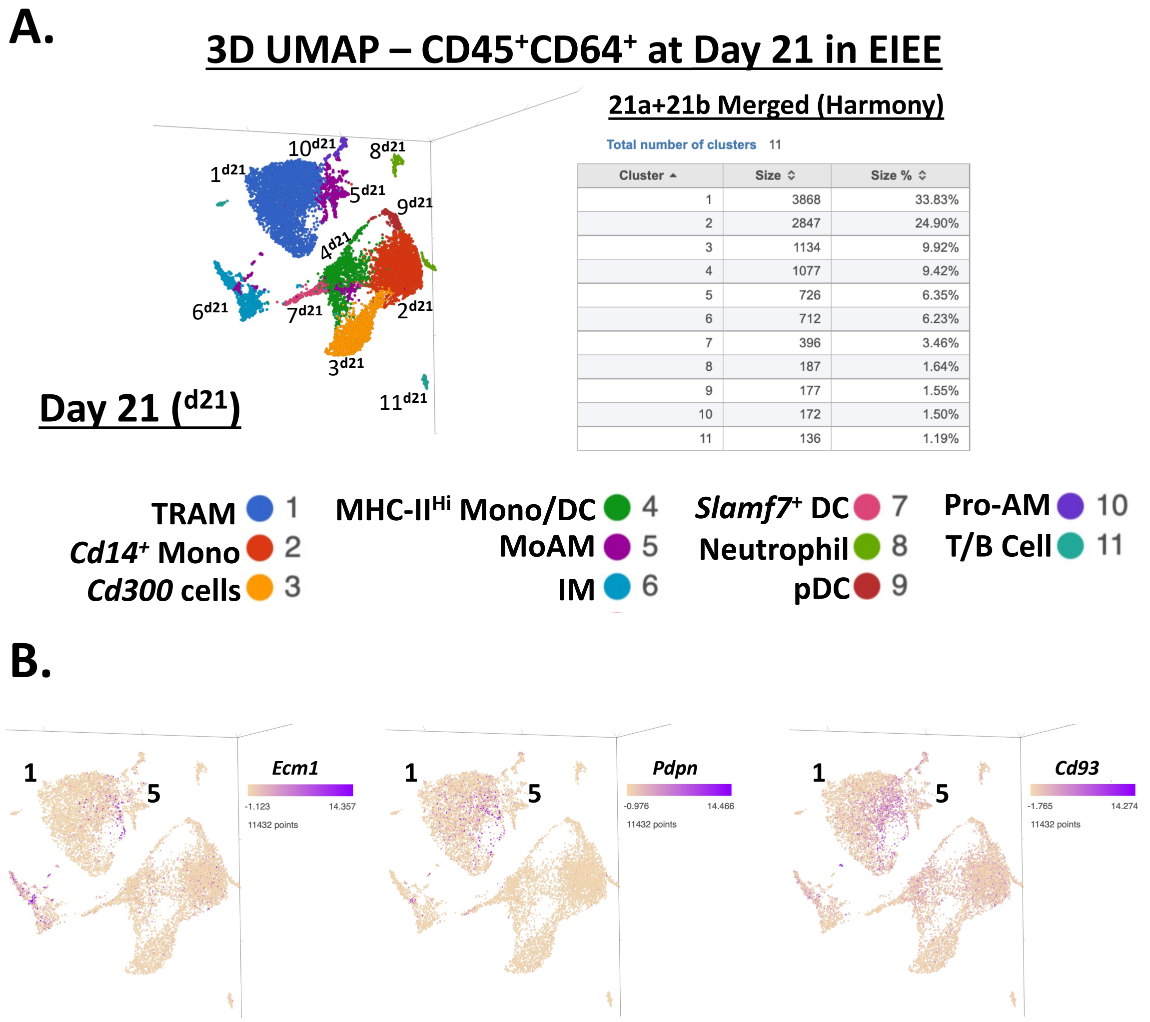

Total number of clusters 11

Cluster ▲	Size ⇕	Size % ⇕
1	3868	33.83%
2	2847	24.90%
3	1134	9.92%
4	1077	9.42%
5	726	6.35%
6	712	6.23%
7	396	3.46%
8	187	1.64%
9	177	1.55%
10	172	1.50%
11	136	1.19%

Figure 4.12. Analysis of scRNAseq libraries aquired from mouse lungs at day 21 post-elastase challenge.

All computational tasks were performed in Partek Flow. (**A**) Day 21 libraries (21a and 21b) were acquired in paralell by the 10x platform and computationally integrated with Harmony for generating this completed UMAP with graph-based clustering. (**B**) UMAP illustrations enriched for *Ecm1, Pdpn,* and *Cd93* were re-examined at day 21 post-elastase challenge.

A.

An integrated atlas that defines CD45$^+$CD64$^+$ lung cells in EIEE

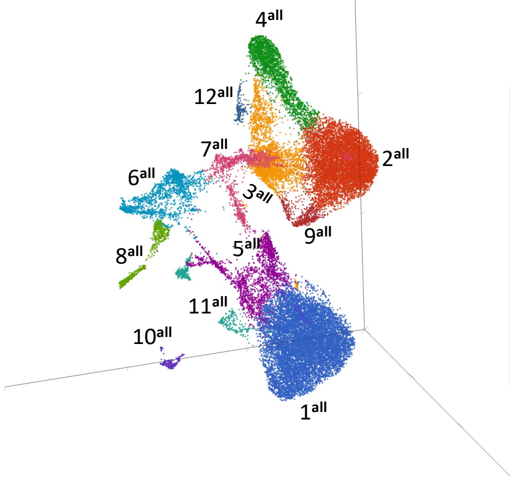

ALL timepoints merged (Harmony)

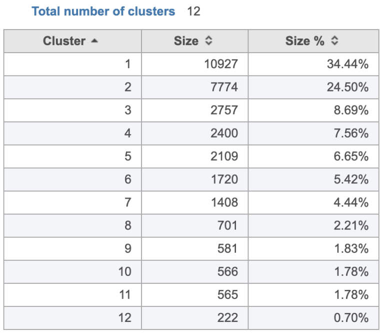

Total number of clusters 12

Cluster ▲	Size ⇕	Size % ⇕
1	10927	34.44%
2	7774	24.50%
3	2757	8.69%
4	2400	7.56%
5	2109	6.65%
6	1720	5.42%
7	1408	4.44%
8	701	2.21%
9	581	1.83%
10	566	1.78%
11	565	1.78%
12	222	0.70%

TRAM ● 1
Cd14$^+$ Mono ● 2
MHC-II^{Hi} Mono ● 3
Cd300 cells ● 4
Mo or Trans-AM ● 5
IM ● 6
Mixed DC ● 7
Neutrophil ● 8
pDC ● 9
T/B Cell ● 10
Pro-AM ● 11
Gm26917 cells ● 12

B.

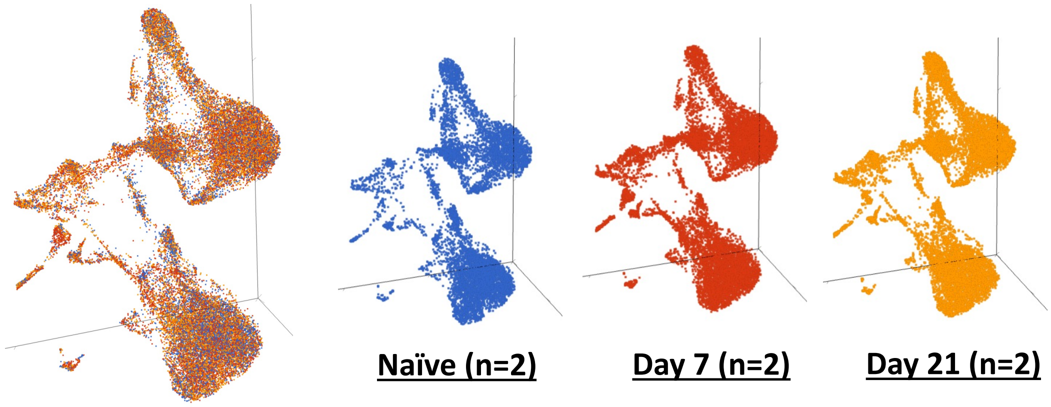

all timepoints merged (Harmony)

Naïve (n=2)

Day 7 (n=2)

Day 21 (n=2)

C.

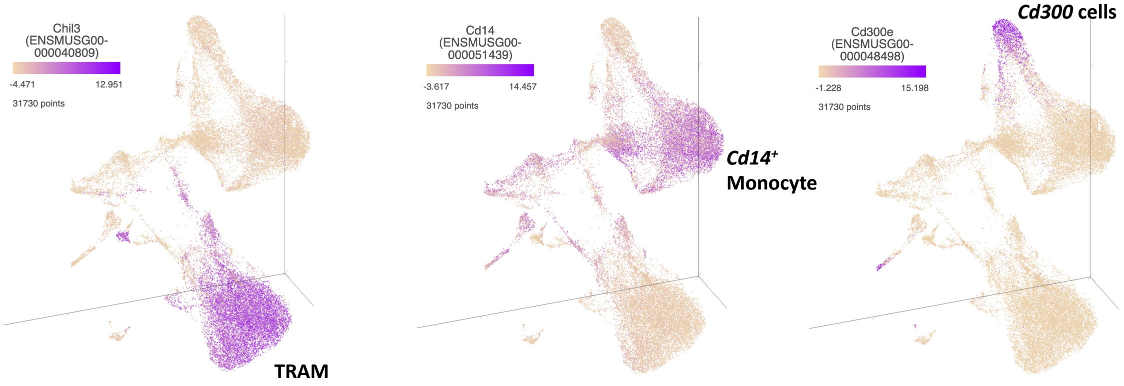

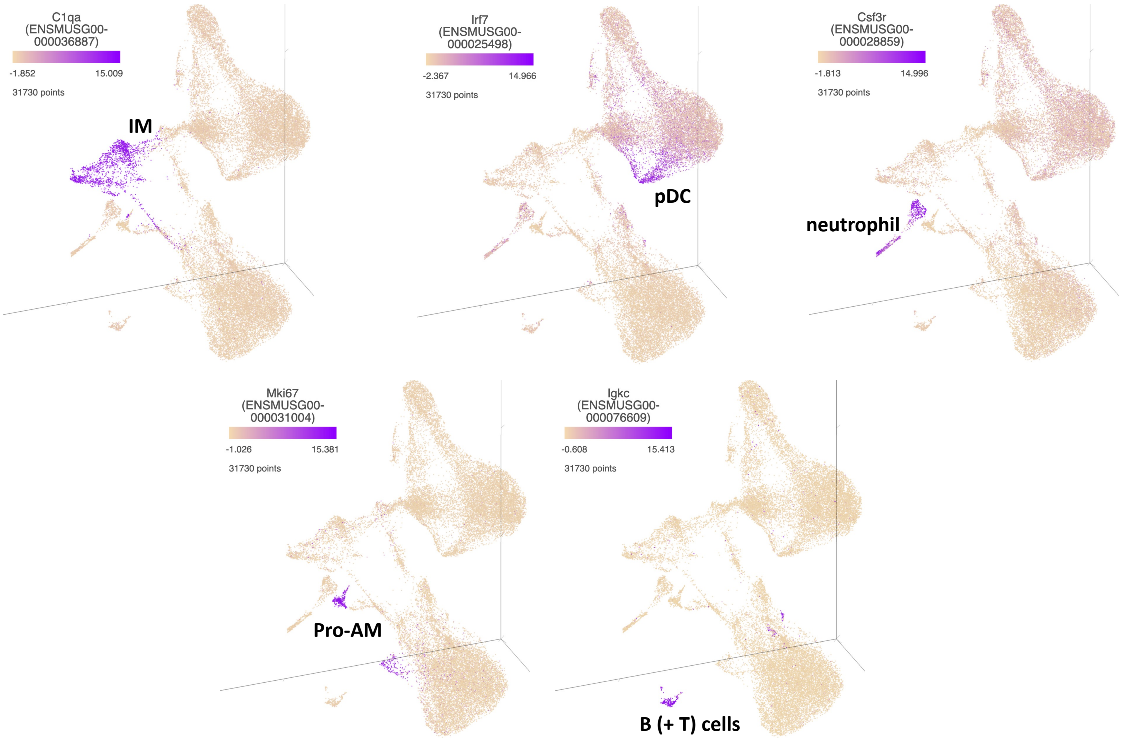
C1qa
(ENSMUSG00-
000036887)
-1.852
15.009
31730 points
IM
Irf7
(ENSMUSG00-
000025498)
-2.367
14.966
31730 points
pDC
Csf3r
(ENSMUSG00-
000028859)
-1.813
14.996
31730 points
neutrophil
Mki67
(ENSMUSG00-
000031004)
-1.026
15.381
31730 points
Pro-AM
Igkc
(ENSMUSG00-
000076609)
-0.608
15.413
31730 points
B (+ T) cells

D.

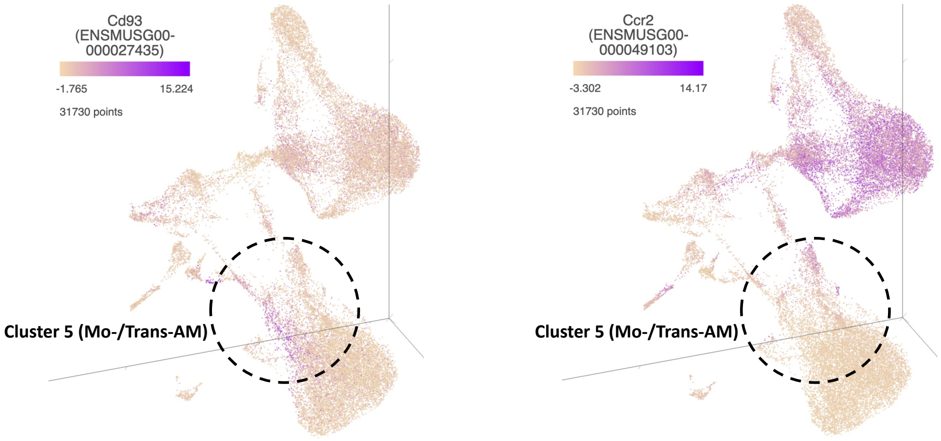
Cd93
(ENSMUSG00-
000027435)
-1.765
15.224
31730 points
Cluster 5 (Mo-/Trans-AM)
Ccr2
(ENSMUSG00-
000049103)
-3.302
14.17
31730 points
Cluster 5 (Mo-/Trans-AM)

E.

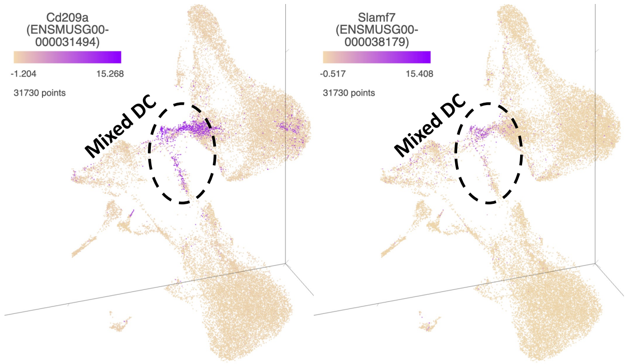
Cd209a
(ENSMUSG00-
000031494)
-1.204
15.268
31730 points
Mixed DC
Slamf7
(ENSMUSG00-
000038179)
-0.517
15.408
31730 points
Mixed DC

F.

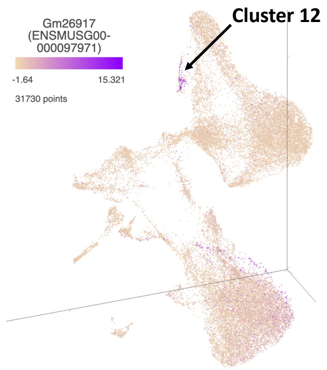
Gm26917
(ENSMUSG00-
000097971)
-1.64
15.321
31730 points
Cluster 12

Figure 4.13. An integrated single-cell atlas that defines $CD45^+CD64^+$ lung cells in EIEE.

All computational tasks were performed in Partek Flow. (**A-B**) Naïve (B1 and B2), Day 7 (7a and 7b), and Day 21 (21a and 21b) single-cell libraries were acquired in paralell by the 10x platform and integrated with Harmony for generating this completed UMAP with graph-based clustering. (**C**) Annotations for TRAM, *Cd14*$^+$ Mono, *Cd300* cells, IM, pDC, neutrophil, pro-AM, B/T cells were retained post-integration of all six libraries. (**D**) MoAM and Trans-AM were resolved mutually in Cluster 5. (**E**) Enrichment of *Cd209a* and *Slamf7* for annotating a mixed DC cluster. (**F**) Identification of *Gm26917* cells.

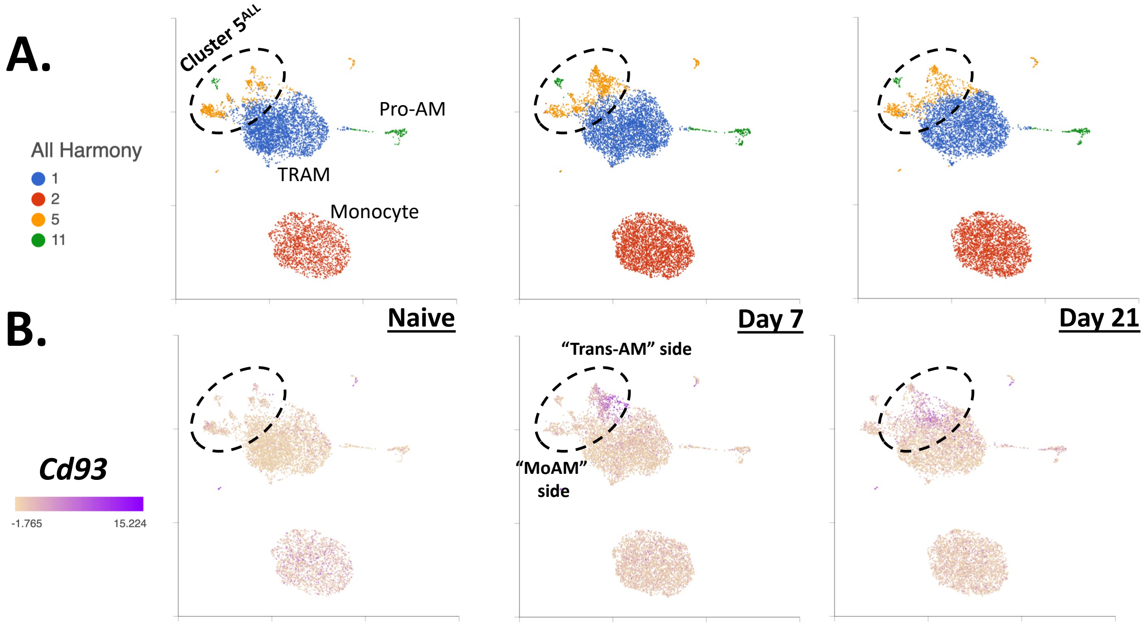

Figure 4.14. Advanced analysis of Cluster 5^{ALL} in EIEE

All computational tasks were performed in Partek Flow. (**A**) Recalculated UMAP post-filtering 8 of 12 clusters previously identified by graph-based methods (refer to **Figure 4.13A**). (**B**) Normalized expression (scTransform) of *Cd93* was enriched by UMAP for studyng Trans-AM dynamics within Cluster 5^{ALL} over time in EIEE.

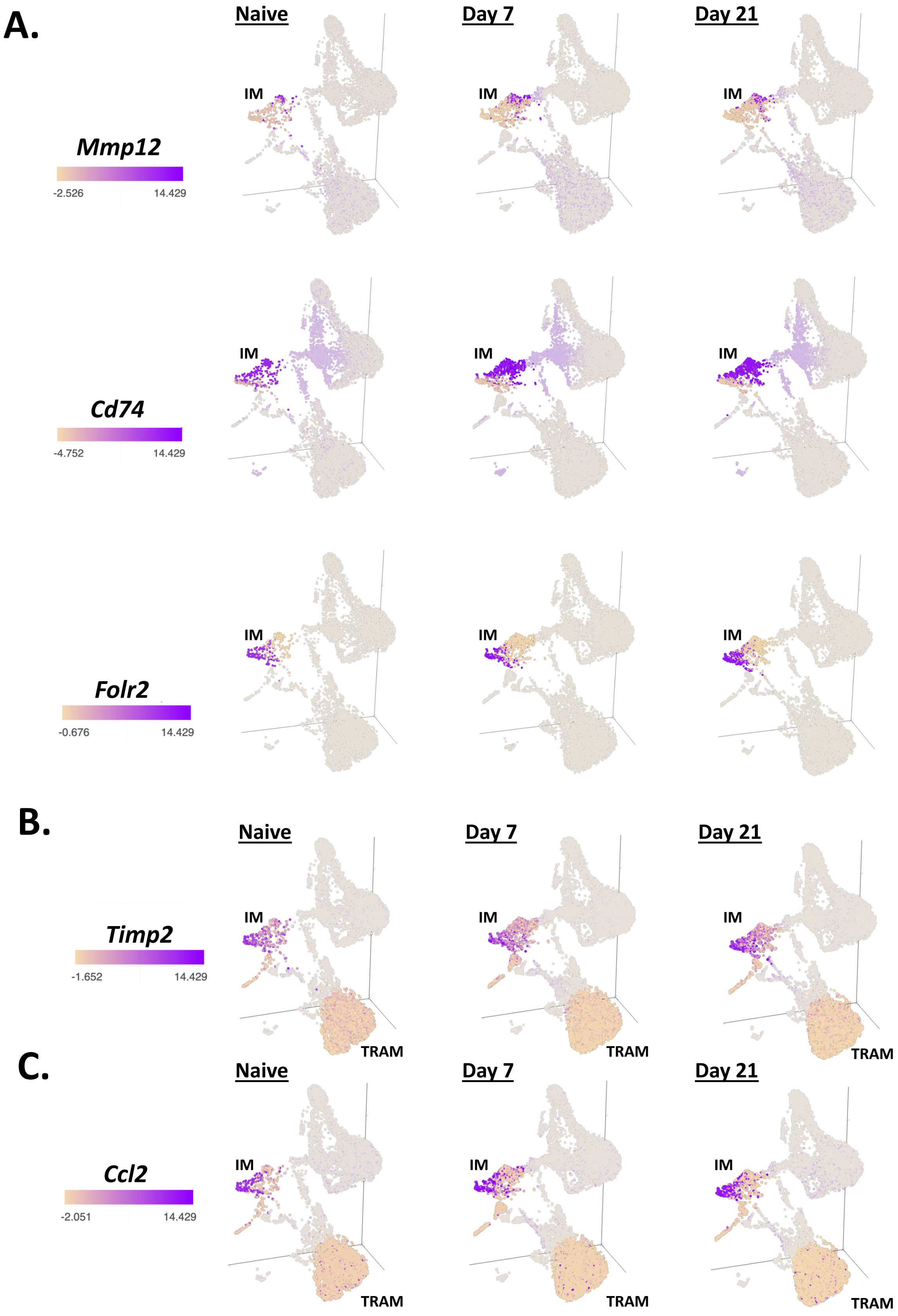
A.
Naive
Day 7
Day 21
IM
Mmp12
-2.526
14.429
Cd74
-4.752
14.429
Folr2
-0.676
14.429
B.
Naive
Day 7
Day 21
IM
Timp2
-1.652
14.429
TRAM
C.
Naive
Day 7
Day 21
IM
Ccl2
-2.051
14.429
TRAM

Figure 4.15. Transcriptional profiling of interstitial macrophages over time in EIEE by UMAP.

All computational tasks were performed in Partek Flow. (**A-C**) The UMAP illustration from **Figure 4.13A** viewed from a split perspective, highlighting interstitial macrophage (IM) dynamics over time in the EIEE model. Normalized expression (scTransform) of *Mmp12, Cd74, Folr2, Timp2,* and *Ccl2* were enriched by UMAP for studying IMs over time in EIEE.

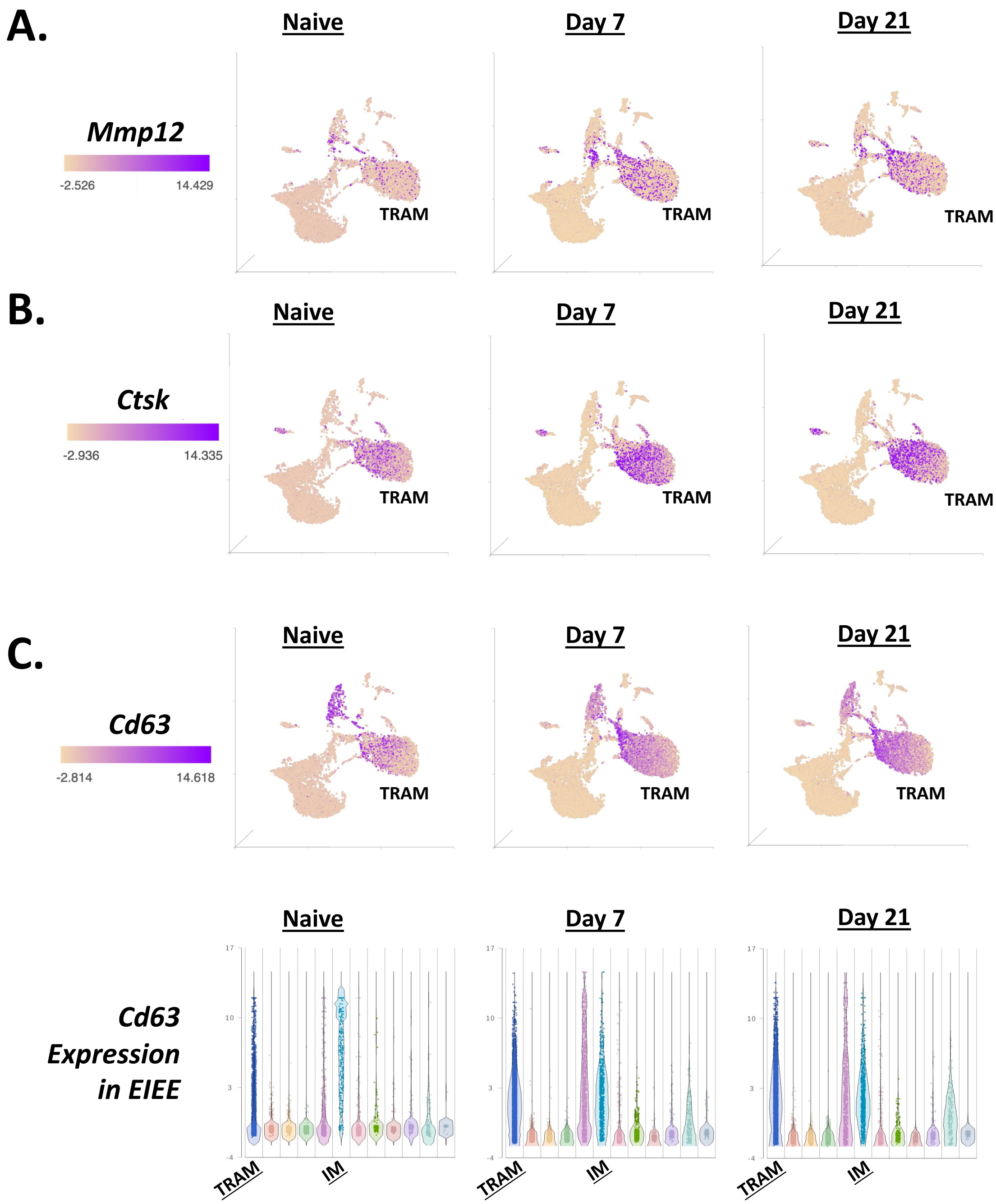

Figure 4.16 Transcriptional profiling of tissue resident alveolar macrophages over time in EIEE by UMAP.

All computational tasks were performed in Partek Flow. NOTE: UMAP is the same as **Figure 4.13A**, but was re-oriented for visually appreciating changes in tissue resident alveolar macrophages (TRAM) over time. (**A**-**B**) Expression of *Mmp12* and *Ctsk* were enriched by UMAP. (**C**) Normalized expression (scTransform) of *Cd63* was illustrated by UMAP and scatter plot.

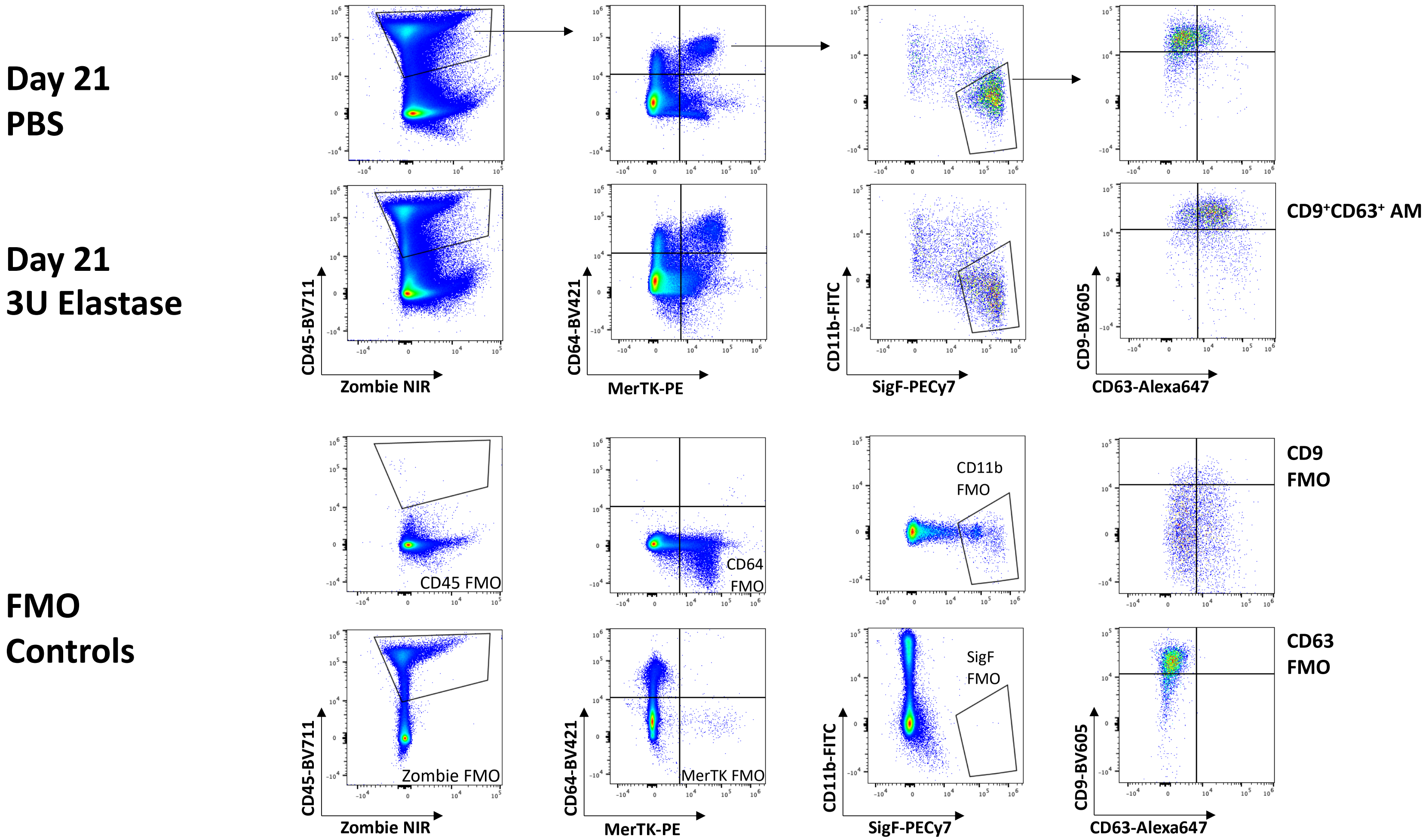
Day 21
PBS
Day 21
3U Elastase
FMO
Controls
CD45-BV711
Zombie NIR
CD64-BV421
MerTK-PE
CD11b-FITC
SigF-PECy7
CD9-BV605
CD63-Alexa647
CD9⁺CD63⁺ AM
CD45 FMO
CD64 FMO
CD11b FMO
CD9 FMO
Zombie FMO
MerTK FMO
SigF FMO
CD63 FMO

Figure 4.17. Flow cytometry for revisiting TRAM phenotypes over time in the EIEE model, aided by an informed bias from our scRNAseq atlas.

In this representation, one elastase- or PBS-treated murine lung was sampled for illustrating gating on CD9$^+$CD63$^+$ alveolar macrophages by flow cytometry. Live (Zombie NIR$^-$) CD45$^+$ cells were discriminated for dual expression of CD64 and MerTK. CD11b$^-$SiglecF$^+$ alveolar macrophages were ultimately scrutinized for dual expression of CD9 and CD63. This illustration was generated from a larger experiment, repeated twice in experimental cohorts that include $N \geq 3$ mice. Samples were acquired on a Cytek Aurora 4L/YG. For gating, samples were compared directly to fluorescent minus one (FMO) controls.

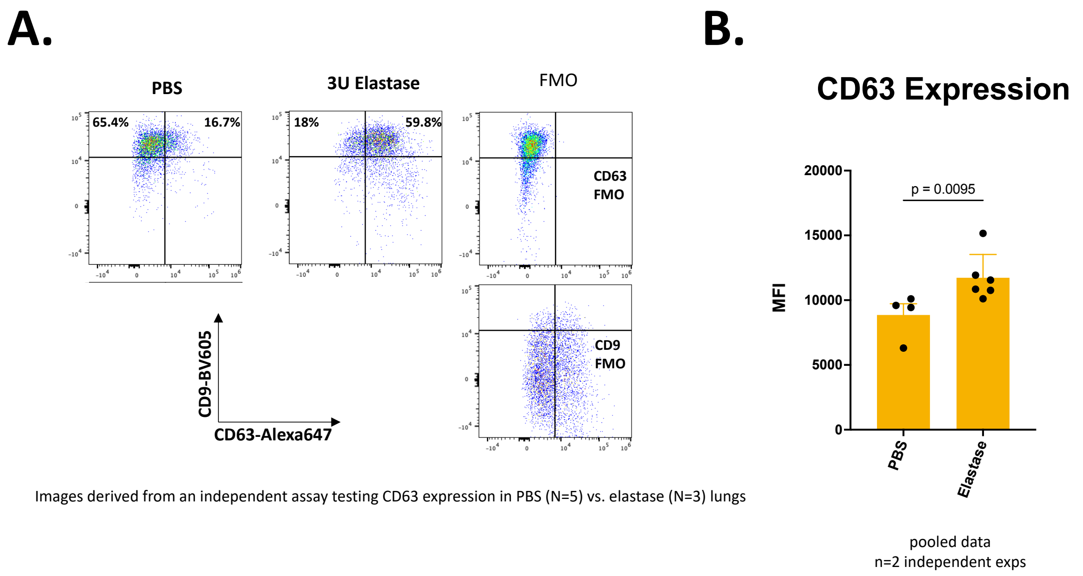

Images derived from an independent assay testing CD63 expression in PBS (N=5) vs. elastase (N=3) lungs

pooled data
n=2 independent exps

Figure 4.18. CD9^{+}CD63^{+} alveolar macrophages at 21 days after receiving 3U elastase IT.

(**A**) For this independent experiment, mice were treated with elastase or PBS and lungs were harvested at day 21 for flow cytometric confirmation of CD63 and CD9 expression on alveolar macrophages. N=3 elastase mice were compared directly to N=5 mice that received PBS. For the representative image, data from one mouse are shown. (**B**) Upon repeat of this assay, data points were pooled for determining statistically meaningful differences in CD63 (median fluorescence itensity, MFI) in elastase vs. PBS mice. Significance ($p < .05$) was determined with the Mann-Whitney U-test. Cytometry data were aqcuired on a Cytek Aurora 4L/YG. For gating, samples were compared directly to fluorescent minus one (FMO) controls.

Chapter 5. Novel therapeutic strategies for attenuating experimental emphysema.

Overview

Emphysema is notoriously unresponsive to therapeutic intervention. The available regimens are limited to symptom management and flare-up prophylaxis, and no therapeutic is known to stop disease progression or reverse tissue damage. There is a significant body of data supporting the hypothesis that tissue damage observed in emphysema and related disorders is mediated by dysregulated immune cells, namely lung macrophages and/or recruited monocytes. As an exploratory approach, we tested drugs and biologics known to target macrophage metabolism for their effectiveness in attenuating the degree and rate of progressive disease in murine elastase-induced experimental emphysema. The agents tested included: metformin, JHU083, DON, TG100, dimethyl itaconate, L-NIL, and therapy with α-CCL2 monoclonal antibody. Drugs were delivered by various means; and pulmonary function tests were used for assessing the extent of lung damage in our model. Unfortunately, each drug or biologic that we tested failed to prevent or reduce emphysema burden in BALB/cJ mice with elastase-induced emphysema.

Introduction

Emphysema is a component of chronic obstructive pulmonary disease (COPD). Pathology is characterized by progressive damage to alveoli and the small diameter conducting airways that results in loss of pulmonary function over time (Walters et al., 2021). Emphysema is also difficult to treat – available drugs merely ease or prevent symptoms, as clinicians have argued this subtype of COPD to be 'uncurable,' or irreversible (Martinez et al., 2018). To date, no FDA-approved COPD drug has been described for hindering disease progression.

The field's current understanding of emphysema pathogenesis is incomplete, making therapeutic intervention a particularly difficult feat to achieve. Key for developing an effective treatment is an understanding of the cellular and molecular drivers of emphysema that have been proposed over the years. Several reports suggest that emphysema is perpetuated by aberrant immune mechanisms likely carried out by macrophages or monocytes in the lung (Hautamaki et al., 1997; Limjunyawong et al., 2015a; Shibata et al., 2018). This notion, perhaps, is unsurprising in the context of other chronic or progressive disorders affecting the body. For example, macrophages and monocytes have been investigated extensively in the field of cancer immunology because they often promote tumor growth and metastasis (DeNardo and Ruffell, 2019; Pittet et al., 2022). Myeloid cell types are thought to be relatively plastic, and thus labs have found success with therapies that 'reprogram' tumorigenic macrophages for eliciting more sustainable, anti-cancer phenotypes (Mantovani et al., 2022), as opposed to merely eliminating them *in situ*. Having recognized the success of 'macrophage reprogramming' in cancer, several groups have considered translating this strategy for use in other disease models thought to be orchestrated by aberrant macrophages, including emphysema (Barnes and Stockle, 2005; Ogger and Byrne, 2021; Wang et al., 2020a). We too hypothesized that limiting the deleterious activity of lung macrophages will result in significant reduction of disease burden in our clinically-relevant, murine model of COPD, designated Elastase-Induced Experimental Emphysema (EIEE). Inspired mainly by their clinical effectiveness or experimental success for targeting immune cells in cancer microenvironments, we derived the following panel of agents for treating experimental emphysema: metformin, JHU083, DON, TG100, dimethyl itaconate, L-NIL, and therapy with α-CCL2 monoclonal antibody.

Although an FDA-approved drug for treating diabetes, metformin has been tested recently for treating cancer subtypes. Experimental metformin therapy has resulted in significant downregulation of PD-L1, which is an immunomodulatory protein often expressed by pro-cancer, tumor-associated macrophages (Cha et al., 2018). Achieving a similar, attenuation phenotype, the experimental therapeutic, DON, and its pro-drug, JHU083, have recently been implemented for reprograming T-cells that also drive tumorigenesis (Lemberg et al., 2018; Leone et al., 2019). Additionally, dimethyl itaconate, which targets the tricarboxylic acid cycle, was included in our panel because this compound has also been used effectively, and extensively, as an experimental therapeutic capable of 'reprogramming' pro-tumorigenic macrophages (O'Neill and Artyomov, 2019). For rigor, we also tested two novel, but unrelated therapies, TG100 (inhibitor of PI3-Kinase) and L-NIL (inhibitor of inducible nitric oxide synthase), since both had previously reduced disease burden in mice challenged by a less-severe, cigarette smoke-induced model for COPD (Doukas et al., 2009; Seimetz et al., 2011). Finally, inspired by the success of biologic therapy for both lung cancer and asthma, we tested an experimental, monoclonal antibody that targets CCL2, a chemoattractant with implications for interstitial macrophage biology in the emphysematous lung (Chen et al., 2011; Shibata et al., 2018). Collectively, we postulated that experimenting with these compounds would serve as a preliminary attempt to identify a metabolism-based approach to change the course of chronic lung damage. Drugs were delivered by diverse means that included oral gavage, intratracheal and intraperitoneal injection; and the readout for each experiment included lung function analysis, measured primarily by total lung capacity. We deemed that systemic delivery of each drug would elicit disease attenuation comparable to reports from the cancer field. However, under the conditions used for these studies, drug-treated animals still developed severe emphysema in a manner comparable to untreated controls. This study had limitations and opened the door for the consideration that further testing might reveal one or more of these compounds as effective for slowing progressive lung disease.

Methods

Mice.

All animal work was conducted in accordance with the standards established by the United States Animal Welfare Acts, set forth in NIH guidelines and the Policy and Procedures Manual of the Johns Hopkins University Animal Care and Use Committee. Animals were maintained in filter-topped cages at approximately 72^{o}C, 50-60% humidity with 14:10 hour light/dark cycle and *ad libitum* access to food and water. Male wildtype (WT) BALB/cJ were originally purchased from Jackson Laboratories (#000651). For the work presented in this Chapter, mice were purchased from Jackson Laboratories and used immediately for experiments, as opposed to pairing breeders and producing offspring on-site.

Elastase-Induced Experimental Emphysema (EIEE).

Male BALB/cJ mice (~25 grams, 7-11 weeks old) were anesthetized by intraperitoneal (IP) injection with a mixture (1:1) of ketamine (100 mg/kg) and Xylazine (10 mg/kg) in sterile water. Mice were intubated with an 18G canula and EIEE was induced with a single administration of 3U porcine pancreatic elastase (Elastin Products Co., LE4205) suspended in 50 µl of PBS, instilled intratracheally (IT). Baseline control animals received one instillation of 50 µl of PBS intratracheally. Some cohorts of mice then received a drug/biologic, while others served as untreated controls. Mice were harvested at 21 days post-elastase/PBS, unless stated otherwise in-text, and disease burden was measured by functional readouts.

Drugs and Biologics.

Table 5.1. Drugs and Biologics Tested in the BALB/cJ EIEE model

Common Name	Scientific Name	Vendor (#)
Metformin	*N*,*N*-dimethylbiguanide	Biogems – a PeproTech Brand (1117045)
DON	6-diazo-5-oxo-l-norleucine	Gift from Jonathon Powell (Ahluwalia et al., 1990)
JHU083	Pro-drug of 6-diazo-5-oxo-l-norleucine	Gift from Barbara Slusher (Rais et al., 2016)
TG100	3-[2,4-diamino-6-(3-hydroxyphenyl)pteridin-7-yl]phenol	MedChemExpress (HY-10111)
Dimethyl itaconate	Dimethyl itaconate	Sigma (592498)
L-NIL	N6-(1-Iminoethyl)-L-lysine hydrochloride	Cayman (80310)
α-CCL2	anti-mouse monocyte chemoattractant protein 1 monoclonal antibody	BioXcell (clone 2H5)

By IP injection, mice received DON (**37.5 µg per injection**; or ~**1.5 mg/kg** dissolved in PBS) or TG100 (**62.5 µg per injection**; or ~**2.5 mg/kg** dissolved in dimethyl sulfoxide), starting on Day 4 post-elastase. In total, mice received seven therapeutic injections of either DON or TG100, every other day until sacrifice on day 21. JHU083 was delivered either by oral gavage or by IT instillation over the course of two, independent experiments. For oral delivery, mice received JHU083 (**25 µg per gavage;** or ~**1 mg/kg** dissolved in 2.5% (v/v) ethanol in PBS) every other day, starting on day 2 post-elastase, until sacrifice at day 21. In total, mice received eight therapeutic gavages containing JHU083. For IT delivery, mice were intubated and received JHU083 (**25 µg per instillation**; or ~**1 mg/kg** dissolved in 2.5% (v/v) ethanol in PBS) approximately every four days, starting on day 4 post-elastase, until sacrifice at day 21. In total, mice received four therapeutic instillations of JHU083. Metformin was also delivered either by oral gavage or by IT instillation over the course of two, independent experiments. For oral delivery, mice received metformin (**7.5 mg per gavage**; or ~**300 mg/kg** dissolved in PBS) approximately every other day, starting on day 2 post-elastase, until sacrifice at Day 21. In total, mice received eight therapeutic gavages containing metformin. For IT delivery, mice were intubated and received metformin (**1.875 mg per instillation;** or ~**75 mg/kg** dissolved in PBS) approximately every four days, starting on day 4 post-elastase, until sacrifice at day 21. In total, mice received three therapeutic instillations of metformin, due to toxicity from IT delivery. Dimethyl itaconate (**20 mg per injection**; or ~**800 mg/kg** dissolved in PBS) was delivered by IP injection, starting on day 2 post-elastase, and every other day until sacrifice at day 21. In total, mice received twelve therapeutic injections of dimethyl itaconate. α-CCL2 monoclonal antibody (**200 µg per injection**; or ~**8 mg/kg** dissolved in manufacturer's buffer – BioXcell #IP0070) was also delivered by IP injection at 4 different timepoints: primary injection at day 0, followed by 'booster' doses at days 3, 4, and 7 post-elastase. Control animals received isotype IgG (BioXcell #BE0091) at each timepoint (**200 µg per injection;** or ~**8 mg/kg** dissolved in manufacturer's buffer – BioXcell #IP0070). Lastly, over the course of two independent assays, L-NIL was available to mice *ad libitum* (**600 µg/mL** in drinking water). For L-NIL only, we conducted separate assays to determine efficacy of this drug as a 'preventative' or 'curative' therapeutic for elastase-induced disease. For the 'preventative' approach, L-NIL was available to mice 2 days prior to intratracheal elastase challenge. Mice were then sacrificed at day 21 post-elastase.

For the ‘curative’ approach, BALB/cJ males were challenged with elastase, and L-NIL was made available to mice at day 14. Mice received L-NIL *ad libitum* until sacrifice at day 42.

Pulmonary Function Testing.

Mice were anesthetized by IP injection with a mixture (1:1) of ketamine (100 mg/kg) and Xylazine (10 mg/kg) in sterile water. Mice were tracheostomized with an 18G canula and directly connected to a FlexiVent (Scireq; Toronto, CA) for measuring total lung capacity. Data for additional functional readouts (compliance, DFCO) were collected as part of the default workflow, but not presented or discussed here. To prevent occasional spontaneous breathing from generating noise in the acquired data, mice were paralyzed with succinyl choline (200 mg/mL), administered by intramuscular injection (50 µl) prior to data acquisition.

Statistical Analysis and Illustrations.

Data visualization and statistical analysis were performed in GraphPad Prism (San Diego, CA). One- or Two-way ANOVA and Student’s t-test were the most utilized methods; and further statistical details, such as multiple comparisons or post-hoc tests, are annotated in the specific figure legends.

Results

Intervention with metformin.

We first tested metformin, an FDA-approved drug for diabetes, as a therapeutic candidate for elastase-induced experimental emphysema. The mechanism of metformin is most often described in the context of hepatocytes, where it’s main action includes activation of AMP kinase, affecting glucose and fatty acid metabolism (Pernicova and Korbonits, 2014; Ye et al., 2018). Over the years, metformin has been explored in diverse therapeutic contexts, including cancer treatment (Cha et al., 2018) and emerging reports suggest that metformin may also effectively modulate pro-inflammatory macrophage or monocyte effector function in chronic diseases like thrombosis and atherosclerosis (Soberanes et al., 2019; Vasamsetti et al., 2015). These data, combined with evidence for metformin as a candidate drug for alleviating other symptoms of lung disease, such as airway hyperresponsiveness (Gu et al., 2022), urged us to implement this drug for attenuating severe pathology in the EIEE model.

In a preliminary experiment, we induced EIEE in two cohorts of mice, treating one group with metformin by oral gavage on day 2 post-elastase, followed by gavage administrations approximately every other day. On day 21, or after eight metformin treatments, mice were sacrificed for pulmonary function testing. The primary readout was total lung capacity, and the main comparator for this assay were a group of mice that received PBS intratracheally on day 0, but also subjected to recuring metformin gavage

(**Figure 5.1A**). In this assay, there were no statistical differences evident when comparing diseased mice with or without metformin treatment. We opted to repeat this assay with key adjustments – additional vehicle controls, as well as delivery of metformin intratracheally, rather than orally (**Figure 5.1B**). We speculated that IT instillation would facilitate drug exposure to lung macrophages. For IT delivery, mice were intubated and given metformin every three days, starting on day 4 post-elastase, until sacrifice at day 21. In total, mice received only three IT doses of metformin because this approach resulted in technical problems. Multiple animals died presumably from an overdose of metformin. We adjusted the dosing in real-time for completing the experiment (we delivered 75 mg/Kg IT, instead of 300 mg/Kg as planned); and mice received one-less dose of metformin because of these circumstances. Regardless, disease burden was severe in surviving, elastase-treated mice with or without metformin intervention. Overall, these metformin experiments had severe technical limitations and relatively low, statistical power. Currently, we do not have support for metformin as a candidate therapeutic for attenuating emphysema.

Intervention with JHU083.

In parallel to our metformin studies, we also tested a panel of drugs that were recently, and successfully, implemented for metabolic reprograming of cells that drive cancer models. JHU083, the less-toxic, prodrug of experimental cancer therapeutic 6-Diazo-5-oxo-L-norleucine (DON), is a glutamine antagonist originally appreciated for reprograming T cells that drive tumorigenesis in four unique, experimental settings

(Lemberg et al., 2018; Leone et al., 2019). Indeed, other groups had demonstrated how glutamine and other substrates related to the tricarboxylic acid (TCA) cycle impact macrophage polarization status (Palmieri et al., 2017). We again hypothesized that JHU083-mediated reprogramming of lung macrophages would attenuate lung damage in EIEE. In a preliminary experiment, we induced EIEE in two cohorts of mice, treating one group with JHU083 by oral gavage on day 2 post-elastase, followed by treatments approximately every other day. On day 21 post-elastase, or after eight JHU083 treatments, mice were sacrificed for pulmonary function testing. Again, the primary readout was total lung capacity, and the main comparator for this assay were a group of mice that received PBS intratracheally on day 0, but also subjected to recuring JHU083 gavage (**Figure 5.2A**). In this assay, there were no statistical differences evident when comparing diseased mice with or without JHU083 treatment. Again, we repeated this assay by delivering JHU083 intratracheally, and with proper vehicle controls (**Figure 5.2B**). For IT delivery, mice were intubated and received JHU083 every 4 days, starting on day 4 post-elastase, until sacrifice on day 21. In total, mice received four therapeutic IT instillations of JHU083. Though a technical success, the disease burden was similar in elastase-treated mice with or without JHU083 intervention.

Finally, we tested the parent molecule of JHU083, DON, despite reports of gastrointestinal toxicity at even moderate doses (Lemberg et al., 2018). These mice also developed significant disease burden (**Figure 5.2C**). For now, use of JHU083 or DON do not seem relevant for treating EIEE under the prescribed experimental conditions.

Intervention with dimethyl itaconate.

Prior to abandoning this concept entirely, and mainly for rigor, we tested dimethyl itaconate in our model, since this compound also significantly disrupts the TCA cycle in macrophages (O'Neill and Artyomov, 2019). In one iteration of our workflow (N = 7-8 mice per group, including elastase-only mice and vehicle controls), we confirmed that treating mice IP with dimethyl itaconate does not attenuate disease at day 21. For this experiment, we induced EIEE in two cohorts of mice, treating one group with dimethyl itaconate IP on day 2 post-elastase, followed by sequential IP administrations of itaconate approximately every other day. Healthy mice, instilled with PBS intratracheally on day 0, were treated with either dimethyl itaconate or PBS (vehicle) for multiple comparisons. On day 21 post-elastase, and after twelve dimethyl itaconate treatments, mice were sacrificed, and total lung capacity was measured (**Figure 5.3**). Disease burden was significant and appreciable in elastase-treated mice with or without itaconate intervention. Similar to the observations for metformin, JHU083 and DON in our model, dimethyl itaconate does not appear to slow development of progressive emphysema in mice.

Intervention with TG100 and L-NIL.

Due to lack of experimental success when using metformin, JHU083, DON, and dimethyl itaconate, we decided to investigate the PI3-Kinase γ/δ inhibitor TG100 that was reported to have modest success in controlling the inflammatory outcome of mice subjected to cigarette smoke or experimental ovalbumin challenge (Doukas et al., 2009).

We perceived our EIEE model as an opportunity for validating if TG100 was also an effective metabolic reprogramming drug for attenuating a particularly severe form of murine, elastase-induced emphysema. For this experiment, we induced EIEE in two cohorts of mice, treating one group with TG100 by IP administration on day 4 post-elastase, followed by treatments approximately every other day. Healthy mice, having been instilled with PBS intratracheally on day 0, were treated with either TG100 or DMSO (vehicle) for multiple group comparisons. On day 21 EIEE, and after seven TG100 treatments, mice were sacrificed, and total lung capacity was assessed (**Figure 5.4**). Disease burden, again, was appreciable in elastase-treated mice with or without TG100 intervention.

Evidence of attenuated COPD was also noted when inducible nitric oxide synthase (iNOS) was blocked with an experimental inhibitor, L-NIL, upon exposing mice to cigarette smoke (Seimetz et al., 2011). While not a metabolic reprogramming drug *per se*, we performed this test to validate whether L-NIL was also effective for treating severe, elastase-induced emphysema. In line with the design laid out by Seimetz and colleagues (2011), we performed a ‘curative’ and ‘preventative’ iteration of this experiment. In both pipelines, we induced EIEE in two cohorts of mice. Mice in the ‘curative’ cohort received L-NIL in their drinking water *ad libitum* starting on day 14 post-elastase. Mice in the ‘preventative’ cohort started L-NIL two days prior to EIEE induction and continued treatment *ad libitum* for the remainder of the time course. Healthy mice, having been instilled with PBS intratracheally as opposed to elastase, were given either L-NIL or water (vehicle) *ad libitum* for conducting multiple comparisons downstream. For the ‘curative’ approach, mice were sacrificed at day 42 post-elastase for assessment of lung damage. For the ‘preventative’ approach, mice were harvested at Day 21 post-elastase. Total lung capacity was reported for both therapeutic approaches (**Figure 5.5**). Disease burden was significant in ‘curative’ and ‘preventative’ EIEE cohorts, independent of L-NIL treatment. Together, we abandoned the notion of attenuating severe emphysema or modulating macrophage activity with TG100 or L-NIL.

Intervention with an experimental biologic.

In a final attempt at attenuating disease in EIEE, we delivered α-CCL2 monoclonal antibody therapeutically, which targets a key trafficking ligand expressed by recruited monocytes and interstitial lung macrophages (IM). This work was inspired, namely, by Shibata and colleagues (2018), who had recently published results supporting a role for IM in driving elastase-induced lung damage. Our lab had also observed robust *Ccl2* expression by IMs from whole lungs post-elastase (refer to figures illustrating IM at single-cell resolution in **Chapter 4**). Therefore, we hypothesized that CCL2-mediated inhibition of IM activity would reduce progressive damage 21 days post-elastase. We induced EIEE in two cohorts of mice, treating one group with α-CCL2, delivered by IP injection at four different timepoints: primary injection at day 0 (i.e. on the same day as EIEE induction), followed by ‘booster’ doses at days 3, 4, and 7 post-elastase. Healthy mice, having been instilled with PBS intratracheally on day 0, were treated with either α-CCL2 or isotype IgG for multiple group comparisons. On day 21 of the EIEE model, mice were sacrificed, and total lung capacity was reported **(Figure 5.6)**. Disease burden, again, was appreciable in elastase-treated mice with or without α-CCL2 therapy. This work was not repeated.

Discussion

In this chapter, we selected a panel of experimental therapeutics with the potential for attenuating disease progression in the EIEE model. Independently, **seven** agents were tested in the EIEE model: metformin, JHU083, DON, TG100, dimethyl itaconate, L-NIL, and therapy with α-CCL2 monoclonal antibody. Drugs were delivered either by oral gavage, intratracheal or intraperitoneal injection. Results from all trials did not support our overarching hypothesis: no experimental compound successfully attenuated severe disease induced by 3U of PPE in male, BALB/cJ mice.

Drugs were chosen either for their proven clinical effectiveness or experimental success in the context of treating chronic, progressive disorders that affect other organs. Although delivered systemically, several drugs tested were expected to modulate, or 'reprogram', lung cell types that may contribute to emphysema progression. Four compounds – metformin, JHU083, DON, and dimethyl itaconate – have been used successfully for reprogramming either macrophages or T-cells that drive tumorigenesis in specific contexts (Cha et al., 2018; Lemberg et al., 2018; Leone et al., 2019; O'Neill and Artyomov, 2019; Pernicova and Korbonits, 2014; Rais et al., 2016). Though we were interested in targeting macrophage biology, substantial evidence in the literature supported that either cell type could be involved in driving disease progression in our EIEE model (Hayashi et al., 2019; Houghton et al., 2006; Lemaire et al., 2021; Shapiro, 1999; Suzuki et al., 2020; Wang et al., 2020b). As mentioned, strategies for therapeutically 'reprograming' cell types that drive emphysema have been discussed for years (Barnes and Stockle, 2005; Ogger and Byrne, 2021; Wang et al., 2020a). At the time, neither metformin, JHU083/DON, nor dimethyl itaconate had been tested previously for attenuating severe emphysema.

Of the seven compounds, reports for metformin as a candidate therapeutic were most diverse, both clinically and experimentally. Metformin was the sole, FDA-approved drug tested in our model and has been used experimentally for modulating hepatocyte metabolism and clinically for treating diabetes since 1958 (Shaw et al., 2005; Sterne, 1957; Watanbe, 1918). Our lab had previously and successfully used this drug for attenuating airway hyperresponsiveness in an experimental model for diet-induced obesity (Gu et al., 2022); and others have expanded the application of metformin for treatments that include cancer, atherosclerosis, and thrombosis (Cha et al., 2018; Soberanes et al., 2019; Vasamsetti et al., 2015). From our preliminary work with metformin, we concluded that this compound was not effective for treating severe, elastase-induced emphysema in male BALB/cJ mice. Unfortunately, our experiments with metformin were limited by technical failures and low, statistical power. Presumably from overdose, multiple animals died during the iteration that included treatment with metformin intratracheally, limiting our ability to achieve a robust readout. Upon modifying the dose, the mice survived, yet still developed significant disease. Indeed, an independent assay that included delivery of a higher dose of metformin by oral gavage resulted in the similar findings, and disease did not improve. However, at least one report has emerged since conducting our metformin experiments that supports use of this drug for attenuating cigarette smoke-induced emphysema (Polverino et al., 2021). Taken together, and prior to excluding metformin as a therapy for preventing severe disease in our EIEE model, we suggest repeating oral gavage experiments with variable doses and larger animal sample sizes.

Experiments that included JHU083, DON, or dimethyl itaconate were also unpromising. These drugs are purported to target the TCA cycle in immune cells including macrophages and T cells (Ahluwalia et al., 1990; Leone et al., 2019; O'Neill and Artyomov, 2019). While we did not test or confirm whether the treatment impacted lung macrophages directly, based on previous studies that used comparable dosing, it was assumed that systemic (oral gavage/IP) or local (intratracheal) delivery of each drug would be sufficient for cellular uptake. Currently, we do not have reason to pursue future work with JHU083/DON or dimethyl itaconate in our severe lung disease model. Further, no COPD-related work has been reported in the literature since conducting these experiments. Though, reports continued to support use of these 'metabolic reprogramming' drugs for cancer therapy (Hanaford et al., 2019; Oh et al., 2020; Yamashita et al., 2020).

Unlike for metformin, JHU083, DON, and dimethyl itaconate, at least one literature report supported our hypothesis that therapy with TG100, the fifth 'metabolic reprogramming' drug in our panel, would attenuate severe disease in our model. A potent PI3-Kinase γ/δ inhibitor, TG100 was tested previously by Doukas and colleagues (2009) for attenuating symptoms of asthma and cigarette smoke-induced inflammation. Their results were arguably more relevant to our EIEE model than drugs tested previously. However, this group did not use functional readouts, affecting our ability to make direct comparisons to their work. Additionally, though superficially comparable to elastase-induced disease, cigarette smoke-induced inflammation causes mild pathology. In work by Doukas et al. (2009), BALB/c mice were challenged passively with smoke from five cigarettes per day and simultaneously nebulized with TG100 at consecutive timepoints. Conclusions were made largely by indirect, cellular readouts obtained from bronchoalveolar lavage fluid after four days of smoke exposure/drug treatment, revealing significantly less neutrophilia in TG100-treated, smoke-exposed animals relative to untreated controls. Though not direct evidence for applying TG100 to our EIEE model, this report was certainly useful when considering experimental design. Ultimately, we concluded that TG100 dissolved in DMSO and delivered intraperitoneally was not effective for attenuating severe emphysema in our BALB/cJ elastase model.

The sixth compound tested in our workflow was L-NIL, a direct inhibitor of inducible nitric oxide synthase (*Nos2* a.k.a. “iNOS”). This drug was mechanistically unique among others in our panel. L-NIL was not expected to induce any long-term, phenotypic ‘reprogramming’ of cell types in the lung. Rather, we hypothesized that iNOS, in general, may be a molecular driver of EIEE pathogenesis and worthy of targeting for therapeutic intervention. Limjunyawong and colleagues (2015) had already reported *Nos2* upregulation in whole lung samples by Day 7 post-elastase. Importantly, Seimetz *et al*. (2011) had successfully used L-NIL therapeutically for attenuating the effects of iNOS upon chronic exposure to cigarette smoke over 8 months. Indeed, for their L-NIL experiments, Siemetz *et al.* (2011) challenged mice with cigarette smoke for a significantly longer duration than did Doukas *et al.* (2009) for studying TG100 therapy. As a result, cigarette-smoke exposed mice in the Siemetz study achieved a more quantifiable, “emphysematous” phenotype, but L-NIL treated animals were not as sick. Notably, this group also collected dynamic compliance as their lung function readout. Total lung capacity, which is our lab’s default metric for determining emphysema severity in BALB/c mice, was not reported. Thus, we attempted to translate L-NIL therapy for attenuating severe emphysema in our BALB/cJ model. We designed our experiments in line with the cigarette smoke study conducted by Siemetz *et al.* (2011) and established a ‘preventative’ and ‘curative’ cohort for studying L-NIL in our model (i.e. one group started L-NIL therapy *ad libitum* two days prior to being challenged with elastase). Regardless, both readouts were negative, as L-NIL-treated animals developed signficant disease and functional deficits similar to elastase-only control animals.

Finally, blocking the recruitment of inflammatory monocytes, as opposed to reprogramming, was attempted using monoclonal antibody therapy as an approach for attenuating experimental emphysema. The notion for using biologics for attenuating chronic lung disease was inspired by the success of α-PD1/L1 therapy for slowing tumorigenesis in the lung (Borghaei et al., 2015; Brahmer et al., 2015). Our final attempt at attenuating EIEE also relied significantly on an informed bias from an unrelated project, as well as from the literature. For this work, we considered a report from Shibata *et al.* (2018), which partially concluded that ‘pathogenic’ interstitial macrophage (IM) subsets were responsible for significant lung damage post-elastase. In their study, *Ccr2*$^{-/-}$ BALB/c animals did not develop severe emphysema post-elastase, relative to WT controls. This finding was significant because bone-marrow (CCR2^{+}) monocytes are thought to traffic to the lung via CCL2, as these cells may ultimately differentiate into IM (Chakarov et al., 2019; Gibbings et al., 2017). In a separate project, we later confirmed at single-cell resolution that mature interstitial macrophages robustly express *Ccl2*, as these cells may be the dominant, CCL2$^+$ mononuclear phagocyte population in the lung. Specifically, our goal with this experiment was to either block monocyte trafficking to the lung or, potentially, deplete IM directly via with systemic delivery of α-CCL2 antibody. In a small (N=3 mice per group), independent assay using this approach, α-CCL2-treated mice developed significant disease comparable to WT, isotype-treated controls. We have no reasonable evidence at this time to accept or reject CCL2 or target cell types as drivers of emphysema in our model.

As mentioned, all of these experiments are limited by inherently low, statistical support and many were only performed once. From a technical standpoint, poor experimental design and unexpected overdoses severely affected our ability to interpret readouts from assays with metformin and DON. Metformin experiments, specifically, tested cohorts with N≤3 animals per group. Additionally, DON was not only difficult to dose due to known, gastrointestinal side effects (Lemberg et al., 2018), but the assay for this drug also did not utilize appropriate vehicle controls for statistical comparison. Future work should be aimed at adjusting the dose and delivery method of both metformin or DON for retesting their efficacy as therapeutics in the EIEE model. Despite being a successful cancer therapy, JHU083 is likely ineffective for attenuating severe, experimental emphysema and, perhaps, does not need to be retested. Readouts from assays that include dimethyl itaconate, TG100, L-NIL or α-CCL2 therapy faced inherent limitations as well. None of these assays were modified or repeated. L-NIL was dissolved in the drinking water, and thus it is unclear whether mice had received a sufficient dose of this drug during the time course. Future work should address concerns with this delivery method, as well as testing different doses. For dimethyl itaconate, TG100, and α-CCL2, drug delivery was likely sufficient; though IT delivery of α-CCL2 may be more effective for targeting lung macrophages, if this assay were to be repeated. Indeed, TG100 and L-NIL experiments should certainly be modified and retested, considering literature-based evidence for each drug as independent modulators of severe, inflammatory lung phenotypes (Doukas et al., 2009; Seimetz et al., 2011). Currently, we have no evidence to support use of dimethyl itaconate, TG100, L-NIL and α-CCL2 for treating severe emphysema.

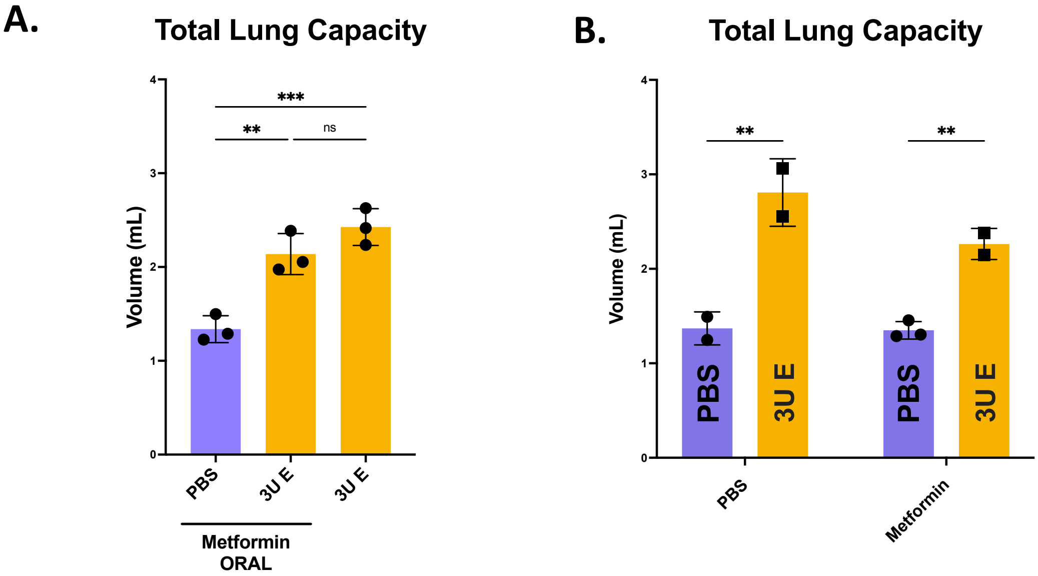

Figure 5.1. Lung function analysis from male, BALB/cJ mice with EIEE, having received metformin treatment over twenty-one days.

Pulmonary function testing was performed with a FlexiVent. (**A**) Total lung capacity of male BALB/cJ mice, having received elastase or PBS intratracheally twenty-one days earlier. During this period, several groups were treated with metformin by oral gavage (**7.5 mg per gavage**, dissolved in PBS), approximately every other day, starting on Day 2 post-elastase. Statistical comparisons were calculated by ordinary one-way ANOVA with Tukey's post-hoc test. *** $p < .001$; ** $p \leq .005$; n.s. = not significant. (**B**) Total lung capacity of healthy and diseased mice treated with metformin or PBS intratracheally (**1.875 mg per instillation**, dissolved in PBS), approximately every four days, starting on Day 4 post-elastase. Statistical comparisons were calculated by two-way ANOVA with Tukey's post-hoc test. ** $p < .005$. Both illustrations represent independent experiments; neither were repeated.

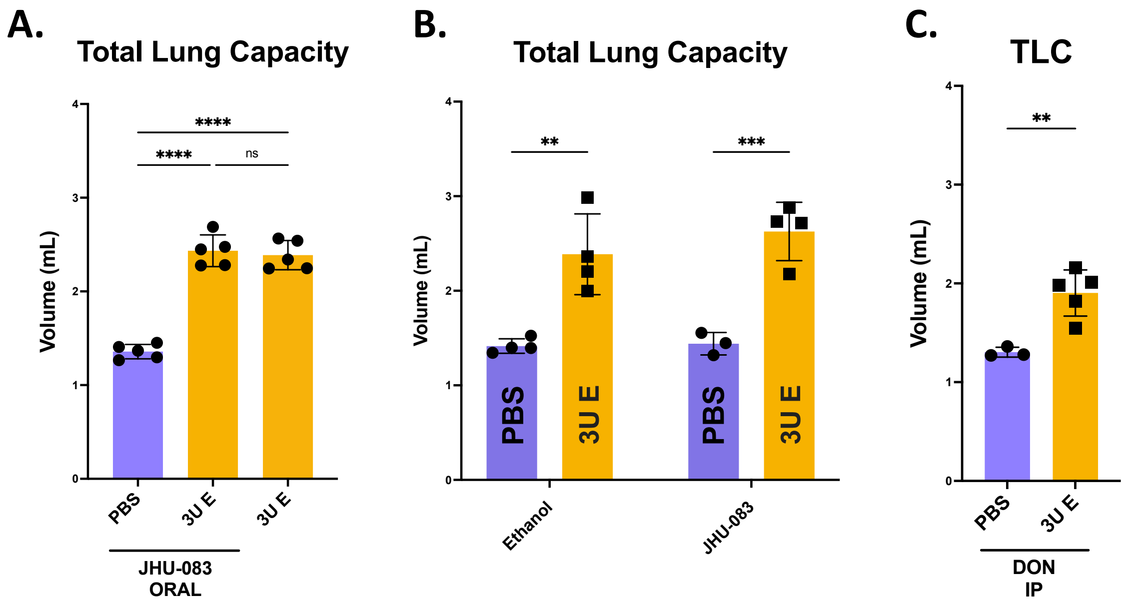

Figure 5.2. Lung function analysis of BALB/cJ mice with EIEE treated with JHU083 or parent compound DON over twenty-one days by various delivery methods.

Pulmonary function testing was performed with a FlexiVent. (**A**) Total lung capacity of male BALB/cJ mice, having received elastase or PBS intratracheally twenty-one days earlier. During this period, healthy and diseased mice were treated with JHU083 orally (**25 µg per gavage,** dissolved in 2.5% (v/v) ethanol in PBS), approximately every other day, starting on Day 2 post-elastase. Statistical comparisons were calculated by ordinary one-way ANOVA with Tukey's post-hoc test. **** p < .0001; n.s. = not significant. (**B**) This assay was repeated with JHU083 delivered intratracheally (**25 µg per instillation**, dissolved in 2.5% (v/v) ethanol in PBS), and with vehicle controls. Statistical comparisons for these experiments were calculated by two-way ANOVA with Tukey's post-hoc test. *** p = .0009; ** p < .005 (C) Total lung capacity of BALB/cJ mice, having received elastase or PBS intratracheally twenty-one days earlier, followed by DON treatment IP (**37.5 µg per injection**, dissolved in PBS). Comparison for this assay is supported by Student's t-test. ** p = .0054. All illustrations represent independent experiments; none were repeated.

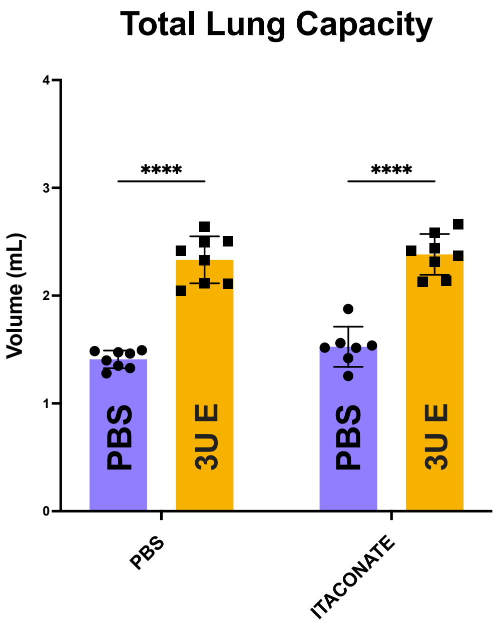

Figure 5.3. Lung function analysis of BALB/cJ mice with EIEE treated intraperitoneally with dimethyl itaconate over twenty-one days.

Pulmonary function testing was performed with a FlexiVent. Male BALB/cJ mice (N≥7 per group) were sacrificed for measuring total lung capacity, having received elastase or PBS intratracheally twenty-one days earlier. During this period, healthy and diseased mice were treated with dimethyl itaconate or vehicle control (PBS) by IP injection (**20 mg per injection**, dissolved in PBS), approximately every other day, starting on Day 2 post-elastase. Statistical comparisons for these experiments were calculated by two-way ANOVA with Tukey's post-hoc test. **** p < .0001. This work was not repeated.

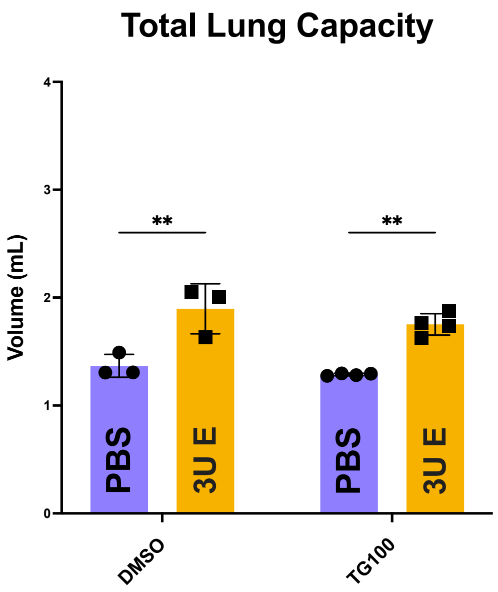

Figure 5.4. Lung function analysis of BALB/cJ mice with EIEE treated intraperitoneally with TG100 over twenty-one days.

Pulmonary function testing was performed with a FlexiVent. Male BALB/cJ mice (N≥3 per group) were sacrificed for measuring total lung capacity, having received elastase or PBS intratracheally twenty-one days earlier. For the duration of the EIEE time course, experimental cohorts of healthy and diseased mice were treated with TG100 or vehicle control (DMSO) by IP injection (**62.5 µg per injection**, dissolved in dimethyl sulfoxide), approximately every other day, starting on Day 4 post-elastase. Statistical comparisons within each group were calculated by two-way ANOVA with Tukey's post-hoc test. ** p ≤ .002; this work was not repeated.

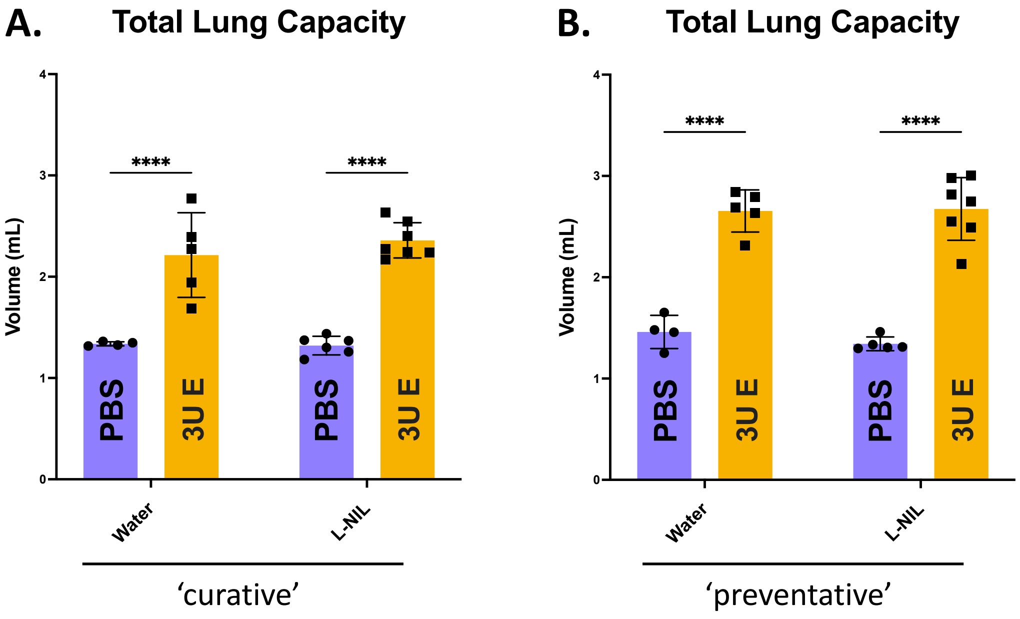

Figure 5.5. Lung function analysis of BALB/cJ mice treated with L-NIL over twenty-one days, either before or after induction of EIEE.

Pulmonary function testing was performed with a FlexiVent. (**A**) Total lung capacity of male BALB/cJ animals in the 'curative' cohort, having received elastase or PBS intratracheally forty-two days earlier. During this period, healthy and diseased mice were provided water with L-NIL *ad libitum* (**600 µg/mL**), starting on Day 14 post-elastase. (**B**) Male BALB/cJ mice in the 'preventative' cohort, which began L-NIL treatment two days prior to the induction of EIEE, were also sacrificed for measuring total lung capacity. During this twenty-one day EIEE time course, healthy and diseased mice continued therapy with L-NIL available in the drinking water *ad libitum.* Statistical comparisons for both experiments were calculated by two-way ANOVA with Tukey's post-hoc test. **** p < .0001 This work was not repeated.

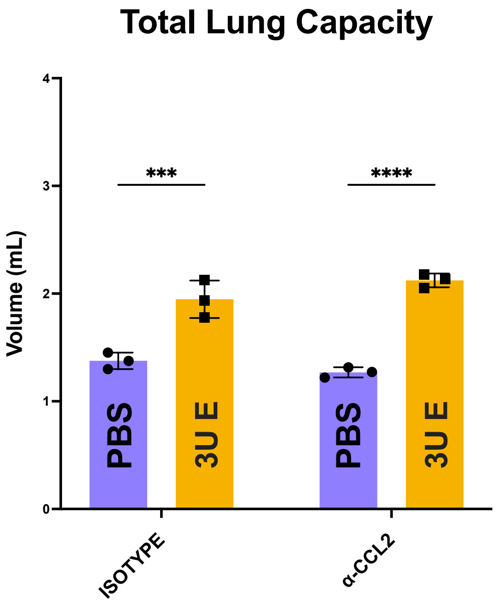

Figure 5.6. Lung function analysis of BALB/cJ mice with EIEE treated with α-CCL2 therapy over twenty-one days.

Pulmonary function testing was performed with a FlexiVent. Male BALB/cJ mice were sacrificed for measuring total lung capacity, having received elastase or PBS intratracheally twenty-one days earlier. During this period, healthy and diseased mice were treated with monoclonal anti-mouse CCL2 antibody or isotype control intraperitoneally (**200 μg per injection**, dissolved in manufacturer's buffer – BioXcell #IP0070) at 4 different timepoints. Statistical comparisons for these experiments were calculated by two-way ANOVA with Tukey's post-hoc test. **** p < .0001; *** = .0006. This work was not repeated.

Conclusion

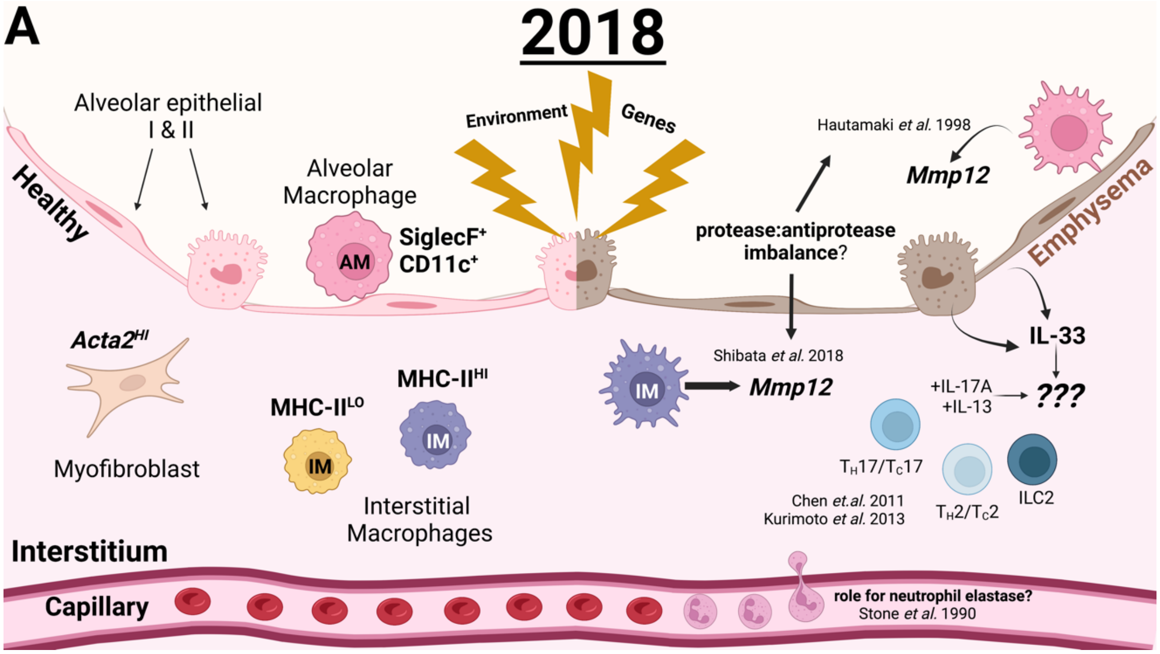
A
2018
Alveolar epithelial
I & II
Healthy
Alveolar
Macrophage
AM
SiglecF+
CD11c+
Environment
Genes
Hautamaki et al. 1998
Mmp12
Emphysema
protease:antiprotease
imbalance?
IL-33
Acta2HI
Myofibroblast
MHC-IIHI
MHC-IILO
IM
IM
Interstitial
Macrophages
Shibata et al. 2018
IM
Mmp12
+IL-17A
+IL-13
???
TH17/TC17
TH2/TC2
ILC2
Chen et.al. 2011
Kurimoto et al. 2013
Interstitium
Capillary
role for neutrophil elastase?
Stone et al. 1990

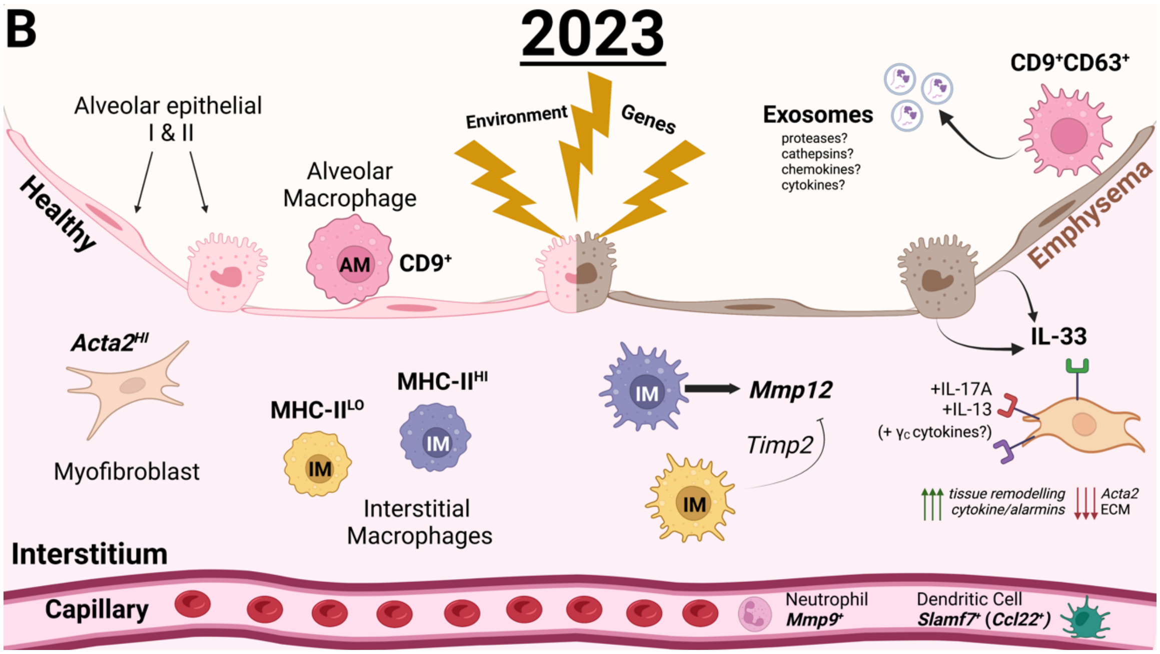
B
2023
Alveolar epithelial
I & II
Healthy
Alveolar
Macrophage
AM
CD9+
Environment
Genes
Exosomes
proteases?
cathepsins?
chemokines?
cytokines?
CD9+CD63+
Emphysema
IL-33
Acta2HI
Myofibroblast
MHC-IIHI
MHC-IILO
IM
IM
Interstitial
Macrophages
IM
Mmp12
Timp2
IM
+IL-17A
+IL-13
(+ γc cytokines?)
tissue remodelling
cytokine/alarmins
Acta2
ECM
Interstitium
Capillary
Neutrophil
Mmp9+
Dendritic Cell
Slamf7+ (Ccl22+)

Our lab has made several contributions to the field of COPD research in this dissertation. I employed the elastase-induced experimental emphysema (EIEE) model and next-generation methods to demonstrate that lung macrophages and fibroblasts are key cells that mediate uncontrolled, progressive lung remodeling as seen in COPD. Mechanistically, we broadly defined the contributions of IL-33, IL-13, and IL-17A in the EIEE model for understanding how they impact severe disease outcomes.

At the time of my joining the lab in 2018 and depicted in the graphical abstract in (**A**), macrophage dysfunction had been strongly associated with tissue damage and emphysema severity in humans and mice. In general, pathology from COPD is thought to be mediated by cell types involved in wound healing processes in the lung. Several genetic factors are thought to predispose animals to developing severe disease; but lung cells ultimately become dysregulated during the response to a primary insult (*i.e.,* cigarette smoke or elastase-challenge). As opposed to regenerating, alveoli lose their structural integrity over time because of overexpression of remodeling proteases like *macrophage metalloelastase*, or *Mmp12*, by either alveolar macrophages (CD11c$^+$SiglecF$^+$) or interstitial macrophage (CD11b$^+$MHC-II^{HI}) subsets in the lung. We and others had indirect mechanistic evidence to suggest that cytokines IL-33, IL-13, and IL-17A contribute to the development of "pathogenic" macrophage subsets that drive emphysema. IL-33 overexpression in whole lungs was previously appreciated by our lab during the acute stages of EIEE and thought to the be the consequence of robust epithelial cell death from elastase challenge. IL-13 and IL-17A are highly upregulated during the acute-to-chronic transition of EIEE pathogenesis, and the source of each cytokine could be either innate or adaptive immune cell types.

Illustrated in (**B**), we now understand that lung fibroblasts are the targets of IL-33, IL-13, and IL-17A *in vitro*, and macrophage activation in our model of emphysema may be dependent on fibroblast-derived factors. *Acta2*$^+$ myofibroblasts, specifically, may contribute directly to protease:anti-protease imbalance in the emphysematous lung through expression of several metalloenzymes and other remodeling factors upon stimulation with these cytokines. We later characterized macrophage subsets with single-cell sequencing and proposed several pathways for dysregulation *in vivo* among CD45$^+$CD64$^+$ cell types in our model. The MHC-II^{LO} subset of interstitial macrophages in the lung was noted as a potent expressor of *Timp2*, which may imply a role for modulating the effects of MHC-II^{Hi}*Mmp12* interstitial macrophages post-elastase, first noted by Shibata *et al.* in 2018. We identified CD9 as a robust surface marker for studying alveolar macrophage function post-elastase, which, in the context of CD63 upregulation, may implicate alveolar macrophages as significant producers of exosomes during the injury response. We identified additional, innate cell types at single cell resolution with 'pathogenic' potential, including *Mmp9*$^+$ neutrophils and *Slamf7*$^+$ dendritic cells, as others have suggested previously that cells of this nature contribute to COPD pathology. Further, attenuated emphysema pathology in $Rag2^{-/-}\gamma_c^{-/-}$ global knockout animals suggests that other cell types and cytokines likely contribute to alveolar degradation and development of disease over time.

References

1. (2022). American Lung Association. In Key Facts About Emphysema.
2. Adams, T.S., Schupp, J.C., Poli, S., Ayaub, E.A., Neumark, N., Ahangari, F., Chu, S.G., Raby, B.A., DeIuliis, G., Januszyk, M*., et al.* (2020). Single-cell RNA-seq reveals ectopic and aberrant lung-resident cell populations in idiopathic pulmonary fibrosis. Sci. Adv. *6*.
3. Adeloye, D., Song, P., Zhu, Y., Campbell, H., Sheikh, A., and Rudan, I. (2022). Global, regional, and national prevalence of, and risk factors for, chronic obstructive pulmonary disease (COPD) in 2019: a systematic review and modelling analysis. Lancet Respir Med *10*.
4. Aegerter, H., Lambrecht, B.N., and Jakubzick, C.V. (2022). Biology of lung macrophages in health and disease. Immunity *55*.
5. Ahluwalia, G.S., GREM, J.L., HAO, Z., and COONEY, D.A. (1990). METABOLISM AND ACTION OF AMINO ACID ANALOG ANTI-CANCER AGENTS. Pharmac. Ther. *46*.
6. Anders, S., and Huber, W. (2010). Differential expression analysis for sequence count data. Genome Biology *11*.
7. Andrews, T.S., Kiselev, V.Y., McCarthy, D., and Hemberg, M. (2021). Tutorial: guidelines for the computational analysis of single-cell RNA sequencing data. Nat. Protocols *16*.
8. Aneas, I., Decker, D.C., Howard, C.L., Sobreira, D.R., Sakabe, N.J., Blaine, K.M., Stein, M.M., Hrusch, C.L., Montefiori, L.E., Tena, J*., et al.* (2021). Asthma-associated genetic variants induce IL33 differential expression through an enhancer- blocking regulatory region. Nat. Comm.
9. Aono, K., Matsumoto, J., Nakagawa, S., Matsumoto, T., Koga, M., Migita, K., Tominaga, K., Sakai, Y., and Yamauchi, A. (2021). Testosterone deficiency promotes the development of pulmonary emphysema in orchiectomized mice exposed to elastase. Biochemical and Biophysical Research Communications *558*.
10. Aran, D., Looney, A.P., Liu, L., Wu, E., Fong, V., Hsu, A., Chak, S., Naikawadi, R.P., Wolters, P.J., Abate, A.R*., et al.* (2019). Reference-based analysis of lung single-cell sequencing reveals a transitional profibrotic macrophage. Nat. Immunol. *20*.
11. Aryal, S., DIAZ-GUZMAN, E., and MANNINO, a.D.M. (2013). COPD and gender differences: an update. Trans. Res. *162*.
12. Ashburner, M., Ball, C.A., Blake, J.A., Botstein, D., Butler, H., Cherry, J.M., Davis, A.P., Dolinski, K., Dwight, S.S., Eppig, J.T*., et al.* (2000). Gene Ontology: tool for the unification of biology. Nat Genet *25*.
13. Ather, J.L., and Poynter, M.E. (2018). Serum amyloid A3 is required for normal weight and immunometabolic function in mice. PLOS ONE *13*.
14. Bain, C.C., and MacDonald, A.S. (2022). The impact of the lung environment on macrophage development, activation and function: diversity in the face of adversity. Mucosal Immunology *15*.

15. Balnis, J., Korponay, T.C., Vincent, C.E., Singer, D.V., Adam, A.P., Lacomis, D., Lee, C.G., Elias, J.A., Harold A. Singer, and Jaitovich, A. (2020). IL-13-driven pulmonary emphysema leads to skeletal muscle dysfunction attenuated by endurance exercise. J Appl Physiol *128*.
16. Barin, J.G., Baldeviano, C., Talor, M.V., Wu, L., Ong, S., Farha, Quader, Chen, P., Zheng, D., Caturegli, P.*, et al.* (2012). Macrophages participate in IL17-mediated inflammation. Eur J Immunol.
17. Barnes, P.J. (2018). Targeting cytokines to treat asthma and chronic obstructive pulmonary disease. Nat. Rev. Immunol. *18*.
18. Barnes, P.J., and Stockle, R.A. (2005). COPD: current therapeutic interventions and future approaches. Eur Respir J.
19. Becht, E., McInnes, L., Healy, J., Dutertre, C.-A., Kwok, I.W.H., Ng, L.G., Ginhoux, F., and Newell, E.W. (2018). Dimensionality reduction for visualizing single-cell data using UMAP. Nat. Biotech.
20. Bedoret, D., Wallemacq, H., Marichal, T., Desmet, C., Calvo, F.Q., Henry, E., Closset, R., Dewals, B., Thielen, C., Gustin, P.*, et al.* (2009). Lung interstitial macrophages alter dendritic cell functions to prevent airway allergy in mice. J. Clin. Invest. .
21. Bhat, T.A., Panzica, L., Kalathil, S.G., and Thanavala, Y. (2015). Immune Dysfunction in Patients with Chronic Obstructive Pulmonary Disease. Ann Am Thorac Soc *12*.
22. Borghaei, H., Paz-Ares, L., Horn, L., Spigel, D.R., Steins, M., Ready, N.E., Chow, L.Q., Vokes, E.E., Felip, E., Holgado, E.*, et al.* (2015). Nivolumab versus Docetaxel in Advanced Nonsquamous Non–Small-Cell Lung Cancer. N Engl J Med *373*.
23. Borrego, F. (2013). The CD300 molecules: an emerging family of regulators of the immune system. Blood *121*.
24. Brahmer, J., Reckamp, K.L., Baas, P., Crinò, L., Eberhardt, W.E.E., Poddubskaya, E., Antonia, S., Pluzanski, A., Vokes, E.E., Holgado, E.*, et al.* (2015). Nivolumab versus Docetaxel in Advanced Squamous-Cell Non–Small-Cell Lung Cancer. N Engl J Med *373*.
25. Buettner, F., Natarajan, K.N., Casale, F.P., Proserpio, V., Scialdone, A., Theis, F.J., Teichmann, S.A., Marioni, J.C., and Stegle, O. (2015). Computational analysis of cell-to-cell heterogeneity in single-cell RnA-sequencing data reveals hidden subpopulations of cells. Nat. Biotech. *33*.
26. Busch, C.J.-L., Favret, J., Geirsdottir, L., Molawi, K., and Sieweke, M.H. (2019). Isolation and long-term cultivation of mouse alveolar macrophages. Bio. Protoc.
27. Butler, A., Hoffman, P., Smibert, P., Papalexi, E., and Satija, R. (2018). Integrating single-cell transcriptomic data across different conditions, technologies, and species. Nat. Biotech. *36*.
28. Castro-Dopico, T., Fleming, A., Dennison, T.W., John R. Ferdinand, Harcourt, K., Stewart, B.J., Cader, Z., Tuong, Z.K., Jing, C., Lok, L.S.C.*, et al.* (2020). GM-CSF Calibrates Macrophage Defense and Wound Healing Programs during Intestinal Infection and Inflammation. Cell Reps. *32*.
29. Cha, J.-H., Yang, W.-H., Xia, W., Wei, Y., Chan, L.-C., Lim, S.-O., Li, C.-W., Kim, T., Chang, S.-S., Lee, H.-H.*, et al.* (2018). Metformin Promotes Antitumor Immunity via Endoplasmic-Reticulum-Associated Degradation of PD-L1. Molecular Cell *71*.

30. Chakarov, S., Lim, H.Y., Tan, L., Lim, S.Y., See, P., Lum, J., Zhang, X.-M., Foo, S., Nakamizo, S., Duan, K.*, et al.* (2019). Two distinct interstitial macrophage populations coexist across tissues in specific subtissular niches. Science *363*.
31. Chen, K., Pociask, D.A., McAleer, J.P., Chan, Y.R., Alcorn, J.F., Kreindler, J., Keyser, M.R., Shapiro, S.D., Houghton, A.M., Kolls, J.K., and Zheng, M. (2011). IL-17RA Is Required for CCL2 Expression, Macrophage Recruitment, and Emphysema in Response to Cigarette Smoke. PLoS ONE *6*.
32. Cohen, M., Giladi, A., Gorki, A.-D., Solodkin, D.G., Zada, M., Hladik, A., Miklosi, A., Salame, T.-M., Halpern, K.B., David, E.*, et al.* (2018). Lung Single-Cell Signaling Interaction Map Reveals Basophil Role in Macrophage Imprinting. Cell *175*.
33. Craig, J.M., Scott, A.L., and Mitzner, W. (2017). Immune-Mediated Inflammation in the Pathogenesis of Emphysema: Insights from Mouse Models. Cell Tissue Res.
34. Das, A., Yang, C.-S., Arifuzzaman, S., Kim, S., Kim, S.Y., Jung, K.H., Lee, Y.S., and Chai, Y.G. (2018). High-resolution Mapping and Dynamics of the Transcriptome, Transcription Factors, and Transcription co-Factor networks in classically and alternatively activated Macrophages. Front. Immunol. *9*.
35. DeNardo, D.G., and Ruffell, B. (2019). Macrophages as regulators of tumour immunity and immunotherapy. Nat. Rev. Immunol. *19*.
36. Dick, S.A., Wong, A., Hamidzada1, H., Nejat1, S., Nechanitzky, R., Vohra, S., Mueller, B., Zaman, R., Kantores, C., Aronoff, L.*, et al.* (2022). Three tissue resident macrophage subsets coexist across organs with conserved origins and life cycles. Sci. Immunol.
37. Doucet, C., Brouty-Boyé, D., Pottin-Clémenceau, C., Canonica, G.W., Jasmin, C., and Azzarone, B. (1998). Interleukin (IL) 4 and IL-13 Act on Human Lung Fibroblasts. J. Clin. Invest. *101*.
38. Doukas, J., Eide, L., Stebbins, K., Racanelli-Layton, A., Dellamary, L., Martin, M., Dneprovskaia, E., Noronha, G., Soll, R., Wrasidlo, W.*, et al.* (2009). Aerosolized Phosphoinositide 3-Kinase g/d Inhibitor TG100-115 [3-[2,4-Diamino-6-(3-hydroxyphenyl)pteridin-7-yl]phenol] as a Therapeutic Candidate for Asthma and Chronic Obstructive Pulmonary Disease. J. PHARM. EXP. THER.
39. Doyle, A.D., Mukherjee, M., LeSuer, W.E., Bittner, T.B., Pasha, S.M., Frere, J.J., Neely, J.L., Kloeber, J.A., Shim, K.P., Ochkur, S.I.*, et al.* (2019). Eosinophil-derived IL-13 promotes emphysema. Eur Respir J *53*.
40. Edelman, B.L., and Redente, E.F. (2018). Isolation and Characterization of Mouse Fibroblasts, Vol 1809.
41. Edelson, J.D., MacFadden, D.K., Klein, M., and Rebuck, A.S. (1985). AUTOFLUORESCENCE OF ALVEOLAR MACROPHAGES: PROBLEMS AND POTENTIAL SOLUTIONS. Medical Hypotheses *17*.
42. Eissmann, M.F., Dijkstra, C., Jarnicki, A., Phesse, T., Brunnberg, J., Poh, A.R., Etemadi, N., Tsantikos, E., Thiem, S., Huntington, N.D.*, et al.* (2019). IL-33-mediated mast cell activation promotes gastric cancer through macrophage mobilization. Nat. Comm. *10*.
43. Epelman, S., Lavine, K.J., Beaudin, A.E., Sojka, D.K., Carrero, a.A., Calderon, B., Brija, T., Gautier, E.L., Ivanov, S., Satpathy, A.T.*, et al.* (2014). Embryonic and Adult-Derived

Resident Cardiac Macrophages Are Maintained through Distinct Mechanisms at Steady State and during Inflammation. Immunity *40*.

44. Evren, E., Ringqvist, E., Tripath, K.P., Sleiers, N., Rives, I.C., Alisjahbana, A., Gao, Y., Sarhan, D., Halle, T., Sorini, C.*, et al.* (2021). Distinct developmental pathways from blood monocytes generate human lung macrophage diversity. Immunity *54*.
45. Ewing, B., and Green, P. (1998). Base-Calling of Automated Sequencer Traces Using Phred. II. Error Probabilities. Genome Res. *8*.
46. Ewing, B., Hillier, L., Wendl, M.C., and Green, P. (1998). Base-Calling of Automated Sequencer Traces Using Phred. I. Accuracy Assessment. Genome Res. *8*.
47. Fabrik, I., Bilkei-Gorzo, O., Fabrikova, D., Öberg, M., Fuchs, J., Sihlbom, C., Göransson, M., and Härtlova, A. (2022). Lung macrophages utilize unique cathepsin K-dependent phagosomal machinery to degrade intracellular collagen. BioRxiv *PrePrint*.
48. Fallica, J., Das, S., Horton, M., and Mitzner, W. (2011). Application of carbon monoxide diffusing capacity in the mouse lung. J Appl Physiol *110*.
49. Finak, G., McDavid, A., Yajima, M., Deng, J., Gersuk, V., Shalek, A.K., Slichter, C.K., Miller, H.W., McElrath, M.J., Prlic, M.*, et al.* (2015). MAST: a flexible statistical framework for assessing transcriptional changes and characterizing heterogeneity in single-cell RNA sequencing data. Genome Biology *16*.
50. FitzPatrick, R.D., Kennedy, M.H.E., Lawrence, K.M., Gauthier, C.M., Moeller, B.E., Robinson, A.N., and Reynolds, L.A. (2020). Littermate-Controlled Experiments Reveal Eosinophils Are Not Essential for Maintaining Steady-State IgA and Demonstrate the Influence of Rearing Conditions on Antibody Phenotypes in Eosinophil-Deficient Mice. Front. Immmunol. *11*.
51. Foreman, M.G., Zhang, L., Murphy, J., Hansel, N.N., Make, B., Hokanson, J.E., Washko, G., Regan, E.A., Crapo, J.D., Silverman, E.K., and DeMeo, D.L. (2011). Early-Onset Chronic Obstructive Pulmonary Disease Is Associated with Female Sex, Maternal Factors, and African American Race in the COPDGene Study. Am J Respir Crit Care Med *184*.
52. Foster, J.A., Rich, C.B., and Miller, M.F. (1990). Pulmonary Fibroblasts: an in Vitro Model of Emphysema. J. Biol. Chem.
53. Fulkerson, P.C., Fischetti, C.A., Hassman, L.M., Nikolaidis, N.M., and Rothenberg, M.E. (2006). Persistent Effects Induced by IL-13 in the Lung. Am J Respir Cell Mol Biol *35*.
54. Furth, R.v., and Cohn, Z.A. (1968). THE ORIGIN AND KINETICS OF MONONUCLEAR PHAGOCYTES.
55. Galluzzi, L., Kepp, O., and Kroemer, G. (2012). Mitochondria: master regulators of danger signalling. Nat. Rev. Mol. Cell Biol. *13*.
56. Ge, S., Hertel, B., Susnik, N., Rong, S., Dittrich, A.M., Schmitt, R., Haller, H., and Vietinghoff, S.v. (2014). Interleukin 17 Receptor A Modulates Monocyte Subsets and Macrophage Generation In Vivo. PLOS ONE *9*.
57. Gibbings, S.L., Thomas, S.M., Atif, S.M., McCubbrey, A.L., Desch, N., Danhorn, T., Leach, S.M., Bratton, D.L., Henson, P.M., Janssen, W.J., and Jakubzick, C.V. (2017).

Three Unique Interstitial Macrophages in the Murine Lung at Steady State. Am J Respir Cell Mol Biol *57*.

58. Ginhoux, F., Greter, M., Leboeuf, M., Nandi, S., See, P., Gokhan, S., Mehler, M.F., Conway, S.J., Ng, L.G., Stanley, E.R.*, et al.* (2010). Fate Mapping Analysis Reveals That Adult Microglia Derive from Primitive Macrophages. Science *330*.
59. Gordon, S. (2003). ALTERNATIVE ACTIVATION OF MACROPHAGES. Nat Rev Immunol *3*.
60. Gorki, A.-D., Symmank, D., Zahalka, S., Lakovits, K., Hladik, A., Langer, B., Maurer, B., Sexl, V., Kain, R., and Knapp, S. (2022). Murine Ex Vivo Cultured Alveolar Macrophages Provide a Novel Tool to Study Tissue-Resident Macrophage Behavior and Function. Am J Respir Cell Mol.
61. Grunig, G., Warnock, M., Wakil, A.E., Venkayya, R., Brombacher, F., Rennick, D.M., Sheppard, D., Mohrs, M., Donaldson, D.D., Locksley, R.M., and Corry, D.B. (1998). Requirement for IL-13 Independently of IL-4 in Experimental Asthma. Science *282*.
62. Gschwend, J., Sherman, S.P.M., Ridder, F., Feng, X., Liang3, H.-E., Locksley, R.M., Becher2, B., and Schneider, C. (2021). Alveolar macrophages rely on GM-CSF from alveolar epithelial type 2 cells before and after birth. J. Exp. Med. *218*.
63. Gu, C., Loube, J., Lee, R., Bevans-Fonti, S., Wu, T.D., Barmine, J.H., Jun, J.C., McCormack, M.C., Hansel, N.N., Mitzner, W., and Polotsky, V.Y. (2022). Metformin Alleviates Airway Hyperresponsiveness in a Mouse Model of Diet-Induced Obesity. Front. Physiol. *13*.
64. Guilliams, M., Kleer, I.D., Henri, S., Post, S., Vanhoutte, L., Prijck, S.D., Deswarte, K., Malissen, B., Hammad, H., and Lambrecht, B.N. (2013). Alveolar macrophages develop from fetal monocytes that differentiate into long-lived cells in the first week of life via GM-CSF. J Exp Med.
65. Hafemeister, C., and Satija, R. (2019). Normalization and variance stabilization of single-cell RNA-seq data using regularized negative binomial regression. Genome Biology *20*.
66. Hallgren, O., Nihlberg, K., Dahlbäck, M., Bjermer, L., Eriksson, L.T., Erjefält, J.S., Löfdahl, C.-G., and Westergren-Thorsson, G. (2010). Altered fibroblast proteoglycan production in COPD. Respiratory Research *11*.
67. Halpin, D.M.G., Criner, G.J., Papi, A., Singh, D., Anzueto, A., Martinez, F.J., Agusti, A.A., and Vogelmeier, C.F. (2021). Global Initiative for the Diagnosis, Management, and Prevention of Chronic Obstructive Lung Disease. Am J Respir Crit Care Med *203*.
68. Hanaford, A.R., Alt, J., Rais, R., Wang, S.Z., Kaur, H., L.J., D., Thorek, Eberhart, C.G., S., B., Slusher*, et al.* (2019). Orally bioavailable glutamine antagonist prodrug JHU-083 penetrates mouse brain and suppresses the growth of MYC- driven medulloblastoma. Translational Oncology *12*.
69. Hashimoto, D., Chow, A., Noizat, C., Teo, P., Beasley, M.B., Leboeuf, M., Becker, C.D., See, P., Price, J., Lucas, D.*, et al.* (2013). Tissue-Resident Macrophages Self-Maintain Locally throughout Adult Life with Minimal Contribution from Circulating Monocytes. Immunity *38*.

70. Hautamaki, R.D., Kobayashi, D.K., Senior, R.M., and Shapiro, S.D. (1997). Requirement for Macrophage Elastase for Cigarette Smoke–Induced Emphysema in Mice. Science *277*.
71. Hayashi, S., Matsuno, Y., Tsunoda, Y., Sakurai, H., Kiwamoto, T., Morishima, Y., Ishii, Y., Yoh, K., Takahashi, S., and Hizawa, N. (2019). Transcription Factor T-bet Attenuates the Development of Elastase-induced Emphysema in Mice. Am J Respir Cell Mol Biol *61*.
72. He, Y., Bouwstra, R., Wiersma, V.R., Jon, M.d., Lourens, H.J., Fehrmann, R., Bruyn, M.d., Ammatuna, E., Huls, G., Meerten, T.v., and Bremer, E. (2019). Cancer cell-expressed SLAMF7 is not required for CD47-mediated phagocytosis. Nat. Comm. *10*.
73. Hey, J., Paulsen, M., Toth, R., Weichenhan, D., Butz, S., Schatterny, J., Liebers, R., Lutsik, P., Plass, C., and Mall, M.A. (2021). Epigenetic reprogramming of airway macrophages promotes polarization and inflammation in muco-obstructive lung disease. . Nat. Comm. *12*.
74. Hill, D.A., Lima, H.-W., Kima, Y.H., Hoa, W.Y., Foong, Y.H., Nelsona, V.L., Nguyena, H.C.B., Chegireddy, K., Kima, J., Habertheuere, A.*, et al.* (2018). Distinct macrophage populations direct inflammatory versus physiological changes in adipose tissue. Proc. Natl. Acad. Sci. USA *115*.
75. Hoeffel, G., Wang, Y., Greter, M., See, P., Teo, P., Malleret, B., Leboeuf, M., Low, D., Oller, G., Almeida, F.*, et al.* (2012). Adult Langerhans cells derive predominantly from embryonic fetal liver monocytes with a minor contribution of yolk sac–derived macrophages. J. Exp. Med *209*.
76. Hofmann, U., Knorr, S., Vogel, B., Weirather, J., Frey, A., Ertl, G., and Frantz, S. (2014). Interleukin-13 Deficiency Aggravates Healing and Remodeling in Male Mice After Experimental Myocardial Infarction. Circ Heart Fail.
77. Holmdahl, R., and Malissen, B. (2012). The need for littermate controls. Eur. J. Immunol. *42*.
78. Hou, X., Chen, G., Bracamonte-Baran, W., Choi, H.S., Diny, N.L., Sung, J., Hughes, D., Won, T., Wood, M.K., Talor, M.V.*, et al.* (2019). The Cardiac Microenvironment Instructs Divergent Monocyte Fates and Functions in Myocarditis. *Cell Reports*.
79. Houghton, A.M., Quintero, P.A., Perkins, D.L., Kobayashi, D.K., Kelley, D.G., Marconcini, L.A., Mecham, R.P., Senior, R.M., and Shapiro, S.D. (2006). Elastin fragments drive disease progression in a murine model of emphysema. J. Clin. Invest. *113*.
80. Huber, G.L., Davies, P., Zwilling, G.R., Pochay, V.E., Hinds, W.C., Nicholas, H.A., Mahajan, V.K., Hayashi, M., and First, M.W. (1981). A morphologic and physiologic bioassay for quantifying alterations in the lung following experimental chronic inhalation of tobacco smoke. Bulletin europeen de physiopathologie respiratoire *17*.
81. Hunninghake, G.W., Davidson, J.M., Rennard, S., Szapiel, S., Gadek, E., and Crystal, R.G. (1981). Elastin Fragments Attract Macrophage Precursors to Diseased Sites in Pulmonary Emphysema. Science *212*.
82. III, R.L.G., Wilson, M.S., and Wynn, T.A. (2018). Type 2 immunity in tissue repair and fibrosis. Nat. Rev. Immun. *18*.

83. Ilicic, T., Kim, J.K., Kolodziejczyk, A.A., Bagger, F.O., McCarthy, D.J., Marioni, J.C., and Teichmann, S.A. (2016). Classification of low quality cells from single-cell RNA-seq data. Genome Biology *17*.
84. Ingram, J.L., Huggins, M.J., Church, T.D., Li, Y., Francisco, D.C., Degan, S., Firszt, R., Beaver, D.M., Lugogo, N.L., Wang, Y.*, et al.* (2011). Airway Fibroblasts in Asthma Manifest an Invasive Phenotype. Am J Respir Crit Care Med.
85. Ingram, J.L., Rice, A.B., Geisenhoffer, K., Madtes, D.K., and Bonner, J.C. (2004). IL-13 and IL-1β promote lung fibroblast growth through coordinated up-regulation of PDGF-AA and PDGF-Rα. FASEB.
86. Islam, S., Zeisel, A., Joost, S., Manno, G.L., Zajac, P., Kasper, M., Lönnerberg, P., and Linnarsson, S. (2014). Quantitative single-cell rna-seq with unique molecular identifiers. Nat. Methods *11*.
87. Izbicki, G., SEGEL, M.J., CHRISTENSEN, T.G., CONNER, M.W., and BREUER, R. (2002). Time course of bleomycin-induced lung fibrosis. Int. J. Exp. Path. *83*.
88. Jaitin, D.A., Adlung, L., Thaiss, C.A., Weiner, A., Li, B., Descamps, H., Lundgren, P., Bleriot, C., Liu, Z., Deczkowska, A.*, et al.* (2019). Lipid-Associated Macrophages Control Metabolic Homeostasis in a Trem2-Dependent Manner. Cell *178*.
89. Jaitin, D.A., Kenigsberg, E., Keren-Shaul, H., Elefant, N., Paul, F., Zaretsky, I., Mildner, A., Cohen, N., Jung, S., Tanay, A., and Amit, I. (2014). Massively Parallel Single-Cell RNA-Seq for Marker-Free Decomposition of Tissues into Cell Types. Science *343*.
90. John, A.E., Wilson, M.R., Habgood, A., Porte, J., Tatler, A.L., Stavrou, A., Miele, G., Jolly, L., Knox, A.J., Takata, M.*, et al.* (2016). Loss of epithelial Gq and G11 signaling inhibits TGFb production but promotes IL-33–mediated macrophage polarization and emphysema. Sci. Signal. *9*.
91. Joo, H., Park, S.J., Min, K.H., and Rhee4, C.K. (2021). Association between plasma interleukin-33 level and acute exacerbation of chronic obstructive pulmonary disease. BMC Pulm Med *21*.
92. Kang, M.-J., Choi, J.-M., Kim, B.H., Lee, C.-M., Cho, W.-K., Choe, G., Kim, D.-H., Lee, C.G., and Elias, J.A. (2012). IL-18 Induces Emphysema and Airway and Vascular Remodeling via IFN-g, IL-17A, and IL-13. Am J Respir Crit Care Med *185*.
93. Kaplan, M.H., Schindler, U., Smiley, S.T., and Grusby, M.J. (1996). Stat6 Is Required for Mediating Responses to IL-4 and for the Development of Th2 Cells. Immunity *4*.
94. Kim, D., Paggi, J.M., Park, C., Bennett, C., and Salzberg, S.L. (2019). Graph-based genome alignment and genotyping with HISAT2 and HISAT-genotype. Nat Biotech.
95. Korsunsky, I., Millard, N., Fan, J., Slowikowski, K., Zhang, F., Wei, K., Baglaenko, Y., Brenner, M., Loh, P.-r., and Raychaudhuri, S. (2019). Fast, sensitive and accurate integration of single-cell data with Harmony. Nat. Methods *16*.
96. Kurimoto, E., Miyahara1, N., Kanehiro, A., Waseda, K., Taniguchi, A., Ikeda, G., Koga, H., Nishimori, H., Tanimoto, Y., Kataoka, M.*, et al.* (2013). IL-17A is essential to the development of elastase-induced pulmonary inflammation and emphysema in mice. Respiratory Research *14*.
97. Kurowska-Stolarska, M., Stolarski, B., Kewin, P., Murphy, G., Corrigan, C.J., Ying, S., Pitman, N., Mirchandani, A., Rana, B., Rooijen, N.v.*, et al.* (2009). IL-33 Amplifies the

Polarization of Alternatively Activated Macrophages That Contribute to Airway Inflammation. J Immunol.

98. Lajoie, S., Lewkowich, I.P., Suzuki, Y., Clark, J.R., Sproles, A.A., Dienger, K., Budelsky, A.L., and Wills-Karp, M. (2010). Complement-mediated regulation of the IL-17A axis is a central genetic determinant of the severity of experimental allergic asthma. Nat Immunol.
99. Lancien, M., Bienvenu, G., Salle, S., Gueno, L., Magalie Feyeux, Merieau, E., Remy, S., Even, A., Moreau, A., Molle, A.*, et al.* (2021). Dendritic Cells Require TMEM176A/B Ion Channels for Optimal MHC Class II Antigen Presentation to Naive CD4+ T Cells. J Immunol *207*.
100. Lavin, Y., Winter, D., Blecher-Gonen, R., David, E., Keren-Shaul, H., Merad, M., Jung, S., and Amit, I. (2014). Tissue-Resident Macrophage Enhancer Landscapes Are Shaped by the Local Microenvironment. Cell.
101. Lee, J.H., Hailey, K.L., Vitorino, S.A., Jennings, P.A., Bigby, T.D., and Breen, E.C. (2019). Cigarette Smoke Triggers IL-33–associated Inflammation in a Model of Late-Stage Chronic Obstructive Pulmonary Disease. Am J Respir Cell Mol Biol *61*.
102. Lemaire, F., Audonnet, S., Perotin, J.M., Gaudry, P., Dury, S., Ancel, J., Lebargy, F., Antonicelli, F., Gaëtan Deslée3, and Naour, R.L. (2021). The elastin peptide VGVAPG increases CD4+ T-cell IL-4 production in patients with chronic obstructive pulmonary disease. Respir Res *22*.
103. Lemberg, K.M., Vornov, J.J., Rais, R., and Slusher, B.S. (2018). We're Not "DON" Yet: Optimal Dosing and Prodrug Delivery of 6- Diazo-5-oxo-L-norleucine. Mol Cancer Ther. *17*.
104. Leone, R.D., Zhao, L., Englert, J.M., Sun, I.-M., Oh, M.-H., Sun, I.-H., Arwood, M.L., Bettencourt, I.A., Patel, C.H., Wen, J.*, et al.* (2019). Glutamine blockade induces divergent metabolic programs to overcome tumor immune evasion. Science.
105. Ley, K. (2017). M1 Means Kill; M2 Means Heal. J Immunol *199*.
106. Li, D., Guabiraba, R., Besnard, A.-G., Komai, M., Jabir, M.S., and Zhang, L. (2014). IL-33 promotes ST2-dependent lung fibrosis by the induction of alternatively activated macrophages and innate lymphoid cells in mice. J Allergy and Clinical Immunology *134*.
107. Li, F., Piattini, F., Pohlmeier, L., Feng, Q., Rehrauer, H., and Kopf, M. (2022). Monocyte-derived alveolar macrophages autonomously determine severe outcome of respiratory viral infection. Sci. Immunol.
108. Li, X., Noell, G., Tabib, T., Gregory, A.D., Trejo, H.E., Vats, B.R., Kaminski, T.W., Sembrat, J., Snyder, M.E., Chandra, D.*, et al.* (2021). Single cell RNA sequencing identifies IGFBP5 and QKI as ciliated epithelial cell genes associated with severe COPD. Respir. Res.
109. Liegeois, M., Bai, Q., Fievez, L., Pirottin, D., Legrand, C.l., Guiot, J., Schleich, F., Corhay, J.-L., Louis, R., Marichal, T., and Bureau, F. (2022). Airway Macrophages Encompass Transcriptionally and Functionally Distinct Subsets Altered by Smoking. Am J Respir Cell Mol Biol *67*.

110. Limjunyawong, N., Craig, J.M., Lagassé, H.A.D., Scott, A.L., and Mitzner, W. (2015a). Experimental progressive emphysema in BALB/cJ mice as a model for chronic alveolar destruction in humans. Am J Physiol Lung Cell Mol Physiol *309*.

111. Limjunyawong, N., Fallica, J., ARamakrishnan, Datta, K., Gabrielson, M., Horton, M., and Mitzner, W. (2015b). Phenotyping mouse pulmonary function in vivo with the lung diffusing capacity. J Vis Exp. *95*.

112. Livak, K.J., and Schmittgen, T.D. (2001). Analysis of Relative Gene Expression Data Using Real- Time Quantitative PCR and the 2-ΔΔCt Method. Methods *25*.

113. Love, M.I., Huber, W., and Anders, S. (2014). Moderated estimation of fold change and dispersion for RNA-seq data with DESeq2. Genome Biology *15*.

114. Lucey, E.C., Keane, J., Kuang, P.-P., Snider, G.L., and Goldstein, R.H. (2002). Severity of elastase-induced emphysema is decreased in tumor necrosis factor-alpha and interleukin-1beta receptor-deficient mice. Lab Invest. *82*.

115. Luo, M., Lai, W., He, Z., and Wu, L. (2021). Development of an Optimized Culture System for Generating Mouse Alveolar Macrophage−like Cells. J. Immunol.

116. Mangan, N.E., Dasvarma, A., McKenzie, A.N.J., and Fallon, P.G. (2007). T1/ST2 expression on Th2 cells negatively regulates allergic pulmonary inflammation. Eur. J. Immunol. *37*.

117. Mantovani, A., Allavena, P., Marchesi, F., and Garlanda, C. (2022). Macrophages as tools and targets in cancer therapy. Nat. Rev. Drug Discov.

118. Martine, F.J., Collard, H.R., Pardo, A., Raghu, G., Richeldi, L., Selman, M., Swigris, J.J., Taniguchi, H., and Wells, A.U. (2017). Idiopathic pulmonary fibrosis. Nat. Rev. Dis. Pri. *3*.

119. Martinez, F.J., Han, M.K., Allinson, J.P., Barr, R.G., Boucher, R.C., M.A.Calverley, P., BartolomeR.Celli, StephanieA.Christenson, RonaldG.Crystal, Fagera, M.*, et al.* (2018). At the Root: Defining and Halting Progression of Early Chronic Obstructive Pulmonary Disease. Am J Respir Crit Care Med *197*.

120. Matthews, D.J., Emson, C.L., McKenzie, G.J., Jolin, H.E., Blackwell, J.M., and McKenzie, A.N.J. (2000). IL-13 Is a Susceptibility Factor for Leishmania major Infection. J Immunol *164*.

121. McKenzie, G.J., Bancroft, A., Grencis, R.K., and McKenzie, A.N.J. (1998a). A distinct role for interleukin-13 in Th2-cell-mediated immune responses. Current Biol. *8*.

122. McKenzie, G.J., Emson, C.L., Bell, S.E., Anderson, S., Fallon, P., Zurawski, G., Murray, R., Grencis, R., and McKenzie, A.N.J. (1998b). Impaired Development of Th2 Cells in IL-13-Deficient Mice. Immunity *9*.

123. Meghraoui-Kheddar, A., Pierre, A., Sellami, M., Audonnet, S., Lemaire, F., and Naour, R.L. (2017). Elastin receptor (S-gal) occupancy by elastin peptides modulates T-cell response during murine emphysema. Am J Physiol Lung Cell Mol Physiol *313*.

124. Mi, S., Li, Z., Yang, H.-Z., Liu, H., Wang, J.-P., Ma, Y.-G., Wang, X.-X., Liu, H.-Z., Sun, W., and Hu, Z.-W. (2011). Blocking IL-17A Promotes the Resolution of Pulmonary Inflammation and Fibrosis Via TGF-β1−Dependent and −Independent Mechanisms. J Immunol *187*.

125. Mills, C.D., Kincaid, K., Alt, J.M., Heilman, M.J., and Hill, A.M. (2000). M-1/M-2 Macrophages and the Th1/Th2 Paradigm. J Immunol *164*.

126. Misharin, A.V., Morales-Nebreda, L., Mutlu, G.M., Budinger, G.R.S., and Perlman, H. (2013). Flow Cytometric Analysis of Macrophages and Dendritic Cell Subsets in the Mouse Lung. Am J Respir Cell Mol Biol *49*.

127. Misharin, A.V., Morales-Nebreda, L., Reyfman, P.A., Cuda, C.M., Walter, J.M., McQuattie-Pimentel, A.C., Chen, C.-I., Anekalla, K.R., Joshi, N., Williams, K.J.N*., et al.* (2017). Monocyte-derived alveolar macrophages drive lung fibrosis and persist in the lung over the life span. J. Exp. Med.

128. Montanari, E., Stojkovic, S., Kaun, C., Lemberger, C.E., Martin, R.d., Rauscher, S., Gröger, M., Maurer, G., Neumayer, C., Huk, I*., et al.* (2016). Interleukin-33 stimulates GM-CSF and M-CSF production by human endothelial cells. Thromb Haemost *116*.

129. Mostaço-Guidolin, L.B., Osei, E.T., Ullah, J., Hajimohammadi, S., Fouadi, M., Li, X., Li, V., Shaheen, F., Yang, C.X., Chu, F*., et al.* (2019). Defective Fibrillar Collagen Organization by Fibroblasts Contributes to Airway Remodeling in Asthma. Am J Respir Crit Care Med *200*.

130. Mould, K.J., Jackson, N.D., Henson, P.M., Seibold, M., and Janssen, W.J. (2019). Single cell RNA sequencing identifies unique inflammatory airspace macrophage subsets. JCI Insight *4*.

131. Niikura, Y., Ishii, T., Hosoki, K., Nagase, T., and Yamashita, N. (2015). Ovary-dependent emphysema augmentation and osteopontin induction in adult female mice. Biochemical and Biophysical Research Communications *461*.

132. Ning, S., Pagano, J., and Barber, G. (2011). IRF7: activation, regulation, modification and function. Genes and Immunity *12*.

133. O'Beirne, S.L., Kikkers, S.A., Oromendia, C., Salit, J., Rostmai, M.R., Ballman, K.V., Kaner, R.J., and Crystal, R.G. (2020). Alveolar Macrophage Immunometabolism and Lung Function Impairment in Smoking and Chronic Obstructive Pulmonary Disease. Am J Respir Crit Care Med *201*.

134. O'Connell, P., Pepelyayeva, Y., Blake, M.K., Hyslop, S., Crawford, R.B., Rizzo, M.D., Pereira-Hicks, C., Godbehere, S., Dale, L., Gulick, P*., et al.* (2019). SLAMF7 is a critical negative regulator of interferon-α-mediated CXCL10 production in chronic HIV infection. J Immunol *202*.

135. O'Neill, L.A.J., and Artyomov, M.N. (2019). Itaconate: the poster child of metabolic reprogramming in macrophage function. Nat. Rev. Immunol.

136. Ogger, P.P., and Byrne, A.J. (2021). Macrophage metabolic reprogramming during chronic lung disease. Mucosal Immunology.

137. Oh, M.-H., Sun, I.-H., Zhao, L., Leone, R.D., Sun, I.-M., Xu, W., Collins, S.L., Tam, A.J., Blosser, R.L., Patel, C.H*., et al.* (2020). Targeting glutamine metabolism enhances tumor-specific immunity by modulating suppressive myeloid cells. J Clin Invest. *130*.

138. Palmieri, E.M., Menga, A., Martın-Perez, R., Quinto, A., Riera-Domingo, C., Tullio, G.D., Hooper, D.C., Lamers, W.H., Ghesquie, B., McVicar, D.W*., et al.* (2017). Pharmacologic or Genetic Targeting of Glutamine Synthetase Skews Macrophages toward an M1-like Phenotype and Inhibits Tumor Metastasis. Cell Reps. *20*.

139. Pauwels, R.A., and Rabe, K.F. (2004). Burden and clinical features of chronic obstructive pulmonary disease (COPD). Lancet *364*.

140. Pernicova, I., and Korbonits, M. (2014). Metformin—mode of action and clinical implications for diabetes and cancer. Nat. Rev. Endocrin. *10*.

141. Pisu, D., Huang, L., Narang, V., Theriault, M., LeBury, G., Lee, B., Lakudzala, A.E., Mzinza, D.T., Mhango, D.V., Mitini-Nkhoma, S.C.*, et al.* (2021). Single cell analysis of M. tuberculosis phenotype and macrophage lineages in the infected lung. J. Exp. Med *218*.

142. Pittet, M.J., Michielin, O., and Migliorini, D. (2022). Clinical relevance of tumour-associated macrophages. Nat. Rev. Clin. Oncol. *19*.

143. Podolin, P.L., Foley, J.P., Carpenter, D.C., Bolognese, B.J., Logan, G.A., III, E.L., Harrison, O.J., and Walsh, P.T. (2013). T cell depletion protects against alveolar destruction due to chronic cigarette smoke exposure in mice. Am J Physiol Lung Cell Mol Physiol *304*.

144. Polverino, F., Wu, T.D., Rojas-Quintero, J., Wang, X., Mayo, J., Tomchaney, M., Tram, J., Packard, S., Zhang, D., Cleveland, K.H.*, et al.* (2021). Metformin: Experimental and Clinical Evidence for a Potential Role in Emphysema Treatment. Am J Respir Crit Care Med *204*.

145. Qiu, C., Li, Y., Li, M., Min Li, Liu, X., McSharry, C., and Xu, D. (2012). Anti-interleukin-33 inhibits cigarette smoke-induced lung inflammation in mice. Immunology *138*.

146. Raes, G., Bergh, R.V.d., Baetselier, P.D., and Ghassabeh, G.H. (2005). Arginase-1 and Ym1 Are Markers for Murine, but Not Human, Alternatively Activated Myeloid Cells. J Immunol *174*.

147. Rais, R., Jancăřík, A., Tenora, L., Nedelcovych, M., Alt, J., Engler, J., Rojas, C., Le, A., Elgogary, A., Tan, J.*, et al.* (2016). Discovery of 6-Diazo-5-oxo-L-norleucine (DON) Prodrugs with Enhanced CSF Delivery in Monkeys: A Potential Treatment for Glioblastoma. J. Med. Chem. *59*.

148. Rao, W., Wang, S., Duleba, M., Niroula, S., Goller, K., Xie, J., Mahalingam, R., Neupane, R., Liew, A.-A., Vincent, M.*, et al.* (2020). Regenerative Metaplastic Clones in COPD Lung Drive Inflammation and Fibrosis. Cell.

149. Reizis, B. (2019). Plasmacytoid Dendritic Cells: Development, Regulation, and Function. Immunity *50*.

150. Reyfman, P.A., Walter, J.M., Joshi, N., Anekalla, K.R., McQuattie-Pimentel, A.C., Chiu, S., Fernandez, R., Akbarpour, M., Ren, C.-I.C.Z., Verma, R.*, et al.* (2018). Single-Cell Transcriptomic Analysis of Human Lung Provides Insights into the Pathobiology of Pulmonary Fibrosis. Am J Respir Crit Care Med *199*.

151. Robertson, S.J., Lemire, P., Maughan, H., Goethel, A., Turpin, W., Bedrani, L., Guttman, D.S., Croitoru, K., Girardin, S.E., and Philpott, D.J. (2019). Comparison of Co-housing and Littermate Methods for Microbiota Standardization in Mouse Models. Cell Reps *27*.

152. Sauler, M., McDonough, J.E., Adams, T.S., Kothapalli, N., Barnthaler, h., Werder, R.B., Schupp, J.C., Nouws, J., Robertson, M.J., Coarfa, C.*, et al.* (2022).

Characterization of the COPD alveolar niche using single-cell RNA sequencing. Nat. Comm. *13*.

153. Schyns, J., Bai, Q., Ruscitti, C., Radermecker, C., Schepper, S.D., Chakarov, S., Farnir, r., Pirottin, D., Ginhoux, F., Bureau, F., and Marichal, T. (2019). Non-classical tissue monocytes and two functionally distinct populations of interstitial macrophages populate the mouse lung. Nat. Comm.
154. Seimetz, M., Parajuli, N., Pichl, A., Veit, F., Kwapiszewska, G., Weisel, F.C., Milger, K., Egemnazarov, B., Turowska, A., Fuchs, B.*, et al.* (2011). Inducible NOS Inhibition Reverses Tobacco-Smoke-Induced Emphysema and Pulmonary Hypertension in Mice. Cell *147*.
155. Sellami, M., Meghraoui-Kheddar, A., Terryn, C., Fichel, C., Bouland, N., Diebold, M.-D., Guenounou, M., Héry-Huynh, S., and Naour, R.L. (2016). Induction and regulation of murine emphysema by elastin peptides. Am J Physiol Lung Cell Mol Physiol *310*.
156. Seluanov, A., Vaidya, A., and Gorbunova, V. (2010). Establishing Primary Adult Fibroblast Cultures From Rodents. JoVE *44*.
157. Senior, R.M., GRIFFIN, G.L., and MECHAM, R.P. (1980). Chemotactic Activity of Elastin-derived Peptides. J. Clin. Invest. *66*.
158. Shapiro, S.D. (1999). The Macrophage in Chronic Obstructive Pulmonary Disease. Am J Respir Crit Care Med *160*.
159. Shaw, R.J., Lamia, K.A., Vasquez, D., Koo, S.-H., Bardeesy, N., DePinho, R.A., Montminy, M., and Cantley, L.C. (2005). The Kinase LKB1 Mediates Glucose Homeostasis in Liver and Therapeutic Effects of Metformin. Science *310*.
160. Shibata, S., Miyakea, K., Tateishib, T., Yoshikawaa, S., Yamanishia, Y., Miyazakib, Y., Inaseb, N., and Karasuyamaa, H. (2018). Basophils trigger emphysema development in a murine model of COPD through IL-4–mediated generation of MMP-12–producing macrophages. PNAS.
161. Simmons, D.P., Nguyen, H.N., Gomez-Rivas, E., Jeong, Y., Jonsson, A.H., Chen, A.F., Lange, J.K., Dyer, G.S., Blazar, P., Earp, B.E.*, et al.* (2022). SLAMF7 engagement superactivates macrophages in acute and chronic inflammation. Sci. Immunol. *7*.
162. Singh, D. (2022). IL-33 in COPD: the hunt for responder subgroups. Lancet Respir Med *10*.
163. Snider, G., Kleinerman, J., Thurlbeck, W., and Bengali, Z. (1985). The definition of emphysema: Report of a National Heart, Lung, and Blood Institute workshop. . Am Rev Respir Dis. *132*.
164. Snider, G.L., HAYES, J.A., and KORTHY, A.L. (1978). Chronic Interstitial Pulmonary Fibrosis Produced in Hamsters by Endotracheal Bleomycin: Pathology and Stereology. Am Rev Respir Dis *117*.
165. Soberanes, S., Misharin, A.V., Jairaman, A., Morales-Nebreda, L., McQuattie-Pimentel, A.C., Cho, T., Hamanaka, R.B., Angelo Y. Meliton, Reyfman, P.A., Walter, J.M.*, et al.* (2019). Metformin Targets Mitochondrial Electron Transport to Reduce Air-Pollution-Induced Thrombosis. Cell Metabolism *29*.

166. Spix, B., Butz, E.S., Chen, C.-C., Rosato, A.S., Tang, R., Jeridi, A., Kudrina, V., Plesch, E., Wartenberg, P., Arlt, E.*, et al.* (2022). Lung emphysema and impaired macrophage elastase clearance in mucolipin 3 deficient mice. Nat. Comm. *13*.
167. Stegle, O., Teichmann, S.A., and Marioni, J.C. (2015). Computational and analytical challenges in single-cell transcriptomics. Nat. Rev. Gen. *16*.
168. Sterne, J. (1957). Du nouveau dans les antidiabétiques. La NN diméthylamino guanyl guanidine (NNDG). . Maroc Med *36*.
169. Stuart, T., Butler, A., Hoffman, P., Hafemeister, C., Papalexi, E., III, W.M.M., Hao, Y., Stoeckius, M., Smibert, P., and Satija, R. (2019). Comprehensive Integration of Single-Cell Data. Cell *177*.
170. Su, X., Xu, Y., Fox, G.C., Xiang, J., Kwakwa, K.A., Davis, J.L., Belle, J.I., Lee, W.-C., Wong, W.H., Fontana, F.*, et al.* (2021). Breast cancer–derived GM-CSF regulates arginase 1 in myeloid cells to promote an immunosuppressive microenvironment. J. Clin. Invest. *131*.
171. Subramanian, S., Busch, C.J.-L., Molawi, K., Geirsdottir, L., Maurizio, J., Aguilar, S.V., Belahbib, H., Gimenez, G., Anis, R., Yuda, A.*, et al.* (2022). Long-term culture-expanded alveolar macrophages restore their full epigenetic identity after transfer in vivo. Nat. Immunology.
172. Suzuki, S., Ishii, X.M., Asakura, T., Namkoong, H., Okamori, S., Yagi, K., Kamata, H., Kusumoto, T., Kagawa, S., Hegab, A.E.*, et al.* (2020). ADAM17 protects against elastase-induced emphysema by suppressing CD62L leukocyte infiltration in mice. Am J Physiol Lung Cell Mol Physiol *318*.
173. Svedberg, F.R., Brown, S.L., Krauss, M.Z., Campbell, L., Sharpe, C., Clausen, M., Howell, G.J., Clark, H., Madsen, J., Evans, C.M.*, et al.* (2019). The lung environment controls alveolar macrophage metabolism and responsiveness in type 2 inflammation. Nat. Immunology.
174. Tan, S.Y.S., and Krasnow, M.A. (2016). Developmental origin of lung macrophage diversity. Development *143*.
175. Tang, F., Barbacioru, C., Wang, Y., Nordman, E., Lee, C., Xu, N., Wang, X., Bodeau, J., Tuch, B.B., Siddiqui, A.*, et al.* (2009). mRNA-Seq whole-transcriptome analysis of a single cell. Nat. Methods *6*.
176. Tang, S., Ma, T., Zhang, H., Zhang, J., Zhong, X., Tan, C., Qiu, Y., Zeng, W., and Feng, X. (2019). Erythromycin Prevents Elastin Peptide-Induced Emphysema and Modulates CD4+T Cell Responses in Mice. Int J COPD *14*.
177. Termini, C., and Gillette, J. (2017). Tetraspanins Function as Regulators of Cellular Signaling. Front. Cell Dev. Biol. *5*.
178. Tighe, R.M., Redente, E.F., Yu, Y.-R., Herold, S., Sperling, A.I., Curtis, J.L., Duggan, R., Swaminathan, S., Nakano, H., Zacharias, W.J.*, et al.* (2019). Improving the Quality and Reproducibility of Flow Cytometry in the Lung. Am J Respir Cell Mol Biol *61*.
179. Togo, S., Holz, O., Liu, X., Sugiura, H., Kamio, K., Wang, X., Kawasaki, S., Ahn, Y., Fredriksson, K., Skold, C.M.*, et al.* (2008). Lung Fibroblast Repair Functions in Patients with Chronic Obstructive Pulmonary Disease Are Altered by Multiple Mechanisms. Am J Respir Crit Care Med *178*.

180. Tomasek, J., Gabbiani, G., Hinz, B., Chaponnier, C., and A.Brown, R. (2002). MYOFIBROBLASTS AND MECHANO- REGULATION OF CONNECTIVE TISSUE REMODELLING. Nat Rev Mol Cell Biol *3*.

181. Townsend, M.J., Fallon, P.G., Matthews, D.J., Jolin, H.E., and McKenzie, A.N. (2000). T1/ST2-deficient Mice Demonstrate the Importance of T1/ST2 in Developing Primary T Helper Cell Type 2 Responses. J. Exp. Med. *191*.

182. Travaglini, K.J., Nabhan, A.N., Penland, L., Sinha, R., Gillich, A., Sit, R.V., Chang, S., Conley, S.D., Mori, Y., Seita, J.*, et al.* (2020). A molecular cell atlas of the human lung from single-cell RNA sequencing. Nature *587*.

183. Uchida, K., Beck, D.C., Yamamoto, T., Berclaz, P.-Y., Abe, S., Staudt, M.K., Carey, B.C., Filippi, M.-D., Wert, S.E., Denson, L.A.*, et al.* (2007). GM-CSF Autoantibodies and Neutrophil Dysfunction in Pulmonary Alveolar Proteinosis. N Engl J Med *356*.

184. Ural, B.B., Yeung, S.T., Damani-Yokota, P., Devlin, J.C., Vries, M.d., Vera-Licona, P., Samji, T., Sawai, C.M., Jang, G., Perez, O.A.*, et al.* (2020). Identification of a nerve-associated, lung-resident interstitial macrophage subset with distinct localization and immunoregulatory properties. Sci. Immunol. *5*.

185. Vannella, K.M., and Wynn, T.A. (2017). Mechanisms of Organ Injury and Repair by Macrophages. Annu. Rev. Physiol. *79*.

186. Vasamsetti, S.B., Karnewar, S., Kanugula, A.K., Thatipalli, A.R., Kumar, e.M., and Kotamraju, S. (2015). Metformin Inhibits Monocyte-to-Macrophage Differentiation via AMPK-Mediated Inhibition of STAT3 Activation: Potential Role in Atherosclerosis. Diabetes *64*.

187. Villani, A.-C., Satija, R., Reynolds, G., Siranush Sarkizova, Shekhar, K., Fletcher, J., Griesbeck, M., Butler, A., Zheng, S., Lazo, S.*, et al.* (2017). Single-cell RNA-seq reveals new types of human blood dendritic cells, monocytes, and progenitors. Science *356*.

188. Walters, E.H., Shukla, S.D., Mahmood, M.Q., and Ward, C. (2021). Fully integrating pathophysiological insights in COPD: an updated working disease model to broaden therapeutic vision. Eur Respir Rev *30*.

189. Waltman, L., and Van Eck, N.J. (2013). A smart local moving algorithm for large-scale modularity-based community detection. 2013. The European Physical Journal B *86*.

190. Wang, C., Zhou, J., Wang, J., Li, S., Fukunaga, A., Yodoi, J., and Tian, H. (2020a). Progress in the mechanism and targeted drug therapy for COPD. Signal Transduction and Targeted Therapy.

191. Wang, X., Rojas-Quintero, J., Zhang, D., Nakajima, T., Walker, K.H., Peh, H.Y., Li, Y., Fucci, Q.-A., Tesfaigzi, Y., and Owen, C.A. (2020b). A disintegrin and metalloproteinase domain-15 deficiency leads to exaggerated cigarette smoke-induced chronic obstructive pulmonary disease (COPD)-like disease in mice. Mucosal Immunology *14*.

192. Watanbe, C. (1918). STUDIES IN THE METABOLIC CHANGES INDUCED BY ADMINISTRATION OF GUANIDINE BASES. J. Biol. Chem. *33*.

193. WHO (2022). Chronic obstructive pulmonary disease (COPD) - Key Facts. (https://www.who.int/news-room/fact-sheets/detail/chronic-obstructive-pulmonary-disease-(copd)).

194. Wieland, C.W., Windt, G.J.W.v.d., Florquin, S., McKenzie, A.N.J., and Poll, T.v.d. (2009). ST2 deficient mice display a normal host defense against
195. pulmonary infection with Mycobacterium tuberculosis. Microbes and Infection *11*.
196. Wijsenbeek, M.S., Kool, M., and Cottin, V. (2018). Targeting interleukin-13 in idiopathic pulmonary fibrosis: from promising path to dead end. Eur Respir J *52*.
197. Wills-Karp, M., Luyimbazi, J., Xu, X., Schofield, B., Neben, T.Y., Karp, C.L., and Donaldson, D.D. (1998). Interleukin-13: Central Mediator of Allergic Asthma. Science *282*.
198. Wong, L.-Y.R., and Perlman, S. (2022). Immune dysregulation and immuno-pathology induced by SARS-CoV-2 and related coronaviruses — are we our own worst enemy? Nat. Rev. Immun.
199. Wright, J., and Churg, A. (1990). Cigarette smoke causes physiologic and morphologic changes of emphysema in the guinea pig. . Am Rev Respir Dis *142*.
200. Wu, Y., Wang, Q., Li, M., Lao, J., Tang, H., Ming, S., Wu, M., Gong, S., Li, L., Liu, L., and Huang, X. (2023). SLAMF7 Regulates Inflammatory Response in Macrophages During Polymicrobial Sepsis. J Clin Invest.
201. Xia, J., Zhao, J., Shang, J., Li, M., Zeng, Z., Zhao, J., Wang, J., Xu, Y., and Xie, J. (2015). Increased IL-33 expression in chronic obstructive pulmonary disease. Am J Physiol Lung Cell Mol Physiol *308*.
202. Xie, T., Wang, Y., Deng, N., Huang, G., Taghavifar, F., Geng, Y., Liu, N., Kulur, V., Yao, C., Chen, P*., et al.* (2018). Single-Cell Deconvolution of Fibroblast Heterogeneity in Mouse Pulmonary Fibrosis. Cell Reps *22*.
203. Xu-Vanpala, S., Deerhake, M.E., Wheaton, J.D., Parker, M.E., Juvvadi, P.R., MacIver, N., Ciofani, M., and Shinohara, M.L. (2020). Functional heterogeneity of alveolar macrophage population based on expression of CXCL2. Sco. Immunol. *5*.
204. Yamashita, A.S., Rosa, M.d.C., Stumpo, V., Rais, R., Slusher, B.S., and Riggins, G.J. (2020). The glutamine antagonist prodrug JHU-083 slows malignant glioma growth and disrupts mTOR signaling. Neuro-Oncology Adv. *3*.
205. Yang, I.A., Jenkins, C.R., and Salvi, S.S. (2022). Chronic obstructive pulmonary disease in never-smokers: risk factors, pathogenesis, and implications for prevention and treatment. Lancet Respir Med *10*.
206. Yao, Y., Liu, Q., Adrianto, I., Wu, X., Glassbrook, J., Khalasawi, N., Yin, C., Yi, Q., Dong, Z., Geissmann, F*., et al.* (2020). Histone deacetylase 3 controls lung alveolar macrophage development and homeostasis. Nat. Comm.
207. Ye, J., Zhu, N., Sun, R., Liao, W., Fan, S., Shi, F., Lin, H., Jiang, S., and Ying, Y. (2018). Metformin Inhibits Chemokine Expression Through the AMPK/NF-kB Signaling Pathway. Journal of Interferon & Cytokine Research *38*.
208. Yla-Herttuala, S., LIPrON, B.A., ROSENFELD, M.E., GOLDBERG, I.J., STEINBERG, D., and WITZTUM, J.L. (1991). Macrophages and smooth muscle cells express lipoprotein lipase in human and rabbit atherosclerotic lesions. Proc. Natl. Acad. Sci. USA *88*.
209. Yona, S., Kim, K.-W., Wolf, Y., Mildner, A., Varol, D., Breker, M., Strauss-Ayali, D., Viukov, S., Guilliams, M., Misharin, A*., et al.* (2013). Fate Mapping Reveals Origins

and Dynamics of Monocytes and Tissue Macrophages under Homeostasis. Immunity *38*.

210. Yu, X., Buttgereit, A., Lelios, I., Utz, S.G., Cansever, D., Becher, B., and Greter, M. (2017). The Cytokine TGF-b Promotes the Development and Homeostasis of Alveolar Macrophages. Immunity *47*.

211. Zhang, J., Wang, D., Wang, L., Wang, S., Roden, A.C., Zhao, H., Li, X., Prakash, Y.S., Matteson, E.L., Tschumperlin, D.J., and Vassallo, R. (2019). Profibrotic effect of IL-17A and elevated IL-17RA in idiopathic pulmonary fibrosis and rheumatoid arthritis-associated lung disease support a direct role for IL-17A/IL-17RA in human fibrotic interstitial lung disease. Am J Physiol Lung Cell Mol Physiol *316*.

212. Zhao, S., and Zhang, B. (2015). A comprehensive evaluation of ensembl, RefSeq, and UCSC annotations in the context of RNA-seq read mapping and gene quantification. BMC Genomics *16*.

213. Zheng, G.X.Y., Terry, J.M., Belgrader, P., Ryvkin, P., Bent, Z.W., Wilson, R., Ziraldo, S.B., Wheeler, T.D., McDermott, G.P., Zhu, J.*, et al.* (2017). Massively parallel digital transcriptional profiling of single cells. Nat. Comm. *8*.

214. Zheng, T., Zhu, Z., Wang, Z., Homer, R.J., Ma, B., Richard J. Riese, J., Chapman, H.A., Shapiro, S.D., and Elias1, J.A. (2000). Inducible targeting of IL-13 to the adult lung causes matrix metalloproteinase– and cathepsin-dependent emphysema. J. Clin. Invest. *106*.

215. Zilionis, R., Engblom, C., Pfirschke, C., Savova, V., Zemmour, D., Saatcioglu, H.D., Krishnan, I., Maroni, G., Meyerovitz, C.V., Kerwin, C.M.*, et al.* (2019). Single-Cell Transcriptomics of Human and Mouse Lung Cancers Reveals Conserved Myeloid Populations across Individuals and Species. Immunity *50*.